Delft University of Technology

ISBN: 978-94-6108-562-7

Optimum Design of Steered Fibre Composite Cylinders with Arbitrary Cross-Sections

ALI KHANI

Optimum Design of Steered Fibre Composite Cylinders with Arbitrary Cross-Sections

ALI KHANI

Propositions

accompanying the dissertation

OPTIMUM DESIGN OF STEERED FIBRE COMPOSITE CYLINDERS WITH ARBITRARY CROSS-SECTIONS

by

Ali KHANI

1. Circumferential stiffness tailoring increases the buckling capacity of a longitudinally stiffened circular cylinder under bending by two load redistribution mechanisms; one global and the other one local.
2. Optimal *steering* of fibres is more complex than *staring* at the wall and coming up with intuitive ideas.
3. Slower functioning of the brain during frequent task switching is partially due to the multiple pause, restart and refocus steps, which is similar to the extra time required for cut-restart during fiber placement.
4. Lack of mental and physical stress can lead to health problems.
5. Many problems are solved once they are well defined.
6. *"There is only one thing in the long run more expensive than research: no research"*. John F. Kennedy
7. A Persian proverb says *"one who has a larger roof has more snow on it"*, the same stands for a thesis, the thicker the thesis is, more typos there are.
8. No matter how much computational power is increased, structural optimisation remains a challenge.
9. A shortcut sometimes takes longer time and more effort.
10. As a foreigner, no matter what you come to study in Netherlands, you have to learn more about medicine.
11. The odrer of the lerttes in a wrod is not ipmortnat, as lnog as the frist and lsat lerttes are in the rhigt palce you can raed it.

These propositions are regarded as opposable and defendable, and have been approved as such by the supervisor prof. dr. Z. Gürdal.

Stellingen

behorende bij het proefschrift

OPTIMUM DESIGN OF STEERED FIBRE COMPOSITE CYLINDERS WITH ARBITRARY CROSS-SECTIONS

door

Ali KHANI

1. De maximale kinkbelasting van een in de lengte verstevigde cylinder belast door een buigmoment is te verhogen door de laminaatstijfheid in omtreksrichting te variëren, dit dankzij twee verschillende kracht herverdelingsmechanismen, een globale krachtherverdeling en lokale krachtherverdeling.
2. Het optimaal sturen van vezelpaden is ingewikkelder dan naar een muur staren en met intuïtieve ideeën komen.
3. De hersen functies worden langzamer bij het frequent schakelen tussen verschillende taken, dit komt deels door the feit dat je hersenen moeten pauzeren, opnieuw opstarten en zich heroriënteren. Een vergelijkbaar proces ("cut-restart") is ook aanwezig bij het bepalen van vezelpaden.
4. Een tekort aan mentale of fysieke stress kan tot gezondheidsproblemen leiden.
5. Veel problemen worden opgelost zodra ze goed zijn gedefinieerd.
6. *"Het enige wat op lange termijn meer kost dan onderzoek: geen onderzoek"* - John F. Kennedy
7. Een Perzisch gezegde luid: *"Iemand met een groter dak heeft meer sneeuw"*, hetzelfde geldt voor een proefschrift, hoe langer het proefschrift, des te meer spelfouten/typefouten het bevat.
8. Ongeacht de toename in rekenkracht, blijft de optimalisatie van constructies een groot uitdaging.
9. Een kortere route kan soms meer tijd en moeite kosten.
10. Het maakt niet uit wat je als buitenlander in Nederland komt studeren, je zult meer over geneeskunde moeten leren.
11. De vlorgode van lerttes in een wrod is neit blinegrajk, als de eretse en de ltsaate lerttes op de jsiute pltaas satan, is het wrood te leezn.

Deze stellingen worden opponeerbaar en verdedigbaar geacht en zijn als zodanig goedgekeurd door de promotor prof. dr. Z. Gürdal.

Optimum Design of Steered Fibre Composite Cylinders with Arbitrary Cross-sections

Optimum Design of Steered Fibre Composite Cylinders with Arbitrary Cross-sections

Proefschrift

ter verkrijging van de graad van doctor
aan de Technische Universiteit Delft,
op gezag van de Rector Magnificus Prof. ir. K. C. A. M. Luyben,
voorzitter van het College voor Promoties,
in het openbaar te verdedigen op dinsdag 10 december 2013 om 10:00 uur

door

Ali Khani

Master of Science in Mechanical Engineering,
University of Imam Hossein, Tehran, Iran
en geboren te Esfahan, Iran.

Dit proefschrift is goedgekeurd door de promotor:

Prof. dr. Z. Gürdal

Copromotor: Dr. M.M. Abdalla

Samenstelling promotiecommissie:

Rector Magnificus,	voorzitter
Prof. dr. Z. Gürdal	Technische Universiteit Delft, promotor
Dr. M.M. Abdalla	Technische Universiteit Delft, copromotor
Prof. dr. ir. M.L. Kaminski	Technische Universiteit Delft
Prof. dr. L. Lessard	McGill University, Canada
Prof. dr. P. Marzocca	Clarkson University, USA
Prof. dr. ing. P. Middendorf	Universität Stuttgart, Duitsland
Prof. dr. Y. Narita	Hokkaido University, Japan
Prof. dr. ir. L.J. Sluys	Technische Universiteit Delft, reservelid

TU Delft

Keywords: Variable Stiffness, Cylindrical Shells, Fibre steering, Fibre Placement, Buckling, Strength

Printed by: Gildeprint Drukkerijen, Enschede, The Netherlands

Cover design: by Maryam Taghipour

Front cover: Artistic impression of two aircrafts made of composite laminates with steered and straight fibre layers

Back cover: Steered fibre paths in one layer of laminate of a longitudinally stiffened circular cylinder under bending plotted on the expanded surface of the cylinder

ISBN: 978-94-6108-562-7

An electronic version of this dissertation is available at
http://repository.tudelft.nl/.

There was a Door to which I found no Key
There was a Veil past which I could not see
Some little Talk awhile of ME and THEE
There seemed–and then no more of THEE and ME

Robaiyat of Omar Khayyám
Translated by Edward FitzGerald

اسرار ازل را نه تو دانی و نه من   وین حرف معما نه تو خوانی و نه من

هست از پس پرده گفتگوی من و تو   چون پرده در افتد نه تو مانی و نه من

رباعیات عمر خیام

To Fatemeh

Contents

1 Introduction **3**
- 1.1 Introduction . . . 3
- 1.2 Tailoring of composite laminates . . . 4
  - 1.2.1 Types of composite laminates . . . 4
- 1.3 Automated fibre placement . . . 5
  - 1.3.1 AFP manufacturing limitations . . . 8
- 1.4 Design of fibre steered laminates . . . 10
  - 1.4.1 Functional fibre path definition . . . 11
  - 1.4.2 Discrete stiffness variation . . . 14
- 1.5 Laminated cylindrical shells . . . 16
  - 1.5.1 Stiffness tailoring methods . . . 16
- 1.6 Overview of this thesis and motivation . . . 24

2 Basic background **27**
- 2.1 Introduction . . . 27
- 2.2 Background on geometry of thin shells . . . 29
  - 2.2.1 Middle surface . . . 29
  - 2.2.2 Thin shell . . . 32
- 2.3 Strain-displacement relations in thin shells . . . 32
  - 2.3.1 Linear strain-displacement relations . . . 33
  - 2.3.2 Nonlinear von Karman strain-displacement relations . . . 38
- 2.4 Strain-displacement relations in thin cylindrical shells . . . 39
  - 2.4.1 Cylindrical surfaces . . . 40
  - 2.4.2 Equations of Sanders . . . 41
  - 2.4.3 Longitudinally stiffened thin cylindrical shells . . . 42
- 2.5 Constitutive relations of laminates . . . 45
  - 2.5.1 Classical lamination theory . . . 46
  - 2.5.2 Lamination parameters . . . 51
  - 2.5.3 Feasible region of lamination parameters . . . 52

3 Semi-analytical static and buckling solutions of cylinders 55
3.1 Introduction . . . 55
3.2 St. Venant's problem of anisotropic inhomogeneous cylinders . . . 58
3.2.1 Semi-analytical finite element solution . . . 60
3.2.2 Displacement fields for Saint-Venant's solution . . . 63
3.2.3 Extension-bending-torsion problem . . . 64
3.3 Static analysis of cylindrical shells . . . 67
3.3.1 Unstiffened cylindrical shells . . . 68
3.3.2 Longitudinally stiffened cylindrical shells . . . 76
3.4 Buckling analysis of cylindrical shells . . . 78
3.4.1 Unstiffened cylindrical shells . . . 79
3.4.2 Longitudinally stiffened cylindrical shells . . . 81
3.5 Analysis verification and parametric study . . . 83
3.5.1 Static analysis verification . . . 83
3.5.2 Parametric study of structural stiffness . . . 85
3.5.3 Buckling analysis verification . . . 91

4 Multi-step optimisation framework 97
4.1 Introduction . . . 97
4.2 Multi-step optimisation framework . . . 99
4.3 Structural approximation methods . . . 102
4.3.1 Local function approximation . . . 104
4.3.2 Convex conservative separable approximations . . . 105
4.3.3 Convex separable approximation . . . 106
4.3.4 Enforcing strict conservativeness . . . 111
4.4 Step one: Conceptual stiffness design . . . 112
4.4.1 Approximate subproblem . . . 113
4.4.2 Multi-modal and min-max optimization . . . 115
4.4.3 Constraint screening . . . 118
4.5 Step two: Realistic stacking sequence design . . . 119
4.5.1 Steering curvature . . . 119
4.5.2 Gradient-based optimisation . . . 120
4.5.3 Initialisation of retrieval procedure . . . 123
4.6 Step three: Steered fibre paths . . . 124

5 Strength evaluation and approximation 127
5.1 Introduction . . . 127
5.2 Conservative Tsai-Wu failure envelope . . . 129
5.3 Elliptical formulation of the conservative envelope . . . 133
5.4 Strength constraint formulation . . . 137

5.5 Convex approximation of failure index . . . 141
5.5.1 Local Convex Approximation . . . 142
5.5.2 Hybrid approximation . . . 143
5.6 Verification of strength formulation . . . 143

6 Optimisation results for unstiffened cylinders 147
6.1 Introduction . . . 147
6.2 Circular cylinder under bending . . . 148
6.2.1 Theoretical constant thickness laminate . . . 149
6.2.2 Theoretical variable thickness laminate . . . 156
6.2.3 Realistic constant thickness laminate . . . 163
6.3 Elliptical cylinder under axial compression . . . 170
6.3.1 Theoretical constant thickness laminate . . . 171
6.3.2 Theoretical variable thickness laminate . . . 173
6.3.3 Realistic constant thickness laminate . . . 177

7 Optimisation results for stiffened circular cylinder 185
7.1 Introduction . . . 185
7.2 Maximum buckling moment design . . . 187
7.2.1 Theoretical constant thickness laminate . . . 188
7.2.2 Theoretical variable thickness laminate . . . 193
7.2.3 Realistic constant thickness laminate . . . 201
7.3 Maximum buckling moment design with constraint on strength . . 207
7.3.1 Theoretical Constant thickness laminate . . . 207
7.3.2 Realistic constant thickness laminate . . . 214

8 Conclusions and recommendations 219
8.1 Conclusions . . . 219
8.2 Recommendations . . . 224

A Sensitivity analysis 227
A.1 Strength . . . 227

References 229
References . . . 229

Summary 243

Samenvatting 247

PREFACE

In the past few years, my main research interest was design optimisation of composite laminated structures with a focus on steered fibre laminates. During my PhD, I investigated steered fibre laminate design aspects of cylindrical shells with arbitrary cross-sections, details of which are documented in this thesis. Being involved in other research and industrial projects, gave me the opportunity to explore the benefits of using steered fibre laminates in some different applications, both numerically and experimentally. All in all, my contribution to the field may seem like a tiny step in the long journey started and continued by the pioneers of the field and other researchers, to whom I am grateful. In case my tiny step can help future researchers to move forward, I would be happy. Bob Marley said it best, *"Though the road's been rocky it sure feels good to me."*

Every moment of my journey is filled in with the memories of people, specially those whose profound impact requires sincere acknowledgment. My cordial gratitude to these people cannot be expressed by words; my promoter, co-promoter, collaborators, colleagues, friends, my family, devoted parents, brothers and my lovely wife and her family. I am indebted to all of you since this journey could not be undertaken and accomplished without your help. Thank you for the support, discussions, correcting my mistakes, sharing your thoughts, ideas and codes, sharing your moments of happiness and encouragement in the moments of frustration and sadness. Finally, thank you reader, you have already read one page of my dissertation.

Ali Khani
Delft, December 2013

1

Introduction

1.1 Introduction

Composite materials consist of two or more materials which together produce desirable properties that cannot be achieved with any of the constituents alone [1]. The different synthetic composite materials in use today, range from ceramics composites and construction concretes to fibre-reinforced polymers (FRPs).

Fibre-reinforced composite materials contain high strength and high modulus fibres e.g. carbon or glass as the main load carrying element and a matrix material e.g. a thermoset or thermoplastic polymer as the element which bonds fibres together. Due to their composition, fibre-reinforced materials have higher specific strength and stiffness properties than metals, which makes them suitable candidates for light-weight structures. The various types of fibre-reinforced composites include short fibre composites, woven and laminated composites which consist of fibre-matrix layers.

Due to the higher stiffness and strength of fibres in the fibre direction, fibre-reinforced composites, and as such laminated composites, exhibit directional or anisotropic material properties. This means that a material property at a certain location will differ depending on the direction in which it is measured. The directional properties of a fibre-reinforced lamina are symmetric with respect to the orthogonal planes of symmetry, which are normal to the laminate in the fibre direction and perpendicular to it. Laminates with anisotropic properties, which are symmetric about some orthogonal planes, are called orthotropic laminates.

1.2 TAILORING OF COMPOSITE LAMINATES

The directional properties of composite materials provide extra design variables compared to isotropic materials e.g. metals. The directional stiffness properties of a laminate with a certain number of layers and made of certain materials can be altered by changing the ply fibre angles or by varying the order of placing the plies with certain fibre angles in the laminate i.e. the stacking sequence. These design variables together with the number of layers and the material type, which can be different for different plies, provide a larger design space than that available when metals are used.

Composite laminates are traditionally composed of a number of plies consisting of straight fibres set in a matrix. Therefore, directional stiffness properties are the same everywhere in the laminate. However, due to the recent improvements in the composites manufacturing technology, non-conventional laminates can be built which have different stiffness properties in different regions or points of the laminate. Spatial variation of laminate stiffness properties enlarges the design space compared to the laminates with constant laminate stiffness properties and hence provides a larger room for structural performance improvements. The different types of laminates are discussed below.

1.2.1 TYPES OF COMPOSITE LAMINATES

Composite laminates are divided into two categories; constant stiffness and variable stiffness laminates.

Constant stiffness laminates

In conventional laminates, which are made of straight fiber plies, only one set of stiffness properties exists for the whole laminate. Therefore, these laminates are called constant stiffness or simply CS laminates (figure 1.1). The design variables of CS laminates may include the ply fibre angles, order of placement of plies with certain fibre angles, number of the plies and material type. For a broad review of the design methods of CS laminates, the interested reader is referred to [2].

Variable stiffness laminates

Stiffness properties of non-conventional laminate will vary from one location in the laminate to another. Therefore, these laminates are called variable stiffness or simply VS laminates. Stiffness variation can be achieved by altering the layup from one location to the other, either by blending different CS laminates located in different regions of a structure or by steering the fibres in each ply of the laminate using curvilinear rather than straight paths.

-Blended laminates

Blended laminates consist of discrete regions with different numbers of straight fibre layers (figure 1.1). Between the neighboring regions, some of the layers are dropped and some are common. The neighboring laminates are blended through the common layers ensuring continuity of the whole laminate. Therefore, the stacking sequences and stiffness properties of blended laminates is altered in different regions through changing the number of layers and the stacking sequence. The design space of blended laminates is larger than the design space of the CS laminates and usually larger improvements in structural performance can be expected. Different design methods for blended laminates are reviewed by Ghiasi et al. [3] and Van Campen [4].

-Steered fibre laminates

Using automated fiber placement (AFP) machines, it is possible to place fibres in curvilinear paths in each ply of a laminate. Steered fibre laminates contain layers with curvilinear fibres instead of straight fibres (figure 1.1). Due to the continuous fibre angle variation within each steered fibre ply, laminate stiffness will be continuously altered in the laminate. Therefore, the design space includes the stacking sequence at every spatial location of the laminate. Due to the larger design space available for steered fibre laminates compared to CS and blended laminates, larger structural improvements and more complicated structural optimisation problems can be expected. For extensive reviews on different modeling, analysis and optimisation methods of steered fibre laminates, the interested reader is referred to [3], [5] and [6].

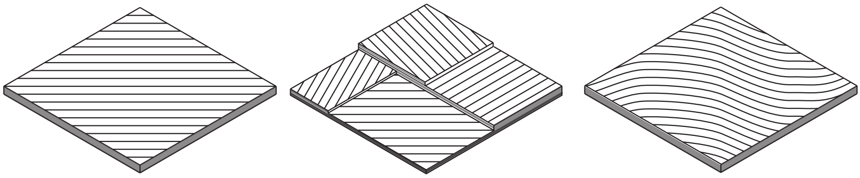

FIGURE 1.1: Different levels of complexity in laminate tailoring

1.3 AUTOMATED FIBRE PLACEMENT

Automated fibre placement (AFP) and automated tape laying (ATL) are two computer - controlled composite manufacturing methods which layup a surface using tows and tapes, respectively. Each tow or tape comprises a bundle of unidirectional fibres. Tows are typically 1/8, 1/4 or 1/2 inch wide, while tapes are wider,

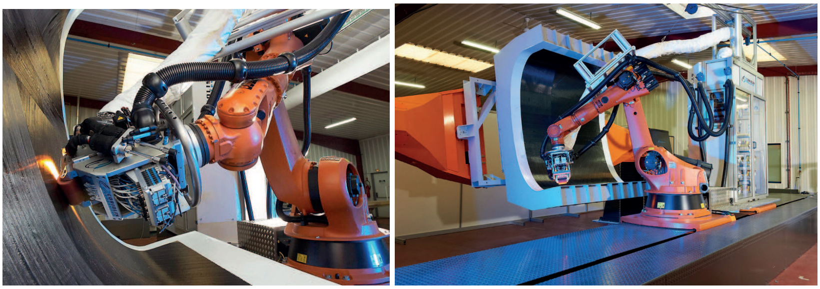

(a) (b)

FIGURE 1.2: An automated fibre placement machine placing 8 tows each 1/4 inch wide (Coriolis Composites)

typically 3, 6 or 12 inch wide. Usually fibre placement heads are capable of placing up to 32 tows in one pass. Each band of simultaneously placed tows is called a course.

Although fibre placement machines are capable of placing different materials including thermoset and thermoplastic materials or dry fibres, here the material is assumed to be a thermoset pre-impregnated tow, which is the most commonly used material for fibre placement. A fibre placement machine is typically composed of a control unit, a robotic arm or a gantry system, a material storage center and a fibre placement head (figure 1.2). The fibre placement head is mounted on the robotic arm or gantry system which is controlled via the control unit and provides enough degrees of freedom for the head to access every point of the tool surface. Sometimes in addition to the degrees of freedom due to the robotic arm or the gantry system, an extra degree of freedom is available via the mandrel rotation. The resin pre-impregnated tows are stored on spools in a storage chamber in which the air temperature, humidity, etc. are controlled. The prepreg tows are pre-tensioned and guided to the tool surface through some pinching rollers (figure 1.3). Prior to the tow placement on the tool surface, the tows experience controlled heating by a heating unit to increase their tackiness to the surface. The preheated tows are placed on the surface with a compaction roller which helps to remove the trapped air between the tow and the surface and to adhere the tows securely to the tool surface. The driving force which moves the tows for the spools to the surface is the friction between the tow, compaction roller and the tool surface [5].

In AFP, individual supply of tows and their relatively small width, material tack-

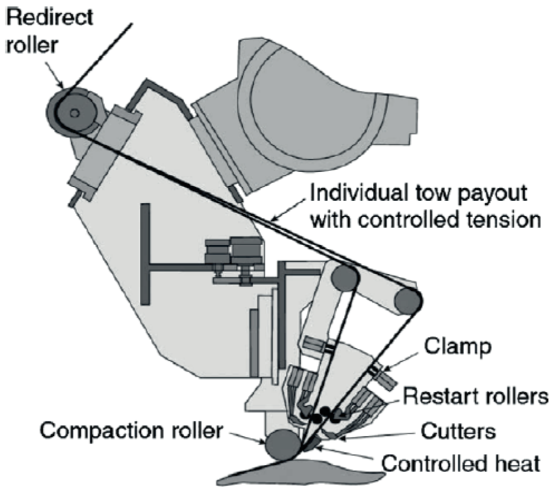

FIGURE 1.3: AFP machine head (Evans [7])

iness and the compaction roller allow the prepreg tows to be placed on complex surfaces, e.g. double curved, and/or in curved paths. However, it is only possible to lay wider tapes, which are used in ATL, on flat or simple surfaces and in straight paths. In AFP and ATL, tows or tapes are not always placed in the perpendicular direction to the part boundaries and hence jagged or saw-tooth boundaries appear which should be cut for the final product. Due to the small widths of tows in AFP, the amount of scrap material at the part boundaries is less than that of ATL (figure 1.4).

As mentioned before, AFP machines can be used to manufacture laminates with steered fiber path plies. Typical fibre placed straight and steered fibre laminates are shown in figure 1.5. In general, the steered fibre paths in a ply are not constrained to be parallel to each other and since the width of each course is constant, some gaps and overlaps appear between every two successive courses (figure 1.9). Therefore, in addition to the spatial change of fibre angles in the plies of steered fibre laminates, the laminate thickness and number of layers may also change from one location to the other. Gaps and overlaps may appear even with straight fibres placed on some surface geometries. For example in conical surfaces, the cross-section is reduced from the base to the vertex. Therefore, if the straight courses are placed adjacent to each other to cover the base, they would overlap on the smaller cross-sections.

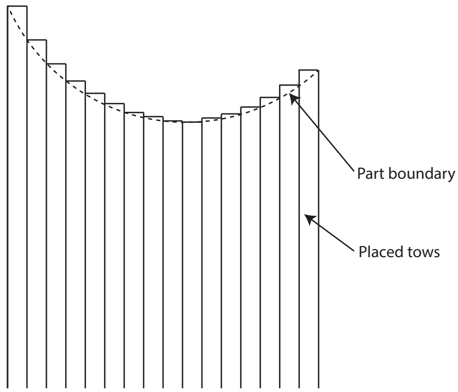

FIGURE 1.4: Jagged or saw-tooth boundaries (regenerated from Tatting and Gürdal [8])

Another advantage of AFP over ATL is the ability to cut and restart individual tows using cutters and restart rollers in the machine head (figure 1.3). Therefore, the course width can be changed in any location by dropping or restarting individual tows. This course width variation can be used to minimise gaps and overlaps due to fibre steering or a specific surface geometry. Cutting the tows individually at the edge of the tool surface, further eliminates the amount of scrap material (figure 1.4).

In spite of all the above discussed advantages of AFP over ATL, the deposition rate and manufacturing throughput for AFP is lower than for ATL and hence AFP is usually used for layup of relatively small surfaces. Therefore, a trade-off is always made between the advantages of AFP and manufacturing throughput of ATL.

1.3.1 AFP MANUFACTURING LIMITATIONS

The AFP manufacturing method has some limitations which should be considered by the designer, these include [6]:

- collision of machine head and mould,
- fibre bridging,
- jagged or saw-tooth boundaries,
- deviation of manufactured fibre angles from the designs,
- rate of fibre placement,

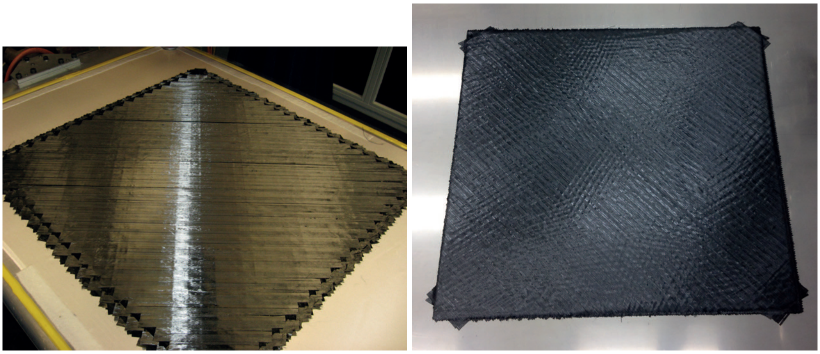

(a) Straight fibre laminate (b) Steered fibre laminate

FIGURE 1.5: Fibre placed laminates (Courtesy of CoDeT engineering)

- minimum length of tows due to cutting,
- gaps and overlaps,
- maximum curvature of steered tows,

Depending on the AFP machine characteristics and the part geometry, collision of the machine head with the mould and fibre bridging may happen. In addition, material tackiness and fibre path influence the possibility of fibre bridging. If the tows are not placed in the perpendicular direction to the part boundaries, jagged or saw-tooth boundaries appear (figure 1.4). The manufactured steered fibre paths may deviate from the designs due to machine tolerances e.g. when using dry fibres. Even if the centreline of a steered course is aligned exactly in the direction for which it is designed, the fibre angles at the boundaries of the course will deviate from that in the centreline. The fibre paths and the course width influence the amount of this deviation. The rate of the fibre placement depends on the machine, geometry, material, fibre path and course width. There is a distance between the cutters and the compaction roller in a fibre placement machine head which determines the minimum length of the tow between starting the placement and the cut. As mentioned before gaps and overlaps happen due to the surface geometry or the steered fibre paths and their amount is influenced by the course width [6].

By placing the tows in curved paths, the fibres which are located inside each turn are compressed. A maximum steering curvature exists for each course, which depends on the type of the material used and the course width, and steering beyond this maximum may cause the tows to wrinkle inside of the turn (figure 1.6) and reduce the product quality.

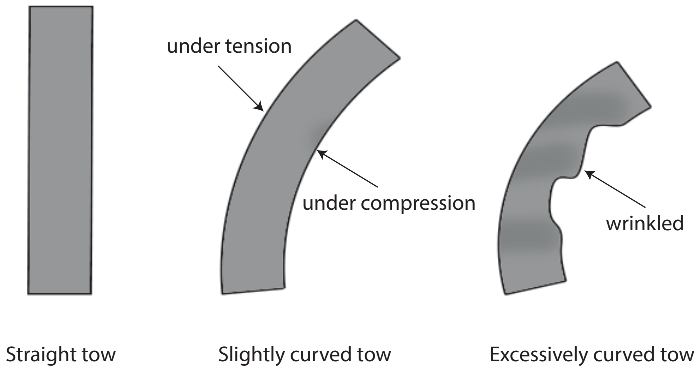

FIGURE 1.6: Wrinkling due to increased steering curvature (regenerated from Van Campen [4])

1.4 DESIGN OF FIBRE STEERED LAMINATES

The effect of curvilinear fibre paths in improving the efficiency of composite structures is investigated by different researchers, for example; Deturk et al. [9], Yau and Chou [10], and Gunderson and Lute [11] produced curvilinear fibres around a hole in a composite plate by putting metal pins into the woven fabric or laminate before curing (figure 1.7). Their research showed improvement in open hole compressive and tensile strength of curvilinear fibre composite plates compared to traditional straight fibre ones with drilled holes. Jones and Platts [12] used different internal fibre geometries to compare the strength and stiffness performance of pin-loaded holes in composite plates. Tosh and Kelly [13] used the strategy of aligning the fibres with principal stress vectors and load paths to increase the strength of a component with an open hole and a pin-loaded hole under tension.

Although the enlarged design space, due to fibre steering, provides a larger room for structural performance improvements, the complexity of the optimisation problem is also increased. Extensive and broad reviews on different modeling, analysis and optimisation methods of steered fibre laminates are available

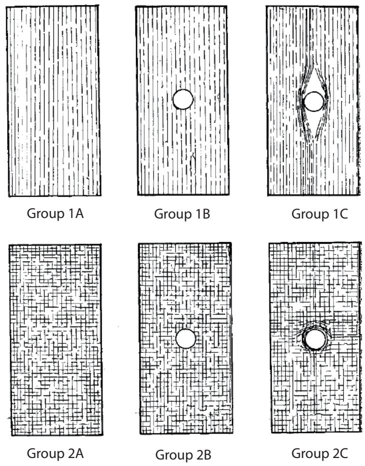

FIGURE 1.7: Different fibre orientations around the hole in the test specimen (Deturk et al. [9])

in [3], [5] and [6]. However, here as an introduction to different design methods of steered fibre laminates, methods of stiffness variation modeling and some examples are briefly explained.

Two main approaches are used by different researchers to model the laminate stiffness variation in steered fibre laminates; continuously varying the fibre angles by defining a functional fibre path which is the reference for other fibre paths covering the whole laminate or assigning different stiffness properties to different discrete regions, locations or points of a composite structure.

1.4.1 FUNCTIONAL FIBRE PATH DEFINITION

Continuous variation of laminate stiffness properties can be modeled by using curvilinear fibre paths which are expressed as functions of location in the laminate. Parameters defining these functions can be used as design variables to optimise the structural efficiency. Gürdal and Olmedo [14] introduced a fibre path parameterisation in which the fibre angle varies linearly in x or y directions of a plate. This definition of fibre paths was generalised by Tatting and Gürdal [15] through allowing the linear fibre angle variation to happen in any arbitrary direction in the plate (figure 1.8). The limited design space, due to the predefined fibre angle variation scheme, can be enlarged by dividing the fibre angle variation direction into multiple segments and assigning an independent fibre path function to each segment. For example Blom et al. [16] and Blom et al. [17] divided the axial direction on a conical surface and circumferential direction on a circular cylinder into multiple segments and used a linear fibre angle variation and a constant curvature fibre path for each segment, respectively.

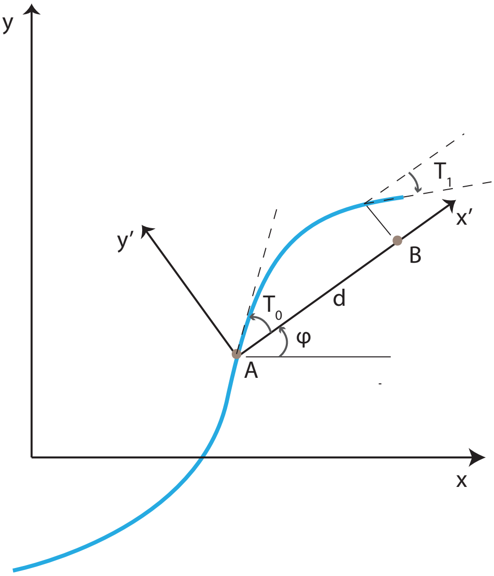

FIGURE 1.8: Linear fibre angle variation between fibre angle T_0 at point A and T_1 at point B placed on x' axis (the angle between x' and x axes is denoted by φ) (Tatting and Gürdal [15])

Blom et al. [18] defined geodesic, constant angle and constant curvature fibre paths for conical surfaces. Examples of other functions used for defining the fibre path along a single direction are the cubic polynomial, parabolic, cubic Bezier curves and linear combination of b-splines used by Parnas et al. [19], Honda et al. [20], Parnas et al. [19], and Honda et al. [21], respectively. Nagendra et al. [22] represented the fibre paths as a linear combination of certain predefined basis fibre paths and coefficients of different basis fiber paths are used as design variables. Each basis fiber path is a non-uniform rational b-spline (NURBS) curve which interpolates between certain control points. Honda and Narita [23] used a cubic polynomial, defined as a function of both coordinates of a surface, for fibre angle distribution. Also Alhajahmad et al. [24] defined a nonlinear function using Lobatto- Legendre polynomials for spatial distribution of fibre angle in terms of both coordinates of a surface.

The configuration of the curvilinear fibre paths, required to cover the steered

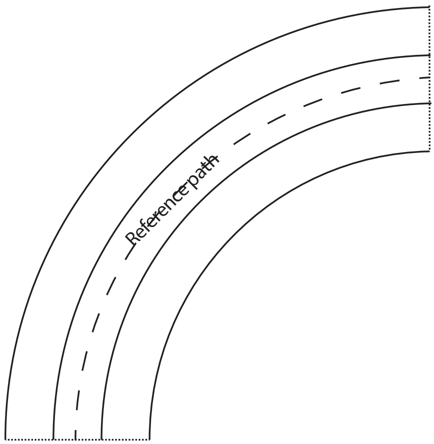

(a) Parallel fibre paths

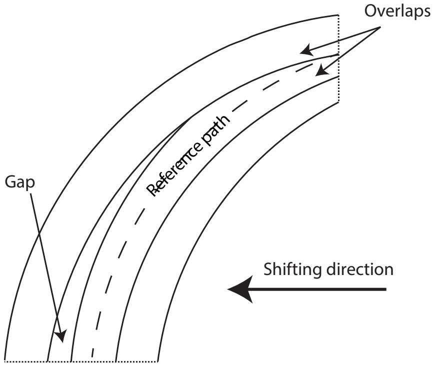

(b) Shifted fibre paths

FIGURE 1.9: Parallel and shifted methods

fibre ply area, can be constructed from the optimised reference fibre path using either of the two methods proposed by Waldhart et al. [25]; shifted or parallel methods (figure 1.9). In the shifted method, the reference fibre path is shifted in the perpendicular direction to the direction of fibre angle variation to cover the whole ply area. In the parallel method, all the fibre paths in a ply are placed parallel to the reference fibre path.

The functional fibre path definition has the advantage of ensuring the continuity of fibre paths and implementation of AFP manufacturing constraints in the curvilinear fibre path definition. The drawback is the limited design space due to the predefined function and fibre paths which are restrained to be parallel to or shifted from the original fibre path. Another drawback is that the optimisation problem for some structural responses is non-convex when formulated in terms of fibre angles and hence local optima exist. The non-convex optimisation problems need solution strategies such as genetic algorithm (GA) to find the global optimum. These algorithms usually need to perform a lot of structural analyses, and become computationally intractable specially when high fidelity models containing manufacturing details are used.

1

1.4.2 DISCRETE STIFFNESS VARIATION

One of the primary attempts to model the laminate stiffness variation in a steered fibre laminate was to divide the structure domain into several discrete regions and assign an independent laminate stiffness to each region (figure 1.10). Optimisation of the ply angles and stacking sequence at each region independently is investigated by different researchers such as Katz et al. [26], Hyer and Lee [27], Hyer and Charette [28] and Haftka and Starnes [29]. One of the disadvantages of assigning independent laminate stiffness properties to different discrete regions of the structure, is the discontinuity of the optimum stacking sequences between discrete regions.

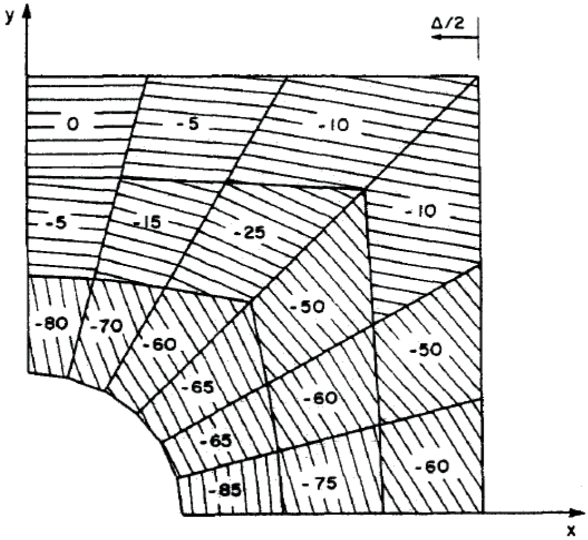

FIGURE 1.10: Distribution of fibre angles in 18 discrete regions which maximises the buckling load in a $[\pm 45, \theta_6]_s$ laminate (Hyer and Lee [27])

Independent laminate stiffness properties could be assigned to each node or element in the finite element model. For example Huang and Haftka [30] performed stiffness tailoring to improve the compressive strength of a plate with a hole by assigning local fibre angles to each element in the finite element model. Honda and Narita [23] assigned the fiber angle of each element in the finite element model of each layer as a design variable to maximise the fundamental frequency (figure 1.11). The advantage of discrete stiffness modeling strategy is providing a larger design space than the functional fibre path definition and therefore larger improvements are expected. The drawbacks are the possible fibre discontinuity or abrupt fibre angle variation between nodes or elements, the dependency of the number of design variables to the mesh density and the non-convexity of the structural optimisation problems when formulated in terms of fibre angles.

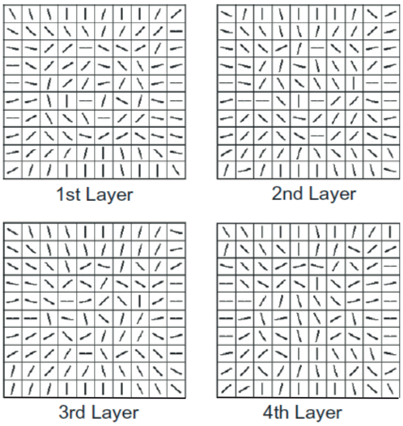

FIGURE 1.11: Optimal distribution of fibre angles in the layers of a symmetric 8-layered laminate for maximum fundamental frequency of a fully clamped plate (Honda and Narita [23])

To remedy the local optima problem, Setoodeh et al. [31], Abdalla et al. [32], and IJsselmuiden et al. [33] built convex approximations of structural stiffness, fundamental frequency and buckling factor, respectively, in terms of laminate stiffness matrices. Using the developed convex approximations of structural responses, the original optimisation problem is substituted by an approximate convex subproblem which is solved using a successive approximation scheme to find the optimum distribution of laminate stiffness matrices. The laminate stiffness properties are parameterised in terms of lamination parameters (see subsection 2.5.2) and laminate stiffness variation is modeled by assigning an independent set of lamination parameters to discretisation point. Since the laminate stiffness properties can be expressed as linear functions of lamination parameters and the feasible region of lamination parameters is convex, a convex optimisation problem is formulated. Lamination parameters have other properties which make them suitable for laminate stiffness parameterisation (see subsection 2.5.2).

The disadvantage of using lamination parameters as design variables is the lack of detailed tow, course and ply information which is required for an evaluation of manufacturing constraints. Therefore, a post-processing step is required to retrieve the optimum fibre angles from the optimum distribution of lamination parameters. Pilaka [34], Van Campen et al. [35], Setoodeh et al. [36], Blom et al. [37] and Nagy et al. [38] developed methods for retrieving the fibre angles, while implementing the manufacturing constraints, and generation of smooth steered fibre paths. The multi-step optimisation framework introduced in chapter 4 is based on the aforementioned approach of finding the optimum laminate stiffness distribution and retrieving the fibre angles from that in a post-processing step.

1.5 LAMINATED CYLINDRICAL SHELLS

Cylindrical shells are one of the widely used structural components in aircrafts and aerospace vehicles, e.g. fuselage and rocket motor skirt, in containers, e.g. tanks, reservoirs, pressure vessels, in pipes and tubes, in submarine and ship structures and etc.. Although a lot of cylindrical shells have circular cross-sections, some specific applications may dictate using cylindrical shells with non-circular cross-sections e.g. the non-circular cross-section fuselage used for blended wing-body aircrafts and non-circular cross-section fuel tanks used in launch vehicles which are dictated by the specific aerodynamic or geometric requirements [39]. The high specific stiffness and strength properties of composites have motivated the design and manufacturing of lightweight and efficient fibre reinforced laminated composite thin cylinders. Different design tailoring methods of composite cylindrical shells are reviewed in subsection 1.5.1.

1.5.1 STIFFNESS TAILORING METHODS

In this subsection, the different tailoring methods for laminated cylindrical shells with straight fibre, segmented-stiffness, variable thickness and steered fibre laminates are reviewed.

Straight fibre laminated cylinders

Stiffness tailoring methods for straight fibre laminated cylinders are divided into two groups; the first group uses ply angles and number of plies as design variables and the second group uses lamination parameters and laminate thickness. Most of the research on tailoring of straight fibre laminated cylinders fall under the first group. However, as mentioned before, lamination parameters are used as intermediate design variables in the multi-step optimisation framework developed in chapter 4. Therefore, in this subsection tailoring methods using ply angles as design variables are briefly described and more emphasis is on the methods using lamination parameters.

-Ply angles as design variables

Some researchers e.g. Tasi [40], ZitzEvancih [41], Tripathy and Rao [42] and Rao and Shyju [43] found the optimum stacking sequence from a predefined set of ply angles by choosing number of each ply angle and their order in the laminate. For example, Rao and Shyju [43] use a meta-heuristic algorithm, which combines the good features of the popular guided local search algorithms such as simulated annealing (SA) and tabu search (TS), to find the optimum stacking sequence composed of $0°$, $+45°$, $-45°$ and $90°$ plies in a hybrid laminate composite cylinder made of carbon-epoxy and glass-epoxy under loads including axial thrust and torque. The optimisation problem is formulated to minimise the weight and cost subject to constraints on the buckling load factor and strength level factor. Combinatorial constraints include ply balancing, ply contiguity e.g. no more than four plies in the same direction and no more than $45°$ difference between the ply angle of adjacent layers.

In some investigations e.g. the works by Kobayashi et al. [44], Hu and Wang [45], Liang and Chen [46], Kim et al. [47], the optimum stacking sequence is selected from a combination of predefined set of ply angles and variable ply angles. For example, Kobayashi et al. [44] find the optimum laminate including layers with 0, 90, $+\theta$ and $-\theta$ fiber orientations for maximum buckling load composite cylinders with 2, 3, 4, 6 and 8 layers. The effect of pre-buckling deformation on the buckling loads was also investigated.

In other studies, stacking sequence is not restricted by containing one or a set of predefined ply angles and all the ply angle values are selected as design variables. Examples include the investigations by Hirano [48], Nshanian and Pappas [49], Min and De Charentenay [50], Sun and Hansen [51], Sun [52], Adali et al. [53], Zimmermann [54], Xie et al. [55], Walker et al. [56] Walker et al. [57], Smerdov [58] and Smerdov [59], Adali et al. [60], Foldager et al. [61], Messager et al. [62], Walker and Smith [63], Tabakov and Summers [64], Azarafza et al. [65], Lindgaard et al. [66], Maalawi [67], and Yuan et al. [68]. For example, Sun and Hansen [51] use a two step optimisation approach to find the optimum laminae fibre orientations to maximise the buckling capacity of a laminated circular cylinder under axial compression, external pressure, torsion or a combination of these. The two step approach is implemented using a random search to select an initial guess in the first step and a systematic search based on Powell's technique [69]. The function expressing the buckling load in terms of the ply orientations is not convex and hence many local maxima exist. The random search in the two step strategy is intended to separate the largest local maxima for the second step. Adali et al. [60] found the optimum fibre orientation of each ply which minimises the sensitivity of buckling load with respect to variations in the ply angles in laminated cylindrical shell of finite length under combined axial compression and external pressure. Foldager et al. [61] use mathematical programming to find the optimal layups in unstiffened or stiffened cylinders with fixed weights and under axial compression.The buckling load is maximised by considering the manufacturing-induced thermal stresses and the optimum designs are compared to designs in which the thermal stresses are ignored. Lindgaard et al. [66] use mathematical programming, method of moving asymptotes (MMA), to find the optimal fibre angles which maximise the nonlinear buckling load in an orthotropic thin-walled cylinder subjected to axial compression.

-Lamination parameters as design variables

Onoda [70] has found the optimum laminate configuration, formulated in terms of 12 lamination parameters, for the maximum buckling load of a composite circular cylindrical shell under axial compression. Using lamination parameters, gives complete freedom to the ply angle variation through the thickness of a laminate. The optimal values of lamination parameters are obtained numerically and many different optimal configurations are obtained which have the same buckling load. Although it is shown that the optimal lamination parameters should satisfy certain constraints to assure the existence of a real laminate, Onoda [70] does not enforce these constraints in the optimisation problem. Instead, Onoda [70] showed that the optimal lamination parameters satisfy these constraints by making sure that the corresponding laminate exists. The optimality conditions for laminate configuration is derived in terms of lamination parameters semi-empirically from the numerical results and the optimum buckling load is found in terms of material properties. Onoda [70] concludes that one of the optimal laminates is the one with an infinite number of infinitely thin layers organised such that the shell is quasi-isotropic in the surface and quasi-homogeneous across the thickness. In addition, some anisotropic configurations with the same buckling load as the quasi-isotropic one exist. Fukunag and Vanderplaats [71] use mathematical programming to find the optimum lamination parameters for maximum buckling load design of cylindrical shells under combined loading. Grenestedt [72] has found the optimum layup, thickness and radius of a laminated circular cylinder under bending which minimise the cross-section area subject to constraints on the buckling load and global bending stiffness. Grenestedt [72] uses two in-plane and two out of plane lamination parameters as design variables to find the optimum layup of a circular cylinder under bending using the feasible regions of lamination parameters determined by Grenestedt and Gudmundson [73] and Fukunag and Vanderplaats [71]. The optimum lamination parameters are approximated by a real stacking sequence $[\pm\theta_{h1}, 0_{h2}, 90_{h3}, 0_{h4}]_s$ and the corresponding fibre angle (θ) and thicknesses (h_1, h_2, h_3, h_4) were found. Diaconu et al. [74] use mathematical programming to find the optimum 12 lamination parameters and the corresponding laminate configurations, including the ply angle and thickness, in laminated long cylindrical shells under combined axial compression and torsion to maximise the buckling load. Matsuzaki and Todoroki [75] use the improved fractal branch and bound method to find the optimum unsymmetrical balanced stacking sequence of cylindrical shells under axial compressive load, external lateral pressure and torsional load for maximum buckling load, using 9 lamination parameters as design variables.

Segmented-stiffness laminated cylinders
Riddick [76] has investigated the pre-buckling, buckling and post-buckling behaviour of composite cylinders constructed from two different stacking sequences; one laminate stacking sequence for the crown and keel and another laminate stacking sequence for the two sides (figure 1.12). This construction is called a segmented-stiffness cylinder and is considered to represent an aircraft fuselage. To compare the numerical results with the experimental measurements, small scale segmented-stiffness cylinders were fabricated on a mandrel by splicing adjacent segments together to form overlaps.

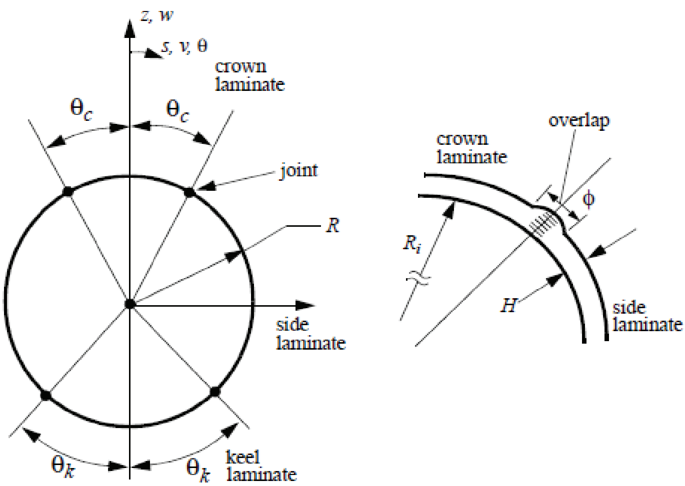

FIGURE 1.12: Segmented cylinder construction (Riddick [76])

Riddick and Hyer [77] and Hyer and Riddick [78] have investigated the response of infinite and finite-length cylinders under end-shortening and internal pressure, respectively. The characteristic which distinguishes these segmented-stiffness cylinders from the conventional single-laminate cylinders, are the circumferential displacements. It is concluded that the feature which is responsible for circumferential displacement is the difference in effective laminate Poisson's ratios from one segment to the next for cylinders under end-shortening [77] and the mismatch in the effective extensional moduli of the segments for cylinders under internal pressure [78]. Riddick and Hyer [79] and Riddick and Hyer [80] have investigated the buckling and post-buckling response of two segmented-stiffness cylinders referred to as axially stiff and circumferentially stiff configurations under axial end-shortening. The results show that as the end-shortening is increased toward the buckling value, depending on the level of axial stress resultant supported by each segment, some segments start to wrinkle while the rest remain unwrinkled. The post-buckled cylinders are characterised by large local inward dimples and sharp outward ridges in the radial direction. Load drops of 20% and 57% are predicted for end-shortening beyond buckling in the axially and circumferentially stiff cylinders, respectively. Riddick and Hyer [81] have also studied the effect of imperfections on the buckling and post-buckling of small-scale axially and circumferentially stiff segmented-stiffness cylinders under end shortening. They conclude that the measured imperfection have an influence of the response of axially stiff segmented-stiffness cylinders during transition from the pre-buckling to post-buckling state, while the imperfections have a relatively small influence on the buckling and post-buckling behaviour of circumferentially stiff cylinders.

Variable thickness laminated cylinders

Adali et al. [53] use the golden section method to find the optimum fibre angle, and constant or axially variable laminate thickness of a cylindrical pressure vessel with closed ends under internal pressure, axial force and torque. The objective function is to maximise the burst pressure or minimise the weight under the Tsai-Wu failure constraint. Variable thickness shells show about 20% improvement over the constant thickness shells for low internal pressure values and the difference is decreased by increasing the pressure. Darlow and Creonte [82] use the OPT program to find the minimum weight design of a composite drive shaft under torsional strength, buckling and lateral frequency constraints. The design variables used include ply thickness and angle and number of layers varying along the shaft, shaft inner radius and number of mid-span bearings. Dramatic weight savings are obtained for the shaft with an axially varying layup compared to that with a uniform layup. Paschero and Hyer [83] have found the optimal circumferential variation of the wall thickness of homogeneous, isotropic elliptical cylinders to improve the axial buckling load. A classical equation is used to predict the axial stress level, which leads to buckling of a geometrically perfect, homogeneous and isotropic circular cylinder. The critical stress is proportional to the ratio of wall thickness to radius of curvature. The critical axial stress of an elliptical cylinder with the same circumference can be predicted using the same equation. In constant and circumferentially varying thickness elliptical cylinders, the critical stress values correspond to the locations with maximum radius of curvature or with minimum ratio of wall thickness to radius of curvature. The logic behind finding the optimum thickness variation is to have a constant ratio of wall thickness to radius of curvature around the cross-section such that all the points of the cross-section are uniformly stable. The value of this constant ratio is determined such that the buckling stress, or buckling load or cross-sectional area of the variable thickness elliptical cylinder are the same as those of the constant thickness circular cylinder with the same circumference.

Steered fibre laminated cylinders

It has been proven in previous studies that circumferential tailoring can increase the buckling load of thin cylinders by compensating for the non-uniform sectional loading such as bending and/or varying radius of curvature in arbitrary cross-section cylinders. The effect of varying the stiffness of circular cylinders to improve the buckling load was first studied by Tatting [84]. The general governing equations are formulated in closed form using energy methods and solved using finite difference after limiting the stiffness variation to the axial or circumferential direction. The effect of stiffness variation was investigated using the linear membrane approximation of the governing equations and stepwise linear angle variations. Initially an axial stiffness variation for axisymmetric loading was tried and the results showed little improvement compared to traditional laminates. In a follow-on case, circumferential tailoring for general load cases was examined. The most significant improvements in buckling load is found for cases which involve loads that vary circumferentially, i.e. bending and shear forces. It is concluded by Tatting [84] that circumferential stiffness tailoring contributes to buckling load improvement through load and stiffness redistribution. Wu [85] has designed two cylindrical shells with an 8 ply tow steered laminate configuration $[\pm 45, \pm\theta]_s$. The ply angle θ is measured with respect to the cylinder axis and varies continuously from 10° on the crown to 45° on each side and then back to 10° on the keel. The cylinders resemble an aircraft fuselage and since bending about the cross-section diameter resulting from aerodynamic and inertial loads is the dominant operational loading in this case, the layup is oriented along the fuselage length in the crown and keel to obtain high extensional stiffness to resist the flight bending loads. In addition, the shell sides provide high shear stiffness to resist the relative deflection of the crown and keel. One of the cylinders is designed to be manufactured by placing 24 tows in each fibre placement pass, resulting in many overlaps on the shell laminate and the other one is designed to be fabricated using the individual tow cut and restart capability of the fibre placement machine, resulting in a more uniform laminate thickness. Finite element results show improvements in the buckling moment and stiffness of the tow-steered cylinder with overlaps compared to a quasi-isotropic shell, when a bending moment around the horizontal axis passing two side shells is applied, however, the buckling moment and stiffness of cylinders without overlaps are decreased compared to the baseline quasi-isotropic shell. Wu [85] also investigated the effect of using an angle-ply straight fibre laminate for the crown and keel and concluded that large improvements in the shell bending stiffness are also possible for this configuration. In a follow-on study, Wu et al. [86] report on the detailed manufacturing process of the aforementioned cylinders and discuss manufacturing issues such as the presence of waves or bumps in the placed tows. Post-fabrication surface surveys were performed on the inner and outer surfaces of the cured shells to determine their initial imperfections and thickness variations. The cured cross-sections of both shells vary along their length, and are generally elliptical with the major axes rotated 90° between the shells with and without overlaps. In a follow-on study, Chauncey Wu et al. [87] performed axial compression tests on the tow-steered shells to determine their nonlinear and buckling structural response experimentally. The test and analysis results generally compare well, with an average difference of 10% for pre-buckling axial stiffness and buckling load. The improvements of the shell with overlaps over the uniform thickness shell, when normalised with respect to the corresponding shell weight, are 28% and 78% in the pre-buckling stiffness and buckling load, respectively. Although, cylindrical shells with a uniform stacking sequence has been shown to be highly sensitive to imperfections, the tow-steered cylinders do not exhibit the same high degree of sensitivity. Chauncey Wu et al. [87] have performed some preliminary comparisons between the linear bifurcation buckling loads and the nonlinear limit point buckling loads, which show minor differences and hence insensitivity to imperfections. Chauncey Wu et al. [87] mention that further investigation should be done to identify the exact reason of insensitivity of tow-steered cylinders to imperfections, however, they made an assumption that the non-uniform stiffness distribution in the tow-steered cylinders is the cause of insensitivity. Circumferential tailoring of a circular cylinder to maximise the buckling load under bending was studied by Blom [5] including the Tsai-Wu strength constraint. A surrogate model optimiser is applied to find the optimum design using constant curvature fibre paths within the segments around the circumference (figure 1.13). The thickness build-ups due to manufacturing using fiber placement are included in the predictions by Blom [5] and manufacturing and testing are performed for validation. Her findings show that circumferential tailoring is beneficial for buckling load improvement due to internal load redistribution such that the axial force is relieved in the compression side and concentrated in the tension side, and the buckling mode shapes are altered.

Variable stiffness design of elliptical cross-section cylinders under axial com-

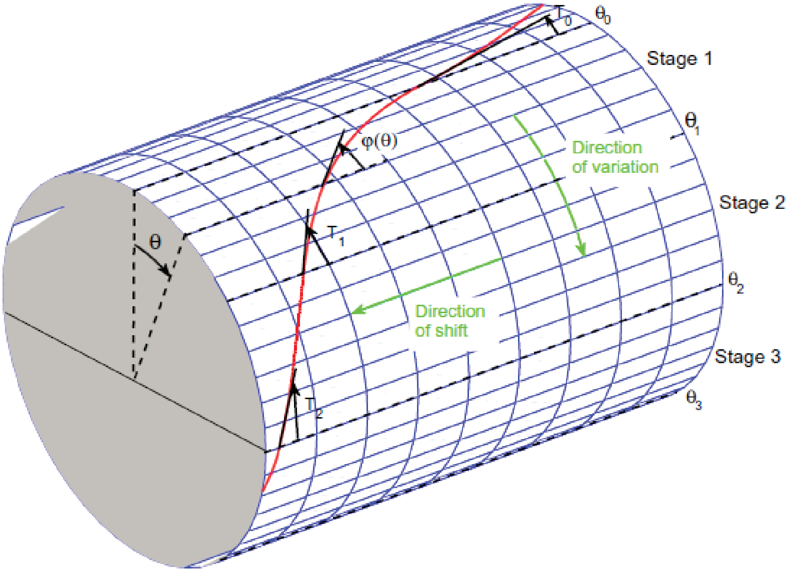

FIGURE 1.13: Fibre angle and segment definition (Blom [5])

pression has been studied by Sun and Hyer [88] through circumferentially varying one ply angle in the considered stacking sequence. The idea of changing the stacking sequence around the circumference is considered to be a suitable approach to compensate for the effect of varying the radius of curvature around the circumference which is the source of the reduction in buckling load in the elliptical cylinder compared to a circular cylinder with the same circumference. A simple approximate prediction of axial buckling load for simply-supported circular cylinders is used by Sun and Hyer [88] as the basis for tailoring the stacking sequence of elliptical cylinders. The buckling strain value of circular cylinders with radii changing from the minimum to maximum radius of curvature of the considered elliptical cylinder are obtained for stacking sequences with the variable ply angle changing from 0° to 90°. Looking at the constant buckling strain contours, a different ply angle can be found for each of the circular cylinders, ranging from minimum to maximum radius, which results in the same level of buckling strain for all the circular cylinders. The criterion set out by Sun and Hyer [88] for circumferential tailoring of the elliptical cylinders is based on finding the ply angles which give the highest possible buckling strain value that is the same for all cylinders. Therefore, the ply angle at each point around the circumference of the elliptical cylinder is set equal to the ply angle found for the corresponding circular cylinder. Lo and Hyer [89] have investigated the effect of linear ply angle variations in some or all of the layers of laminated thin-walled elliptical and circular cylinders on the fundamental vibration frequencies. The finite element results show that even for a significantly large range of ply angle variation, the fundamental vibration frequency of elliptical and circular cylinders is not influenced, although the circumferential wave numbers are altered.

1.6 OVERVIEW OF THIS THESIS AND MOTIVATION

The primary goal of the research reported in this thesis is to establish a computationally efficient framework for circumferential stiffness tailoring of unstiffened and longitudinally stiffened laminated cylindrical shells with general cross-sections. This framework is applied on circular and elliptical cross-section cylinders to design optimum straight and steered fibre laminates for maximum buckling capacity with consideration of material failure constraints. By comparing the performance of optimum straight and steered fibre laminates, superiority of steered fibre laminates is shown and the mechanisms involved in improvement of the buckling capacity of steered fibre laminates compared to straight fibre laminates are investigated .

Some basic background about the geometric definition and the strain - displacement relations of thin general and cylindrical shells and the constitutive relations in the classical lamination theory is presented in chapter 2. Using the information in chapter 2, a computationally efficient semi-analytical solution is developed for static and buckling analysis of unstiffened and longitudinally stiffened cylindrical shells with general cross-sections in chapter 3.

A multi-step optimisation framework, used to find the optimum straight and steered fibre laminate designs, is introduced in chapter 4. The multi-step optimisation framework is based on the convex conservative separable approximations of the design drivers, construction of which is also explained in chapter 4.

Application of material strength as a laminate design driver in the multi-step optimisation framework requires a special treatment which is described in chapter 5. In this chapter, construction of the convex separable approximation of the failure index, which is introduced as the strength measure, is also explained.

In chapter 6, the effect of circumferential stiffness tailoring is investigated on the buckling capacity of two cases; a circular cylinder under bending and an elliptical cylinder under axial compression. To this end, straight and steered fibre laminate designs are obtained for maximum buckling capacity with strength constraints using the semi-analytical solution, developed in chapter 3, the multi-step optimisation framework and the convex conservative approximation of buckling factor, introduced in chapter 4, and the strength envelope and the convex conservative approximation of failure index, explained in chapter 5. To investigate the effect of laminate thickness variation in addition to fibre steering in the buckling capacity improvement, variable thickness VS laminates with the same weight as the constant thickness laminates are obtained for maximum buckling capacity. The mechanisms involved in buckling capacity improvements of the steered fibre laminates over straight fibre laminates in the aforementioned case studies are also investigated.

Similar to the unstiffened cylindrical shells investigated in chapter 6, the developed framework for circumferential stiffness tailoring of cylindrical shells is applied in chapter 7 for maximum buckling moment design of longitudinally stiffened circular cylinders under bending and the buckling moment improvement mechanisms are investigated. Finally, some general conclusions about this research on optimum design of fibre steered laminated cylindrical shells with general cross-sections and recommendations and thoughts for the future research are presented in chapter 8.

2

Basic background

2.1 Introduction

The structural elements, investigated in this thesis, were thin cylindrical shells with arbitrary cross-sections i.e. both circular and non circular cross-sections. A thin shell is a three-dimensional (3-D) body bounded by two curved surfaces such that their distance is relatively small compared to the other shell dimensions. The locus of the points placed on the midway between these two surfaces is called the middle surface of the shell. The static and buckling problems of thin shell structures can be formulated variationally using the total potential energy. The kinematic strain-displacement relations and the constitutive relations are the two necessary elements to formulate the total potential energy.

Different shell theories relate the deformation field of the shell to the deformation of the middle surface. These shell theories are easier to use than the 3-D theory of elasticity since they reduce the number of degrees of freedom (DOFs) required for analysis. One of the simplest ways to express shell displacements in terms of the displacements and rotations of the middle surface is based on Kirchhoff's hypothesis. This hypothesis assumes that the normal lines to the middle surface remain straight, unstretched and normal to the middle surface after deformation. Therefore, the strains at each point of the shell can be related to the strains and changes of curvatures of the corresponding point on the middle surface.

Different strain-displacement relations can be formulated depending on the class of shell deformations. Linear strain-displacement relations can be derived for thin shells, which undergo small deformations, based on the assumptions of Love's first order approximation [90]. Small deformations or infinitesimal strains and rotations allow us to linearise the strain-displacement relations by neglecting the higher order terms compared to the first order terms. Different linear strain-displacement relations can be obtained depending on the derivation method and the derivation step in which the Love's assumptions are applied. In the case of large deformations or finite strains and rotations, the general nonlinear form of the strain-displacement relations, called the Green-Lagrange strain tensor, is used. In addition to the above mentioned classes of deformation, there is another class of deformation; infinitesimal strains and finite rotations. This class of deformation is useful for formulating the linear or eigenvalue buckling problem of a shell structure and provides the basis for definition of von Karman strains which neglects the higher order terms of the strains and retains the higher order terms of rotations in the nonlinear Green-Lagrange strain tensor.

The strain-displacement relations of general thin shells are expressed in terms of the first fundamental quantities of the middle surface. These quantities define some of the intrinsic geometric properties of the surface. Using the specific geometric properties of cylindrical surfaces, the strain-displacement relations of general thin shells can be simplified for cylindrical shells.

In addition to unstiffened cylindrical shells, cylindrical shells stiffened with longitudinal stiffeners were also of interest in this thesis. One of the methods for modeling the stiffened shells is the smeared stiffness approach. In this approach, the stiffened shell is mathematically converted to an unstiffened uniform thickness shell with equivalent stiffness properties. In other words, the stiffness properties of stiffeners are smeared to the shell. The kinematic relations between the strains, changes of curvatures and change of twist of the stiffeners and the cylindrical shell DOFs are required to model the longitudinally stiffened cylindrical shells using the smeared stiffness approach.

Classical lamination theory (CLT) formulates the constitutive relations of the laminated thin shells based on Kirchhoff assumptions. In CLT, it is assumed that all the isotropic and/or orthotropic layers in the laminate are perfectly bonded together with an infinitely thin and non-shear-deformable bonding layer. Therefore, it is assumed that the laminate performs as a single lamina with integrated properties which are represented by the in-plane, coupling and out of plane stiffness matrices. These stiffness matrices include information about the material properties and ply angles. In the most general laminate, the laminate stiffness matrices can be parameterised using twelve lamination parameters instead of the fibre angles of all layers. Each lamination parameter includes information about the ply angles of the laminate.

In this chapter, first some geometric background on general thin shells including the curvilinear coordinate system and the first quadratic form of the middle surface and the components of the metric tensor of general shells, which are required for definition of the shell strain-displacement relations, is presented in section 2.2. Some different strain-displacement relations for general thin shells and the assumptions used in their derivation are explained in section 2.3. In section 2.4, the appropriate shell strain-displacement relation for the cylindrical shells is selected and simplified. Also the kinematic relations between the strains, changes of curvatures and change of twist of the stiffeners and the cylindrical shell DOFs are derived for longitudinally stiffened cylindrical shells. In section 2.5, the constitutive relations of the laminates are formulated using the classical lamination theory (CLT). The stiffness matrices and lamination parameters are also introduced in section 2.5.

2.2 BACKGROUND ON GEOMETRY OF THIN SHELLS

The geometry of a thin shell can be defined by the geometry of the middle surface and a thickness value at each point of the middle surface. The thickness of the shell is the distance between the top and bottom surfaces measured along the normal line to the middle surface. At each point of the middle surface, the maximum and the minimum curvatures of the curves resulted from the intersection of the middle surface and the planes normal to it, are the principal curvatures. Two examples of shell structures are flat panels and cylinders, in which both and one of the two principal curvatures of the middle surface are equal to zero, respectively.

The curvilinear coordinate system and the first fundamental form of a general surface are defined in subsection 2.2.1. The coefficients of the metric tensor of a thin shell, which are required for formulating the strain-displacement relations, are expressed in terms of the first fundamental quantities of the middle surface in subsection 2.2.2.

2.2.1 MIDDLE SURFACE

The geometry of a general surface can be parameterised by a curvilinear two - dimensional (2-D) coordinate system. Two sets of curves can be defined on the surface by keeping either of the two coordinates constant and varying the other one. The infinitesimal lengths of the curves on the surface, the angle between two curves, and the area of a region on the surface can be described by the first fundamental form of the surface. The quantities describing the first fundamental form of a surface are the first fundamental quantities and are used in the expressions for strain-displacement relations. The second fundamental form of the surface is related to the curvatures of the curves on the surface [90]. The first and second fundamental quantities are not functionally independent and are related by three compatibility differential equations; the Guass characteristic equation and two Mainardi-Codazzi equations [90]. It has been proved by Bonnet [91] that if a set of given fundamental quantities satisfy the three compatibility differential equations, a unique surface is completely determined except for its location and orientation in space. In this subsection, first the curvilinear coordinate system of the middle-surface is introduced and then the first quadratic form of the surface, which is useful in defining the strain-displacement relations, is described.

Coordinate system

The geometry of an undeformed middle surface of a thin shell can be expressed using the position or radius vector which is a function of two independent surface parameters, α and β:

$$\mathbf{r} = \mathbf{r}(\alpha, \beta) \tag{2.1}$$

These two parameters, α and β, form a 2-D curvilinear coordinate system on the surface. If the parameter α is kept constant at a value of α_0 and the parameter β is allowed to change in equation 2.1, the resulting equation represents a space curve placed on the surface represented by equation 2.1. The family of curves which are found by setting the parameter α to constant values are called β curves and α curves are defined in an analogous manner as depicted in figure 2.1.

Supposing that the α and β parameters vary on a 2-D definite region, a one to one correspondence between the points on this definite region and the points on the surface exist according to equation 2.1. The rate and direction of changes of the position vector, $\mathbf{r}$, with respect to the variations of α and β parameters are denoted by two vectors:

$$\mathbf{r}_{,\alpha} = \frac{\partial \mathbf{r}}{\partial \alpha}, \qquad \mathbf{r}_{,\beta} = \frac{\partial \mathbf{r}}{\partial \beta} \tag{2.2}$$

where the vectors $\mathbf{r}_{,\alpha}$ and $\mathbf{r}_{,\beta}$ are tangents to the α and β curves. The length of these vectors are denoted by:

$$|\mathbf{r}_{,\alpha}| = A, \qquad |\mathbf{r}_{,\beta}| = B \tag{2.3}$$

Therefore the unit vectors tangent to the parametric curves are:

$$\mathbf{i}_\alpha = \frac{\mathbf{r}_{,\alpha}}{A}, \qquad \mathbf{i}_\beta = \frac{\mathbf{r}_{,\beta}}{B} \tag{2.4}$$

The angle between the parametric curves is χ and defined by:

$$\mathbf{i}_\alpha.\mathbf{i}_\beta = \cos(\chi) \tag{2.5}$$

and the unit vector normal to the surface and orthogonal to unit vectors $\mathbf{i}_\alpha$ and $\mathbf{i}_\beta$ is defined as:

$$\mathbf{i}_n = \frac{\mathbf{i}_\alpha \times \mathbf{i}_\beta}{\sin(\chi)} \tag{2.6}$$

The unit vectors $\mathbf{i}_\alpha$, $\mathbf{i}_\beta$ and $\mathbf{i}_n$ are called the basic vectors of the surface.

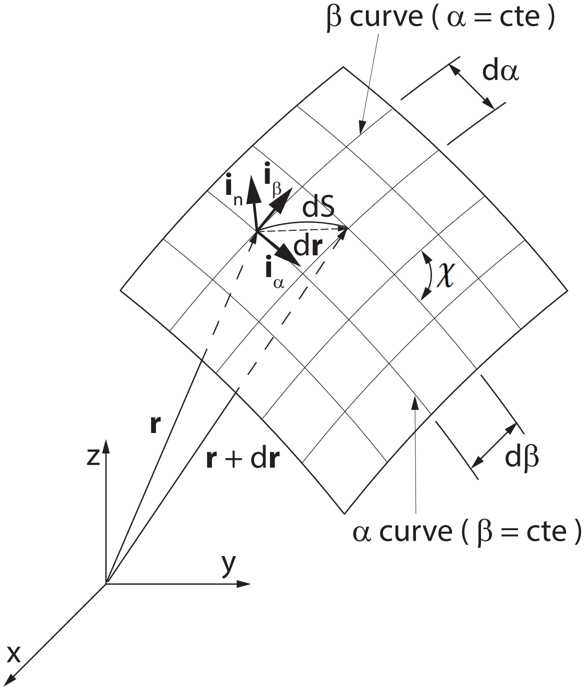

FIGURE 2.1: Geometry and coordinate system of the middle surface of a general shell (regenerated from Leissa [90])

First quadratic form

Suppose that two points (α, β) and $(\alpha + d\alpha, \beta + d\beta)$ are placed close to each other on the same surface. As shown in figure 2.1, the increment of the position vector when moving from the first point to the second point is denoted by $d\mathbf{r}$, which can be expressed in terms of the change of surface parameters, $d\alpha$ and $d\beta$, as:

$$d\mathbf{r} = \mathbf{r}_{,\alpha}\ d\alpha + \mathbf{r}_{,\beta}\ d\beta \tag{2.7}$$

From equations 2.3 and 2.4 we know that $\mathbf{r}_{,\alpha} = A\ \mathbf{i}_\alpha$ and $\mathbf{r}_{,\beta} = B\ \mathbf{i}_\beta$ and by substituting these in Eq. 2.7, the square of the differential arc length on the surface between the two points (α, β) and $(\alpha + d\alpha, \beta + d\beta)$ is expressed as:

$$ds^2 = d\mathbf{r}.d\mathbf{r} = A^2\ d\alpha^2 + 2\ A\ B\ \cos(\chi)\ d\alpha\ d\beta + B^2\ d\beta^2 \tag{2.8}$$

2

The right-hand side of Eq. 2.8 is the first quadratic form of the surface. The intrinsic geometry of the surface such as the infinitesimal lengths of the curves on the surface, the angle between two curves, and the area of a region on the surface are determined by this form, however, this form is not sufficient to describe a surface and the second order form which deals with the curvatures of the curves on the surface is also necessary to define a surface. The coefficients of the first quadratic forms ($A^2, 2\ A\ B\ \cos(\chi), B^2$) are called the first fundamental quantities.

2.2.2 THIN SHELL

Having described the locus of points on the middle surface of the shell using equation 2.1, the position of the points in a shell can be expressed by:

$$\mathbf{R}(\alpha, \beta, z) = \mathbf{r}(\alpha, \beta) + z\ \mathbf{i}_n \tag{2.9}$$

where z is the coordinate of the corresponding point along $\mathbf{i}_n$, which is zero on the middle surface and ranges from $-h/2$ to $h/2$ as shown in figure 2.2.

The square of the differential increment of position vector, $\mathbf{R}$, can be expressed as:

$$ds^2 = d\mathbf{R}.d\mathbf{R} = (d\mathbf{r} + z\ d\mathbf{i}_n + \mathbf{i}_n\ dz).(d\mathbf{r} + z\ d\mathbf{i}_n + \mathbf{i}_n\ dz) \tag{2.10}$$

In an orthogonal curvilinear coordinate system using equations 2.4 and 2.6 for basic vectors of the surface, and calculating the derivatives of these basic vectors with respect to the surface parameters, α and β, then using the chain rule to express $d\mathbf{i}_n$ and considering equations 2.7 and 2.8, one can obtain:

$$ds^2 = g_1\ d\alpha^2 + g_2\ d\beta^2 + g_3\ dz^2 \tag{2.11}$$

where g_i $(i = 1, 2, 3)$, which are the coefficients of the metric tensor, are defined as:

$$g_1 = [A\ (1 + \frac{z}{R_\alpha})]^2\ , \qquad g_2 = [B\ (1 + \frac{z}{R_\beta})]^2\ , \qquad g_3 = 1 \tag{2.12}$$

The details of the mathematical manipulations are omitted here for the sake of brevity (see [90]).

2.3 STRAIN-DISPLACEMENT RELATIONS IN THIN SHELLS

Different strain measures can be defined based on the class of deformations; infinitesimal strain theory deals with small deformations which result in infinitesimal strains and rotations, finite strain theory deals with large deformations leading to arbitrarily large strains and rotations, and large rotation theory deals with infinitesimal strains and moderately large rotations. In this section, the linear and nonlinear von Karman strain-displacement relations, which correspond

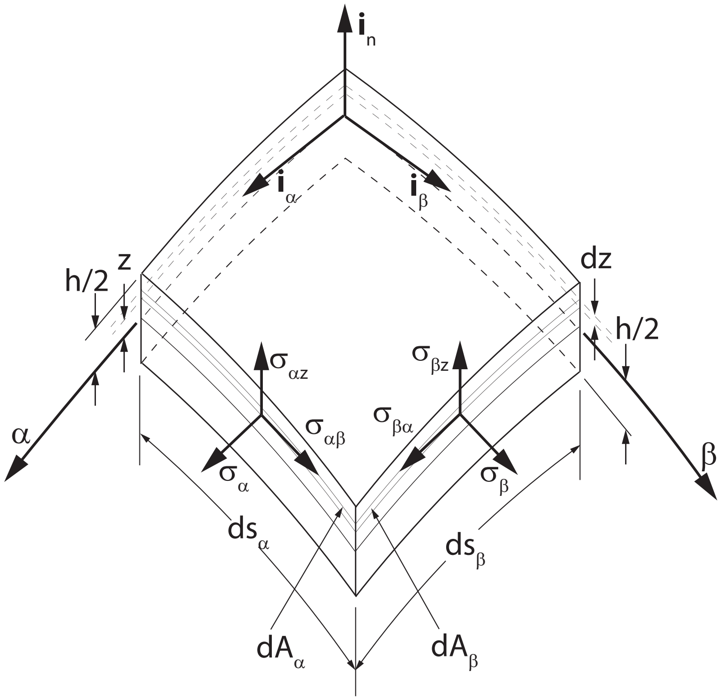

FIGURE 2.2: A shell element (regenerated from Leissa [90])

to the infinitesimal strain theory and large rotation theory respectively, are introduced for general thin shells in subsections 2.3.1 and 2.3.2 respectively. The linear and nonlinear von Karman strain-displacement relations strain-displacement relations can be used to formulate the linear static and eigenvalue buckling problems, respectively.

2.3.1 LINEAR STRAIN-DISPLACEMENT RELATIONS

Small deformations allow us to formulate the strain-displacement relations as linear expressions. Linear strain-displacement relations of thin shells are formed based on four assumptions made by Love [90], which are called Love's first approximation in the thin shell theory:

1. the shell thickness is small compared with other dimensions of the shell, e.g. the smallest radius of curvature of the middle surface of the shell.

2. the strains and displacements are sufficiently small.
3. the transverse normal stress is small in comparison with other normal stresses and can be neglected.
4. the normals to the undeformed middle surface remain straight and normal to the deformed middle surface and are not extended.

Love's first assumption sets out the definition of a thin shell. If the thickness of the shell is denoted by h, the through-the-thickness coordinate which is measured along the normal to the middle surface and from the middle surface is denoted by z and the minimum radius of curvature is denoted by R, then it will be convenient to neglect higher orders of z/R or h/R at different steps of derivation of the shell theories. Love's second assumption allows us to refer all calculations to the original configuration of the shell. In addition, the higher-order terms in the strain-displacement relations can be neglected compared to the first-order terms leading to linear differential equations. The result of Love's fourth assumption, which is also known as Kirchhoff's hypothesis, is that the transverse shear strains,$\gamma_{\alpha z}$ and $\gamma_{\beta z}$ and the transverse normal strain, e_z, are equal to zero:

$$\gamma_{\alpha z} = 0, \qquad \gamma_{\beta z} = 0 \tag{2.13}$$

and

$$e_z = 0 \tag{2.14}$$

Different linear stress-displacement relations can be obtained based on the derivation method used and the derivation step in which the assumptions of the Love's first approximation are applied. In the following, two sets of linear stress-displacemnt relations are introduced. These are derived using two different but very similar methods.

Equations of Byrne, Flügge, Goldenveizer, Lur'ye and Novozhilov

In the theory of elasticity, the linear strain-displacement relations of a 3-D body with small deformations can be expressed in orthogonal curvilinear coordinates as [92], [93]:

$$\begin{aligned} e_{ii} &= \frac{\partial}{\partial\alpha_i}\left(\frac{U_i}{\sqrt{g_i}}\right) + \frac{1}{2g_i}\sum_{k=1}^{3}\frac{\partial g_i}{\partial\alpha_k}\frac{U_k}{\sqrt{g_k}}, \qquad i = 1,2,3 \\ \gamma_{ij} &= e_{ij} + e_{ji}, \qquad i,j = 1,2,3 \qquad i \neq j \end{aligned} \tag{2.15}$$

where e_{ii}, γ_{ij}, U_i, α_i and g_i are normal strains, shear strains, displacement components at an arbitrary point, the orthogonal curvilinear coordinates and the components of the metric tensor of the 3-D body, respectively and e_{ij} is expressed as [93]:

$$e_{ij} = \frac{1}{\sqrt{g_j}} \frac{\partial U_i}{\partial \alpha_j} - \frac{U_j}{\sqrt{g_i g_j}} \frac{\partial \sqrt{g_j}}{\partial \alpha_i}, \qquad i,j = 1,2,3 \qquad i \neq j \tag{2.16}$$

In a shell element, the indices 1, 2 and 3 of the strain components and the the coordinates α_i $(i = 1,2,3)$ in equations 2.15 and 2.16 are replaced by α, β and z, respectively and the strains with two similar indices are indicated by one of the two indices, e.g. $e_{\alpha\alpha} = e_\alpha$. The displacement components U_i $(i = 1,2,3)$ are replaced by $\mathcal{U}$, $\mathcal{V}$ and $\mathcal{W}$, respectively, which indicate the displacement components of each point in the shell in the $\mathbf{i}_\alpha$, $\mathbf{i}_\beta$ and $\mathbf{i}_n$ directions, respectively. The coefficients of the metric tensor, g_i $(i = 1,2,3)$, are given by equation 2.12. Using the Gauss characteristic equation and Mainardi-Codazzi relations, the shell strain-displacement relations can be expressed as [90], [93]:

$$e_\alpha = \frac{1}{1+z/R_\alpha}\left(\frac{1}{A}\frac{\partial \mathcal{U}}{\partial \alpha} + \frac{\mathcal{V}}{AB}\frac{\partial A}{\partial \beta} + \frac{\mathcal{W}}{R_\alpha}\right) \tag{2.17}$$

$$e_\beta = \frac{1}{1+z/R_\beta}\left(\frac{\mathcal{U}}{AB}\frac{\partial B}{\partial \alpha} + \frac{1}{B}\frac{\partial \mathcal{V}}{\partial \beta} + \frac{\mathcal{W}}{R_\beta}\right) \tag{2.18}$$

$$e_z = \frac{\partial \mathcal{W}}{\partial z} \tag{2.19}$$

$$e_{\alpha\beta} = \frac{1}{1+z/R_\beta}\left(\frac{1}{B}\frac{\partial \mathcal{U}}{\partial \beta} - \frac{\mathcal{V}}{AB}\frac{\partial B}{\partial \alpha}\right) \tag{2.20}$$

$$e_{\beta\alpha} = \frac{1}{1+z/R_\alpha}\left(\frac{1}{A}\frac{\partial \mathcal{V}}{\partial \alpha} - \frac{\mathcal{U}}{AB}\frac{\partial A}{\partial \beta}\right) \tag{2.21}$$

$$e_{\alpha z} = \frac{\partial \mathcal{U}}{\partial z} \tag{2.22}$$

$$e_{z\alpha} = \frac{1}{1+z/R_\alpha}\left(\frac{1}{A}\frac{\partial \mathcal{W}}{\partial \alpha} - \frac{\mathcal{U}}{R_\alpha}\right) \tag{2.23}$$

$$e_{\beta z} = \frac{\partial \mathcal{V}}{\partial z} \tag{2.24}$$

$$e_{z\beta} = \frac{1}{1+z/R_\beta}\left(\frac{1}{B}\frac{\partial \mathcal{W}}{\partial \beta} - \frac{\mathcal{V}}{R_\beta}\right) \tag{2.25}$$

2

and the shear strains in their compact form are [90]:

$$\gamma_{\alpha\beta} = \frac{A(1+z/R_\alpha)}{B(1+z/R_\beta)}\frac{\partial}{\partial\beta}[\frac{\mathcal{U}}{A(1+z/R_\alpha)}] + \frac{B(1+z/R_\beta)}{A(1+z/R_\alpha)}\frac{\partial}{\partial\alpha}[\frac{\mathcal{V}}{B(1+z/R_\beta)}] \tag{2.26}$$

$$\gamma_{\alpha z} = \frac{1}{A(1+z/R_\alpha)}\frac{\partial\mathcal{W}}{\partial\alpha} + A(1+z/R_\alpha)\frac{\partial}{\partial z}[\frac{\mathcal{U}}{A(1+z/R_\alpha)}] \tag{2.27}$$

$$\gamma_{\beta z} = \frac{1}{B(1+z/R_\beta)}\frac{\partial\mathcal{W}}{\partial\beta} + B(1+z/R_\beta)\frac{\partial}{\partial z}[\frac{\mathcal{V}}{B(1+z/R_\beta)}] \tag{2.28}$$

The displacement components of each point in the shell are related to the displacement components of each point on the middle surface through the Kirchhoff's hypothesis:

$$\mathcal{U}(\alpha,\beta,z) = u(\alpha,\beta) + z\theta_\alpha(\alpha,\beta) \tag{2.29}$$

$$\mathcal{V}(\alpha,\beta,z) = v(\alpha,\beta) + z\theta_\beta(\alpha,\beta) \tag{2.30}$$

$$\mathcal{W}(\alpha,\beta,z) = w(\alpha,\beta) \tag{2.31}$$

where u, v and w are the displacement components of the middle surface in the $\mathbf{i}_\alpha$, $\mathbf{i}_\beta$ and $\mathbf{i}_n$ directions respectively and θ_α and θ_β are rotations of the normal to the middle surface, $\mathbf{i}_n$, around the $\mathbf{i}_\beta$ and $\mathbf{i}_\alpha$ axes, respectively:

$$\theta_\alpha = \frac{\partial\mathcal{U}(\alpha,\beta,z)}{\partial z}\,, \qquad \theta_\beta = \frac{\partial\mathcal{V}(\alpha,\beta,z)}{\partial z} \tag{2.32}$$

Comparing equations 2.22, 2.24 and 2.32, it can be concluded that:

$$\theta_\alpha = e_{\alpha z}\,, \qquad \theta_\beta = e_{\beta z} \tag{2.33}$$

The expressions in equation 2.13, as two consequences of the Kirchhoff's hypothesis, can be satisfied by substituting the displacement components from equations 2.29, 2.30 and 2.31 in equations 2.27 and 2.28 provided that:

$$\theta_\alpha = e_{\alpha z} = -e_{z\alpha} = \frac{u}{R_\alpha} - \frac{1}{A}\frac{\partial w}{\partial\alpha}\,, \qquad \theta_\beta = e_{\beta z} = -e_{z\beta} = \frac{v}{R_\beta} - \frac{1}{B}\frac{\partial w}{\partial\beta} \tag{2.34}$$

Therefore, the rotations of the normal to the middle surface of the shell can be related to the middle surface displacements using equation 2.34. The expression in equation 2.14, as another consequence of the Kirchhoff's hypothesis, is satisfied by substituting the $\mathcal{W}$ displacement from equation 2.31 in equation 2.19, since $\mathcal{W}$ is independent of z and is only defined by the middle surface component w.

Substituting the displacements from equations 2.29, 2.30 and 2.31 in the strain-displacement relations for e_α, e_β and $\gamma_{\alpha\beta}$ from equations 2.17, 2.18 and 2.26 yields:

$$e_\alpha = \frac{1}{1+z/R_\alpha}(\epsilon_\alpha + z\kappa_\alpha) \tag{2.35}$$

$$e_\beta = \frac{1}{1+z/R_\beta}(\epsilon_\beta + z\kappa_\beta) \tag{2.36}$$

$$\gamma_{\alpha\beta} = \frac{1}{(1+z/R_\alpha)(1+z/R_\beta)}[(1-\frac{z^2}{R_\alpha R_\beta})\epsilon_{\alpha\beta} + z(1+\frac{z}{2R_\alpha}+\frac{z}{2R_\beta})\kappa_{\alpha\beta}] \tag{2.37}$$

where ϵ_α, ϵ_β and $\epsilon_{\alpha\beta}$ are the normal and shear strains in the middle surface ($z=0$), expressed as:

$$\epsilon_\alpha = \frac{1}{A}\frac{\partial u}{\partial \alpha} + \frac{v}{AB}\frac{\partial A}{\partial \beta} + \frac{w}{R_\alpha} \tag{2.38}$$

$$\epsilon_\beta = \frac{u}{AB}\frac{\partial B}{\partial \alpha} + \frac{1}{B}\frac{\partial v}{\partial \beta} + \frac{w}{R_\beta} \tag{2.39}$$

$$\epsilon_{\alpha\beta} = \frac{A}{B}\frac{\partial}{\partial \beta}(\frac{u}{A}) + \frac{B}{A}\frac{\partial}{\partial \alpha}(\frac{v}{B}) \tag{2.40}$$

and κ_α, κ_β and $\kappa_{\alpha\beta}$ are the changes in the curvature and change in twist of the middle surface, given by:

$$\kappa_\alpha = \frac{1}{A}\frac{\partial \theta_\alpha}{\partial \alpha} + \frac{\theta_\beta}{AB}\frac{\partial A}{\partial \beta} \tag{2.41}$$

$$\kappa_\beta = \frac{\theta_\alpha}{AB}\frac{\partial B}{\partial \alpha} + \frac{1}{B}\frac{\partial \theta_\beta}{\partial \beta} \tag{2.42}$$

$$\kappa_{\alpha\beta} = \frac{A}{B}\frac{\partial}{\partial \beta}(\frac{\theta_\alpha}{A}) + \frac{B}{A}\frac{\partial}{\partial \alpha}(\frac{\theta_\beta}{B}) + \frac{1}{R_\alpha}(\frac{1}{B}\frac{\partial u}{\partial \beta} - \frac{v}{AB}\frac{\partial B}{\partial \alpha}) + \frac{1}{R_\beta}(\frac{1}{A}\frac{\partial v}{\partial \alpha} - \frac{u}{AB}\frac{\partial A}{\partial \beta}) \tag{2.43}$$

These strain-displacement relations are derived by Byrne, Flügge, Goldenveizer, Lur'ye and Novozhilov. Some other strain-displacement relations can be obtained from these relations using various simplifications in different stages of the derivation, which are not presented here (see [90]).

Equations of Sanders

Sanders established an eighth-order shell theory based on the principle of virtual work expressed in terms of the generalised displacements and forces. The generalised displacements include the displacement components of the middle surface, u, v and w and the rotations of normal to the middle surface, $\mathbf{i}_n$, around $\mathbf{i}_\alpha$,

$\mathbf{i}_\beta$ and $\mathbf{i}_n$ directions denoted by θ_β, θ_α and θ_n, respectively. The generalised forces associated with these generalised displacements are obtained from a generally accepted set of equilibrium equations neglecting body forces and moments and surface loads [90].

The strain-displacement relations of Sanders theory are obtained after some manipulation and considering the assumptions of Love's first approximation, . These relations are the same as Flügge relations for $\epsilon_\alpha, \epsilon_\beta, \epsilon_{\alpha\beta}, \kappa_\alpha$ and κ_β in equations 2.38-2.42 while $\kappa_{\alpha\beta}$ from Sanders theory is expressed as:

$$\kappa_{\alpha\beta} = \frac{A}{B}\frac{\partial}{\partial\beta}(\frac{\theta_\alpha}{A}) + \frac{B}{A}\frac{\partial}{\partial\alpha}(\frac{\theta_\beta}{B}) + \frac{1}{2AB}(\frac{1}{R_\beta} - \frac{1}{R_\alpha})(\frac{\partial Bv}{\partial\alpha} - \frac{\partial Au}{\partial\beta}) \tag{2.44}$$

The total strains at any point in a shell according to the Sanders theory can be expressed as:

$$e_\alpha = \epsilon_\alpha + z\kappa_\alpha \tag{2.45}$$

$$e_\beta = \epsilon_\beta + z\kappa_\beta \tag{2.46}$$

$$\gamma_{\alpha\beta} = \epsilon_{\alpha\beta} + z\kappa_{\alpha\beta} \tag{2.47}$$

which are the counterparts of equations 2.35, 2.36, 2.37 from the theory of Byrne, Flügge, Goldenveizer, Lur'ye and Novozhilov.

2.3.2 NONLINEAR VON KARMAN STRAIN-DISPLACEMENT RELATIONS

In finite strain theory, the strain for large deformations is measured using the Green-Lagrange strain tensor or Lagrangian finite strain tensor. In an orthogonal coordinate system, for any 3-D elastic body, the Green-Lagrange nonlinear strains are expressed as summation of a linear and a nonlinear part [93]:

$$\begin{aligned} e_{ii}^{GL} &= e_{ii} + \frac{1}{2}\sum_{k=1}^{3}(e_{ik})^2, \qquad i = 1,2,3 \\ \gamma_{ij}^{GL} &= e_{ij} + e_{ji} + \sum_{k=1}^{3}(e_{ik}e_{kj}), \qquad i,j = 1,2,3 \qquad i \neq j \end{aligned} \tag{2.48}$$

where e_{ii} and e_{ij} are the linear strains and rotations defined in equations 2.15 and 2.16.

If the deformations are confined to be small, the linear strains and rotations in equations 2.15 and 2.16 are infinitesimal and hence the higher order terms in equation 2.48 can be neglected compared to the first order terms. Therefore, the linear strains are a special case of the Green-Lagrange strains for small deformations or infinitesimal strains and rotations.

In addition to the two mentioned classes of deformation, another class of deformation exists which is useful for formulating the linear or eigenvalue buckling problem; infinitesimal strains and finite rotations. In this class of deformation, the shell strains and rotations are both smaller than unity but the rotations are larger than the strains i.e. the rotations are moderately large. This order of magnitude is expressed mathematically as:

$$O(e_\alpha) = O(e_\beta) = O(e_{\alpha\beta}) = O(e_{\beta\alpha}) < O(e_{\alpha z}) = O(e_{z\alpha}) = O(e_{\beta z}) = O(e_{z\beta}) < 1 \quad (2.49)$$

The von Karman nonlinear strain-displacement relations are defined by neglecting the second order terms in the nonlinear Green-Lagrange strain-displacement relations in equation 2.48 which contain strains i.e. product of two strains or product of a strain and a rotation, however, the second order terms containing the product of two rotations are retained. Considering these simplifications and the Kirchhoff's hypothesis conclusions i.e. $e_z = 0$, $e_{\alpha z} = -e_{z\alpha}$ and $e_{\beta z} = -e_{z\beta}$, the von Karman strains for shells are expressed as:

$$\begin{aligned} e_\alpha^{VK} &= e_\alpha + \frac{1}{2}(e_{\alpha z})^2 \\ e_\beta^{VK} &= e_\beta + \frac{1}{2}(e_{\beta z})^2 \\ \gamma_{\alpha\beta}^{VK} &= e_{\alpha\beta} + e_{\beta\alpha} + e_{\alpha z}e_{\beta z} \end{aligned} \quad (2.50)$$

These equations can be simplified by considering equations 2.15 and 2.33:

$$\begin{aligned} e_\alpha^{VK} &= e_\alpha + \frac{1}{2}(\theta_\alpha)^2 \\ e_\beta^{VK} &= e_\beta + \frac{1}{2}(\theta_\beta)^2 \\ \gamma_{\alpha\beta}^{VK} &= \gamma_{\alpha\beta} + \theta_\alpha\theta_\beta \end{aligned} \quad (2.51)$$

2.4 STRAIN-DISPLACEMENT RELATIONS IN THIN CYLINDRICAL SHELLS

The scope of the research reported in this thesis was limited to the thin cylindrical shells with arbitrary cross sections, either unstiffened or longitudinally stiffened. The strain-displacement equations of general thin shells, introduced in section 2.3, can be simplified for cylindrical shells considering their specific geometry. The simplified strain-displacement equations can be readily used in chapter 3 to formulate the linear static and buckling problems of the unstiffened thin cylindrical shells where longitudinally stiffened thin cylindrical shells are modeled using the smeared stiffness approach i.e. the stiffened shell is mathematically converted to an unstiffened uniform thickness shell with equivalent stiffness properties. In the smeared stiffness approach, the kinematic relations between the stiffeners and the cylindrical shell DOFs are required to formulate the static and buckling problems of the longitudinally stiffened cylindrical shells.

In this section, the geometry, coordinate system and the first fundamental quantities of the cylindrical surfaces are explained in subsection 2.4.1. In subsection 2.4.2, the Sanders strain-displacement relations are simplified for cylindrical shells. The kinematic relations between the stiffeners and the cylindrical shell DOFs in longitudinally stiffened cylindrical shells are explained in subsection 2.4.3.

2.4.1 CYLINDRICAL SURFACES

The geometry of a cylindrical shell can be described in terms of the geometry of its middle-surface. A generalised cylindrical surface is defined as the surface swept by a line called a generatrix moving parallel to itself along a general planar curve called a directrix, as shown in figure 2.3. If the generatrix line is an infinite line, an infinite cylindrical surface is formed while if a finite length generatrix line is transfered parallel to itself with one end of the line on the directrix curve, a finite length cylindrical surface is constructed. Such a cylindrical surface, either an infinitely long or finite is an open ended cylindrical surface since the two ends are open. A closed cylindrical surface can be formed by cutting the open cylindrical surface using two parallel planes which are not parallel to the generatrix. If the generatrix of an open or closed cylinder is perpendicular to the directrix or the end planes respectively, a straight or right cylinder is traced, otherwise the cylinder is oblique.

In the research reported in this thesis, our interest was limited to cylindrical middle surfaces with a generatrix line perpendicular to the directrix which is an arbitrary closed planar curve, i.e. straight cylinders with arbitrary closed cross sections. The case studies were usually done on open cylindrical surfaces, unless it is mentioned that the cylindrical shell was closed with two end caps which is of interest when studying the effect of internal pressure. Although in practice an infinitely long cylinder does not exist, Saint-Venant's solution, and hence the static and buckling analysis methods, discussed in chapter 3 were developed for infinitely long cylindrical shells neglecting the boundary effects.

The geometry of the middle surface of a cylindrical shell can be parameterised using the surface parameters, α and β, introduced in subsection 2.2.1. In the curvilinear coordinate system of the cylindrical surface, the α parameter changes only in the axial or the generatrix direction while the β parameter varies only in the circumferential or directrix direction. In other words, on the cylindrical surface the α curves are the longitudinal straight lines parallel to the cylinder generatrix while

β curves are the circumferential curves orthogonal to the α curves ($\chi = \frac{\pi}{2}$) as depicted in figure 2.3.

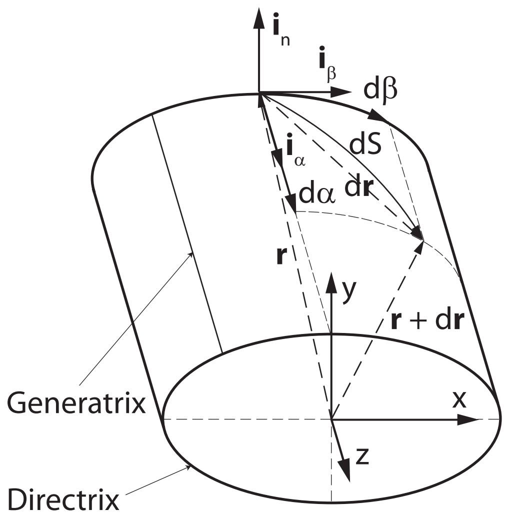

FIGURE 2.3: Geometry and coordinate system of the middle surface of a cylindrical shell

The A and B parameters which define the first fundamental quantities of the surface are calculated using equations 2.2 and 2.3. For a cylindrical surface and all other surfaces which are developable to a plane, these parameters are equal to unity:

$$A = |\mathbf{r}_{,\alpha}| = |\frac{\partial \mathbf{r}}{\partial \alpha}| = 1\,, \qquad B = |\mathbf{r}_{,\beta}| = |\frac{\partial \mathbf{r}}{\partial \beta}| = 1 \tag{2.52}$$

2.4.2 EQUATIONS OF SANDERS

As described in section 2.3.1, the Sanders strain-displacement equations are similar to the Byrne, Flügge, Goldenveizer, Lur'ye and Novozhilov equations, presented in section 2.3.1, except for the change in twist. In Sanders theory, the total strains at each point of the shell are related to the middle surface strains, changes of curvatures and change in twist through equations 2.45-2.47. These equations are simpler than the total strain equations from the theory of Byrne, Flügge, Goldenveizer, Lur'ye and Novozhilov, equations 2.35-2.37. In addition, equations of the total strains in the Sanders theory are used in the classical lamination theory (CLT). Therefore, Sanders equations were selected to express the strain-displacement relations of thin cylindrical shells.

The Sanders strain-displacement relations, equations 2.38-2.42 and equation 2.44, can be simplified for thin cylindrical shells considering $A = B = 1$ and $R_\alpha = \infty$. The simplified Sanders relations for the normal and shear strains on the middle surface of cylindrical shells are:

$$\epsilon_\alpha = \frac{\partial u}{\partial \alpha}, \qquad \epsilon_\beta = \frac{\partial v}{\partial \beta} + \frac{w}{R}, \qquad \epsilon_{\alpha\beta} = \frac{\partial u}{\partial \beta} + \frac{\partial v}{\partial \alpha} \tag{2.53}$$

where $R = R_\beta$. The changes in curvatures and change in twist on the middle surface of cylindrical shells are:

$$\kappa_\alpha = \frac{\partial \theta_\alpha}{\partial \alpha}, \qquad \kappa_\beta = \frac{\partial \theta_\beta}{\partial \beta}, \qquad \kappa_{\alpha\beta} = \frac{\partial \theta_\alpha}{\partial \beta} + \frac{\partial \theta_\beta}{\partial \alpha} + \frac{1}{2R}\left(\frac{\partial v}{\partial \alpha} - \frac{\partial u}{\partial \beta}\right) \tag{2.54}$$

where θ_α and θ_β are the rotations of the normal to the middle surface, $\mathbf{i}_n$, about the $\mathbf{i}_\beta$ and $\mathbf{i}_\alpha$ directions and are obtained from:

$$\theta_\alpha = -\frac{\partial w}{\partial \alpha}, \qquad \theta_\beta = \frac{v}{R} - \frac{\partial w}{\partial \beta} \tag{2.55}$$

2.4.3 LONGITUDINALLY STIFFENED THIN CYLINDRICAL SHELLS

It will be shown in chapter 3 that in long cylindrical shells under extension, bending, torsion and internal or external pressure, which were the load cases of interest in the research reported in this thesis, the state of strain is constant with the axial location and changes only with the circumferential location. This limited strain state variation in cylindrical shells allows for design and analysis simplifications; tailoring of the laminate stiffness properties is limited to the circumferential direction and to solve the static and buckling problems, computationally efficient semi-analytical methods have been developed which require only the cross-section of the cylindrical shell to be discretised. Therefore, although the cylindrical shells can be stiffened in different patterns, in this thesis the stiffening pattern was limited to the longitudinal stiffeners which neither violates the circumferential variation of stiffness nor the conditions of the applicability of the developed semi-analytical methods.

The longitudinal stiffeners in the shell were assumed to be perfectly bonded to the cylindrical shell. The smeared stiffness approach will be used in chapter 3 to model the stiffened cylinder as an unstiffened uniform thickness cylinder with equivalent stiffness properties i.e. the stiffness properties of the stiffeners are smeared to the cylindrical shell. The equivalent stiffness cylindrical shell can be readily analysed using the developed semi-analytical static and buckling methods given in chapter 3. These semi-analytical methods are formulated variationally from the total potential energy which is the summation of the total potential energy of the stiffeners and the cylindrical shell. For smearing the stiffness of stiffeners to the cylindrical shell, the total potential energy of the stiffeners should be expressed in terms of the cylindrical shell DOFs and then added to the total potential energy of the cylindrical shell. Therefore, it is essential to know the kinematic relations between the stiffeners and cylindrical shell DOFs.

Stiffener-shell kinematic relations

The state of strain in the longitudinal stiffeners of a shell, modeled as beams, under extension, bending or torsion is constant everywhere and can be expressed using four parameters, axial strain, two curvatures and twist, which are the axial derivatives of the displacements and rotations of the beam neutral axis. Assuming that the stiffeners are perfectly bonded to the cylindrical shell, within any cross section of a stiffened cylindrical shell, the displacements and rotations of any point on the the cross section of a stiffener can be expressed in terms of the displacements and rotations of the connection point of the stiffener and shell. In practice, a stiffener is connected to the cylindrical shell at more than one point in each cross section. However, in the smeared stiffness approach, the displacements and rotations of the points on the stiffener cross-section are related to those of one connection point in the shell. As depicted in figure 2.4, the connection point is assumed to be placed on the middle surface of the shell and hence, when calculating the offset of the centroid of the stiffener from the connection point on the shell middle surface, the shell thickness should be considered in addition to the stiffener dimensions.

In the cross section of the stiffened cylindrical shell, which is depicted in figure 2.4, the offset of the centroid of the cross section of a stiffener from the connection point on the middle surface of the cylindrical shell in the $\mathbf{i}_\beta$ and $\mathbf{i}_n$ directions is shown by β^{stf} and z^{stf}. The three translational DOFs at the centroid of the cross section of the stiffener, $u^{\text{stf}}, v^{\text{stf}}, w^{\text{stf}}$, are related to the translational and rotational DOFs of the middle surface of the cylindrical shell at the connection point, u, v, w, $\theta_\beta, \theta_\alpha, \theta_n$, as:

$$\begin{bmatrix} u^{\text{stf}} \\ v^{\text{stf}} \\ w^{\text{stf}} \end{bmatrix} = \begin{bmatrix} u \\ v \\ w \end{bmatrix} + \begin{bmatrix} \theta_\beta \\ \theta_\alpha \\ \theta_n \end{bmatrix} \times \begin{bmatrix} 0 \\ \beta^{\text{stf}} \\ z^{\text{stf}} \end{bmatrix} \tag{2.56}$$

The rotational DOFs of the centroid of the cross section of the stiffener, $\theta_\beta^{\text{stf}}, \theta_\alpha^{\text{stf}}, \theta_n^{\text{stf}}$, and the rotational DOFs of the connection point on the middle surface of the cylin-

2

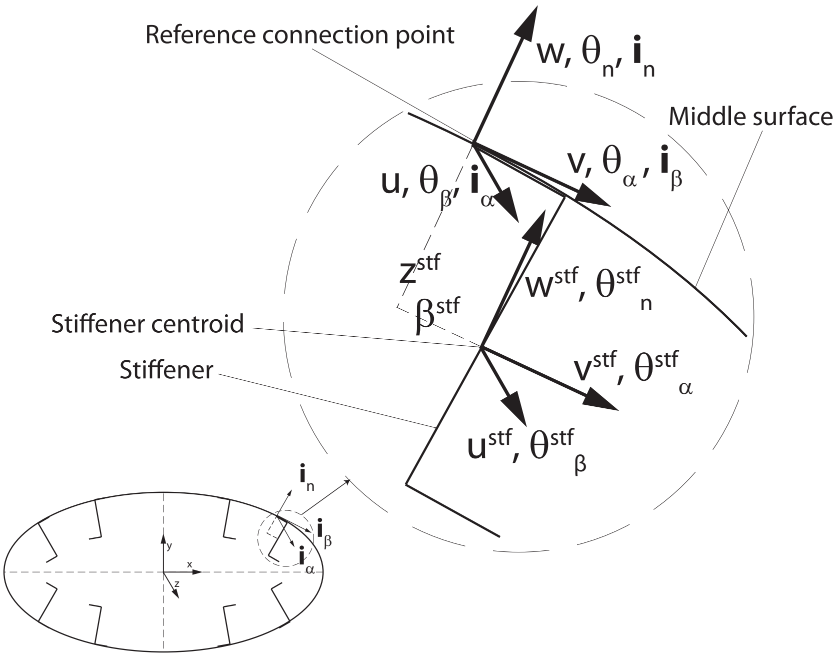

FIGURE 2.4: The cross-section of a stiffened cylinder, DOFs of the connection point of the shell to the stiffener and DOFs of the stiffener centroid

drical shell, $\theta_\beta, \theta_\alpha, \theta_n$, are equal:

$$\begin{bmatrix} \theta_\beta^{\text{stf}} \\ \theta_\alpha^{\text{stf}} \\ \theta_n^{\text{stf}} \end{bmatrix} = \begin{bmatrix} \theta_\beta \\ \theta_\alpha \\ \theta_n \end{bmatrix} \tag{2.57}$$

where θ_n is the drilling DOF which is not defined for the shell and hence θ_n^{stf} is also neglected ($\theta_n^{\text{stf}} = \theta_n = 0$). Therefore, the kinematic expressions relating the DOFs of the centroid of the cross section of the stiffener and the DOFs of the connection point on the middle surface of the cylindrical shell are simplified to:

$$\begin{aligned} &u^{\text{stf}} = u + z^{\text{stf}}\theta_\alpha\,, \qquad v^{\text{stf}} = v - z^{\text{stf}}\theta_\beta\,, \qquad w^{\text{stf}} = w + \beta^{\text{stf}}\theta_\beta \\ &\theta_\beta^{\text{stf}} = \theta_\beta\,, \qquad \theta_\alpha^{\text{stf}} = \theta_\alpha \end{aligned} \tag{2.58}$$

Since the stiffeners are modeled as beam elements under extension, bending and torsion, their deformation can be defined by an axial strain, two changes of curvatures and a change in twist of the neutral axis. These four parameters are defined in terms of the DOFs of the centroid of the cross section of the stiffener and subsequently in terms of the DOFs of the connection point on the middle surface of the cylindrical shell using equations 2.58:

$$\begin{aligned}
\epsilon_\alpha^{\mathrm{stf}} &= \frac{\partial u^{\mathrm{stf}}}{\partial \alpha} = \frac{\partial u}{\partial \alpha} + z^{\mathrm{stf}} \frac{\partial \theta_\alpha}{\partial \alpha} \\
\kappa_\alpha^{\mathrm{stf}} &= \frac{\partial \theta_\alpha^{\mathrm{stf}}}{\partial \alpha} = \frac{\partial \theta_\alpha}{\partial \alpha} \\
\kappa_n^{\mathrm{stf}} &= \frac{\partial \theta_n^{\mathrm{stf}}}{\partial \alpha} = \frac{\partial \theta_n}{\partial \alpha} \\
\tau^{\mathrm{stf}} &= \frac{\partial \theta_\beta^{\mathrm{stf}}}{\partial \alpha} = \frac{\partial \theta_\beta}{\partial \alpha}
\end{aligned} \tag{2.59}$$

As mentioned earlier, θ_n^{stf} and hence κ_n^{stf} are neglected ($\kappa_n^{\mathrm{stf}} = 0$). From equations 2.54 and 2.55 the change in twist of the shell can be stated as:

$$\kappa_{\alpha\beta} = 2\,\frac{\partial \theta_\beta}{\partial \beta} - \frac{1}{2R}\left(\frac{\partial u}{\partial \alpha} + \frac{\partial v}{\partial \alpha}\right) \tag{2.60}$$

Using equations 2.53, 2.54 and 2.60 with equation 2.59, the axial strain, the change of curvature and the change in twist of the neutral axis of the stiffener can be expressed in terms of the axial strain, changes of curvature, change in twist and the displacement v of the connection point on the middle surface of the cylindrical shell:

$$\begin{aligned}
\epsilon_\alpha^{\mathrm{stf}} &= \epsilon_\alpha + z^{\mathrm{stf}} \kappa_\alpha \\
\kappa_\alpha^{\mathrm{stf}} &= \kappa_\alpha \\
\tau^{\mathrm{stf}} &= \frac{1}{2}\kappa_{\alpha\beta} + \frac{1}{4R}\left(\epsilon_\alpha + \frac{\partial v}{\partial \alpha}\right)
\end{aligned} \tag{2.61}$$

2.5 CONSTITUTIVE RELATIONS OF LAMINATES

The structural theories which are used for the analysis of laminated composites are classified into two categories; three-dimensional (3-D) elasticity theory and two-dimensional (2-D) equivalent single layer (ESL) theories. In the 3-D elasticity theory, each layer is modeled as a 3-D solid. In the ESL theories, the heterogeneous laminate is treated as a statically equivalent single layer with integrated properties. These theories are derived from the 3-D elasticity theory by making appropriate assumptions for the kinematics of deformation or stress state through the thickness of the laminate. These assumptions allow us to express the deformations, strains or stresses of the laminate in terms of those values on the middle surface and have the advantage of reducing the 3-D problem to a 2-D problem.

The simplest ESL theory is the classical lamination theory (CLT), which is consistent with the assumptions made when deriving of the strain-displacement relations in section 2.3. In CLT, the strain state in the through-the-thickness direction is either constant or varies linearly due to Kirchhoff's assumptions, however, since the material properties and/or orientation angle of different layers in a laminate are usually different constant values, the stress state jumps between the adjacent layers. Therefore, stress resultants and moment resultants are defined by integration of the stresses and moment of stresses throughout the thickness of laminates. The constitutive relations in CLT relate the stress resultants and moment resultant to the strains and curvatures of the middle surface of the laminate through the stiffness matrices, which includes the integrated information about the stiffness of all layers.

Many of the structural responses can be expressed in terms of stiffness matrices. The stiffness matrices can be expressed either as trigonometric functions of the ply angles or linear functions of some lamination parameters. Linear formulation of stiffness matrices in terms of lamination parameters can be useful in structural optimisation. If lamination parameters are selected as design variables, their feasible region, i.e. the bounded space in which lamination parameters are physically meaningful, should be identified and incorporated in the optimisation formulation as a constraint.

In this section, modeling the laminate stiffness properties using CLT is described in subsection 2.5.1. Lamination parameters are introduced in subsection 2.5.2 as a suitable way to parameterise the stiffness properties of the laminate. The feasible region of lamination parameters is explained in subsection 2.5.3.

2.5.1 CLASSICAL LAMINATION THEORY

Classical lamination theory (CLT) assumes that the laminate is comprised of n orthotropic and/or isotropic layers which are bonded perfectly together by an infinitely thin, non-shear-deformable bonding surface. The CLT is the simplest form of the equivalent single layer (ESL) laminate theories which treat the heterogeneous laminate as a statically equivalent single layer. In CLT the bending of this equivalent single layer follows the Kirchhoff's hypothesis i.e. the normals to the undeformed middle surface remain straight and normal to the deformed middle surface and are not extended. In addition, in CLT it is assumed that all the layers are thin compared to the other dimensions of each of the layers in the laminate, e.g. the in-plane dimensions of a plate or the smallest radius of curvature of the middle surface of a shell.

As indicated in equations 2.13 and 2.13, the Kirchhoff's hypothesis implies that all the transverse strains, $e_z, \gamma_{\alpha z}, \gamma_{\beta z}$, are zero. Therefore, the transverse shear stresses, $\sigma_{\alpha z}, \sigma_{\beta z}$, in an orthotropic laminate are zero by definition. Although the transverse normal stress, σ_z, is not identically zero, since $e_z = 0$, the normal stress does not appear in the virtual work expression and hence is neglected. Therefore, in theory there are plane strain and plane stress states together, however, in practice a thin or moderately thick shell is in the plane stress state since the thickness is small compared to the other dimensions. Therefore, in CLT it is assumed:

$$\sigma_z = \sigma_{\alpha z} = \sigma_{\beta z} = 0 \tag{2.62}$$

These assumptions are also used in the derivation of the Sanders shell strain - displacement relations in subsection 2.3.1. Therefore, using CLT to formulate the constitutive relations of the laminates is consistent with Sanders shell strain-displacement relations.

The linear constitutive relation of the k th orthotropic lamina in the principal material coordinates of that lamina is:

$$\begin{bmatrix} \sigma_1 \\ \sigma_2 \\ \tau_{12} \end{bmatrix} = \begin{bmatrix} Q_{11} & Q_{12} & 0 \\ Q_{12} & Q_{22} & 0 \\ 0 & 0 & Q_{66} \end{bmatrix} \begin{bmatrix} e_1 \\ e_2 \\ \gamma_{12} \end{bmatrix} \tag{2.63}$$

where Q_{ij} s are the plane stress-reduced stiffness matrices of the k th lamina in the material coordinate system. Q_{ij} s can be defined in terms of the longitudinal modulus, E_1, transverse modulus, E_2, shear modulus, G_{12} and poison ratio, ν_{12} as:

$$Q_{11} = \frac{E_1}{1-\nu_{12}\nu_{21}}, \quad Q_{12} = \frac{\nu_{12}E_1}{1-\nu_{12}\nu_{21}}, \quad Q_{22} = \frac{E_2}{1-\nu_{12}\nu_{21}}, \quad Q_{66} = G_{12} \tag{2.64}$$

A laminate is formed by stacking several laminae such that a thickness, t_k, and an orientation with respect to the laminate axes, θ_k, is assigned to the k th lamina as shown in figure 2.5.

In plane stresses of the k th lamina in the direction of laminate axes can be expressed as:

$$\begin{bmatrix} \sigma_x \\ \sigma_y \\ \tau_{xy} \end{bmatrix} = \begin{bmatrix} \bar{Q}_{11} & \bar{Q}_{12} & \bar{Q}_{16} \\ \bar{Q}_{12} & \bar{Q}_{22} & \bar{Q}_{26} \\ \bar{Q}_{16} & \bar{Q}_{26} & \bar{Q}_{66} \end{bmatrix} \begin{bmatrix} e_x \\ e_y \\ \gamma_{xy} \end{bmatrix} \tag{2.65}$$

where $\bar{Q}_{ij}$ s are the plane stress-reduced stiffness matrices of the k th lamina in the

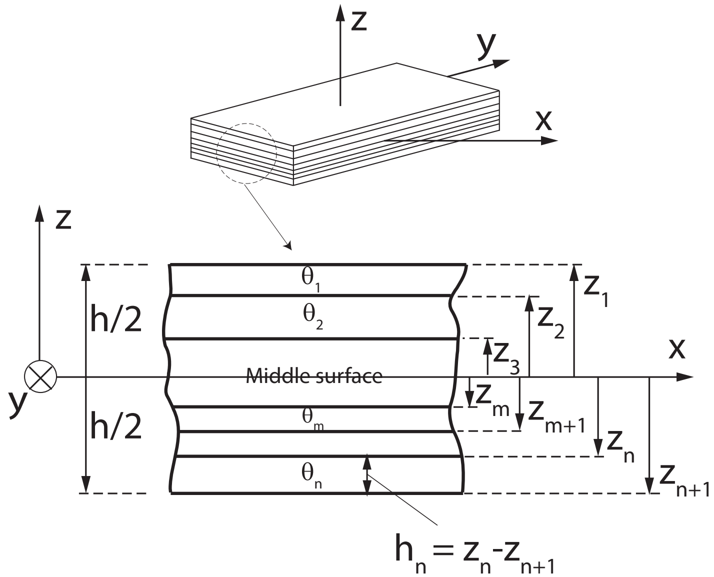

FIGURE 2.5: Composite laminate consisting n layers with thickness h_k, and orientation angle θ_k for layer k placed at z_k through-the-thickness coordinate measured from the middle surface (regenerated from Reddy [1])

laminate coordinate system:

$$
\begin{aligned}
\bar{Q}_{11} &= U_1 + U_2 \cos 2\theta_k + U_3 \cos 4\theta_k \\
\bar{Q}_{12} &= U_4 - U_3 \cos 4\theta_k \\
\bar{Q}_{22} &= U_1 - U_2 \cos 2\theta_k + U_3 \cos 4\theta_k \\
\bar{Q}_{66} &= U_5 - U_3 \cos 4\theta_k \\
\bar{Q}_{16} &= (U_2 \cos 2\theta_k + 2U_3 \cos 4\theta_k)/2 \\
\bar{Q}_{26} &= (U_2 \cos 2\theta_k - 2U_3 \cos 4\theta_k)/2
\end{aligned}
\tag{2.66}
$$

where θ_k is the orientation angle of the k th layer and U_i s are completely defined by the material properties of the k th layer and are invariant with respect to the orientation of that layer:

$$
\begin{aligned}
U_1 &= (3Q_{11} + 3Q_{22} + 2Q_{12} + 4Q_{66})/8 \\
U_2 &= (Q_{11} - Q_{22})/2 \\
U_3 &= (Q_{11} + Q_{22} - 2Q_{12} - 4Q_{66})/8 \\
U_4 &= (Q_{11} + Q_{22} + 6Q_{12} - 4Q_{66})/8 \\
U_5 &= (Q_{11} + Q_{22} - 2Q_{12} + 4Q_{66})/8
\end{aligned}
\tag{2.67}
$$

2

The total strains can be expressed in terms of the middle surface strains and curvatures using equation 2.47. Therefore, equation 2.65 for the k th layer, which is placed at the through-the-thickness coordinate z, is re-expressed as:

$$
\begin{bmatrix} \sigma_x \\ \sigma_y \\ \tau_{xy} \end{bmatrix} = \begin{bmatrix} \bar{Q}_{11} & \bar{Q}_{12} & \bar{Q}_{16} \\ \bar{Q}_{12} & \bar{Q}_{22} & \bar{Q}_{26} \\ \bar{Q}_{16} & \bar{Q}_{26} & \bar{Q}_{66} \end{bmatrix} \begin{bmatrix} \epsilon_x + z\kappa_x \\ \epsilon_y + z\kappa_y \\ \epsilon_{xy} + z\kappa_{xy} \end{bmatrix} \tag{2.68}
$$

where $z_{k-1} < z < z_k$. Equation 2.68 shows that the in-plane stresses in layer k either are constant, when the curvatures are zero ($\kappa_x = \kappa_y = \kappa_{xy} = 0$), or vary linearly with the through-the-thickness coordinate z, when the curvatures are not zero. However, even if all the layers are made of the same material, the discrepancy between the fibre orientations in the adjacent layers results in jumping of the stress values at the boundary of the adjacent layers as shown in figure 2.6.

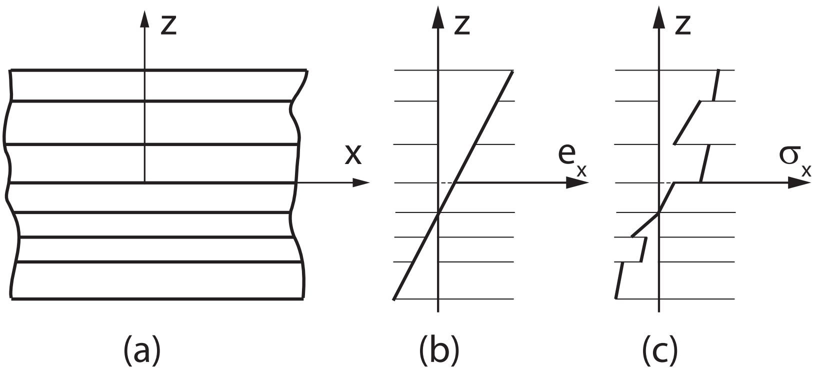

FIGURE 2.6: Variation of strains and stresses through the laminate thickness (a) Laminate, (b) Variation of a typical in-plane strain, (c) Variation of the corresponding stress component (regenerated from Reddy [1])

2

Although the spatial distribution of strains in a laminate can be easily expressed in terms of the middle surface strains and curvatures, there is not a unique equation for expressing the spatial distribution of stresses in the laminate. Therefore, the stress-strain relations can be formulated for each individual layer and not for the entire laminate. The constitutive relations can be expressed for the whole laminate by using the stress resultant and moment resultant quantities instead of the stress quantities. Stress resultants are defined by integration of the stresses throughout the thickness of the laminate:

$$N_x = \int_{-\frac{h}{2}}^{\frac{h}{2}} \sigma_x dz, \quad N_y = \int_{-\frac{h}{2}}^{\frac{h}{2}} \sigma_y dz, \quad N_{xy} = \int_{-\frac{h}{2}}^{\frac{h}{2}} \tau_{xy} dz, \tag{2.69}$$

Similarly, moment resultants are obtained by through-the-thickness integration of the moments of the stresses:

$$M_x = \int_{-\frac{h}{2}}^{\frac{h}{2}} \sigma_x z dz, \quad M_y = \int_{-\frac{h}{2}}^{\frac{h}{2}} \sigma_y z dz, \quad M_{xy} = \int_{-\frac{h}{2}}^{\frac{h}{2}} \tau_{xy} z dz, \tag{2.70}$$

Substituting the stresses of each layer from equation 2.68 in equations 2.69 and 2.70, the constitutive relations of the laminate are obtained based on CLT:

$$\begin{bmatrix} N_x \\ N_y \\ N_{xy} \end{bmatrix} = \begin{bmatrix} A_{11} & A_{12} & A_{16} \\ A_{12} & A_{22} & A_{26} \\ A_{16} & A_{26} & A_{66} \end{bmatrix} \begin{bmatrix} \epsilon_x \\ \epsilon_y \\ \epsilon_{xy} \end{bmatrix} + \begin{bmatrix} B_{11} & B_{12} & B_{16} \\ B_{12} & B_{22} & B_{26} \\ B_{16} & B_{26} & B_{66} \end{bmatrix} \begin{bmatrix} \kappa_x \\ \kappa_y \\ \kappa_{xy} \end{bmatrix} \tag{2.71}$$

$$\begin{bmatrix} M_x \\ M_y \\ M_{xy} \end{bmatrix} = \begin{bmatrix} B_{11} & B_{12} & B_{16} \\ B_{12} & B_{22} & B_{26} \\ B_{16} & B_{26} & B_{66} \end{bmatrix} \begin{bmatrix} \epsilon_x \\ \epsilon_y \\ \epsilon_{xy} \end{bmatrix} + \begin{bmatrix} D_{11} & D_{12} & D_{16} \\ D_{12} & D_{22} & D_{26} \\ D_{16} & D_{26} & D_{66} \end{bmatrix} \begin{bmatrix} \kappa_x \\ \kappa_y \\ \kappa_{xy} \end{bmatrix} \tag{2.72}$$

where:

$$\begin{aligned} A_{ij} &= \sum_{k=1}^{N} (\bar{Q}_{ij})_k \, (z_k - z_{k-1}) \\ B_{ij} &= \frac{1}{2} \sum_{k=1}^{N} (\bar{Q}_{ij})_k \, (z_k^2 - z_{k-1}^2) \\ D_{ij} &= \frac{1}{3} \sum_{k=1}^{N} (\bar{Q}_{ij})_k \, (z_k^3 - z_{k-1}^3) \end{aligned} \tag{2.73}$$

The **A** matrix is the extensional stiffness matrix, which relates the stress resultants to the middle surface strains of the laminate. The **B** matrix is the bending-extension coupling matrix which relates the stress resultants to the curvatures and the moment resultants to the middle surface strains of a laminate. The **D** matrix is the flexural, bending, stiffness matrix, which relates the moment resultants to the curvatures of the middle surface of a laminate.

The bending-extension coupling can be useful in certain structural applications, but usually it is considered undesirable in ordinary applications. Therefore, the **B** matrix can be set to zero by symmetric placement of the layers in the laminate about the middle surface. There are other ways to avoid the extension-shear and bending-twisting coupling through elimination of A_{16} and A_{26} terms and D_{16} and D_{26} terms, respectively [94].

2

2.5.2 LAMINATION PARAMETERS

Lamination parameters, introduced by Tsai and Hahn [95] and [96], provide a compact definition of the layup configuration. Lamination parameters are expressed as non-dimensional through-the-thickness integration of the trigonometric functions of the orientation angles:

$$
\begin{aligned}
(V_{1A}, V_{2A}, V_{3A}, V_{4A}) &= \int_{-\frac{1}{2}}^{\frac{1}{2}} (\cos 2\theta(\bar{z}),\ \sin 2\theta(\bar{z}),\ \cos 4\theta(\bar{z}),\ \sin 4\theta(\bar{z}))\, d\bar{z} \\
(V_{1B}, V_{2B}, V_{3B}, V_{4B}) &= 4\int_{-\frac{1}{2}}^{\frac{1}{2}} \bar{z}(\cos 2\theta(\bar{z}),\ \sin 2\theta(\bar{z}),\ \cos 4\theta(\bar{z}),\ \sin 4\theta(\bar{z}))\, d\bar{z} \\
(V_{1D}, V_{2D}, V_{3D}, V_{4D}) &= 12\int_{-\frac{1}{2}}^{\frac{1}{2}} \bar{z}^2(\cos 2\theta(\bar{z}),\ \sin 2\theta(\bar{z}),\ \cos 4\theta(\bar{z}),\ \sin 4\theta(\bar{z}))\, d\bar{z}
\end{aligned}
\tag{2.74}
$$

where V_A, V_B and V_D are the in-plane, coupling and out of plane lamination parameters, $\bar{z} = z/h$ is the normalized through-the-thickness coordinate and $\theta(\bar{z})$ is the orientation angle at $\bar{z}$. The laminate stiffness matrices can be expressed as linear functions of the lamination parameters as:

$$
\begin{aligned}
\mathbf{A} &= h(\boldsymbol{\Gamma}_0 + \boldsymbol{\Gamma}_1 V_{1A} + \boldsymbol{\Gamma}_2 V_{2A} + \boldsymbol{\Gamma}_3 V_{3A} + \boldsymbol{\Gamma}_4 V_{4A}) \\
\mathbf{B} &= \frac{h^2}{4}(\boldsymbol{\Gamma}_0 + \boldsymbol{\Gamma}_1 V_{1B} + \boldsymbol{\Gamma}_2 V_{2B} + \boldsymbol{\Gamma}_3 V_{3B} + \boldsymbol{\Gamma}_4 V_{4B}) \\
\mathbf{D} &= \frac{h^3}{12}(\boldsymbol{\Gamma}_0 + \boldsymbol{\Gamma}_1 V_{1D} + \boldsymbol{\Gamma}_2 V_{2D} + \boldsymbol{\Gamma}_3 V_{3D} + \boldsymbol{\Gamma}_4 V_{4D})
\end{aligned}
\tag{2.75}
$$

where $\mathbf{\Gamma}_i$ s are completely defined by the material invariants:

$$\mathbf{\Gamma}_0 = \begin{bmatrix} U_1 & U_4 & 0 \\ U_4 & U_1 & 0 \\ 0 & 0 & U_5 \end{bmatrix}, \mathbf{\Gamma}_1 = \begin{bmatrix} U_2 & 0 & 0 \\ 0 & -U_2 & 0 \\ 0 & 0 & 0 \end{bmatrix}, \mathbf{\Gamma}_2 = \begin{bmatrix} 0 & 0 & U_2/2 \\ 0 & 0 & U_2/2 \\ U_2/2 & U_2/2 & 0 \end{bmatrix}$$
$$\mathbf{\Gamma}_3 = \begin{bmatrix} U_3 & -U_3 & 0 \\ -U_3 & U_3 & 0 \\ 0 & 0 & -U_3 \end{bmatrix}, \mathbf{\Gamma}_4 = \begin{bmatrix} 0 & 0 & U_3 \\ 0 & 0 & -U_3 \\ U_3 & -U_3 & 0 \end{bmatrix} \tag{2.76}$$

where U_i s are the material invariants defined in equation 2.67.

In many structural design problems, the structural response of laminated composites can be fully described in terms of the stiffness matrices. The stiffness matrices cannot be directly used as design variables since their components are related to each other and cannot be selected arbitrarily. Instead the laminate stiffness matrices can be parameterised in terms of the orientation angles or lamination parameters. As will be described in subsection 4.4.1, the linear relation of the stiffness matrices and lamination parameters, equation 2.75, and the convex feasible region of lamination parameters, described in subsection 2.5.3, motivate using lamination parameters as design variables in some laminate optimisation problems instead of the orientation angles. In addition, lamination parameters are continuous design variables which are suitable for gradient-based optimisation. They provide the largest possible design space and hence the best conceptual design. The stiffness properties of a stacking sequence in the most general form can be expressed in terms of twelve lamination parameters. The number of lamination parameters required to describe the stiffness properties of a balanced symmetric laminate is reduced to four. Therefore, the number of design variables in the stacking sequence optimisation problem of a laminate with large number of layers is reduced when using lamination parameters than when using ply angles, which is very beneficial in terms of the computational cost of optimisation.

2.5.3 FEASIBLE REGION OF LAMINATION PARAMETERS

Lamination parameters cannot be chosen arbitrarily, since they are defined by the trigonometric expressions in equation 2.74 and are bounded and related. Therefore, if lamination parameters are selected as design variables, it is necessary to define the feasible region of lamination parameters, i.e. range of lamination parameters which correspond to a realistic laminate. If the structural response has an in-plane nature, the in-plane lamination parameters are sufficient to parameterise the in-plane stiffness matrix and hence the in-plane structural response. The feasible region for in-plane lamination parameters is defined as [97]:

$$\begin{aligned}
&2V_{1A}^2(1-V_{3A})+2V_{2A}^2(1-V_{2A})+V_{3A}^2+V_{4A}^2-4V_{1A}V_{2A}V_{4A}\leq 1\\
&V_{1A}^2+V_{2A}^2\leq 1\\
&-1\leq V_{iA}\leq 1 \quad (i=1,\dots,4)
\end{aligned} \tag{2.77}$$

For balanced symmetric laminates, $V_{2A} = V_{4A} = 0$, and therefore the feasible region simplifies to:

$$\begin{aligned}
&2V_{1A}^2-1\leq V_{3A}^2\\
&-1\leq V_{iA}\leq 1 \quad (i=1,3)
\end{aligned} \tag{2.78}$$

The same set of inequalities can be obtained for the out of plane lamination parameters, V_{iD}. The feasible region defined in equations 2.77 and 2.78 can be used for the design problems which are either completely dominated by the in-plane behaviour or completely dominated by the out of plane behaviour.

In practice, the structural responses are functions of both the in-plane and out of plane stiffness matrices. Therefore, the feasible region of combined in-plane and out of plane lamination parameters should be defined where solving the corresponding structural problems. So far no general analytical expressions have been found for the feasible region of combined in-plane and out of plane lamination parameters. Diaconu et al. [98] approximated the feasible region of any set of lamination parameters using a variational approach. Bloomfield et al. [99] give a method that can be used to obtain the analytical expressions for approximating the feasible region of combined in-plane and out of plane lamination parameters, when the set of ply angles are predefined and Grenestedt and Gudmundson [73] and Foldager et al. [100] have proved that the feasible region of any arbitrary set of lamination parameters is convex. Setoodeh et al. [101] use the convex nature of the feasible region to find an approximations of the feasible region. The developed numerical strategy is based on successive convex hull approximations and represent the approximate feasible region in the form of a set of linear inequalities. These linear inequalities can be readily included as constraints in any structural optimisation problem. The approximate feasible region of lamination parameters developed by Setoodeh et al. [101] is used in this thesis.

3

SEMI-ANALYTICAL STATIC AND BUCKLING SOLUTIONS OF CYLINDERS

3.1 INTRODUCTION

Exact analytical solutions of the governing partial differential equations (PDEs) of some structures are difficult to obtain and then only by using many simplifications or difficult calculations. The need to model the spatial variation of laminate stiffness in variable stiffness composite structures and the arbitrary geometry of the cross-section of cylindrical shells, which are of interest in this thesis, further preclude using analytical solutions for analysis of these structures. Therefore, approximate semi-analytical or numerical methods have been used to design variable stiffness structures.

The finite element method, as the most popular numerical method used for structural analysis, has several advantages; its applicability to a large range of problems, its robustness and its computational efficiency. In the semi-analytical methods such as Ritz method, parametric analytical expressions are usually used to predefine the structural response and then the parameter defining the analytical expressions are found using numerical methods. Therefore, if both finite element

Parts of this chapter have been published in Composite Structures **94** (2012) 2851-2860 [102] and Proceedings of the 8th World Congress on Structural and Multidisciplinary Optimization, June 1-5, 2009, Lisbon, Portugal: ISSMO [103].

and semi-analytical methods can be used to analyse a certain structure, less degrees of freedom (DOFs) are usually required in the semi-analytical methods. As the number of DOFs is increased in a structural model, the bandwidth of the stiffness matrix and hence the computational cost of analysis is increased. Therefore, the semi-analytical methods are usually computationally more efficient than the finite element method. The effect of computational efficiency becomes more pronounced when the analysis has to be repeated several times, which is the case during a design and optimisation process. The semi-analytical methods may not be as accurate as the finite element method, but they provide the designer with a fundamental understanding of the problem and the sensitivity of the structural responses with respect to the design variables. However, the range of applicability of semi-analytical methods is limited compared to the finite element method.

The static problem of a cylinder under pointwise tractions on the two end cross sections and with a traction-free lateral surface is called the Saint-Venant's problem. The Saint-Venat's solution is the solution of the relaxed formulation of the Saint-Venant's problem, in which the pointwise traction on the two ends is substituted by its integrals over the cross sections. In general, these integrals result in the axial force, transverse shear force (flexure), bending moments and torsion. It is indicated by Voigt [104] that in the Saint-Venant's solution of cylinders under extension, bending, torsion, the state of strain is constant in the axial direction of the cylinder and varies only in the circumferential direction. The same situation stands for the state of strain of the cylindrical shell under internal or external pressure, since the pressure distribution is uniform. However, it is shown by Voigt [104] that in the Saint-Venant's solution of cylinders under transverse shear force, the state of strain varies linearly in the axial direction.

According to the Saint-Venant's solution for cylindrical shells under extension, bending, torsion, internal or external pressure or any combination thereof, it is enough to tailor the laminate stiffness properties only in the circumferential direction to find the optimum variable stiffness design. As mentioned in subsection 1.5.1, it has been also shown by several researchers e.g. Tatting [84], Blom et al. [17], Sun and Hyer [39], Paschero and Hyer [105] and Paschero and Hyer [106] that the structural behaviour of cylindrical shells under the aforementioned load cases is improved by circumferential stiffness tailoring. Circumferential stiffness tailoring is beneficial for structural optimisation of cylindrical shells by limiting the number of design variables, and it motivates using a semi-analytical method for static and buckling analysis of cylindrical shells based on the Saint-Venant's solution, in which only the cross-section of the cylinder is discretised and hence it is computationally more efficient than a full finite element discretisation. The scope of this thesis is limited to circumferential stiffness tailoring of cylindrical shells with arbitrary cross-sections under load cases including extension, bending, torsion, internal or external pressure or any combination of them.

A semi-analytical finite element (SAFE) method is developed by Dong et al. [107] for static analysis of the inhomogeneous, anisotropic cylindrical bodies. In the SAFE method, the static problem of a cylindrical body is formulated by setting the first variation of the total potential energy to zero and then the Saint-Venant's displacement field is used to solve the static problem. The Saint-Venant's displacement field for the cylindrical body under extension, bending, torsion or any combination thereof, is composed of three parts; the primal and rigid-body displacement fields which are a linear function of axial location, and the warpings which only vary in the cross-sectional plane. The state of strain obtained from this displacement field is independent of the axial location and changes only in the cross-section. Therefore, only the cross-section of the cylinder is discretised using finite elements to find the warpings which are driven by the primal field. The primal field embodies the elementary hypothesis of bar and beam theories and the rigid-body field is eliminated before solution. The bending, torsion problem, and four parameters, which are the amplitudes of both the primal field and warpings, are found from the formulated static problem of the cylindrical body under extension. The solution process is very similar to that used for the traditional Kantorovich-Krylov method [108] which decouples the displacement field into two components in the longitudinal and circumferential directions.

In this chapter, the linear static and buckling problems of circumferentially variable stiffness cylindrical shells are formulated variationally. The classical laminate theory is used to formulate the total potential energy. The strains, changes of curvatures and rotations are related to the displacements using the Sanders strain-displacement relations. To formulate the eigenvalue buckling problem, the strains are generalised by adding the von Karman terms due to moderately large rotations. The Saint-Venant's displacement field is used for the static problem, while for the buckling problem, the displacement field is assumed to be the product of a sinusoidal axial displacement field and an unknown circumferential displacement field.

The primal part of the Saint-Venant's displacement field of a cylinder under extension, bending, torsion or any combination of them, which embodies the elementary hypothesis of bar and beam theories, varies linearly with the axial location. The primal part can be fully described in terms of four parameters consisting of the axial strain, two curvatures and a twist on the neutral axis of the cylinder. The cross-sectional warpings and the rigid-body displacement field are fully described by the displacements of the discretisation points on the circumference. Therefore, it is necessary to discretise the cylindrical shell only in the circumferential direction to describe fully the Saint-Venant's displacement field. The state of strain from this Saint-Venant's displacement field is independent of the axial location and only changes with the circumferential location. The strains, changes of curvatures and rotations consist of derivatives of the displacement field with respect to the axial and circumferential locations. In the developed semi-analytical method, the derivatives with respect to the axial location are expressed in terms of four parameters consisting of the axial strain, two curvatures and a twist on the neutral axis of the cylinder, and the derivatives with respect to the circumferential location are expressed as finite differences of the cross-sectional warpings.

In the buckling problem, the dependency of the total potential energy and hence the eigenvalue buckling problem on the axial location is eliminated by choosing a certain number of half-waves for the axial displacement. Therefore, the cylindrical shell is only discretised in the circumferential direction and finite difference is used to approximate the derivatives of the displacement field with respect to the circumferential location. The developed method for static and buckling analysis of variable stiffness cylindrical shells is called a semi-analytical finite difference (SAFD) method due to using analytical expressions for the displacement fields and finite difference for approximating the displacement derivatives.

In this chapter, first the SAFE method for static analysis of the inhomogeneous, anisotropic cylindrical bodies is described in section 3.2. The SAFE method is based on the Saint-Venant's solution and is the basis for the SAFD method developed for static analysis of circumferentially variable stiffness cylindrical shells in section 3.3. The SAFD method developed for buckling analysis of circumferentially variable stiffness cylindrical shells is described in section 3.4. The SAFD static and buckling analysis methods are verified in section 3.5 by comparing their results with those obtained using the commercial finite element code Abaqus^{TM}. In addition, a parametric study is reported in section 3.5 in which the effect of circumferential variation of the fibre angle orientation on the structural stiffness of some different composite cylindrical shells is investigated.

3.2 ST. VENANT'S PROBLEM OF ANISOTROPIC INHOMOGENEOUS CYLINDERS

A semi-analytical finite element (SAFE) method is developed by Dong et al. [107] based on the Saint-Venant's solution for static analysis of a finite length cylindrical body. The cross-section of this cylindrical body has an arbitrary geometry and is composed of any number of different linear elastic anisotropic materials. This SAFE method is used as the foundation for developing a semi-analytical finite difference (SAFD) method for computationally efficient static analysis of circumferentially variable stiffness cylindrical shells with arbitrary cross-sections in section 3.3.

The inhomogeneous, anisotropic cylindrical body considered was made of materials which were perfectly bonded providing full intersurface kinematic and traction continuity (see figure 3.1). Traction were applied to the two ends of the cylinder on a pointwise basis and the lateral surface of the cylinder has traction-free. Application of traction to the two ends resulted in axial force, transverse shear force (flexure), bending moments and torsion, such that the overall equilibrium of the cylinder was maintained.

The above problem for the special case of a homogeneous isotropic material is the well-known Saint-Venant's problem. Saint-Venant's solutions are the solutions for the relaxed formulation of Saint-Venant's problem in which the traction applied on the two ends in a pointwise basis is replaced by its integrals on the cross-sections representing the axial force, transverse shear force (flexure), bending moments and torsion. Saint-Venant's principle states that the difference between his solution and any other solutions for equivalent traction states are limited to the regions close to the ends of cylinder. There are unlimited end traction states upon integration of which the same force and moment resultants as in the relaxed formulation are produced, and hence many solutions exist which compete with the Saint-Venant's solution. There are certain characteristics which make Saint-Venant's solutions different from other solutions. Voigt [104] has shown that for extension, bending and torsion, the strain and stress fields are independent of axial coordinate and for flexure, they vary at most linearly along the axis of the cylinder. Sternberg and Knowles [109] indicate that the strain energy from the Saint-Venant's solution for the case of extension, bending and torsion of a homogeneous isotropic cylinder is the absolute minimum. They proved that for flexural loading in the special case of Poisson's ratio equal or close to zero, the strain energy occupies the minimum state.

In the SAFE method, only the cross section of the cylindrical body is discretised using two-dimensional finite elements. The displacement field of the cylinder is expressed as a product of two parts; a displacement field which is only a function of the axial coordinate and the interpolation functions which are the functions of the cross-sectional location. Using this form of displacement field, the static problem of the inhomogeneous, anisotropic cylinder with an arbitrary cross-section is formulated variationally in the two-dimensional finite element context. To solve the formulated static problem, the displacement field from the Saint-Venant's solution is used. Since a finite element method is used in combination with the analytical Saint-Venant's solution to formulate and solve the static problem of the inhomogeneous, anisotropic cylinder, the method is called the semi-analytical finite element (SAFE) method.

In this section the SAFE method is explained in subsection 3.2.1. The displacement field from the Saint-Venant's solution is described in subsection 3.2.2. The

SAFE method for the static problem of the inhomogeneous, anisotropic cylindrical body under axial force, bending moments and torsion is formulated in subsection 3.2.3.

3.2.1 SEMI-ANALYTICAL FINITE ELEMENT SOLUTION

The static problem formulation is described for a cantilevered cylindrical body of length L with an arbitrary shaped cross-section composed of any number of perfectly bonded linear elastic anisotropic material as depicted in figure 3.1. The open

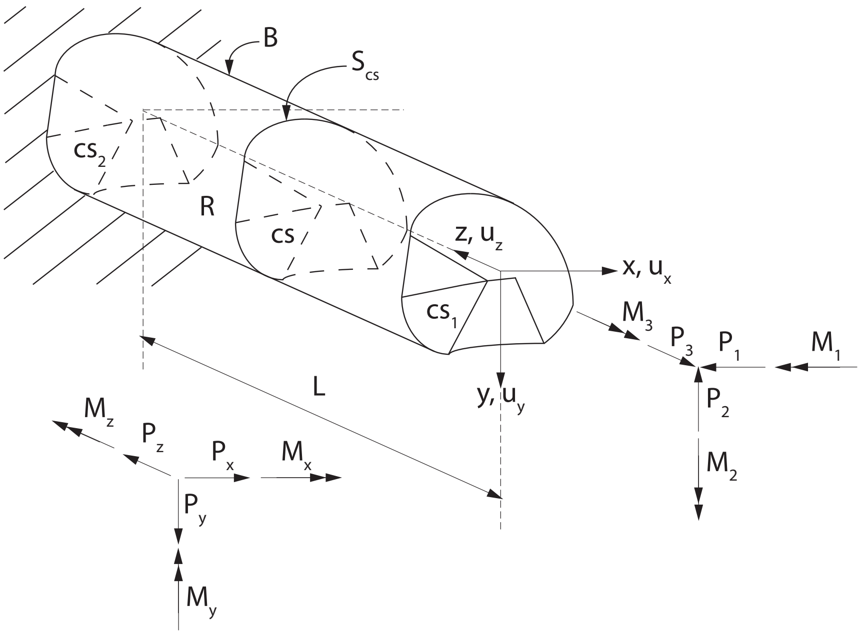

FIGURE 3.1: Geometry and coordinate system of the inhomogeneous, anisotropic cylinder (regenerated from Dong et al. [107])

volume occupied by the cylinder is denoted by R with the lateral surface defined by B. The generic cross-section of the cylinder is denoted by cs and the boundary curve of the cross-section is S_{cs}. The cross-sections at the tip and root are identified by cs_1 and cs_2, respectively. A right-hand Cartesian coordinate system (x, y, z) with the origin at some point on the tip cross-section, cs_1, is selected as the reference such that the xy plane is parallel to the cross-sectional planes and z axis is parallel to the cylinder axis. Stress, strain and displacement states at each point of the cylinder are denoted by $\boldsymbol{\sigma}(x, y, z) = \left[\sigma_x, \sigma_y, \sigma_z, \sigma_{yz}, \sigma_{xz}, \sigma_{xy}\right]^T$, $\boldsymbol{\epsilon}(x, y, z) = \left[\epsilon_x, \epsilon_y, \epsilon_z, \epsilon_{yz}, \epsilon_{xz}, \epsilon_{xy}\right]^T$ and $\mathbf{u}(x, y, z) = \left[u_x, u_y, u_z\right]^T$. The constitutive equation for a given anisotropic material in the cross-section has the form $\boldsymbol{\sigma} = \mathbf{C}\boldsymbol{\epsilon}$, where the symmetric (6×6) matrix $\mathbf{C}$ contains the 21 independent elastic moduli for the most general type of anisotropy.

The applied semi-analytical finite element (SAFE) method is based on discretising only the cross-sectional area of the cylinder into two-dimensional finite elements. The displacement field on each element is formulated as the product of the interpolation functions, $\mathbf{n}(x, y)$, and the cross-section and nodal variables, $\mathbf{u}_x, \mathbf{u}_y, \mathbf{u}_z$, which are functions of axial coordinate z. For example, if six-node triangular or eight-node quadrilateral elements are used to discretise the cross-section, the interpolation functions are complete second-order polynomials. Therefore, the displacement field can be expressed as:

$$\begin{bmatrix} u_x(x, y, z) \\ u_y(x, y, z) \\ u_z(x, y, z) \end{bmatrix} = \begin{bmatrix} \mathbf{n}(x, y) & 0 & 0 \\ 0 & \mathbf{n}(x, y) & 0 \\ 0 & 0 & \mathbf{n}(x, y) \end{bmatrix} \begin{bmatrix} \mathbf{u}_x(z) \\ \mathbf{u}_y(z) \\ \mathbf{u}_z(z) \end{bmatrix} \tag{3.1}$$

or

$$\mathbf{u}(x, y, z) = \mathbf{n}_e(x, y)\mathbf{u}_e(z) \tag{3.2}$$

Expressing the displacement field as a product of two parts allows to use a solution technique introduced by Kantorovich and Krylov [108]. In this method, the partial differential equations (PDEs) are reduced to ordinary differential equations (ODEs) by assuming the displacement field to be separable in different directions. One part of the displacement field is chosen a priori and the other part is determined based on the nature of the problem. This one step solution process does not require any iteration, and in terms of accuracy is placed between the exact and Ritz/Galerkin solution methods. In the extended version of the Kantorovich-Krylov method [108], an iterative solution between the separable components of displacement field is performed until convergence.

The differential operators in the strain-displacement relations can be partitioned into two parts according to the dependence of displacement field in equation 3.2:

$$\boldsymbol{\epsilon} = \mathbf{L}\mathbf{u} = \mathbf{L}_{xy}\mathbf{u} + \mathbf{L}_z\mathbf{u} \tag{3.3}$$

3

where $\mathbf{L}_{xy}$ and $\mathbf{L}_z$ are the matrices containing linear differential operators:

$$\mathbf{L}_{xy} = \begin{bmatrix} \frac{\partial}{\partial x} & 0 & 0 \\ 0 & \frac{\partial}{\partial y} & 0 \\ 0 & 0 & 0 \\ 0 & 0 & \frac{\partial}{\partial y} \\ 0 & 0 & \frac{\partial}{\partial x} \\ \frac{\partial}{\partial y} & \frac{\partial}{\partial x} & 0 \end{bmatrix} \qquad \mathbf{L}_z = \begin{bmatrix} 0 & 0 & 0 \\ 0 & 0 & 0 \\ 0 & 0 & \frac{\partial}{\partial z} \\ 0 & \frac{\partial}{\partial z} & 0 \\ \frac{\partial}{\partial z} & 0 & 0 \\ 0 & 0 & 0 \end{bmatrix} \tag{3.4}$$

substituting the displacement field from equation 3.2 in equation 3.4 gives the strain-displacement equations as:

$$\boldsymbol{\epsilon} = \mathbf{b}_1 \mathbf{u}_e + \mathbf{b}_2 \mathbf{u}_{e,z} \tag{3.5}$$

where:

$$\mathbf{b}_1 = \begin{bmatrix} \mathbf{n}_{,x} & 0 & 0 \\ 0 & \mathbf{n}_{,y} & 0 \\ 0 & 0 & 0 \\ 0 & 0 & \mathbf{n}_{,y} \\ 0 & 0 & \mathbf{n}_{,x} \\ \mathbf{n}_{,y} & \mathbf{n},x & 0 \end{bmatrix} \qquad \mathbf{b}_2 = \begin{bmatrix} 0 & 0 & 0 \\ 0 & 0 & 0 \\ 0 & 0 & \mathbf{n} \\ 0 & \mathbf{n} & 0 \\ \mathbf{n} & 0 & 0 \\ 0 & 0 & 0 \end{bmatrix} \tag{3.6}$$

The equilibrium equation is derived from the total potential energy using the variational principle:

$$\delta\,(\frac{1}{2}\int_0^L (\int\int_{cs} \boldsymbol{\epsilon}^T \mathbf{C} \boldsymbol{\epsilon} dxdy)\, dz - \mathcal{V}\,) = 0 \tag{3.7}$$

where $\mathcal{V}$ denotes the work done by the external tractions applied on the tip cross-section cs_1. Taking the first variation of $\mathcal{V}$ gives the information on boundary tractions, and hence knowing the boundary conditions of the Saint-Venant's problem is required for finding the proper expression of $\mathcal{V}$. Summing up the strain energy for all the elements and taking the first variation, results in the following equilibrium equation for the anisotropic cylinder:

$$\mathbf{K}_1 \mathbf{U}_{,zz} + \mathbf{K}_2 \mathbf{U}_{,z} - \mathbf{K}_3 \mathbf{U} = 0 \tag{3.8}$$

where $\mathbf{U} = \left[\mathbf{U}_x^T, \mathbf{U}_y^T, \mathbf{U}_z^T\right]^T$ shows the vector of assembled nodal displacement components, and the stiffness matrices $\mathbf{K}_1$, $\mathbf{K}_2$ and $\mathbf{K}_2$ are given by:

$$[\,\mathbf{K}_1 \quad \mathbf{K}_2 \quad \mathbf{K}_3\,] = \sum_{n=1}^{N} \int\int [\,(\mathbf{b}_2^T \mathbf{C} \mathbf{b}_2) \quad (\mathbf{b}_2^T \mathbf{C} \mathbf{b}_1 + \mathbf{b}_1^T \mathbf{C} \mathbf{b}_2) \quad (\mathbf{b}_1^T \mathbf{C} \mathbf{b}_1)\,]\, dx\, dy \tag{3.9}$$

where N is total number of elements in the cross-section. The stiffness matrices $\mathbf{K}_1$ and $\mathbf{K}_3$ are symmetric while $\mathbf{K}_2$ is anti-symmetric. The effect of each of these stiffness matrices can be determined by their dependence on $\mathbf{b}_1$ and $\mathbf{b}_2$. The stiffness matrix $\mathbf{K}_3$ is built from $\mathbf{b}_1$ and governs the cross-sectional plane strain and $\mathbf{K}_1$ is constructed from $\mathbf{b}_2$ and hence controls the behaviour complement to the cross-sectional plane strain, while $\mathbf{K}_2$ relates these two behaviours. The standard isoparametric finite element method can be used to derive the stiffness matrices. In the Saint-Venant's relaxed formulation, force and moment resultants are used instead of tractions on a cross-section. On a generic cross-section cs at some arbitrary axial coordinate z, the vector of forces and moments is denoted by $\mathbf{F}^T(z) = [P_x, P_y, P_z, M_x, -M_y, M_z]$ and related to the corresponding stress components by:

$$\int\int_{cs} \mathbf{h}^T \boldsymbol{\sigma}\, dx\, dy = \mathbf{F}(z) \tag{3.10}$$

where $\mathbf{h}(x, y)$ is given by:

$$\mathbf{h}(x,y) = \begin{bmatrix} 0 & 0 & 0 & 0 & 0 & 0 \\ 0 & 0 & 0 & 0 & 0 & 0 \\ 0 & 0 & 1 & y & x & 0 \\ 0 & 1 & 0 & 0 & 0 & x \\ 1 & 0 & 0 & 0 & 0 & -y \\ 0 & 0 & 0 & 0 & 0 & 0 \end{bmatrix} \tag{3.11}$$

Replacing the pointwise traction at the end cross-sections by their corresponding force and moment resultants, the work $\mathcal{V}$ done by the external forces gets the form:

$$\mathcal{V} = \mathbf{F}^T(0)\, \mathbf{a} = (P_1 a_1 + P_2 a_2 + P_3 a_3 + M_1 a_4 + M_2 a_5 + M_3 a_6)_{cs_1} \tag{3.12}$$

where a_i are displacement amplitudes from the Saint-Venant's solution, which are associated with the deformations corresponding to these force and moment resultants. The root end cs_2 is fully restrained.

3.2.2 DISPLACEMENT FIELDS FOR SAINT-VENANT'S SOLUTION

According to Iesan's scheme [110], the displacement fields for Saint-Venant's solution of extension-bending-torsion problem and flexure problem are constructed by integrating the rigid-body displacement field once and twice, respectively, with respect to the axial coordinate of the cylinder. Rigid-body displacement has six different modes which identically satisfy the equilibrium equation of the cylinder (equation 3.8) and result in zero strains when substituted into the strain-displacement equation 3.5. These six rigid-body modes form the basis for the description of the rigid-body displacement field and are expressed as six $\mathbf{R}_i$ $(3M \times 1)$ vectors:

$$\mathbf{R}_1 = \left[\mathbf{I}_1^T, \mathbf{0}^T, \mathbf{0}^T\right]^T, \quad \mathbf{R}_2 = \left[\mathbf{0}^T, \mathbf{I}_1^T, \mathbf{0}^T\right]^T, \quad \mathbf{R}_3 = \left[\mathbf{0}^T, \mathbf{0}^T, \mathbf{I}_1^T\right]^T,$$
$$\mathbf{R}_4 = \left[\mathbf{0}^T, \mathbf{0}^T, \mathbf{y}^T\right]^T, \quad \mathbf{R}_5 = \left[\mathbf{0}^T, \mathbf{0}^T, \mathbf{x}^T\right]^T, \quad \mathbf{R}_6 = \left[-\mathbf{y}^T, \mathbf{x}^T, \mathbf{0}^T\right]^T \tag{3.13}$$

where M is the total number of nodes in the finite element model and $\mathbf{I}_1$, $\mathbf{0}$, $\mathbf{x}$ and $\mathbf{y}$ are $(M \times 1)$ vectors with their elements being unity, zero, x and y coordinates of the M nodes, respectively. The rigid-body displacement is expressed by $\mathbf{U}_{RB}$ $(3M \times 1)$ vector:

$$\mathbf{U}_{RB} = \boldsymbol{\Phi}_{RB}\mathbf{a}_{RB} = \left[-z\mathbf{N}_1 + \mathbf{N}_2\right]\mathbf{a}_{RB} \tag{3.14}$$

where $\mathbf{a}_{RB} = [u_0, v_0, w_0, \omega_1, \omega_2, \omega_3]^T$ is the vector of six translational and rotational amplitudes and $\boldsymbol{\Phi}_{RB}$ is the $(3M \times 6)$ matrix denoting the rigid-body displacement field and:

$$\mathbf{N}_1 = [\mathbf{0}, \mathbf{0}, \mathbf{0}, \mathbf{R_2}, \mathbf{R_1}, \mathbf{0}], \quad \mathbf{N}_2 = [\mathbf{R_1}, \mathbf{R_2}, \mathbf{R_3}, \mathbf{R_4}, \mathbf{R_5}, \mathbf{R_6}] \tag{3.15}$$

Substituting equation 3.14 into the equilibrium equation 3.8 and strain-displacement equation 3.5 gives:

$$\mathbf{K}_3\mathbf{R}_i = \mathbf{0}\ (i = 1,2,3,6), \quad \mathbf{K}_3\mathbf{R}_4 = -\mathbf{K}_2\mathbf{R}_2, \quad \mathbf{K}_3\mathbf{R}_5 = -\mathbf{K}_2\mathbf{R}_1$$
$$\mathbf{b}_1\mathbf{r}_i = \mathbf{0}\ (i = 1,2,3,6), \quad \mathbf{b}_1\mathbf{r}_4 = \mathbf{b}_2\mathbf{r}_2, \quad \mathbf{b}_1\mathbf{r}_5 = \mathbf{b}_2\mathbf{r}_1 \tag{3.16}$$

where $\mathbf{r}_i$ s are equivalents of $\mathbf{R}_i$ s at element level.

3.2.3 EXTENSION-BENDING-TORSION PROBLEM

The displacement field for Saint-Venant's solution of extension-bending-torsion problem of the cylinder can be obtained by integrating the strain-displacement relations for a strain field independent of z or according to Iesan's scheme [110] by integrating the rigid-body displacement with respect to z. The extension-bending-torsion displacement field can be expressed as:

$$\mathbf{U}(x,y,z) = [\boldsymbol{\Phi}_I(x,y,z) + \boldsymbol{\Psi}_I(x,y)]\mathbf{a}_I + \boldsymbol{\Phi}_{RB}(x,y,z)\mathbf{a}_{RB} \tag{3.17}$$

where $\mathbf{U} = \left[\mathbf{U}_x^T, \mathbf{U}_y^T, \mathbf{U}_z^T\right]^T$ is a $(3M \times 1)$ vector and denotes the assembled ordered nodal displacement components, and $\boldsymbol{\Phi}_I$ and $\boldsymbol{\Psi}_I$ are the primal field and cross-sectional warpings which are $(3M \times 6)$ matrices [107]:

$$\boldsymbol{\Phi}_I = -\frac{z^2}{2}\mathbf{N}_1 + z\mathbf{N}_2 \tag{3.18}$$

and:

$$\boldsymbol{\Psi}_I = [\boldsymbol{\Psi}_{I1}, \boldsymbol{\Psi}_{I2}, \boldsymbol{\Psi}_{I3}, \boldsymbol{\Psi}_{I4}, \boldsymbol{\Psi}_{I5}, \boldsymbol{\Psi}_{I6}] \tag{3.19}$$

3

The rigid-body displacements are included in equation 3.17 for completeness. The primal field in equation 3.18 is derived from the integration of the rigid-body displacement field using Iesan's scheme [110], $\boldsymbol{\Phi}_I = \int \boldsymbol{\Phi}_{RB}\, dz$, and it will be shown that the warpings are driven by the primal field. The amplitudes of primal field and warpings are denoted by $\mathbf{a}_I$ which is a (6×1) vector:

$$\mathbf{a}_I = [a_{I1}, a_{I2}, a_{I3}, a_{I4}, a_{I5}, a_{I6}]^T \tag{3.20}$$

a_{I1} and a_{I2} are the amplitudes associated with the longitudinal shear deformations, a_{I3} with extension, where a_{I4} and a_{I5} with bending and a_{I6} with torsion. The longitudinal shear deformation modes appear in the displacement field of the extension-bending-torsion problem as a direct result of integrating the most general form of rigid-body displacement field. These deformation modes produce shear tractions on the lateral surface of the cylinder, B, which violate the condition of the Saint-Venant's problem stating that the lateral surface of the cylinder, B, should be traction free, however it will be shown shortly, these two shear deformation modes and their corresponding amplitudes, a_{I1} and a_{I2}, become uncoupled from the extension-bending-torsion problem and do not affect the results. Parts of the primal field with the amplitudes a_{I3} to a_{I6} represent the kinematic hypothesis governing the elementary structural rod and beam theories for extension, pure bending and torsion.

Substituting the displacement field of equation 3.17 in equilibrium equation, equation 3.8, and setting the terms multiplied by the amplitude coefficients, a_{Ii}, to zero, the following relations are obtained for the cross-sectional warpings:

$$\begin{aligned}
\mathbf{K}_3 \boldsymbol{\Psi}_{Ii} &= \mathbf{K}_2 \mathbf{R}_i \ (i = 1,2,3,6) \\
\mathbf{K}_3 \boldsymbol{\Psi}_{I4} &= \mathbf{K}_2 \mathbf{R}_4 - \mathbf{K}_1 \mathbf{R}_2 \\
\mathbf{K}_3 \boldsymbol{\Psi}_{I5} &= \mathbf{K}_2 \mathbf{R}_5 - \mathbf{K}_1 \mathbf{R}_1
\end{aligned} \tag{3.21}$$

It is clear that the cross-sectional warpings, $\boldsymbol{\Psi}_{Ii}$, are driven by the components of the primal field on the right-hand side of equation 3.21. warpings are defined as the elastic responses due to the cross-elasticity (Poisson) effect and longitudinal shear warpings due to free torsion. It can be seen from equations 3.16 and 3.21 that $\boldsymbol{\Psi}_{I1}$ and $\boldsymbol{\Psi}_{I2}$ are related to the rigid-body modes as:

$$\boldsymbol{\Psi}_{I1} = -\mathbf{R}_5\,, \qquad \boldsymbol{\Psi}_{I2} = -\mathbf{R}_4 \tag{3.22}$$

The stiffness matrix, $\mathbf{K}_3$, needs to be inverted for solving equation 3.21, however, $\mathbf{K}_3$ is singular due to the presence of rigid-body motion and cannot be inverted before eliminating the rigid-body modes. Therefore, three rigid-body translations along the three coordinate directions and the rigid-body rotation about the

3

z-axis must be suppressed in $\mathbf{K}_3$ before its inversion. Finding the nodal warpings $\boldsymbol{\Psi}_{Ii}$ from equation 3.21, the displacement field in equation 3.17 is completely defined and can be re-expressed at each point as:

$$
\begin{aligned}
u_x(x,y,z) &= a_{I1}z - a_{I5}\frac{z^2}{2} - a_{I6}yz + \sum_{i=1}^{6} a_{Ii}\Psi_{Iiu}(x,y) - \omega_3 y - \omega_2 z + u_0 \\
u_y(x,y,z) &= a_{I2}z - a_{I4}\frac{z^2}{2} + a_{I6}xz + \sum_{i=1}^{6} a_{Ii}\Psi_{Iiv}(x,y) + \omega_3 x - \omega_1 z + v_0 \\
u_z(x,y,z) &= (a_{I3}z + a_{I5}x + a_{I4}y)z + \sum_{i=1}^{6} a_{Ii}\Psi_{Iiw}(x,y) + \omega_1 y + \omega_2 x + w_0
\end{aligned}
\tag{3.23}
$$

Substituting the defined displacement field, equation 3.17, in the strain-displacement relation, equation 3.5, the element strain can be expressed as:

$$
\boldsymbol{\epsilon} = [\mathbf{b}_2\mathbf{n}_2 + \mathbf{b}_1\boldsymbol{\Psi}_{Ie}]\,\mathbf{a}_I = [\mathbf{h} + \mathbf{b}_1\boldsymbol{\Psi}_{Ie}]\,\mathbf{a}_I = \boldsymbol{\epsilon}_0\mathbf{a}_I \tag{3.24}
$$

where $\mathbf{n}_2$ and $\boldsymbol{\Psi}_{Ie}$ are the counterparts of $\mathbf{N}_2$ and $\boldsymbol{\Psi}_I$ at element level. The expression $\mathbf{b}_2\mathbf{n}_2$ in equation 3.24, is replaced by $\mathbf{h}$ defined in equation 3.11 considering the shape function properties in isoparametric finite element:

$$
\sum_{i=1}^{\text{nodes}} n_i = 1, \qquad \sum_{i=1}^{\text{nodes}} n_i x_i = \mathbf{nx} = x, \qquad \sum_{i=1}^{\text{nodes}} n_i y_i = \mathbf{ny} = y \tag{3.25}
$$

where nodes is the number of nodes in each element. The first two elements of the strain vector, $\boldsymbol{\epsilon}$, are the longitudinal shear strains, ϵ_{xz} and ϵ_{yz}, which are associated with the a_{I1} and a_{I2} amplitudes, respectively. Substituting the displacement field from equations 3.17 and 3.22 in equation 3.24, one can see that these two longitudinal shear strains become identically zero and are not involved in the extension-bending-torsion problem. Using the anisotropic stress-strain relation, the element stress can be obtained as:

$$
\boldsymbol{\sigma} = \mathbf{C}\boldsymbol{\epsilon}_0\mathbf{a}_I = \boldsymbol{\sigma}_0\mathbf{a}_I \tag{3.26}
$$

In the extension-bending-torsion problem, the two first component of the (6×1) force vector on the end cross-section cs_1 are zero:

$$
\mathbf{F} = [0, 0, P_3, M_1, M_2, M_3]^T \tag{3.27}
$$

These resultants are found by integrating the stress components $(\sigma_{zz}, \sigma_{xz}, \sigma_{yz})$ over each element cross-section as indicated in equation 3.10 and summing up the contributions from N elements of the total cross-section:

$$
\sum_{i=1}^{N} \int\int_{\mathrm{cs}_1} \mathbf{h}^T\boldsymbol{\sigma}\,dx\,dy = \sum_{i=1}^{N} \left[\int\int_{\mathrm{cs}_1} \mathbf{h}^T\mathbf{C}\,[\mathbf{h} + \mathbf{b}_1\boldsymbol{\Psi}_{Ie}]\,dx\,dy\right]\mathbf{a}_I = \mathbf{F} \tag{3.28}
$$

which can be also expressed in terms of cross-sectional (independent from z axis) stiffness relation:

$$\underset{(6\times6)}{\mathbf{k}_I}\underset{(6\times1)}{\mathbf{a}_I} = \underset{(6\times1)}{\mathbf{F}} \rightarrow \begin{bmatrix} \underset{(2\times2)}{\mathbf{0}} & \underset{(2\times4)}{\mathbf{0}} \\ \underset{(4\times2)}{\mathbf{0}} & \underset{(4\times4)}{\mathbf{k}_{Ibb}} \end{bmatrix} \begin{bmatrix} \underset{(2\times1)}{\mathbf{a}_{Ia}} \\ \underset{(4\times1)}{\mathbf{a}_{Ib}} \end{bmatrix} = \begin{bmatrix} \underset{(2\times1)}{\mathbf{0}} \\ \underset{(4\times1)}{\mathbf{F}_b} \end{bmatrix} \tag{3.29}$$

The expanded form of the nontrivial part $\mathbf{k}_{Ibb}$ is:

$$\begin{bmatrix} k_{I33} & k_{I34} & k_{I35} & k_{I36} \\ k_{I34} & k_{I44} & k_{I45} & k_{I46} \\ k_{I35} & k_{I45} & k_{I55} & k_{I56} \\ k_{I36} & k_{I46} & k_{I56} & k_{I66} \end{bmatrix} \begin{bmatrix} a_{I3} \\ a_{I4} \\ a_{I5} \\ a_{I6} \end{bmatrix} = \begin{bmatrix} P_3 \\ M_1 \\ -M_2 \\ M_3 \end{bmatrix} \tag{3.30}$$

3

The matrix $\mathbf{k}_{Ibb}$ (4×4) is symmetric. All the terms in the first two rows and columns of the matrix $\mathbf{k}_I$ (6×6) are equal to zero which shows that the longitudinal shear components play no role in the extension-bending-torsion problem.

3.3 STATIC ANALYSIS OF CYLINDRICAL SHELLS

The static problems of unstiffened and longitudinally stiffened cylindrical shells with arbitrary cross-sections are variationally formulated in this section. The total potential energy of the unstiffened cylindrical shell is formulated using the Sanders shell strain-displacement equations and assuming the Saint-Venant's displacement field for the extension-bending-torsion problem.

Similar to the Saint-Venant's displacement field of the cylindrical body explained in section 3.2, this displacement field for the cylindrical shell in the extension-bending-torsion problem is composed of the primal field, warpings and the rigid-body field. The primal field of the cylindrical shell can be fully expressed by four parameters, the axial strain, the two bending curvatures and the twist on the neutral axis of the cylinder, obtained from the bar and beam solution of the cylinder. To capture the displacement field due to the warpings, which is the same for all the cross-sections, the cross-section is discretised and the displacements at these discretisation points are used. Therefore, the axial strain, the two bending curvatures, the twist on the neutral axis of the cylinder, and the displacements at all the discretisation points of the cross-section are chosen as the static DOFs of the cylindrical shell.

As mentioned in section 3.2, the state of strain for Saint-Venant's displacement field in the extension-bending-torsion problem is independent of the longitudinal direction and varies only in the circumferential direction. The shell strains and changes of curvatures at each point on the circumference are expressed in terms of the chosen DOFs using Sanders shell strain-displacement, the total potential energy is formulated and the equilibrium equation is found from the total potential energy using the variational principle. This static analysis method is named the semi-analytical finite difference (SAFD) method, which is similar to the semi analytical finite element (SAFE) method described in section 3.2, because the assumed displacement field is found analytically from the Saint-Venant's solution and the finite difference is used to express the strain-displacement relations used in formulating the static problem.

The SAFD method can also be used for static analysis of the longitudinally stiffened cylinders. Longitudinal stiffeners are modeled as beams attached with rigid links to the cylindrical shell. This model can be simplified further using the smeared stiffness approach which finds the unstiffened cylindrical shell with the equivalent stiffness properties as the longitudinally stiffened cylindrical shell. The equilibrium equation of the equivalent stiffness cylindrical shell is found variationally from the total potential energy of the cylindrical shell and stiffeners both expressed in terms of the shell static DOFs. The total potential energy of the stiffeners are expressed in terms of the DOFs of the cylindrical shell using the kinematic relations between the axial strain, the two bending curvatures, the twist on the neutral axis of each stiffener and the DOFs of the shell at the connection point.

In this section, the SAFD method is explained for static analysis of unstiffened cylindrical shells in subsection 3.3.1. Using the SAFD method for static analysis of longitudinally stiffened cylindrical shells with the smeared stiffness modeling approach is explained in subsection 3.3.2.

3.3.1 UNSTIFFENED CYLINDRICAL SHELLS

The static problem is formulated by imposing the condition of being stationary to the total potential energy of the cylindrical shell. Therefore, the first variation of total potential energy is set to zero:

$$\delta\Pi = \delta(\mathscr{U} - \mathscr{V}) = 0 \tag{3.31}$$

where $\mathscr{U}$ is the elastic strain energy stored in the deformed body and $\mathscr{V}$ is the work done by the applied external forces. The strain energy is composed of membrane ($\mathscr{U}^m$) and bending ($\mathscr{U}^b$) parts:

$$\mathscr{U} = \mathscr{U}^m + \mathscr{U}^b = \frac{1}{2}\int_0^L \int_0^{S_{\text{cs}}} (\boldsymbol{\epsilon}^T \mathbf{N})\ d\beta\ d\alpha + \frac{1}{2}\int_0^L \int_0^{S_{\text{cs}}} (\boldsymbol{\kappa}^T \mathbf{M})\ d\beta\ d\alpha \tag{3.32}$$

where $\boldsymbol{\epsilon}$ and $\boldsymbol{\kappa}$ are the vectors of local strain and curvature and $\mathbf{N}$ and $\mathbf{M}$ are the vectors of local stress and moment resultants or vectors of local sectional force and moment, respectively. The strain energy in equation 3.32 can be re-expressed in terms of the stiffness matrices using the constitutive relations from the classical lamination theory, equations 2.71 and 2.72, as:

$$\mathscr{U} = \mathscr{U}^m + \mathscr{U}^b = \frac{1}{2}\int_0^L \int_0^{S_{cs}} (\boldsymbol{\epsilon}^T \mathbf{A} \boldsymbol{\epsilon})\ d\beta\ d\alpha + \frac{1}{2}\int_0^L \int_0^{S_{cs}} (\boldsymbol{\kappa}^T \mathbf{D} \boldsymbol{\kappa})\ d\beta\ d\alpha \tag{3.33}$$

where **A** and **D** are the extensional and bending stiffness matrices, respectively. The bending-extension coupling stiffness matrix, **B**, is zero since it is assumed that the layers in the laminate are placed symmetrically about the middle surface. L and S_{cs} are the length and circumference of the cylinder. The work done by the external forces and moments is:

$$\mathscr{V} = \mathscr{V}^m + \mathscr{V}^b = \int_0^L \int_0^{S_{cs}} (\boldsymbol{\epsilon}^T \mathbf{F}_{\text{ext}})\ d\beta\ d\alpha + \int_0^L \int_0^{S_{cs}} (\boldsymbol{\kappa}^T \mathbf{M}_{\text{ext}})\ d\beta\ d\alpha \tag{3.34}$$

where $\mathbf{F}_{\text{ext}}$ and $\mathbf{M}_{\text{ext}}$ are the local external force and moment vectors. The semi-analytical finite difference (SAFD) method for solving the static problem of cylindrical shells is developed by expressing the strains and curvatures in the total potential energy in terms of the DOFs which are required for describing the displacement field of the Saint-Venant's solution. Strains and curvatures are related to these static DOFs using the Sanders strain-displacement relations.

Displacement fields for Saint-Venant's solution

The displacement field for Saint-Venant's solution of an inhomogeneous, anisotropic cylindrical body is expressed in terms of the Cartesian coordinates in section 3.2. The displacement components at each point on the middle surface of the cylindrical shell are measured in the axial direction, $\mathbf{i}_\alpha$, tangent direction, $\mathbf{i}_\beta$, and normal direction to the shell, $\mathbf{i}_n$, and denoted by u, v, and w, respectively. These displacement components are related to the displacements of the middle surface of the cylindrical shell measured in the Cartesian coordinates, u_x, u_y, and u_z in the x, y, z directions, respectively:

$$\begin{aligned} u &= u_z \\ v &= u_x \frac{dx}{d\beta} + u_y \frac{dy}{d\beta} \\ w &= u_x(-\frac{dy}{d\beta}) + u_y \frac{dx}{d\beta} \end{aligned} \tag{3.35}$$

The complete displacement field is composed of the primal displacement field, $\boldsymbol{\Phi}_I$, warpings, $\boldsymbol{\Psi}_I$, and the rigid-body, $\boldsymbol{\Phi}_{RB}$, displacements:

$$\begin{aligned} u &= u_{\Phi_I} + u_{\Psi_I} + u_{\Phi_{RB}} \\ v &= v_{\Phi_I} + v_{\Psi_I} + v_{\Phi_{RB}} \\ w &= w_{\Phi_I} + w_{\Psi_I} + w_{\Phi_{RB}} \end{aligned} \tag{3.36}$$

The primal part of the displacement field of the cylindrical shell in the axial direction, which embodies the kinematic hypothesis of elementary rod and beam theories, can be expressed in the same form as the expression for u_z in equation 3.23:

$$u_{\Phi_I} = (a_{I3} + y a_{I4} + x a_{I5})\alpha \tag{3.37}$$

where $a_{I3} = \epsilon_\alpha^{\text{beam}}$, $a_{I4} = \kappa_x^{\text{beam}}$ and $a_{I5} = -\kappa_y^{\text{beam}}$. The primal displacement field of the cylindrical shell in the cross-sectional plane can be related to the twist, τ^{beam}, obtained from the rod solution of the cylinder under torsion. The amount of rotation of each cross-section around the cylinder axis is $\phi = \tau^{\text{beam}}\alpha$. As is clear from figure 3.2, the displacement components in the cross-sectional plane due to this rotation, ϕ (in radians), can be expressed in the Cartesian coordinates as:

$$\begin{aligned} u_x &= \phi y = \tau^{\text{beam}}\alpha y \\ u_y &= -\phi x = \tau^{\text{beam}}\alpha x \end{aligned} \tag{3.38}$$

The displacement field in equation 3.38 can be expressed in the $\mathbf{i}_\beta$ and $\mathbf{i}_n$ directions as v and w displacement components, respectively:

$$\begin{aligned} v_{\Phi_I} &= u_x \frac{dx}{d\beta} + u_y \frac{dy}{d\beta} = \tau^{\text{beam}}\alpha\left(y\frac{dx}{d\beta} - x\frac{dy}{d\beta}\right) \\ w_{\Phi_I} &= u_x\left(-\frac{dy}{d\beta}\right) + u_y \frac{dx}{d\beta} = \tau^{\text{beam}}\alpha\left(-y\frac{dy}{d\beta} - x\frac{dx}{d\beta}\right) \end{aligned} \tag{3.39}$$

Therefore using four parameters, the axial strain, $\epsilon_\alpha^{\text{beam}}$, two curvatures, $\kappa_x^{\text{beam}}, \kappa_y^{\text{beam}}$, and the twist, τ^{beam}, shown in figure 3.3, are enough to completely describe the primal displacement field in equations 3.37 and 3.39.

As mentioned in the subsection 3.2.3, warpings are elastic responses due to cross-elasticity effects, i.e. the Poisson effect, and longitudinal shear warpings due to free torsion and as it is clear from equation 3.21, the warpings are driven by the primal displacement field. Among different parts of the displacement field, the rigid-body (equation 3.14) and primal (equation 3.18) fields are functions of axial coordinate, while the displacement field due to the warpings (equation 3.19)

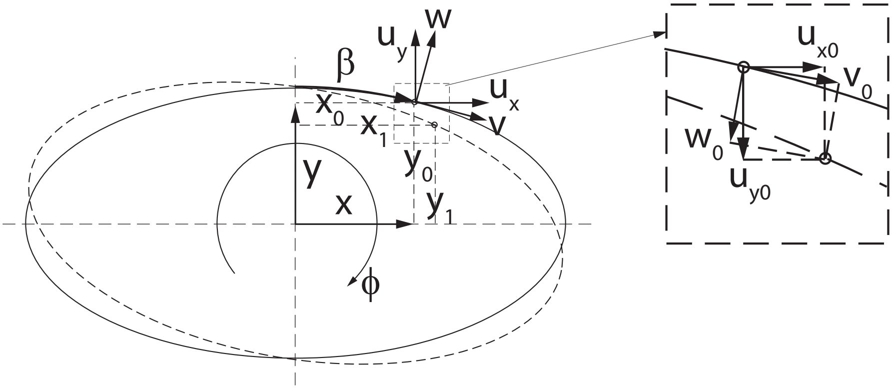

FIGURE 3.2: Displacements in the cross-section plane due to the torsion

is independent of the axial coordinate and is the same for all the cross-sections. Therefore, the cross-section is discretised into n discretisation points as shown in figure 3.3 and the warping displacement field is represented by the vector of displacement components of the n discretisation points on the cross-section:

$$\mathbf{U}^s_{\Psi_I,\Phi_{RB}}(\beta) = [u_1, v_1, w_1, u_2, v_2, w_2, ..., u_n, v_n, w_n]^T \tag{3.40}$$

This displacement vector includes the rigid-body displacement modes which should be eliminated before solving the equilibrium equation.

The four parameters representing the primal field, $\epsilon_\alpha^{\text{beam}}$, κ_x^{beam}, κ_y^{beam}, and τ^{beam}, append to the part of the displacement filed due to the warpings and rigid-body displacements, $\mathbf{U}^s_{\Psi_I,\Phi_{RB}}(\beta)$, to form the vector of total static DOFs, $\mathbf{U}^s$ $(3n + 4 \times 1)$, which is constant with changing the axial position (α) and is only function of circumferential position (β):

$$\mathbf{U}^s(\beta) = \left[\mathbf{U}^s_{\Psi_I,\Phi_{RB}}(\beta)^T, \epsilon_\alpha^{\text{beam}}, \kappa_x^{\text{beam}}, \kappa_y^{\text{beam}}, \tau^{\text{beam}}\right]^T \tag{3.41}$$

The four parameters $\epsilon_\alpha^{\text{beam}}$, κ_x^{beam}, κ_y^{beam}, and τ^{beam} of the cylindrical shell correspond to the four amplitudes of the primal and warping displacement fields of the cylindrical body, a_{I3}, a_{I4}, a_{I5}, a_{I6}, respectively. In the SAFE method for the cylindrical body under extension, bending and torsion, which is described in subsection 3.2.3, the warping deformation modes are driven from the primal displacement field using equation 3.21 and then the amplitudes of the primal and warping displacement fields, a_{I3}, a_{I4}, a_{I5}, a_{I6}, are found from equation 3.30. In the SAFD

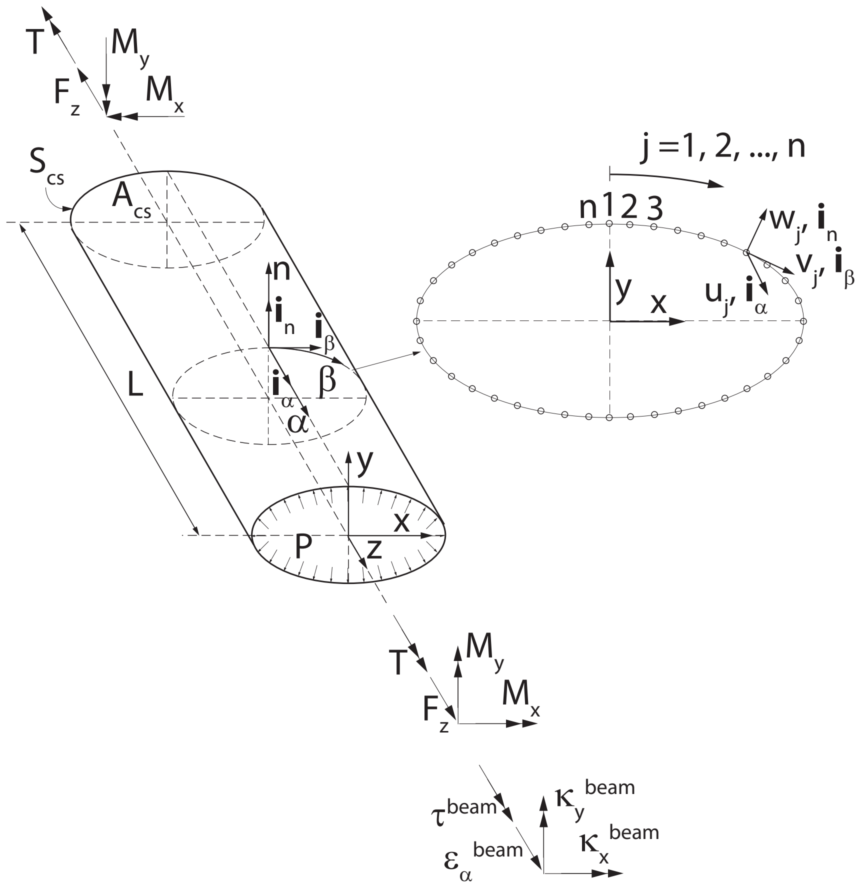

FIGURE 3.3: Geometry, loading and static DOFs of the cylindrical shell

method the difference is that these four parameters and the warping displacement fields for the cylindrical shell are all included in the vector of total static DOFs in equation 3.41 and will be obtained all together by solving the equilibrium equation.

Semi-analytical finite difference method

The Sanders strain-displacement relations in equations 2.53-2.55 are re-expressed in matrix form for each point on the middle surface of a cylindrical shell as:

$$\begin{bmatrix} \epsilon_\alpha \\ \epsilon_\beta \\ \epsilon_{\alpha\beta} \\ \kappa_\alpha \\ \kappa_\beta \\ \kappa_{\alpha\beta} \end{bmatrix} = \begin{bmatrix} \frac{\partial}{\partial\alpha} & 0 & 0 \\ 0 & \frac{\partial}{\partial\beta} & \frac{1}{R} \\ \frac{\partial}{\partial\beta} & \frac{\partial}{\partial\alpha} & 0 \\ 0 & 0 & -\frac{\partial^2}{\partial\alpha^2} \\ 0 & \frac{1}{R}\frac{\partial}{\partial\beta} & -\frac{\partial^2}{\partial\beta^2} \\ -\frac{1}{2R}\frac{\partial}{\partial\beta} & \frac{3}{2R}\frac{\partial}{\partial\alpha} & -2\frac{\partial^2}{\partial\alpha\partial\beta} \end{bmatrix} \begin{bmatrix} u \\ v \\ w \end{bmatrix} \tag{3.42}$$

It has been proved by Voigt [104] that for the Saint-Venant's solution of a cylinder under extension, bending and torsion, the state of strain is independent of the axial coordinate. The complete displacement field is found by substituting the primal displacement fields from equations 3.37 and 3.39 and the warpings and rigid body displacement fields from equation 3.40 in equation 3.36. This displacement field is substituted in the strain-displacement relations in equation 3.42. Using finite difference, the strains and changes of curvatures at each point on the cylindrical shell, which are independent of the axial coordinate, are expressed in terms of the components of the vector of total static DOFs, $\mathbf{U}^s$ $(3n+4\times 1)$:

$$\boldsymbol{\epsilon}_j = \mathbf{B}_j^m \mathbf{U}_j^s, \qquad \boldsymbol{\kappa}_j = \mathbf{B}_j^b \mathbf{U}_j^s \tag{3.43}$$

where $\boldsymbol{\epsilon}_j$ and $\boldsymbol{\kappa}_j$ are the strain and curvature vectors at the j th discretisation point and $\mathbf{U}_j^s$ as the vector of static DOFs and $\mathbf{B}_j^m$ and $\mathbf{B}_j^b$ as the strain-displacement matrices at this point are:

$$\mathbf{U}_j^s = \begin{bmatrix} u_{j-1}, v_{j-1}, w_{j-1}, u_j, v_j, w_j, u_{j+1}, v_{j+1}, w_{j+1}, \epsilon_\alpha^{\text{beam}}, \kappa_x^{\text{beam}}, \kappa_y^{\text{beam}}, \tau^{\text{beam}} \end{bmatrix}^T \tag{3.44}$$

$$\mathbf{B}_j^m = \begin{bmatrix} 0 & 0 & 0 & 0 & 0 & 0 & 0 & 0 & 0 & 1 & y_j & -x_j & 0 \\ 0 & \frac{-1}{2\Delta} & 0 & 0 & 0 & \frac{1}{R_j} & 0 & \frac{1}{2\Delta} & 0 & 0 & 0 & 0 & 0 \\ \frac{-1}{2\Delta} & 0 & 0 & 0 & 0 & 0 & \frac{1}{2\Delta} & 0 & 0 & 0 & 0 & 0 & \mathbf{B}_j^m(3,13) \end{bmatrix} \tag{3.45}$$

$$\mathbf{B}_j^b = \begin{bmatrix} 0 & 0 & 0 & 0 & 0 & 0 & 0 & 0 & 0 & 0 & 0 & 0 & 0 \\ 0 & \frac{-1}{2\Delta R_{j-1}} & \frac{-1}{\Delta^2} & 0 & 0 & \frac{2}{\Delta^2} & 0 & \frac{1}{2\Delta R_{j+1}} & \frac{-1}{\Delta^2} & 0 & 0 & 0 & 0 \\ 0 & 0 & 0 & 0 & 0 & 0 & 0 & 0 & 0 & \frac{-1}{2R_j} & \frac{-y_j}{2R_j} & \frac{x_j}{2R_j} & \mathbf{B}_j^b(3,13) \end{bmatrix} \tag{3.46}$$

where

$$\mathbf{B}_j^m(3,13) = \frac{y_j(x_{j+1} - x_{j-1}) - x_j(y_{j+1} - y_{j-1})}{2\Delta}$$

and

$$\mathbf{B}_j^b(3,13) = 2(1 + y_j\frac{(y_{j+1} - 2y_j + y_{j-1})}{\Delta^2} + x_j\frac{(x_{j+1} - 2x_j + x_{j-1})}{\Delta^2}) + \frac{3}{2R_j}\mathbf{B}_j^m(3,13)$$

and Δ is the distance between two subsequent discretisation points around the circumference of the cylinder.

Substituting the finite difference form of the strains and curvatures, equation 3.43, in the expressions for the total potential energy, equations 3.33 and 3.34, using numerical integration schemes to find the total potential energy and taking its first variation, the static problem can be formulated as:

$$\mathbf{K}^s\,\mathbf{U}^s = \mathbf{F}^s \tag{3.47}$$

where $\mathbf{K}^s$ $(3n+4 \times 3n+4)$ is the global tangent stiffness matrix and $\mathbf{F}^s$ $(3n+4 \times 1)$ is the force vector. The solution of equation 3.47 requires the inverse of $\mathbf{K}^s$ while this matrix is singular due to rigid-body motion. Therefore, four rigid-body modes must be eliminated before inversion.

The global tangent stiffness matrix ($\mathbf{K}^s$) is composed of membrane ($\mathbf{K}^m$) and bending ($\mathbf{K}^b$) parts and are assembled from the membrane ($\mathbf{k}_j^m$) and bending ($\mathbf{k}_j^b$) local stiffness matrices at the j th discretisation point using rectangular midpoint and trapezoidal integration schemes. Different numerical integration schemes are used for the membrane and bending part of the strain energy to avoid numerical issues and are selected based on the degree of derivatives of displacements with respect to β which is one for in-plane strains and two for curvatures. Therefore, the tangent stiffness matrix ($\mathbf{K}^s$) is assembled from the local membrane stiffness matrix calculated at the midpoint between j and $j+1$ ($\mathbf{k}_{j+\frac{1}{2}}^m$) and local bending stiffness matrix at point j ($\mathbf{k}_j^b$):

$$\mathbf{k}_{j+\frac{1}{2}}^m = \frac{L\Delta}{2}\,\mathbf{B}_{j+\frac{1}{2}}^{m\ T}\,\mathbf{A}_{j+\frac{1}{2}}\,\mathbf{B}_{j+\frac{1}{2}}^m, \quad \mathbf{k}_j^b = \frac{L\Delta}{2}\,\mathbf{B}_j^{b\,T}\,\mathbf{D}_j\,\mathbf{B}_j^b \tag{3.48}$$

In the extension-bending-torsion problem, the first $3n$ components of the force vector, $\mathbf{F}^s$, in equation 3.47 are set to zero and the last four components from the $3n+1$ th to the $3n+4$ th are the values of the axial force, two bending moments and torsion, respectively.

Although the Saint-Venant's solution used here is confined to extension-bending-torsion problem, the derived equilibrium equation is applicable for static analysis of a cylinder under uniform internal or external pressure. The reason is that the displacement field of a cylindrical shell under uniform internal or external pressure is constant in the longitudinal direction. Therefore if only uniform pressure is applied on the cylinder, the values corresponding to the extensional force, bending moments and torsion in the last four elements of the force vector are set to zero and uniform pressure can be modeled as a distributed force in the normal direction ($\mathbf{i}_n$) to the shell ($\mathbf{F}^s(i) = PA_{cs}/n$ where $i = 3, 6, 9, ..., 3n$). Consequently the strain, changes of curvature and twist from the beam solution of the cylinder will be zero.

Subsequently after solving the static problem, the strains and changes of curvatures are calculated at the midpoints and discretisation points, respectively. Strains at the midpoints are interpolated to find the strains at the discretisation points. Moreover, using the constitutive relations of the classical lamination theory, equations 2.71 and 2.72, and assuming a symmetric laminate about the middle surface ($\mathbf{B}_j = 0$), the sectional forces and moments at each discretisation point are found:

$$\mathbf{N}_j = \mathbf{A}_j \boldsymbol{\epsilon}_j, \quad \mathbf{M}_j = \mathbf{D}_j \boldsymbol{\kappa}_j \tag{3.49}$$

In the SAFE method for the cylindrical body, the displacement field of the cross-sectional warpings is driven by the primal displacement field through equation 3.21 and then the amplitudes of the warpings and the primal displacement field are found from equation 3.30, however, in the formulated SAFD method for the cylindrical shell the warpings and the four parameters defining the primal displacement field, including the axial stain, changes of curvatures and twist on the neutral axis of the cylinder, form the vector of total static DOFs, $\mathbf{U}^s$, and are obtained all together by solving equation 3.47.

In this thesis, cylindrical shells with simple cross sectional geometries, i.e. elliptical and circular cross-sections, are analysed. Therefore, using finite difference instead of finite element to formulate the problem consisting one dimensional differential equations is justified by the ease of implementation and low computational cost. The accuracy of the SAFD method is verified in section 3.5 by comparing the results of an analysis with those obtained from an analysis of the similar problem using the commercial finite element code Abaqus^{TM}. Moreover, the SAFD analysis method can be easily extended to a one dimensional semi-analytical finite element (SAFE) method for analysis of cylindrical shells with cross-sections that have more complex geometries e.g. the airfoil geometry for a wind turbine blade.

3.3.2 LONGITUDINALLY STIFFENED CYLINDRICAL SHELLS

In longitudinally stiffened cylindrical shells, the stiffeners are modeled as beams attached to the cylindrical shell with rigid links. The SAFD method developed in section 3.3.1 can also be used for static analysis of longitudinally stiffened cylindrical shell using the smeared stiffness approach. In the smeared stiffness approach, the unstiffened cylindrical shell which has stiffness properties equivalent to those of the longitudinally stiffened cylindrical shell is found.

3

Th equilibrium equation is derived by adding the total potential energy of the stiffeners to the total potential energy of the cylindrical shell and setting the first variation of the total potential energy to zero. The strain energy of a beam is formed from the normal and shear strains:

$$\mathscr{U}^{\mathrm{stf}} = \frac{L}{2}\int_{A^{\mathrm{stf}}} (\left[\epsilon_n^{\mathrm{stf}}, \epsilon_s^{\mathrm{stf}}\right] \begin{bmatrix} E\,\epsilon_n^{\mathrm{stf}} \\ G\,\epsilon_s^{\mathrm{stf}} \end{bmatrix}) dA \tag{3.50}$$

where A^{stf} is the stiffener cross sectional area, E and G are the normal and shear elastic moduli, which in case of laminated composite stiffeners are obtained from:

$$E = 1/A_{11}^{-1}, \qquad G = 1/D_{66}^{-1} \tag{3.51}$$

where A_{11} and D_{66} are the components of in-plane and bending stiffness matrices of the stiffener laminate. $\epsilon_s^{\mathrm{stf}}$ is the shear strain of the points on the stiffener cross-section induced by torsion and $\epsilon_n^{\mathrm{stf}}$ is the normal strain of the points on the stiffener cross-section induced by extension or compression and bending:

$$\epsilon_n^{\mathrm{stf}} = [1, y_l, -x_l] \begin{bmatrix} \epsilon_\alpha^{\mathrm{stf}} \\ \kappa_\alpha^{\mathrm{stf}} \\ \kappa_n^{\mathrm{stf}} \end{bmatrix}, \qquad \epsilon_s^{\mathrm{stf}} = r_l \tau^{\mathrm{stf}} \tag{3.52}$$

where r_l, x_l and y_l are the absolute distance and distances in the $\mathbf{i}_\beta$ and $\mathbf{i}_n$ directions, respectively, measured between the local coordinate system on the centroid of the stiffener cross-section as depicted in figure 2.4 and the selected point on the stiffener cross-section. $\epsilon_\alpha^{\mathrm{stf}}$, $\kappa_\alpha^{\mathrm{stf}}$, κ_n^{stf} and τ^{stf} are the longitudinal strain, bending curvatures and twist of the centroid of the stiffener cross-section. Substituting equation 3.52 in equation 3.50 the total strain energy of a stiffener can be expressed as:

$$\mathscr{U}^{\text{stf}} = \frac{L}{2}\int_{A^{\text{stf}}} \begin{bmatrix} \epsilon_\alpha^{\text{stf}} \\ \kappa_\alpha^{\text{stf}} \\ \kappa_n^{\text{stf}} \\ \tau^{\text{stf}} \end{bmatrix}^T \begin{bmatrix} 1\,E & y_l\,E & -x_l\,E & 0 \\ y_l\,E & y_l^2\,E & -x_l y_l\,E & 0 \\ -x_l\,E & -x_l y_l\,E & x_l^2\,E & 0 \\ 0 & 0 & 0 & r_l^2\,G \end{bmatrix} \begin{bmatrix} \epsilon_\alpha^{\text{stf}} \\ \kappa_\alpha^{\text{stf}} \\ \kappa_n^{\text{stf}} \\ \tau^{\text{stf}} \end{bmatrix} dA =$$

$$\frac{L}{2} \begin{bmatrix} \epsilon_\alpha^{\text{stf}} \\ \kappa_\alpha^{\text{stf}} \\ \kappa_n^{\text{stf}} \\ \tau^{\text{stf}} \end{bmatrix}^T \begin{bmatrix} EA^{\text{stf}} & EQ_x^{\text{stf}} & -EQ_y^{\text{stf}} & 0 \\ EQ_x^{\text{stf}} & EI_x^{\text{stf}} & -EI_{xy}^{\text{stf}} & 0 \\ -EQ_y^{\text{stf}} & -EI_{xy}^{\text{stf}} & EI_y^{\text{stf}} & 0 \\ 0 & 0 & 0 & GJ^{\text{stf}} \end{bmatrix} \begin{bmatrix} \epsilon_\alpha^{\text{stf}} \\ \kappa_\alpha^{\text{stf}} \\ \kappa_n^{\text{stf}} \\ \tau^{\text{stf}} \end{bmatrix} \tag{3.53}$$

where Q_x^{stf} and Q_y^{stf} are the first moments of area of the stiffener cross-section about $\mathbf{i}_\beta$ and $\mathbf{i}_n$, respectively. These first moments of area are zero since the local coordinate system is placed on the centroid of the stiffener cross-section, as shown in figure 2.4. I_x^{stf}, I_y^{stf} and I_{xy}^{stf} are the second moments of area and J^{stf} is the polar moment of area of the stiffener cross-section.

In the smeared stiffness modeling approach, the equivalent unstiffened cylindrical shell is found by expressing the axial strain, change of curvature and twist of the centroid of the stiffener cross-section in terms of the strains, changes of curvatures and displacements of the cylindrical shell at the connection point using equation 2.61. The strains and changes of curvature of the cylindrical shell can be stated in terms of the shell static DOFs using equation 3.43. Therefore, the total potential energy of the longitudinally stiffened cylindrical shell can be expressed in terms of the static DOFs, $\mathbf{U}^s$, of the cylindrical shell with equivalent stiffness properties. As stated earlier in section 2.4.3, the change of curvature of the stiffener around the normal vector to the cylindrical shell ,κ_n^{stf}, is neglected because the drilling DOF, θ_n, and the corresponding change of curvature, κ_n, are neglected for the cylindrical shell. Therefore, the axial strain, change of curvature and twist of the centroid of the cross-section of the stiffener can be related to the vector of static DOFs of the shell at point j, $\mathbf{U}_j^s$ (equation 3.44), as:

$$\begin{bmatrix} \epsilon_\alpha^{\text{stf}} \\ \kappa_\alpha^{\text{stf}} \\ \tau^{\text{stf}} \end{bmatrix} = \mathbf{B}^{\text{stf}}\mathbf{U}_j^s \tag{3.54}$$

where

$$\mathbf{B}^{\text{stf}} = \begin{bmatrix} 0 & 0 & 0 & 0 & 0 & 0 & 0 & 0 & 0 & 1 & y_j & -x_j & 0 \\ 0 & 0 & 0 & 0 & 0 & 0 & 0 & 0 & 0 & 0 & 0 & 0 & 0 \\ 0 & 0 & 0 & 0 & 0 & 0 & 0 & 0 & 0 & 0 & 0 & 0 & \mathbf{B}^{\text{stf}}(3,13) \end{bmatrix} \tag{3.55}$$

3

and

$$\mathbf{B}^{\text{stf}}(3,13) = 1 + y_j \frac{(y_{j+1} - 2y_j + y_{j-1})}{\Delta^2} + x_j \frac{(x_{j+1} - 2x_j + x_{j-1})}{\Delta^2} + \frac{7}{4R_j} \frac{y_j(x_{j+1} - x_{j-1}) - x_j(y_{j+1} - y_{j-1})}{2\Delta}$$

Therefore, the potential energy of a stiffener which is attached with rigid links to the j th discretisation point on the shell is expressed as:

$$\mathscr{U}^{\text{stf}} = \frac{L}{2} \mathbf{U}_j^{s\,T} \mathbf{B}^{\text{stf}\ T} \begin{bmatrix} EA^{\text{stf}} & EQ_x^{\text{stf}} & 0 \\ EQ_x^{\text{stf}} & EI_x^{\text{stf}} & 0 \\ 0 & 0 & GJ^{\text{stf}} \end{bmatrix} \mathbf{B}^{\text{stf}} \mathbf{U}_j^s \tag{3.56}$$

which is added to the strain energy of the shell (equation 3.33). The equilibrium equation of the longitudinally stiffened cylinder is found by setting the first derivative of the total potential energy of the cylindrical shell and the stiffeners equal to zero. The local stiffness matrix from the contribution of the stiffener attached to the j th discretisation point of the cylindrical shell is:

$$\mathbf{k}^{\text{stf}} = \frac{L}{2} \mathbf{B}^{\text{stf}\ T} \begin{bmatrix} EA^{\text{stf}} & EQ_x^{\text{stf}} & 0 \\ EQ_x^{\text{stf}} & EI_x^{\text{stf}} & 0 \\ 0 & 0 & GJ^{\text{stf}} \end{bmatrix} \mathbf{B}^{\text{stf}} \tag{3.57}$$

The $\mathbf{k}^{\text{stf}}$ matrices from all the stiffeners are assembled into the tangent stiffness matrix of the cylindrical shell, $\mathbf{K}^s$, to build the tangent stiffness matrix of the equivalent stiffness unstiffened shell and the corresponding static problem is formed and solved as equation 3.47.

3.4 BUCKLING ANALYSIS OF CYLINDRICAL SHELLS

The linear or eigenvalue buckling problem of unstiffened and stiffened general cross-section cylindrical shells is formulated variationally from the total potential energy. The nonlinear von Karman strains, which are defined in equation 2.51, are used instead of the linear strains to formulate this total potential energy. As explained in section 2.3.2, in the von Karman theory it is assumed that the strains and rotations are both small compared to unity, so that the changes of geometry can be ignored, however, the strains are smaller than the rotations such that the squares of rotations are comparable with strains. Due to the existence of relatively large rotations, the in-plane loads are projected in the normal direction to the shell. Linear buckling can be physically interpreted as the instability of the shell caused at a certain increased load level by the significant out of plane deformations due to the projections of the in-plane loads in the normal direction [111].

Sanders strain-displacement relations are used to express the strains, changes of curvatures and rotations of the shell in terms of the displacement field. The Kantorovich-Krylov method [108] is used to express the buckling displacement field (modes) of the cylindrical shell as the product of the axial and cross-sectional modes. The cross-sectional modes are determined by the three displacement components at each of the discretisation points on the cross-section and the axial mode is expressed as a sinusoidal function with a predetermined number of axial half-waves. The assumed form for the buckling mode implies that the cross-sectional modes are the same for all the cross-sections and the wavelength of the sinusoidal axial mode is constant in the axial direction. This form of the buckling mode is consistent with the pre-buckling state of strain due to the Saint Venant's solution which is independent of the axial location and varies only in the circumferential direction. The dependency of the buckling problem to the axial direction is eliminated by selecting the number of axial half-waves. Therefore, it is enough to find the cross-sectional modes to determine the complete buckling mode shape. Similar to the static problem, finite difference is used for the derivatives of displacement components with respect to the circumferential direction in the strain-displacement relations and hence, the solution method is again called semi-analytical finite difference (SAFD).

The linear buckling problem is formulated by setting the second variation of total potential energy to zero and using numerical integration schemes to assemble the stiffness matrices. The buckling eigenvalue problem has to be formulated and solved for different numbers of axial half-waves and the critical buckling mode is selected as the buckling mode which has the minimum buckling load.

3.4.1 UNSTIFFENED CYLINDRICAL SHELLS

The minimum total potential energy criterion is applied to formulate the eigenvalue buckling problem. As it is clear from equation 3.34, there are no second order terms in the work done by the external forces ($\mathscr{V}$). Therefore, the condition for loosing the structural stability is found by setting the second variation of strain energy to zero:

$$\delta^2 \Pi = \delta^2 \mathscr{U} = 0 \tag{3.58}$$

As shown in equation 3.33, the strain energy ($\mathscr{U}$) is composed of membrane ($\mathscr{U}^m$) and bending ($\mathscr{U}^b$) parts. Assuming infinitesimal strains and finite rotations, total von Karman strains are obtained from equation 2.50. Using equations 2.45- 2.47, the von Karman strains on the middle surface ($z = 0$) are expressed in the matrix form as:

$$\begin{bmatrix} \epsilon_{\alpha}^{VK} \\ \epsilon_{\beta}^{VK} \\ \epsilon_{\alpha\beta}^{VK} \end{bmatrix} = \begin{bmatrix} \epsilon_{\alpha} \\ \epsilon_{\beta} \\ \epsilon_{\alpha\beta} \end{bmatrix} + \frac{1}{2} \begin{bmatrix} \theta_{\alpha}^2 \\ \theta_{\beta}^2 \\ 2\,\theta_{\alpha}\,\theta_{\beta} \end{bmatrix} \tag{3.59}$$

Using the von Karman strains in equation 3.59, and keeping in mind that strains and rotations are both small compared to unity and squares of the rotations are comparable with the strains, the membrane part of the strain energy is modified as:

$$\mathscr{U}^m = \frac{1}{2}\int_0^L \int_0^C (\boldsymbol{\epsilon}^{VK\ T} \mathbf{A} \boldsymbol{\epsilon}^{VK})\, d\beta\, d\alpha = \frac{1}{2}\int_0^L \int_0^C (\boldsymbol{\epsilon}^T \mathbf{A} \boldsymbol{\epsilon})\, d\beta\, d\alpha + \frac{1}{2}\int_0^L \int_0^C (\boldsymbol{\theta}^T \mathbf{N} \boldsymbol{\theta})\, d\beta\, d\alpha \tag{3.60}$$

where $\boldsymbol{\theta}$ and $\mathbf{N}$ are the rotation vector of the normal to the mid-surface and the matrix of the in plane forces:

$$\boldsymbol{\theta} = \begin{bmatrix} \theta_{\alpha} \\ \theta_{\beta} \end{bmatrix} = \begin{bmatrix} 0 & 0 & -\frac{\partial}{\partial \alpha} \\ 0 & \frac{1}{R} & \frac{\partial}{\partial \beta} \end{bmatrix} \begin{bmatrix} u \\ v \\ w \end{bmatrix} \tag{3.61}$$

$$\mathbf{N} = \begin{bmatrix} N_{\alpha} & N_{\alpha\beta} \\ N_{\alpha\beta} & N_{\beta} \end{bmatrix} \tag{3.62}$$

To be able to solve the buckling problem, similar to the Kantorovich-Krylov method [108], the buckling mode shapes are expressed as the product of cross-sectional modes and sinusoidal axial modes:

$$\mathbf{U}(\alpha,\beta) = \mathbf{a}(\beta)\, e^{(im\pi\alpha/L)} \tag{3.63}$$

where $\mathbf{a}$ is the cross-sectional mode shape, i is the imaginary unit and m is the number of axial half-waves. Assuming a number of axial half waves, the dependency of buckling problem on the axial coordinate (α) is eliminated. The strain-displacement relations discretised in the circumferential direction for a certain number of axial half-waves are written in the matrix form:

$$\boldsymbol{\epsilon}_j = \mathbf{G}_j^m \mathbf{a}_j, \quad \boldsymbol{\kappa}_j = \mathbf{G}_j^b \mathbf{a}_j, \quad \boldsymbol{\theta}_j = \boldsymbol{\Omega}_j \mathbf{a}_j \tag{3.64}$$

where $\mathbf{a}_j$ as the vector of DOFs and $\mathbf{G}_j^m$, $\mathbf{G}_j^b$ and $\boldsymbol{\Omega}_j$ are the strain-displacement matrices used to calculate the strain, curvature and rotation vectors at point j and are defined as:

$$\mathbf{a}_j = \begin{bmatrix} u_{j-1}, v_{j-1}, w_{j-1}, u_j, v_j, w_j, u_{j+1}, v_{j+1}, w_{j+1} \end{bmatrix}^T \tag{3.65}$$

$$\mathbf{G}_j^m = \begin{bmatrix} 0 & 0 & 0 & \frac{iK}{L} & 0 & 0 & 0 & 0 & 0 \\ 0 & \frac{-1}{2\Delta} & 0 & 0 & 0 & \frac{1}{R_j} & 0 & \frac{1}{2\Delta} & 0 \\ \frac{-1}{2\Delta} & 0 & 0 & 0 & \frac{iK}{L} & 0 & \frac{1}{2\Delta} & 0 & 0 \end{bmatrix} \tag{3.66}$$

$$\mathbf{G}_j^b = \begin{bmatrix} 0 & 0 & 0 & 0 & 0 & (\frac{K}{L})^2 & 0 & 0 & 0 \\ 0 & \frac{-1}{2\Delta R_{j-1}} & \frac{-1}{\Delta^2} & 0 & 0 & \frac{2}{\Delta^2} & 0 & \frac{1}{2\Delta R_{j+1}} & \frac{-1}{\Delta^2} \\ 0 & 0 & \frac{iK}{\Delta L} & \frac{-iK}{2R_j L} & \frac{3iK}{2R_j L} & 0 & 0 & 0 & \frac{-iK}{\Delta L} \end{bmatrix} \tag{3.67}$$

$$\boldsymbol{\Omega}_j = \begin{bmatrix} 0 & 0 & 0 & 0 & 0 & \frac{-iK}{L} & 0 & 0 & 0 \\ 0 & 0 & \frac{1}{2\Delta} & 0 & \frac{1}{R_j} & 0 & 0 & 0 & \frac{-1}{2\Delta} \end{bmatrix} \tag{3.68}$$

Setting the second variation of strain energy equal to zero and using numerical integration schemes for the strain energy, the buckling eigenvalue problem for a given number of axial half waves is formulated as:

$$(\mathbf{K}^t - \lambda_b \mathbf{K}^g)\ \mathbf{a} = 0 \tag{3.69}$$

where $\mathbf{K}^t$ and $\mathbf{K}^g$ are the global material and geometric stiffness matrices, $\mathbf{a}$ is the vector of DOFs representing the cross-sectional mode shape, and λ_b is the load multiplier or buckling factor. The buckling modes are normalised such that:

$$\mathbf{a}^T\ \mathbf{K}^g\ \mathbf{a} = 1 \tag{3.70}$$

The material stiffness matrix, $\mathbf{K}^t$, is assembled from the local membrane, $\mathbf{k}_j^m$, and bending, $\mathbf{k}_j^b$, stiffness matrices. The geometric stiffness matrix, $\mathbf{K}^g$, is assembled from the local geometric stiffness matrix, $\mathbf{k}_j^g$. To avoid numerical issues, different numerical integration schemes are used for the membrane and bending parts of the of strain energy; rectangular midpoint for the membrane part and trapezoidal for the bending part.Therefore, the following local stiffness matrices calculated at point j and between points j and $j+1$ are used to assemble the material and geometric matrices, $\mathbf{K}^t$ and $\mathbf{K}^g$:

$$\mathbf{k}^m_{j+\frac{1}{2}} = \frac{L\Delta}{2}\, \mathbf{G}^{m\ T}_{j+\frac{1}{2}}\, \mathbf{A}_{j+\frac{1}{2}}\, \mathbf{G}^m_{j+\frac{1}{2}}, \quad \mathbf{k}^b_j = \frac{L\Delta}{2}\, \mathbf{G}^{b\,T}_j\, \mathbf{D}_j\, \mathbf{G}^b_j, \tag{3.71}$$
$$\mathbf{k}^g_{j+\frac{1}{2}} = -\frac{L\Delta}{2}\, \boldsymbol{\Omega}^{m\ T}_{j+\frac{1}{2}}\, \mathbf{N}_{j+\frac{1}{2}}\, \boldsymbol{\Omega}^m_{j+\frac{1}{2}}$$

3.4.2 LONGITUDINALLY STIFFENED CYLINDRICAL SHELLS

The smeared stiffness approach, which smears and adds the stiffness of stiffener to the location of the shell where the stiffener is attached, is used to model the stiffened cylindrical shells. The stiffeners are modeled as beams and their strain energy is added to that of the cylindrical shell. The stiffener strain energy for the static problem (equation 3.50) is modified by assuming moderately large rotations of the shell mid-surface and hence adding von Karman nonlinearity:

$$\mathscr{U}^{\text{stf}} = \frac{L}{2}\int_{A^{\text{stf}}} \left[\ \epsilon_n^{\text{stf}} + \frac{1}{2}(\theta_\alpha^{\text{stf}})^2 \ \ \epsilon_s^{\text{stf}}\ \right] \left[\begin{array}{c} E\,(\epsilon_n^{\text{stf}} + \frac{1}{2}(\theta_\alpha^{\text{stf}})^2) \\ G\,\epsilon_s^{\text{stf}} \end{array}\right] dA \tag{3.72}$$

3

Substituting equation 3.52 in equation 3.72, and neglecting the change of curvature of the stiffener around the normal vector to the cylindrical shell, κ_n^{stf}, the stiffener strain energy could be re-expressed as:

$$\mathscr{U}^{\text{stf}} = \frac{L}{2}\begin{bmatrix} \epsilon_\alpha^{\text{stf}} \\ \kappa_\alpha^{\text{stf}} \\ \tau^{\text{stf}} \end{bmatrix}^T \begin{bmatrix} EA^{\text{stf}} & EQ_x^{\text{stf}} & 0 \\ EQ_x^{\text{stf}} & EI_x^{\text{stf}} & 0 \\ 0 & 0 & GJ^{\text{stf}} \end{bmatrix} \begin{bmatrix} \epsilon_\alpha^{\text{stf}} \\ \kappa_\alpha^{\text{stf}} \\ \tau^{\text{stf}} \end{bmatrix} + \frac{L}{2} N_n^{\text{stf}} (\theta_\alpha^{\text{stf}})^2 \tag{3.73}$$

where $N_n^{\text{stf}} = E\,\epsilon_n^{\text{stf}}$ is the load applied in the normal direction to the stiffener cross-section. Substituting the displacement field for a pre-defined number of axial half waves in the form of equation 3.63 in equation 2.61, the stiffener strain, change of curvature, twist and rotation can be expressed in terms of cross-sectional shell buckling mode DOFs:

$$\begin{bmatrix} \epsilon_\alpha^{\text{stf}} \\ \kappa_\alpha^{\text{stf}} \\ \tau^{\text{stf}} \end{bmatrix} = \mathbf{G}^{\text{stf}} \mathbf{a}^{\text{stf}}\ e^{(im\pi\alpha/L)} \tag{3.74}$$

$$\theta_\alpha^{\text{stf}} = \boldsymbol{\Gamma}^{\text{stf}} \mathbf{a}^{\text{stf}}\ e^{(im\pi\alpha/L)} \tag{3.75}$$

where:

$$\mathbf{G}^{\text{stf}} = \begin{bmatrix} 0 & 0 & 0 & \frac{im\pi}{L} & 0 & z^{\text{stf}}\frac{m^2\pi^2}{L^2} & 0 & 0 & 0 \\ 0 & 0 & 0 & 0 & 0 & \frac{m^2\pi^2}{L^2} & 0 & 0 & 0 \\ 0 & 0 & \frac{im\pi}{2\Delta L} & 0 & \frac{im\pi}{R_j L} & 0 & 0 & 0 & -\frac{im\pi}{2\Delta L} \end{bmatrix} \tag{3.76}$$

$$\boldsymbol{\Gamma}^{\text{stf}} = \left[\ 0,0,0,0,0,-\frac{im\pi}{L},0,0,0\ \right] \tag{3.77}$$

and:

$$\mathbf{a}^{\text{stf}} = \left[\ u_{j-1}, v_{j-1}, w_{j-1}, u_j, v_j, w_j, u_{j+1}, v_{j+1}, w_{j+1}\ \right]^T \tag{3.78}$$

Therefore, the contribution of a stiffener attached with rigid links to the j th discretisation point on the shell, to the strain energy of the stiffened shell is:

$$\mathscr{U}^{\text{stf}} = \frac{L}{2}(\mathbf{a}_j)^T \left[(\mathbf{G}^{\text{stf}})^T \begin{bmatrix} EA^{\text{stf}} & EQ_x^{\text{stf}} & 0 \\ EQ_x^{\text{stf}} & EI_x^{\text{stf}} & 0 \\ 0 & 0 & GJ^{\text{stf}} \end{bmatrix} \mathbf{G}^{\text{stf}} + (\boldsymbol{\Gamma}^{\text{stf}})^T \;\; N_n^{\text{stf}} \;\; \boldsymbol{\Gamma}^{\text{stf}} \right] \mathbf{a}_j \tag{3.79}$$

Taking the second derivative of the strain energy of the stiffener gives rise to the following material and geometric stiffness matrices which will be assembled at the discretisation point j to the global material ($\mathbf{K}^m$) and geometric ($\mathbf{K}^g$) stiffness matrices, respectively:

$$\mathbf{k}^{\text{stf}\ m} = \frac{L}{2}(\mathbf{G}^{\text{stf}})^T \begin{bmatrix} EA^{\text{stf}} & EQ_x^{\text{stf}} & 0 \\ EQ_x^{\text{stf}} & EI_x^{\text{stf}} & 0 \\ 0 & 0 & GJ^{\text{stf}} \end{bmatrix} \mathbf{G}^{\text{stf}} \tag{3.80}$$

$$\mathbf{k}^{\text{stf}\ g} = \frac{L}{2}(\boldsymbol{\Gamma}^{\text{stf}})^T \;\; N_n^{\text{stf}} \;\; \boldsymbol{\Gamma}^{\text{stf}} \tag{3.81}$$

3.5 ANALYSIS VERIFICATION AND PARAMETRIC STUDY

In this section, the semi-analytical finite difference (SAFD) method developed for static and buckling analysis is verified by comparing the results with those obtained using the commercial finite element code Abaqus^{TM}. In addition, a parametric study is performed to investigate the effect of circumferential variation of the fibre angle orientation on the structural stiffness of different composite cylindrical shells. In this parametric study the structural stiffness is obtained from the SAFD static analysis and therefore the intuitive observations further verify the SAFD static analysis. The static analysis is verified in section 3.5.1. Then the effect of changing the fibre angle on the structural stiffness is studied in section 3.5.2. The developed SAFD method for buckling analysis of unstiffened and stiffened cylindrical shells is verified in section 3.5.3.

3.5.1 STATIC ANALYSIS VERIFICATION

A variable stiffness laminate design for maximum buckling capacity of a circular cylinder cylinder under bending moment is obtained by Blom et al. [17]. The circular cylinder has a diameter of 609.6 mm (24 in) and a length of 812.8 mm (32 in). The laminate thickness is 4.39 mm (0.1728 in) including 24 layers made of $AS4/8773$ material, the properties of which are given in table 3.1.

TABLE 3.1: Material properties of AS4/8773 [17]

Longitudinal modulus, E_1 [GPa / psi]	129.83 / 18.830e6
Transverse modulus, E_2 [GPa / psi]	9.08 / 1.317e6
Shear modulus, G_{12} [GPa / psi]	5.29 / 7.672e5
Poisson's ratio, ν_{12} [-]	0.32

In figure 3.4(a), the distribution of lamination parameters of the optimum variable stiffness design found by Blom et al. [17] is depicted versus the azimuth angle, starting from the point on the circular cross-section with the maximum axial tensile section force. To verify the SAFD static analysis, the variable stiffness design in figure 3.4(a) is analysed with SAFD method and in figure 3.4(b), the sectional force in the axial direction of the circular cylinder obtained from the SAFD method is compared with the results obtained from the commercial finite element code Abaqus^{TM} by Blom et al. [17]. Although the boundary conditions and multi-point constraints used in the finite element model constructed by Blom et al. [17] are not present in the SAFD method, the axial sectional force distributions from SAFD method and the commercial finite element code Abaqus^{TM} show good agreement in figure 3.4(b).

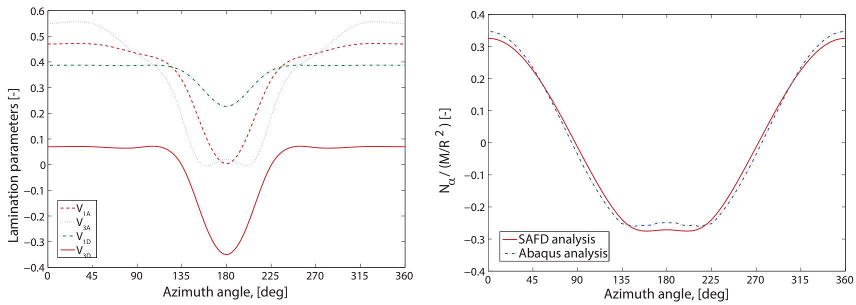

(a) Optimum circumferential distribution of lamination parameters obtained by Blom et al. [17]

(b) Normalised axial cross-section force

FIGURE 3.4: Distribution of lamination parameters for the VS laminate design obtained by Blom et al. [17] and comparison of the analysis results of this design obtained from SAFD developed in this chapter and Abaqus^{TM} analysis performed by Blom et al. [17]

3.5.2 PARAMETRIC STUDY OF STRUCTURAL STIFFNESS

One of the structural responses which could be chosen as a design driver for variable stiffness design of the cylindrical shell is the structural stiffness. A measure of the structural stiffness is the inverse of the structural compliance which is defined as the amount of strain energy stored in the structure under loading and can obtained in terms of the static DOFs, $\mathbf{U}^s$:

$$S = C^{-1} = (\frac{1}{2}\,\mathbf{F}^{s\,T}\,\mathbf{U}^s)^{-1} = (\frac{1}{2}\,\mathbf{U}^{s\,T}\,\mathbf{K}^s\,\mathbf{U}^s)^{-1} \tag{3.82}$$

where S is the measure of structural stiffness and C is the structural compliance.

In this subsection the effect of varying the fibre angle of the composite laminate layers around the circumference of the cylindrical shell on the structural stiffness is studied. This parametric study is performed by choosing a bi-symmetric, i.e. symmetric about the semi-major and semi-minor axes of the elliptical cylinder, and linear fiber angle variation for the variable stiffness demonstration. The fiber angles at the end of semi-minor and semi-major axes of ellipse are denoted by T_1 and T_2 as depicted in figure 3.5 and the fiber angle variation between T_1 and T_2 is linear:

$$\theta(\beta) = \beta\,(T_2 - T_1)/(0.25\,S_{\text{cs}}) \tag{3.83}$$

where for each point β is the curvilinear coordinate in the circumferential direction started from end of the semi-minor axis as shown in figure 3.5 and S_{cs} is the circumference of the cross-section. The laminate stacking sequence is assumed to

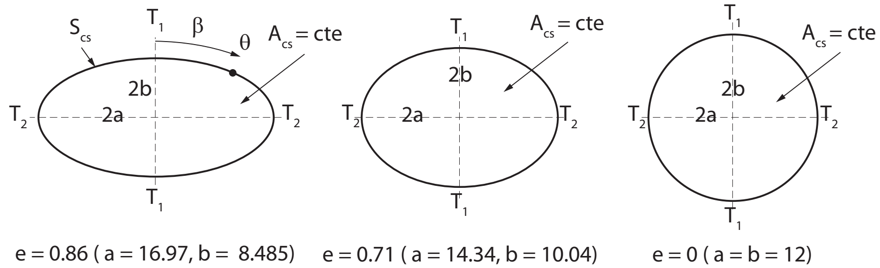

FIGURE 3.5: Elliptical cross-sections with the same area and different eccentricities

be $[\pm\theta]_{ns}$, which is balanced symmetric, and assuming the number of layers to be large, the lamination parameters are easily obtained as:

$$V_{1A} = V_{1D} = \cos 2\theta \qquad V_{3A} = V_{3D} = \cos 4\theta \tag{3.84}$$

TABLE 3.2: Material properties

Longitudinal modulus, E_1 [GPa / psi]	180.98 / 26.25e6
Transverse modulus, E_2 [GPa / psi]	9.79 / 1.42e6
Shear modulus, G_{12} [GPa / psi]	7.17 / 1.04e6
Poisson's ratio, ν_{12} [-]	0.28

3

The laminate thickness is 4.39 mm (0.1728 in) and the orthotropic material properties are listed in table 3.2.

As shown in figure 3.5, the cross-sectional areas, A_{cs}, of all the cylinders in the parametric study are set equal to that of a circular cylinder with radius of 304.8 mm (12 in) ($A_{cs} = \pi\ 304.8^2\ \text{mm}^2$ ($\pi\ 12^2\ \text{in}^2$)). To introduce elliptical cross-sections a parameter called eccentricity is defined:

$$e = (1 - (\frac{b}{a})^2)^{0.5} \tag{3.85}$$

where a is the semi-major and b is the semi-minor axis of the elliptical cross-section which can be found from:

$$a = (A_{cs}/\pi)^{0.5}(1-e^2)^{-0.25} \qquad b = A_{cs}/(\pi a) \tag{3.86}$$

Therefore, a cross-section with eccentricity of $e = 0$ is circular ($a = b$) and by increasing the eccentricity it tends to become more elliptical ($a > b$).

Different parametric studies of structural stiffness are presented in figures 3.6, and 3.8 for different eccentricities, laminate thicknesses and load cases. The results are shown as contours of the values of the structural stiffness expressed for all possible combinations of parametric fibre angles, T_1 and T_2, each one changing from 0° to 90°. The stiffness values shown in these figures are normalised with respect to the stiffness value of the quasi-isotropic (QI) laminate, $[\pm 45]_{ns}$.

In the first part of the parametric study, the effects of changing the eccentricity of the cylinder cross-section and varying the laminate thickness values on the maximum structural stiffness design and the corresponding parametric fibre angles, T_1 and T_2, are investigated. In this parametric study, the cylinders are analysed under combined internal pressure and the axial force induced by the internal pressure assuming two ends of the cylinder to be closed. The value of the applied internal pressure (P) is chosen such that the non-dimensional pressure $(Pa^2)/(E_{11}A_e)$ is unity, where A_e is the material area of the cross-section such that for a circular cross-section, $A_e = 2a\pi H = 2b\pi H$, where H is the laminate thickness.

Under the proposed load case in a circular cross-section ($e = 0$) cylindrical shell, only membrane internal forces exist in the circumferential and axial directions. In a cylinder with an elliptical cross-section, in addition to the membrane forces a bending internal moment exists in the circumferential direction, which tends to deform the elliptical cross-section into circular. The effect of this bending internal moment in the circumferential direction becomes more important compared to the membrane internal forces, as the eccentricity of the cross-section is increased. Intuitively, one knows that aligning the fibres in the axial direction (0°) provides stiffness in the axial direction while fibres aligned in the circumferential direction make the cylinder stiff in the circumferential direction (90°). Therefore, in a maximum stiffness or minimum compliance design if the membrane internal force in the axial direction is the dominant internal load, the fibres tend to align in the 0° direction and if the membrane internal force in the circumferential direction and/or bending internal moment in the circumferential direction are/is dominant, the fibres have the tendency to align in the 90° direction.

The effect of changing the eccentricity of the cylinder cross-section on the maximum stiffness design is shown in figure 3.6. It is clear from these figures that the design with minimum compliance is placed on the diagonal line of the contour plot where $T_1 = T_2$ which means that the fibre angle and hence the stiffness is constant around the circumference. Therefore, under this load-case and for this fibre angle variation pattern the variable stiffness design does not show any improvements in the structural stiffness over the corresponding constant stiffness design. As it is shown in figure 3.6(a), in the circular cylinder for the minimum compliance design fibers are aligned in 56° direction. This fibre angle direction could be interpreted as the effect of the existence of both axial and circumferential membrane internal forces in a circular cylinder under internal pressure and corresponding axial force. In an elliptical cylinder, increasing the eccentricity of cross-section increases the effect of internal bending moment in the circumferential direction. As can be seen from figures 3.6(a) and 3.6(b), the optimum fibre angle for the maximum stiffness design tends toward 90° as the internal circumferential bending effect becomes more dominant.

Figure 3.7 shows the results of the same parametric study performed on a cylinder with an increased thickness laminate. As it is clear from figure 3.7, the optimum fibre angle for maximum stiffness design tends to 90° direction as the eccentricity is increased which is similar to the trend seen for the cylinder with the original thickness laminate in figure 3.6. The interesting phenomenon is that, for a cylinder with an increased thickness laminate, the approach of the optimum fibre angle toward 90° due to increasing the cross-sectional eccentricity happens more slowly than for the cylinder with the original thickness laminate. As it is depicted in figure 3.7(b), for an increased thickness laminate the optimum fibre angle becomes almost equal to 90° at an eccentricity of 0.8, while for the original thickness laminate, the eccentricity at which the optimum fibre angle becomes almost 90° is 0.4.

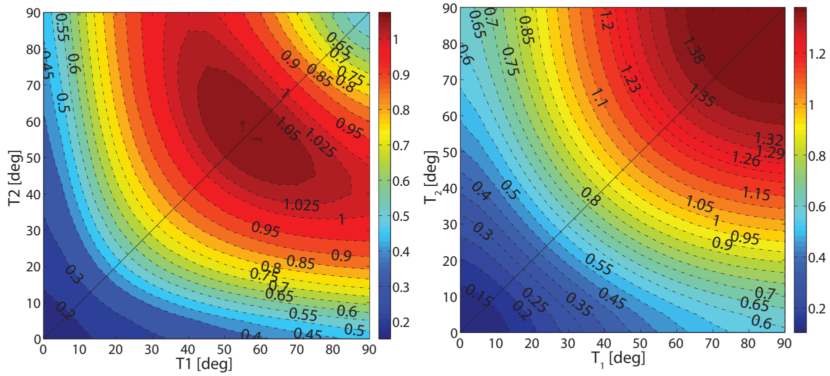

(a) Circular cylinder e=0.0 (b) Elliptical cylinder e=0.4

FIGURE 3.6: Normalised stiffness for internal pressure and corresponding axial force for initial thickness ($H = H_0$)

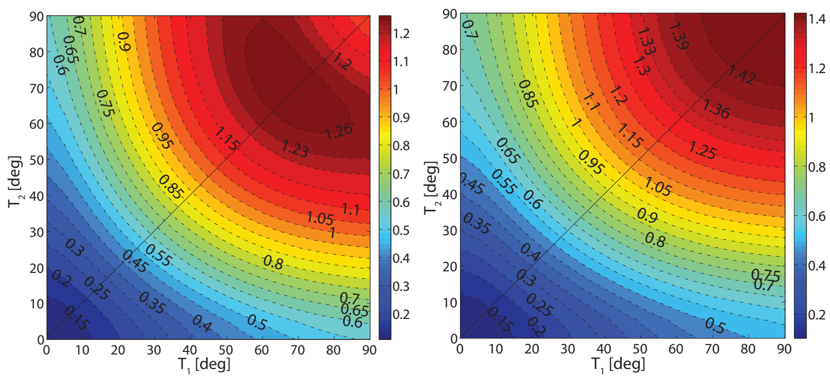

(a) Elliptical cylinder e=0.4 (b) Elliptical cylinder e=0.8

FIGURE 3.7: Normalised stiffness for internal pressure and corresponding axial force for increased thickness ($H = 3H_0$)

The membrane stiffness of the laminate is a homogeneous function of order one of the laminate thickness, while the bending stiffness is a homogeneous function of order three of the laminate thickness, i.e. if the thickness of the laminate is multiplied by c, the membrane stiffness is scaled by c while the bending stiffness is scaled by a factor of c^3. In other words, when the laminate thickness is increased, the bending stiffness is increased by more than the membrane stiffness. Therefore, although the fibres tend to align in the 90° direction when the eccentricities of both thin and thick laminated elliptical cylindrical shells are increased, this tendency is less for the thicker laminate than for the original thin laminate.

The second part of the parametric study is implemented on a cylinder under a combination of bending moment with internal pressure and the resulting axial force assuming the two ends are closed. The bending moment is applied around the semi-major axis of a cylinder with a highly elliptical cross-section, $e = 0.8$. The total load which is applied consists of a combination of $(1-r)$ times non-dimensional pressure $(Pa^2)/(E_{11}A_e)$ and (r) times non-dimensional bending moment $M/(E_{11}A_e a)$. In the elliptical cylinder with an eccentricity of 0.8, when only the internal pressure and its corresponding axial force are applied ($r = 0$), the effect of the internal bending moment in the circumferential direction is so dominant that the fibers are aligned almost in the 90° direction in the maximum stiffness design.

Introducing the external bending moment on this cylinder, the axial internal membrane force and hence the tendency of the fibres to align in the 0° direction is increased. In figure 3.8 it is shown that as the portion of external bending moment (r) is increased, the fiber angle (T_2) related to the points at the end of semi-major axis of the cross-section is remained in the 90° direction. This can be interpreted by the fact that the points at the end of semi-major axis of the cross-section are placed on the the neutral axis and hence no internal membrane axial force due to the external bending moment is carried by these points. This is while the largest internal membrane axial forces due to the external bending is carried by the points at the end of semi-minor axis of the cross-section and the fiber angle at these points, T_1, tends to 0°, for pure bending moment ($r = 1.0$) the fibers are almost aligned in the 0° direction all over the cross-section.

It is worth mentioning that using the bi-symmetric linear fibre angle distribution limits the design space and the improvements of steered fibre designs over the straight fibre designs. The maximum possible improvement which steering can provide over straight fibres can be achieved using the general multi-step optimisation framework presented in chapter 4. In the first step, lamination parameters, which provide the largest possible design space, are used as the design variables in the developed optimisation algorithm to achieve the best theoretically possible optimum designs.

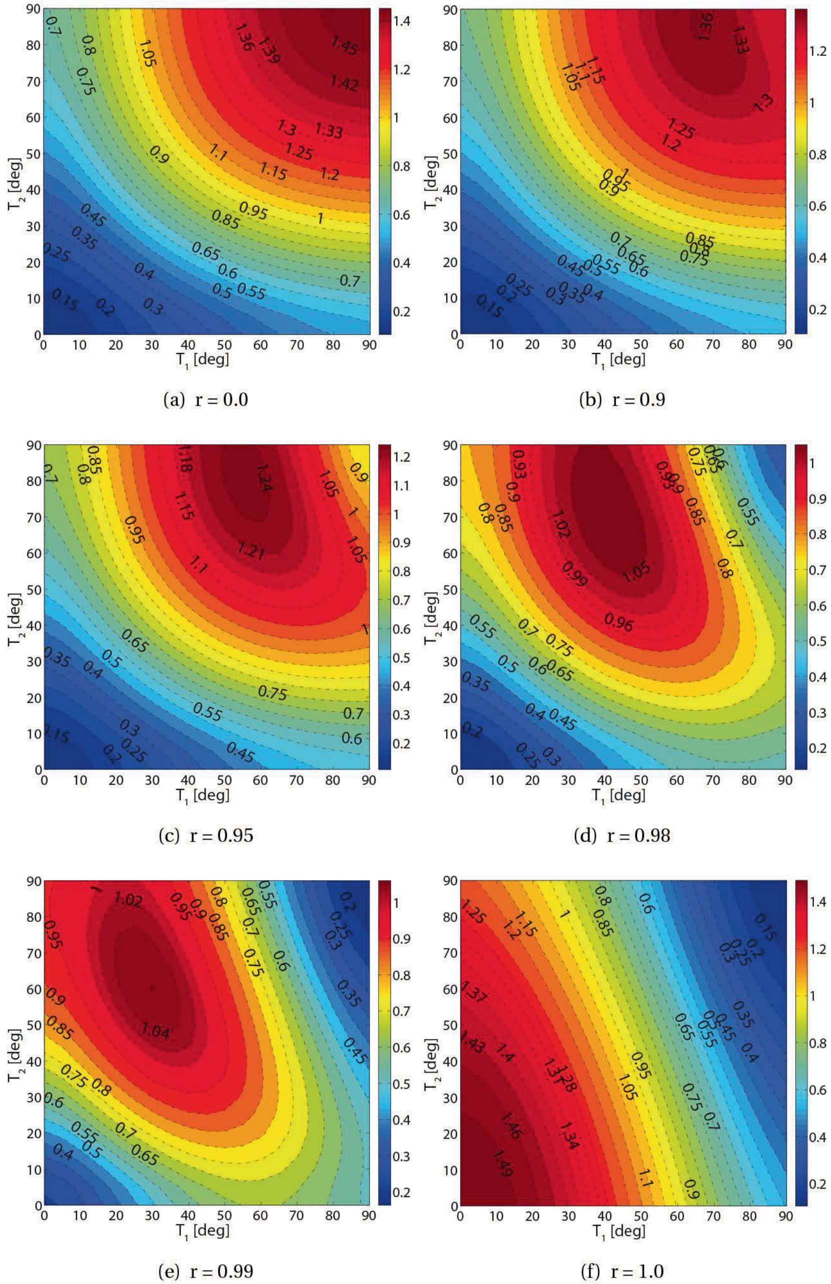

(a) r = 0.0

(b) r = 0.9

(c) r = 0.95

(d) r = 0.98

(e) r = 0.99

(f) r = 1.0

FIGURE 3.8: Normalised stiffness for an elliptical cylinder (e = 0.8) under a load case combined of $(1-r)$ times non-dimensional internal pressure and its corresponding axial force and (r) times non-dimensional bending

3.5.3 BUCKLING ANALYSIS VERIFICATION

The SAFD method for buckling analysis can be evaluated by analysing the baseline constant stiffness and the variable stiffness designs of a circular cylinder under pure bending as presented by Blom et al. [17]. The baseline constant stiffness in [17] is $[\pm 45, 0_2, \pm 45, 0_2, 90, \pm 45, 90]_s$ and the linear buckling load obtained from the commercial finite element software Abaqus^{TM} is reported to be 598 kN.m (5293 in-kips). The value of linear buckling load obtained using the SAFD method is 602.5 kN.m (5333 in-kips), with 11 axial half-waves, and hence the difference is 0.8%. The linear buckling load in [17] is reported to be 699.1 kN.m (6188 in-kips) for the variable stiffness design while this value from the SAFD analysis is 717.2 kN.m (6348 in-kips), with 10 axial half-waves, which is 2.5% higher.

3

Further verification of the SAFD analysis method is performed by comparing the buckling capacity of different QI laminated unstiffened an stiffened circular and elliptical cylinders obtained from the SAFD analysis method with the results obtained using the commercial finite element software Abaqus^{TM}. In Abaqus^{TM}, the cylindrical shell is modeled using the 3D conventional 4-node, quadrilateral, stress/displacement shell element, $S4$. The number and location of nodes in the circumferential direction are selected to be the same as the discretisation points in the SAFD method. To model the circumferential stiffness variation, each longitudinal strip of elements, containing elements in the same circumferential position, is defined as a set and the average laminate stiffness matrices of the nodes are assigned to each element set using the *general shell section* option. The boundary conditions and loads or moments are introduced through two dummy nodes, the 6 DOFs of each are related to the 6 DOFs of nodes of one of the two end cross-sections through *kinematic coupling*. The stiffeners are modeled with 3D linear beam elements, *B31*, placed on the centroid line of the I-beam. The offset between the I-beam centroid and the shell middle-surface is calculated considering the shell thickness. The beam elements are connected to the shell using *BEAM* multi-point constraint, *MPC*, which provide a rigid beam between the beam nodes and shell nodes constraining the displacement and rotation of the first set of nodes to the displacement and rotation of the second [112].

The selected stiffeners have I cross-sections as shown in figure 3.9, the dimensions of which are listed in table 3.3. The Young's modulus, E, and shear modulus, G, of the stiffeners are selected to be 210 GPa and 100 GPa, respectively.

The buckling moment of the unstiffened and stiffened circular cylinders under bending are obtained from SAFD analysis and compared with the Abaqus^{TM} results obtained with clamped boundary conditions. The investigated circular cylinders have a length of 812.8 mm (32 in). The laminate is 4.39 mm (0.1728 in) thick and made of $AS4/8773$ material, the properties of which are given in table 3.1. In table 3.4, the buckling moments from SAFD and Abaqus^{TM} for unstiffened and

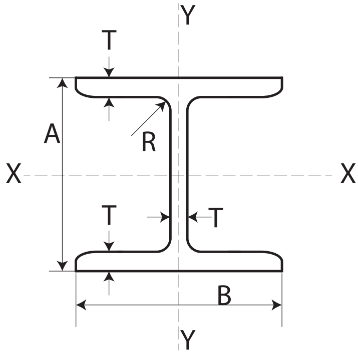

FIGURE 3.9: I cross-section of the stiffeners

TABLE 3.3: Geometric properties of 5 different I cross-sections selected for stiffeners [113]

Property	No. 1	No. 2	No. 3	No. 4	No. 5
A [mm / in]	19.05 / 0.75	31.75 / 1.25	38.1 / 1.5	63.5 / 2.5	101.6 / 4
B [mm / in]	31.75 / 1.25	34.93 / 1.375	38.1 / 1.5	50.8 / 2.0	101.6 / 4
T [mm / in]	1.6 / 0.063	2.39 / 0.094	3.18 / 0.125	2.39 / 0.094	7.95 / 0.313
R [mm / in]	3.18 / 0.125	3.18 / 0.125	3.18 / 0.125	3.96 / 0.156	6.35 / 0.250
Area [1e3 mm^2 / in^2]	0.134 / 0.207	0.235 / 0.364	0.504 / 0.781	0.392 / 0.607	2.277 / 3.53
I_{xx} [1e6 mm^4 / in^4]	0.0086 / 0.0206	0.0404 / 0.0970	0.1313 / 0.3156	0.2735 / 0.6571	3.919 / 9.415
I_{yy} [1e6 mm^4 / in^4]	0.0080 / 0.0193	0.0156 / 0.0375	0.1273 / 0.3058	0.0493 / 0.1184	1.264 3̃.037

stiffened circular cylinders with 3 different radii are compared. Each stiffened cylinder is stiffened with 8 stiffeners as depicted in figure 3.10(b) and the comparison is performed for 3 different stiffener cross-sections. The SAFD analysis is conservative in these cases, meaning that the buckling moments from SAFD are larger than those from Abaqus^{TM}. The percentage of difference, diff, between the buckling loads obtained from the SAFD method and those from Abaqus^{TM} are listed in table 3.4 and vary between −6.6% to −2.4%

To broaden the verification cases, the circular with the radius of 304.8 mm stiffened with 4 and 16 stiffeners, as depicted in figures 3.10(a) and 3.10(c), are investigated. Comparison of buckling moment from SAFD and Abaqus^{TM} is again performed for stiffeners with three different I cross-sections as listed in table 3.5. As it is clear from table 3.5, again the SAFD analysis is conservative and the differences range from −8% to −2.2%.

The buckling loads of unstiffened and longitudinally stiffened elliptical cylin-

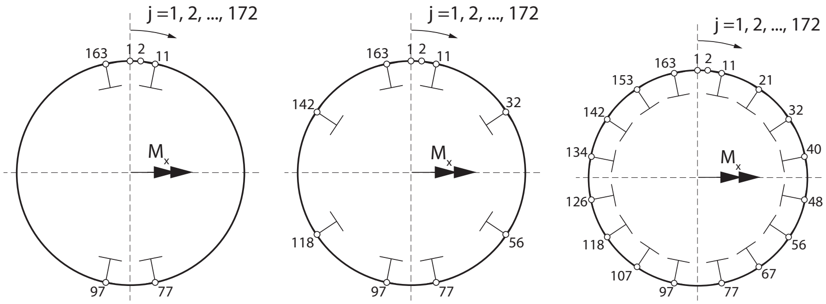

(a) cylinder with 4 stiffeners (b) cylinder with 8 stiffeners (c) cylinder with 16 stiffeners

FIGURE 3.10: Schematic configuration of stiffeners in the investigated circular cylinders, *Note: j = number of discretisation point in the cross-section*

TABLE 3.4: Buckling loads of unstiffened and longitudinally stiffened (8 stiffeners) circular cylinders with different radii and stiffener types obtained from the SAFD and Abaqus^{TM} and their differences (diff), *Note: radii are in mm, buckling loads are in kN.m, and the differences are in percentage (%)*

Radius	304.8			609.6			1219.2		
Buckling analysis	Abaqus	SAFD	diff	Abaqus	SAFD	diff	Abaqus	SAFD	diff
Unstiffened	592.6	578.5	-2.4	1182.5	1150.1	-2.8	2403.6	2298.3	-4.4
Stiffener No. 1	952.9	924.5	-3	1519.4	1479.2	-2.7	2746.5	2618.2	-4.7
Stiffener No. 3	1933.1	1841.3	-4.8	2448	2370.7	-3.2	3677.4	3502.7	-4.8
Stiffener No. 5	6667.5	6229	-6.6	6924.6	6638.6	-4.2	8111.2	7738.4	-4.6

TABLE 3.5: Buckling loads of longitudinally stiffened circular cylinders (Radius = 304.8 mm) with different numbers and types of stiffeners obtained from the SAFD and Abaqus^{TM} and their differences (diff), *Note: buckling loads are in kN.m, and the differences are in percentage (%)*

Number of stiffeners	4			16		
Buckling analysis	Abaqus	SAFD	diff	Abaqus	SAFD	diff
Stiffener No. 1	887.2	868.1	-2.2	1148.1	1105.1	-3.8
Stiffener No. 3	1663.7	1628	-2.2	2683	2523.4	-6
Stiffener No. 5	5458	5264.7	-3.6	10119	9312.4	-8

ders under axial compression are found using the SAFD method and compared with the Abaqus^{TM} results for simply-supported boundary conditions. The investigated elliptical cylinders have a length of 320 mm. The laminate is 1.12 mm thick and made of a medium modulus graphite-epoxy fiber-reinforced composite material with the material properties listed in table 3.6.

TABLE 3.6: Material properties of a medium modulus graphite-epoxy [39]

Longitudinal modulus, E_1 [GPa / psi]	130 / 18.855e6
Transverse modulus, E_2 [GPa / psi]	9.70 / 1.407e6
Shear modulus, G_{12} [GPa / psi]	5 / 7.252e5
Poisson's ratio, ν_{12} [-]	0.30

In table 3.7, the buckling loads from SAFD and Abaqus^{TM} for unstiffened and stiffened elliptical cylinders with 3 different eccentricities are compared. Each cylinder is stiffened with 8 stiffeners as depicted in figure 3.11(b) and the comparison is performed for 3 different stiffener cross-sections. As it is clear from table. 3.7, the SAFD method is conservative for the unstiffened elliptical cylinders while it is not conservative for longitudinally stiffened cylinders. The difference in the predicted buckling load ranges from −3% to 6.3%.

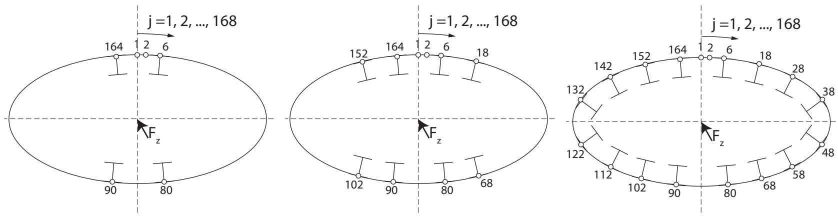

(a) cylinder with 4 stiffeners (b) cylinder with 8 stiffeners (c) cylinder with 16 stiffeners

FIGURE 3.11: Schematic configuration of stiffeners in the investigated elliptical cylinders, *Note: j = number of discretisation point in the cross-section*

The buckling loads of elliptical cylinders under axial compression stiffened with 4 and 16 stiffeners, as depicted in figures 3.11(a) and 3.11(c), with semi-major /semi-minor axis of 125/87.5 mm are obtained and compared from the two analysis methods in table 3.8. As it is shown in table 3.8, the SAFD analysis method is conservative for the cylinders stiffened with 4 stiffener, while it is not conservative for the cylinders stiffened with 16 stiffener. The differences between the predicted buckling loads from the SAFD and Abaqus^{TM} range from −2% to 4%.

In conclusion, the SAFD buckling analysis shows enough accuracy when compared to the Abaqus^{TM} results. The maximum difference is 8% for the largest cir-

TABLE 3.7: Buckling loads of unstiffened and longitudinally stiffened (8 stiffeners) elliptical cylinders with different sizes and stiffener types obtained from the SAFD and Abaqus^{TM} and their differences (diff), *Note: semi-minor and semi-major axes are in mm, buckling loads are in kN.m, and the differences are in percentage (%)*

semi-major axis	87.5			125			250		
semi-minor axis	62.5			87.5			87.5		
Buckling analysis	Abaqus	SAFD	diff	Abaqus	SAFD	diff	Abaqus	SAFD	diff
Unstiffened	156.7	154.1	-1.8	151.6	149.3	-1.6	65	63.1	-3
Stiffener No. 1	2359.8	2422.7	2.6	1463.1	1481.2	1.2	471.8	494.9	4.8
Stiffener No. 2	3931.8	4064.1	3.3	2396.3	2441.7	1.8	746.8	787.6	5.4
Stiffener No. 4	6307.7	6604.5	4.7	3823.1	3928.4	2.7	1166.3	1240.6	6.3

TABLE 3.8: Buckling load of longitudinally stiffened elliptical cylinders, semi-major /semi-minor axis = 125/87.5 mm, with different numbers and types of stiffeners obtained from the SAFD and Abaqus^{TM} and their difference (diff), *Note: buckling loads are in kN.m, and the differences are in percentage (%)*

Number of stiffeners	4			16		
Buckling analysis	Abaqus	SAFD	diff	Abaqus	SAFD	diff
Stiffener No. 1	724.6	710.2	-2	2689.2	2747.3	2.1
Stiffener No. 2	1134.5	1112.2	-2	4516.2	4668.5	3.3
Stiffener No. 4	1768.3	1734.3	-2	7342.8	7641.9	4

cular cylinder stiffened with 16 stiffeners that had the largest size among the investigated stiffeners.

4

MULTI-STEP OPTIMISATION FRAMEWORK

4.1 INTRODUCTION

Designing laminated composites is a challenge due to the non-convex optimisation problems, large number of design variables and combination of discrete and continuous design variables such as the number of layers and the ply angles, respectively. To this list should be added implementation of practical design rules such as the 10% robustness constraint and limitations on the number of adjacent plies with the same ply angle or the difference on the ply angles of adjacent layers. The degree of complexity of designing is increased for Variable Stiffness (VS) laminates since, instead of tailoring one laminate, the stacking sequence should be tailored at each spatial location in the laminate. On the top of these complexities for VS design of laminated composites, comes the necessity for continuity of the fibres across different design zones or between spatial locations, constraints on the maximum steering curvature and restrictions on the amount and distribution of the overlaps and gaps which appear as a result of fibre courses being placed that are not parallel. Application of the 10% robustness constraint, as a practical design rule, is more difficult for VS laminates since there may not exist any layers with fixed traditional orientations, 0°, $\pm 45^\circ$ or 90°.

The laminate design drivers generally consist of structural performance requirements, practical design rules, manufacturing constraints and cost. Improving of structural performance implicitly reduces material and operational cost through weight minimisation. Also, fibre placement reduces the costs compared to manual production due to reductions in the labour costs, waste materials and production times. AFP production times of VS laminates can be reduced by elaborate design of steered fibre paths through controlling the amount of steering and the number of tow cuts and restarts required.

The scope of the laminate optimisation problem in this chapter is limited to improvement of structural performance while considering the AFP manufacturing constraint on the maximum steering curvature. A typical laminate optimisation problem is formulated as:

$$\begin{aligned} &\min_{\mathbf{x}} f_0(\mathbf{x}) \\ &f_j(\mathbf{x}) \leq 0 \qquad j = 1,2,\dots,m \\ &x_i^L \leq x_i \leq x_i^U \qquad i = 1,2,\dots,n \end{aligned} \tag{4.1}$$

In the design optimisation problem of composite laminates, $f_0(\mathbf{x})$ and $f_j(\mathbf{x})$ are structural responses such as structural stiffness, strength, buckling capacity, natural frequency, weight, etc. The constraints $f_j(\mathbf{x})$ include the manufacturing constraint minimum allowable steering radius. The design variables each denoted by x_i, or combined denoted by $\mathbf{x}$, include the geometric definition of steered fibre paths in a VS design or ply angles in a CS design. One of the elements which can contribute to stiffness variation in a VS design, is the laminate thickness which may vary by dropping the plies or by possible overlaps and gaps due to steering. Therefore, the vector of design variables, $\mathbf{x}$, for a VS laminate may include the spatial distribution of laminate thickness which is a discrete design variable by nature.

Different strategies used to design steered fibre laminates are briefly explained in section 1.4 by introduction of two methods to model the stiffness variation of VS laminates; functional fibre path definition and discrete stiffness variation. The complex nature of VS laminate design and the advantages and disadvantages of each design method, discussed in section 1.4, motivates the development of an optimisation framework for efficient design of VS laminates which utilises the advantages of different design approaches while dealing with the disadvantages of each method in a multi-step framework (figure 4.1).

In this chapter, first a multi-step optimisation framework for efficient design of VS laminates, which is developed in the Aerospace Structures and Computational Mechanics, ASCM, group of the Aerospace Faculty at TUDelft, is introduced in section 4.2. The structural approximation methods and the conservative convex separable approximations of the structural performance measures, which are one of the main features of the multi-step framework, are described in section 4.3. The three steps of the multi-step optimisation framework are explained in more detail in sections 4.4, 4.5 and 4.6

4.2 MULTI-STEP OPTIMISATION FRAMEWORK

The idea of a multi-step design for VS structures was first introduced by IJsselmuiden et al. [114]. They used a two-step approach to design a multi-patch panel for minimum weight and subject to local buckling constraints.

In the first step, the buckling factor of each patch is approximated using a reciprocal approximation in terms of the bending stiffness matrix. The multi-modal buckling optimisation problem is formulated using the bound formulation proposed by Olhoff [115] and re-expressed using the dual method [116]. The bending stiffness matrix is a function of lamination parameters and laminate thickness which are chosen as continuous design variables. A gradient-based optimiser is used to solve the problem in a successive approximation scheme. In a successive approximation scheme optimisation algorithm is applied on the first approximation built based on an initial design, after finding the optimum the approximation is updated, optimisation is implemented on the updated approximation and this process is continued until a convergence criterion is achieved.

In the second step, the stacking sequence of each patch is obtained using a genetic algorithm (GA) which uses the approximation of the buckling load as the fitness function. In this step, first the Lagrangians of all the panels, formulated at the optimum continuous design found in the first step, are combined and the GA is implemented on this global approximation to find the initial stacking sequences. Then this design is used to construct the local approximations of the buckling factors of each panel and a GA is used to solve the local optimisation problem for each panel to prevent buckling constraint violation. Using approximations to evaluate the structural response reduces the number of necessary structural analyses and hence the computational cost of the GA optimisation. Finding the stacking sequence of each panel individually usually leads to a manufacturing mismatch between adjacent panel designs which is usually referred to as blending problem. To resolve this problem, a guide-based GA developed by Adams et al. [117] is used to ensure the continuity between adjacent patches. This continuity is obtained by first choosing a thick (guide) laminate for all the panels and then locally eliminating some of the layers in each panel. Elimination of the outermost or innermost layers leads to outwardly or inwardly completely blended laminates.

The multi-step design method of IJsselmuiden et al. [114] has three distinct benefits compared to the previous methods:

1. in the first step, approximation of structural response in terms of lamination parameters which are continuous design variables with largest possible design space. This strategy allows us to find the best possible design with limited number of structural analyses.

2. in the second step, using the approximation of structural response at the optimum continuous design obtained in the first step for finding the best stacking sequence. This method of finding the optimum stacking sequence has the advantage of using a more realistic measure of structural performance than the common approach of finding the stacking sequence which has the least square distance with the optimum continuous design in the lamination parameters space [118].

3. continuity of the adjacent panels, which is a manufacturing constraint, is satisfied in the second step.

Based on the idea of multi-step optimisation used by IJsselmuiden et al. [114] to design a multi-patch panel, a multi-step optimisation framework is developed in the ASCM group at TUDelft to design steered fibre laminates. The structural performance and manufacturing design drivers are separated in different steps of the multi-step design framework and the most suitable optimisation algorithm is used in each step. The outline of the three steps of the multi-step optimisation framework is illustrated in figure 4.1 with an example showing the three steps in VS laminate design for maximum strength of a rectangular panel with large cutouts under tension.

In the first step of the multi-step optimisation framework, the optimum stiffness matrices of the CS laminate design or the optimum spatial distributions of the stiffness matrices of the VS laminate design are found. The laminate stiffness variation in the VS laminate is modeled by assigning different stiffness properties to different discretisation points of the structure. The design drivers are the structural performance requirements. The obtained design is called the conceptual or theoretical stiffness design since it provides fundamental understanding of the optimum design and the mechanisms involved in the structural performance improvement, without knowing the realistic stacking sequence of the laminate.

In the second step of the multi-step optimisation framework, the optimum ply angles of the CS laminate or the optimum spatial distribution of the fibre angles in each layer of the VS laminate is retrieved from the conceptual stiffness design found in the first step without any structural analysis. The manufacturing constraints such as the maximum steering curvature of the VS laminate design, which are parameterised in terms of the fibre angles, can be imposed in this step. The manufacturable optimum stacking sequence, obtained in the second step, is called the realistic design in contrary to the conceptual stiffness design, obtained in the first step. The first and second steps of the multi-step framework take advantage of the conservative convex separable approximations built for the structural performance measures.

Step 1: Conceptual stiffness design (CS or VS)

Design drivers:
Structural performance requirements (buckling, strength, stiffness, weight, ...)

Outputs:
1- Optimum distribution of lamination parameters (laminate stiffness)
2- Optimum Lagrange multipliers
3- Sensitivities at the optimum design

Optimisation method:
Gradient-based optimisation:

- applied on the dual problem
- applied in a successive approximation scheme using the CCSA* of design drivers

↓

Step 2: Realistic stacking sequence design (CS or VS)

Design drivers:
1- Conceptual stiffness design
2- Manufacturing constraint on the fibre steering curvature (only VS)

Outputs:
Optimum ply angles (CS) or optimum spatial distribution of fibre angles in each ply (VS)

Optimisation method:
1- Genetic algorithm (CS or VS):

- fitness function : square distance between the conceptual and realistic designs in the lamination parameters space

2- Gradient-based optimisation initialised by the GA design (only VS):

- objective function: Lagrangian in the dual formulation of the approximate subproblem built at the conceptual design using the optimum Lagrange multipliers and sensitivities from step 1
- constraint: Maximum steering curvature

↓

Step 3: Steered fibre paths (only VS)

Design drivers:
1- Spatial distribution of fibre angles in each layer of the VS laminate
2- Minimum maximum overlap
3- Maximum smoothness of overlaps

Outputs:
1- Steered fibre paths used as the centreline of courses
2- Continuous estimation of thickness distribution

Method:
Streamline analogy

* CCSA: conservative convex separable approximation

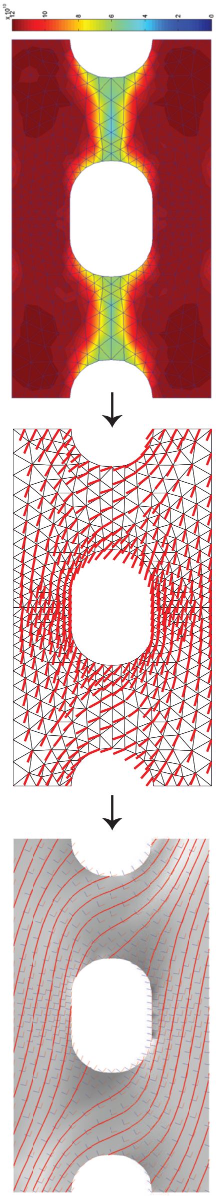

FIGURE 4.1: Multi-step optimisation framework

In the third step of the multi-step optimisation framework, the continuous steered fibre paths in each layer of the VS laminate are constructed from the discrete spatial distribution of fibre angles obtained in the second step. The continuous steered fibre paths are used as the centrelines of the courses which are placed using the AFP machine.

Different researchers in the ASCM group at TUDelft have contributed to develop different components of the multi-step framework, these include, but are not limited to, the works by Setoodeh et al. [119], Setoodeh et al. [101], Abdalla et al. [120], IJsselmuiden et al. [33], IJsselmuiden et al. [121], Pilaka [34], Van Campen et al. [35], Setoodeh et al. [36], Blom et al. [37] and Nagy et al. [38]. In this thesis, construction of the conservative separable approximations is explained in subsection 4.3.2 based on the general approach presented by IJsselmuiden [6]. The first step is explained in section 4.4 based on the scheme developed by IJsselmuiden [6], the second step is described in section 4.5 based on the works by Pilaka [34] and Van Campen et al. [35] and the third step is introduced in section 4.6 based on the implementation by Setoodeh et al. [36], Blom et al. [37], Nagy et al. [38] and Pilaka [34]. The optimisation results in chapters 6 and 7 are obtained using the implementations by IJsselmuiden [6], Pilaka [34], Van Campen et al. [35] and Nagy et al. [38].

The main contributions made by the author to the multi-step optimisation framework are to develop convex separable approximations for the material strength, which is explained in chapter 4 and to implement a constraint screening strategy in the first step, as will be described in subsection 4.4.3, to handle optimisation problems with a huge number of constraints, e.g. buckling optimisation with strength constraints.

4.3 STRUCTURAL APPROXIMATION METHODS

Structural approximation techniques are extensively applied in structural optimisation to reduce the computational cost of optimisation due to repetitive structural analyses. Barthelemy and Haftka [122] divide the approximation techniques into global, local and mid-range categories according to their range of applicability in the design space. The global and local approximations are valid for the whole design space, or a large region of it, and vicinity of the design point, respectively. Mid-range approximations extend the applicability of local approximation to a larger region of the design space. Barthelemy and Haftka [122] also distinguish between function approximation in which an the objective function and/or constraints are approximated in the form of analytical functions of design variables and problem approximation in which the original problem is approximated by another problem which is easier to solve and gives results that have enough accuracy. These approximation concepts can be combined to make a very efficient problem formulation.

Global function approximation or surrogate modeling methods such as the response surface technique and neural networks have been used for optimisation of VS cylinders [17]. Surrogate models introduce smoothness and filter out the noise and irregularities that may be present in the objective and constraint functions. These models can be used to extract sensitivity information analytically instead of finite differences, which are useful for gradient-based optimisation. However, constructing surrogate models usually requires a lot of structural analyses and becomes computationally expensive especially with an increasing the number of design variables.

Local function approximation techniques which have been used for optimisation of VS composite laminates [32], [123] are one of the fundamental features of the multi-step optimisation framework and will be described in section 4.3.1. These approximations, such as first order and higher order Taylor series, are valid only in the vicinity of the design point. To overcome the problem of being valid only locally, these approximations are used within a successive scheme. In this successive approximation approach, approximations are constructed for the objective and constraint functions at an initial design and the optimisation algorithm is implemented on these approximations instead of the real function values. After each implementation, the approximations are updated at the new design and this procedure is repeated until the convergence criterion is met.

There are different global problem approximation methods among which using a simplified analysis model, or using a coarser mesh in a finite element model are the simplest. Using simplified models such as a simple plate model of a wing instead of a full 3-D finite element model is a specific and problem dependent technique which is not always practical. Therefore, this method cannot be a permanent part of the general framework applied for VS design of different structures. A global problem approximation technique was developed in chapter 3 for efficient static and buckling analysis of cylindrical shells. A finite element or finite difference analysis problem can be globally approximated by using a coarser mesh in the model. Although using a coarser mesh reduces the computational cost of the analysis, the accuracy of the response is usually reduced. In a VS structure the design variables are associated with nodes or elements in the finite element or finite difference model and hence by using a coarser mesh the design space will be limited, leading to sub-optimal designs.

Local problem approximation methods include the methods of reducing the number of constraints and design variables. Reduction of number of constraints or constraint screening is very effective in the design of VS laminates when a large number of constraints are imposed, this will be explained in subsection 4.4.3.

4

4.3.1 LOCAL FUNCTION APPROXIMATION

Local function approximations are usually based on a Taylor series expansion of a function, f, around a design point, $\mathbf{x}_0$, and hence are valid only in the vicinity of design point, $\mathbf{x}_0$. These Taylor series expansions are usually limited to first order expansions, only using $\frac{\partial f}{\partial \mathbf{x}}$ evaluated at $\mathbf{x}_0$, and higher order expansions are usually avoided due to the higher computational cost associated with calculating higher order derivatives. If in the first order Taylor series expansion, the function is expanded directly in terms of the design variables, x_i, a linear approximation is formed [124]:

$$f_L = f(\mathbf{x}_0) + \sum_{i=1}^{n} \left(\frac{\partial f}{\partial x_i}|_0 \ (x_i - x_{0i}) \right) \tag{4.2}$$

Linear approximations usually do not capture the physical nature of the function and hence are not accurate even close to the approximation point. Although the accuracy of the approximation can be improved by increasing the degree of approximation, the computational cost due to the need to calculate higher order derivatives will also be increased as well.

Another way of improving the accuracy of the approximation is to expand the function in terms of some intermediate design variables which have a more linear relation with the original function. One of the earliest applications of this method was in the structural optimisation of truss and plane-stress elements. When these structures are statically determinate, stresses and displacements are linear functions of inverse of truss cross-sections and thickness of the plane-stress element. It has also been proved that the statically indeterminate structures behave more linearly in terms of inverse of cross-section and thickness design variables [125, 126]. When the function is expanded in terms of inverse of the design variable, x_i, reciprocal approximation is formed [124]:

$$f_I = f(\mathbf{x}_0) + \sum_{i=1}^{n} \left(\frac{\partial f}{\partial x_i^{-1}}|_0 \ (x_i^{-1} - x_{0i}^{-1}) \right) \tag{4.3}$$

Another type of approximation called conservative approximation [127] is a hybrid of linear and reciprocal approximations which is more conservative than either of them. This approximation is expressed as [124]:

$$f_C = f(\mathbf{x}_0) + \sum_{i=1}^{n} \delta_i \left(\frac{\partial f}{\partial x_i}|_0 \ (x_i - x_{0i}) \right) + \sum_{i=1}^{n} (1-\delta_i) \left(\frac{\partial f}{\partial x_i^{-1}}|_0 \ (x_i^{-1} - x_{0i}^{-1}) \right) \tag{4.4}$$

where δ_i is defined as:

$$\delta_i = \begin{cases} 1 & \text{for } \frac{\partial f}{\partial x_i}|_0 \ x_{0i} >= 0, \\ 0 & \text{otherwise} \end{cases} \tag{4.5}$$

The first and second summations in equation 4.4 represent the linear and reciprocal approximations, respectively. Considering equation 4.5, equation 4.4 states that when the derivative of the function with respect to the design variable, x_i, calculated at the design point multiplied by the value of the design variable at the design point, x_{0i}, is not negative ($\frac{\partial f}{\partial x_i}|_0 \; x_{0i} >= 0$), the function is expanded linearly and otherwise it is expanded reciprocally. In this way, the whole hybrid approximation which is obtained after summing all the terms is more conservative than either of the linear and reciprocal approximations, although there is no guarantee that the hybrid approximation is more conservative than the original function.

All the three mentioned approximations are separable meaning that the approximation function can be represented as the summation of terms each one function of a single design variable. Using separable approximations as design drivers in optimisation problems allows to utilise parallel computing. In addition, it is shown in section 4.3.3 that the reciprocal approximation is convex if the sensitivities, $\frac{\partial f}{\partial x_i^{-1}}|_0$, are positive definite. Therefore, the conservative approximation, which is expressed as a hybrid of linear and reciprocal approximations, is also convex. Local approximations have been successfully used in VS laminate design by [31] for maximum structural stiffness, by [32] for maximum natural frequency and by IJsselmuiden et al. [33] for maximum buckling load.

4

4.3.2 CONVEX CONSERVATIVE SEPARABLE APPROXIMATIONS

A general approach is presented by IJsselmuiden [6] to construct a conservative convex separable approximation (CCSA) for any structural response, based on the classical lamination theory and in terms of the laminate stiffness matrices. The constructed approximations are used in the first and second step of the multi-step optimisation framework by parameterisation of the laminate stiffness in terms of the lamination parameters and fibre angles, respectively.

The idea is based on the CCSA framework developed by Svanberg [128] to solve inequality-constrained nonlinear programming problems. Svanberg [128] has shown that the conservative convex approximations are globally convergent meaning that finding an optimal solution is guaranteed. These local approximations can be used within a successive approximation scheme and their convex and conservative nature ensures that a single global optimum is found for each subproblem in the successive scheme. Separability of these approximations makes them suitable for optimisation problems with large number of design variables by solving them in a parallel fashion using state of the art multi-core processors.

The developed approximation can be stated as:

$$f_S(\mathbf{x}) = f_P(\mathbf{x}) + \rho f_D(\mathbf{x}) \tag{4.6}$$

where the first term, f_P, is an approximation which has a value and a gradient which match the value and gradient of the original function at the approximation point. The second term, f_D, which is scaled by ρ is a convexifying term ensuring the conservativeness and convexity of the approximation as a whole. The approximation in the CCSA framework of Svanberg [128] should satisfy some requirements:

1. Both f_P and f_D must be continuous in their values and first order (gradient) and second order (Hessian) derivatives with respect to the design variables, $\mathbf{x}$. In addition both f_P and f_D must be separable.

2. Function value and first order derivatives of the original function, f, must be equal to those values of the approximation function ,f_P.

3. The Hessian matrix of the approximation function, f_P, must be positive semi-definite.

4. The Hessian matrix of the convexifying function, f_D, must be positive definite.

The general approach for construction of f_P and f_D for structural responses in terms of laminate stiffness matrices is explained in the next two subsections 4.3.3 and 4.3.4.

4.3.3 CONVEX SEPARABLE APPROXIMATION

The first part of the conservative convex separable approximation in equation 4.6, f_P, is a convex separable approximation. In the general approach by IJsselmuiden [6], this approximation is built as a hybrid of linear and reciprocal approximations similar to the conservative approximation in equation 4.4. In the conservative approximation, equation 4.4, either the linear or reciprocal approximation is selected to be used based on the condition in equation 4.5, which is directly related to the design variables. However, the convex separable approximation of a general structural response is built by dividing the response into two parts which are approximated using the first order Taylor series expansion in terms of stiffness matrices, one part expanded linearly and another part expanded reciprocally.

The convex separable approximation of a structural response, f, in the most general case, when it is a function of both in-plane and out of plane laminate stiffness, takes the form:

$$f_P = f(\mathbf{A}_0, \mathbf{D}_0) + \sum_{j=1}^{n} \Big(\frac{\partial \hat{f}}{\partial \mathbf{A}_j^{-1}}|_0 : (\mathbf{A}_j^{-1} - \mathbf{A}_{0j}^{-1}) + \frac{\partial \hat{f}}{\partial \mathbf{D}_j^{-1}}|_0 : (\mathbf{D}_j^{-1} - \mathbf{D}_{0j}^{-1}) + \frac{\partial \check{f}}{\partial \mathbf{A}_j}|_0 : (\mathbf{A}_j - \mathbf{A}_{0j}) + \frac{\partial \check{f}}{\partial \mathbf{D}_j}|_0 : (\mathbf{D}_j - \mathbf{D}_{0j}) \Big) \tag{4.7}$$

where $\hat{f}$ and $\check{f}$ are the parts of the response expanded reciprocally and linearly, respectively. Subscript 0 indicates the design around which the Taylor series is expanded and at which the sensitivities are calculated. subscript j indicates the number of the discretisation point with respect to the stiffness matrices or the inverse of stiffness matrices in that region, the sensitivities of the response are calculated. The : operator is the matrix inner product or generalisation of the dot product to the matrix space, which represents the summation of products of the corresponding elements of two matrices and can also be calculated as the trace of the matrix product. Part of the approximation which contains the design variables and on which the optimisation algorithm is implemented, can be separated from the constant part, f_0, of the approximation and the approximation in equation 4.7 can be re-expressed as:

4

$$f_P = f_0 + \sum_{j=1}^{n} (\boldsymbol{\Phi}_j^m|_0 : \mathbf{A}_j^{-1} + \boldsymbol{\Phi}_j^b|_0 : \mathbf{D}_j^{-1} + \boldsymbol{\Psi}_j^m|_0 : \mathbf{A}_j + \boldsymbol{\Psi}_j^b|_0 : \mathbf{D}_j) \tag{4.8}$$

where $\boldsymbol{\Phi}$ and $\boldsymbol{\Psi}$ are the sensitivities of $\hat{f}$ with respect to inverse of stiffness matrix and $\check{f}$ with respect to stiffness, respectively. The superscripts m and b denote the sensitivities with respect to the in-plane and out of plane compliance or stiffness, respectively. All the constant terms are collected in f_0.

As mentioned earlier, the approximation in equation 4.8 should satisfy the conditions in section 4.3.2. It can be easily identified that this approximation is separable (condition 1). The first order and second order derivatives with respect to the in-plane stiffness of the jth discretisation point are:

$$\frac{\partial f_P}{\partial \mathbf{A}_j} = -\mathbf{A}_j^{-1} \boldsymbol{\Phi}_j^m \mathbf{A}_j^{-1} + \boldsymbol{\Psi}_j^m \tag{4.9}$$

$$\frac{\partial^2 f_P}{\partial \mathbf{A}_j^2} = \mathbf{A}_j^{-\frac{3}{2}} \boldsymbol{\Phi}_j^m \mathbf{A}_j^{-\frac{3}{2}} \tag{4.10}$$

Similar expressions can be derived for derivatives with respect to out of plane stiffness, $\frac{\partial f_P}{\partial \mathbf{D}_j}$ and $\frac{\partial^2 f_P}{\partial \mathbf{D}_j^2}$. The approximation function, f_P, and its first and second order derivatives are continuous with respect to stiffness matrices or other stiffness related design variables such as lamination parameters or ply angles (condition 1). According to equation 4.10, the second order derivative is positive semi-definite if and only if the sensitivity with respect to inverse of in-plane stiffness matrix, $\boldsymbol{\Phi}_j^m$, is positive semi-definite (condition 3). In a similar way, it can be proved that the condition for the second order derivative with respect to the out of plane stiffness ($\frac{\partial^2 f_P}{\partial \mathbf{D}_j^2}$) to be positive semi-definite is that the sensitivity with respect to inverse of out of plane stiffness matrix ($\boldsymbol{\Phi}_j^b$) should be positive semi-definite. Therefore, if the sensitivities of the response function with respect to inverse of stiffness matrices, $\boldsymbol{\Phi}_j^m$ and $\boldsymbol{\Phi}_j^b$, are positive semi-definite, the developed function approximation, f_P in equation 4.8, is convex. Condition 3 can be guaranteed by separating the part of response function which has a positive semi-definite sensitivity with respect to inverse of stiffness matrices from the rest.

Separation of the response function into two parts may be done based on an insight into the physical nature of the structural responses, e.g. the structural stiffness and buckling factor. However, the convexity of the approximation of some structural responses, e.g. strength, cannot be always guaranteed when solely developed based on the physics of the response. Therefore, an alternative method based on a numerical algorithm, developed in subsection 5.5.1, can be used when proper separation of response parts based on investigating the physics of the response is not possible. This numerical algorithm can be used alone or in conjunction with the physical insight method as used for building the convex separable approximation of strength in section 5.5.

After separation of the response function into two parts, the part with positive semi-definite sensitivities with respect to inverse of stiffness matrices is expanded reciprocally and the rest is expanded linearly with respect to stiffness matrices to build a convex approximation. The details for construction of convex separable approximations for structural stiffness and buckling factor are explained in the next two subsections but discussion of the details for strength approximation are postponed to chapter 5 where the conservative Tsai-Wu failure envelop is introduced.

Convex approximation of structural stiffness

A structural stiffness maximisation problem can be substituted by minimisation of structural compliance, which is a homogeneous function of order one in terms of inverse of stiffness matrices. Choosing the the structural compliance to approximate and minimise, has the advantage that the sensitivities of the structural compliance with respect to inverse of stiffness matrices are always positive definite. Therefore, splitting the structural compliance into two parts is not necessary and it is enough to expand the compliance, as a whole, only in terms of inverse of stiffness matrices to have a convex approximation:

$$C \approx C_P = C_0 + \sum_{j=1}^{n} \frac{\partial C}{\partial \mathbf{A}_j^{-1}}|_0 : (\mathbf{A}_j^{-1} - \mathbf{A}_{j0}^{-1}) + \frac{\partial C}{\partial \mathbf{D}_j^{-1}}|_0 : (\mathbf{D}_j^{-1} - \mathbf{D}_{j0}^{-1}) \tag{4.11}$$

where $j(= 1,2,...,n)$ is the number of discretisation points with different stiffness properties and 0 is the design at which the sensitivities are calculated and around which the approximation is built. The details of sensitivity analysis are explained in [6].

Convex approximation of buckling load

Close inspection of buckling eigenvalue problem, equation 3.69, shows that the buckling load, λ_b, is a homogeneous function of order one with respect to the in-plane and out of plane stiffness matrices. This is because by scaling the in-plane and out of plane stiffness matrices, the displacements and strains are scaled inversely, as shown in equations 3.47 and 3.43, however, the sectional forces and moments will remain unchanged, as it is clear from equation 3.49. Therefore, the material stiffness matrix is scaled similarly while the geometric stiffness matrix is not changed.

4

In order to build a convex approximation, instead of the buckling factor, the inverse of buckling factor is approximated which is a homogeneous function of the inverse of stiffness matrices. Therefore, the eigenvalue buckling problem in equation 3.69 is rephrased as:

$$(\mathbf{K}^g - r_b \mathbf{K}^t)\ \mathbf{a} = 0 \tag{4.12}$$

where r_b is inverse of buckling factor and the buckling modes are normalised such that:

$$\mathbf{a}^T\ \mathbf{K}^t\ \mathbf{a} = 1 \tag{4.13}$$

The separation scheme for the inverse of buckling factor, required for construction of a convex separable approximation, becomes clear by inspecting the sensitivities of the inverse of buckling factor with respect to in-plane or out of plane stiffness stiffness matrix of an arbitrary point of the laminate, for example for in-plane stiffness matrix:

$$\frac{\partial r_b}{\partial \mathbf{A}} = r_b \mathbf{a}^T (\frac{\partial \mathbf{K}^t}{\partial \mathbf{A}} - r_b \frac{\partial \mathbf{K}^g}{\partial \mathbf{A}})\mathbf{a} \tag{4.14}$$

Variation of the stiffness matrices of an individual point affects inverse of the buckling factor, r_b, through changing the material stiffness matrix, $\mathbf{K}^t$, and changing the geometric stiffness matrix, $\mathbf{K}^g$. Change of the material stiffness matrix, $\mathbf{K}^t$, is a local effect of the variation of the stiffness matrices at a single point, since only the local material stiffness matrix of that point or the element connected to that point is changed. However, change of the geometric stiffness matrix, $\mathbf{K}^g$, is a global effect of the variation of the stiffness matrices at a single point, since the displacement field and hence the load distribution is changed all over the laminate. Sensitivity analysis of inverse of buckling factor is explained in [6].

It is shown in [6] that the part of sensitivities coming from the material stiffness matrix with respect to the inverse of stiffness matrices of a single point is always positive definite. Therefore, the convex separable approximation of the inverse of buckling load, r_b, is formed by expanding the part of the inverse of buckling load which changes due to the local effect, $\hat{r}_b$, reciprocally and the part which changes due to the global effect, $\check{r}_b$, linearly and is expressed as:

4

$$r_b \approx r_{bP} = r_{b0} + \sum_{j=1}^{n} \frac{\partial \hat{r}_b}{\partial \mathbf{A}_j^{-1}}|_0 : (\mathbf{A}_j^{-1} - \mathbf{A}_{j0}^{-1}) + \frac{\partial \hat{r}_b}{\partial \mathbf{D}_j^{-1}}|_0 : (\mathbf{D}_j^{-1} - \mathbf{D}_{j0}^{-1}) + \frac{\partial \check{r}_b}{\partial \mathbf{A}_j}|_0 : (\mathbf{A}_j - \mathbf{A}_{j0}) + \frac{\partial \check{r}_b}{\partial \mathbf{D}_j}|_0 : (\mathbf{D}_j - \mathbf{D}_{j0}) \quad (4.15)$$

where $j(=1,2,...,n)$ is the number of point with distinct stiffness matrices and 0 is the design point at which the sensitivities are calculated and around which the approximation is built.

The material and geometric stiffness matrices are homogeneous functions of order one and zero with respect to in-plane and out of plane stiffness matrices. Therefore, part of the inverse of buckling load indicated by $\hat{r}_b$ is homogeneous of order one with respect to inverse of stiffness matrices, $\hat{r}_b(c\mathbf{A}^{-1}, c\mathbf{D}^{-1}) = c\hat{r}_b(\mathbf{A}^{-1}, \mathbf{D}^{-1})$, while the part indicated by $\check{r}_b$ is homogeneous of order zero with respect to inverse of stiffness matrices, $\hat{r}_b(c\mathbf{A}^{-1}, c\mathbf{D}^{-1}) = \hat{r}_b(\mathbf{A}^{-1}, \mathbf{D}^{-1})$. Therefore, Euler's homogeneous function theorem implies that at any approximation point:

$$\sum_{j=1}^{n} (\frac{\partial \check{r}_b}{\partial \mathbf{A}_j^{-1}} : \mathbf{A}_j^{-1} + \frac{\partial \check{r}_b}{\partial \mathbf{D}_j^{-1}} : \mathbf{D}_j^{-1}) = 0 \quad (4.16)$$

and:

$$\sum_{j=1}^{n} (\frac{\partial \hat{r}_b}{\partial \mathbf{A}_j^{-1}} : \mathbf{A}_j^{-1} + \frac{\partial \hat{r}_b}{\partial \mathbf{D}_j^{-1}} : \mathbf{D}_j^{-1}) = r_b \quad (4.17)$$

Since the stiffness matrices **A** and **D** are always positive definite, equation 4.16 implies that the sensitivities $\frac{\partial \check{r}_b}{\partial \mathbf{A}_j^{-1}}$ and $\frac{\partial \check{r}_b}{\partial \mathbf{D}_j^{-1}}$ and hence $\frac{\partial \check{r}_b}{\partial \mathbf{A}_j}$ and $\frac{\partial \check{r}_b}{\partial \mathbf{D}_j}$ are not always positive definite. This lack of definiteness does not make problem in building a convex approximation, since these terms are expanded linearly in equation 4.15. This is while, the sensitivities $\frac{\partial \hat{r}_b}{\partial \mathbf{A}_j^{-1}}$ and $\frac{\partial \hat{r}_b}{\partial \mathbf{D}_j^{-1}}$ are always positive definite as shown in IJsselmuiden [6], which guarantees the whole approximation to be convex.

4.3.4 ENFORCING STRICT CONSERVATIVENESS

The convex separable approximation in equation 4.8 may lack strict convexity or conservativeness. If the part of the response expanded reciprocally in terms of stiffness matrices is zero, the approximation is linear and not convex. Even a convex approximation is not strictly conservative if the value of the approximation is not larger than the value of the exact function in the optimisation problem in equation 4.1. Solving an optimisation problem in a successive approximation strategy based on the approximations which are not strictly convex and conservative may lead to some convergence problems. To avoid these problems and ensure strict convexity and the conservativeness of the approximation, the second term of the approximation in equation 4.6 is added. In this subsection, construction of the convexifying term, f_D, and its scaling factor, ρ, is explained.

4

IJsselmuiden [6] suggests using the following expression in terms of the stiffness matrices for f_D:

$$f_D = \sum_{j=1}^{n} w_j \left(\mathbf{A}_{0j} : \mathbf{A}_j^{-1} + \mathbf{D}_{0j} : \mathbf{D}_j^{-1} + \mathbf{A}_{0j}^{-1} : \mathbf{A}_j + \mathbf{D}_{0j}^{-1} : \mathbf{D}_j - 4\mathbf{I} : \mathbf{I}\right) \tag{4.18}$$

where $\mathbf{I}$ is the identity matrix of dimension (3×3). The expression in equation 4.18 is a summation of local terms each one evaluated at the discretisation point j and scaled by a factor w_j. The scaling factor, w_j, is meant to include the true contribution of the stiffness of each discretisation point in f_D and hence in a 1D or 2D structure, w_j is defined as the ratio of the length or area corresponding to a discretisation point, L_j or A_j, to the total area or length:

$$w_j = \frac{A_j}{\sum_{j=1}^{n} A_j} \qquad \text{or} \qquad w_j = \frac{L_j}{\sum_{j=1}^{n} L_j} \tag{4.19}$$

The last term in equation 4.18 ensures that the value of the convex term, f_D, is zero at the approximation point. Therefore, as the problem is converged to an optimum solution in the successive approximation scheme of the first step of the multi-step optimisation framework, the contribution of f_D in the total approximation function, f_S in equation 4.6, tends to zero. The expression developed for f_D satisfies the conditions in section 4.3.2. It is clear from equation 4.18 that f_D ,which is separable, its gradient and Hessian with respect to the stiffness matrices or other design variables are continuous (condition 1). The Hessian of f_D is positive definite since both stiffness and compliance matrices are positive definite (condition 4). The expression for f_D, equation 4.18, has the same form as the expression for f_P, equation 4.8, and hence after calculating f_S from equation 4.6 and deleting the constant part, the final approximation, on which the optimisation is implemented, obtains the form:

$$f_S = \sum_{j=1}^{n} (\breve{\boldsymbol{\Phi}}_j^m|_0 : \mathbf{A}_j^{-1} + \breve{\boldsymbol{\Phi}}_j^b|_0 : \mathbf{D}_j^{-1} + \breve{\boldsymbol{\Psi}}_j^m|_0 : \mathbf{A}_j + \breve{\boldsymbol{\Psi}}_j^b|_0 : \mathbf{D}_j) \tag{4.20}$$

where

$$\breve{\boldsymbol{\Phi}}_j^m|_0 = \boldsymbol{\Phi}_j^m|_0 + \rho w_j \mathbf{A}_{0j} \tag{4.21}$$

The same expressions stand for other sensitivities in equation 4.20.

4

The amount of convexity and conservativeness, imposed by f_D, is scaled by ρ which is called the damping factor. If the approximation function, f_S, is over conservative, due to the large difference between the values of the approximation and actual functions value, a lot of iterations are required in the successive approximation scheme in the first step of the multi-step optimisation framework to converge to an optimum solution. If the amount of convexity added to f_P through the scaled f_D is not enough, the total approximation function, f_S, may loose its strict convexity, again leading to excessive number of iterations to converge. Therefore, the efficiency of the optimisation routine is largely influenced by the selection of damping factor. IJsselmuiden [6] has developed an adaptive damping strategy through which the damping factor is initialised and dynamically changed during the successive approximation scheme. The interested reader is referred to [6] for details of the adaptive damping scheme.

4.4 STEP ONE: CONCEPTUAL STIFFNESS DESIGN

In the first step of the multi-step optimisation framework, implemented by IJsselmuiden [6], the optimisation problem, which is formulated based on the structural performance requirements, is solved in a successive approximation scheme. In the successive approximation scheme, the original optimisation problem is substituted by an approximate subproblem, which is built using the convex conservative separable approximations of the structural responses. The approximate subproblem is built at an initial design and solved to find the optimum stiffness matrices or their optimum spatial distribution, then the approximate subproblem are updated at the new design, the optimisation algorithm is applied to solve the new subproblem and this process is repeated until a convergence criterion is met. Successive approximation scheme reduces the number of structural analyses, required for optimisation, and the related computational costs.

Solution of the convex and separable approximate subproblem, using the dual method by Fleury and Schmit [116], is described in subsection 4.4.1. Since the design drivers in this thesis, e.g. buckling capacity and material strength, are multimodal responses, subsection 4.4.2 is devoted to the solution method for multimodal problems based on the bound formulation by Olhoff [115]. In subsection 4.4.3, implementation of the constraint screening strategy is described, as the contribution of the author to the first step.

4.4.1 APPROXIMATE SUBPROBLEM

In the successive approximation scheme, the original optimisation problem, equation 4.1, is substituted by an approximate subproblem, which is built using the convex conservative separable approximations of the structural responses:

$$\begin{aligned} &\min_{\mathbf{x}} \tilde{f}_0(\mathbf{x}) \\ &\tilde{f}_j(\mathbf{x}) \leq 0 \qquad j = 1,2,\ldots,m \\ &x_i^L \leq x_i \leq x_i^U \qquad i = 1,2,\ldots,n \end{aligned} \tag{4.22}$$

where $\tilde{f}_0$ and $\tilde{f}_j$ are the conservative convex separable approximations (equation 4.6) of the structural responses, f_0 and f_j, in equation 4.1. Due to the convexity and separability of the approximate subproblem, it can be solved efficiently using the dual method by Fleury and Schmit [116].

The Lagrangian of the primal convex approximate subproblem, equation 4.22, is formulated as:

$$L(\boldsymbol{\mu},\mathbf{x}) = \tilde{f}_0(\mathbf{x}) + \sum_{j=1}^{m} \mu_j \tilde{f}_j(\mathbf{x}) \tag{4.23}$$

where μ_j is the non-negative scalar known as the Lagrange multiplier or the dual design variable, which is associated with the j th constraint, $\tilde{f}_j(\mathbf{x})$, and $\mathbf{x}$ is the vector of all primal design variables. The corresponding dual problem is formulated as:

$$\max_{\boldsymbol{\mu}} L_C(\boldsymbol{\mu}) \qquad \textit{subject to} \qquad \mu_j \geq 0 \; (j = 1,2,\ldots,m) \tag{4.24}$$

where L_C is the complementary Lagrangian or the Falk's dual obtained from:

$$L_C = \min_{\mathbf{x}} L(\mathbf{x}(\boldsymbol{\mu})) \tag{4.25}$$

The dual variables, $\boldsymbol{\mu}$, are fixed when solving the minimisation problem in equation 4.25. Therefore, the search for the optimal primal and dual variables is separated in the dual formulation. In general, the solution of the dual problem is a lower bound to the solution of the primal minimisation problem and in convex problems, if enough regularity conditions for constraints are satisfied, solutions of the dual and primal problems are the same.

Separability of the approximations, used to build the approximate subproblem, allows us to find the optimal primal design variables at different discretisation points independently and hence the search for the primal variables is called the local optimisation. On the other hand, the dual variables affect the optimal values of all of the primal variables as depicted in equation 4.25 and hence the search for the dual variables is called the global optimisation.

Local optimisation

In the formulated dual problem, the Lagrangian, equation 4.23, is formed using the conservative convex separable approximation of the structural responses, equation 4.20, which for the j th structural response, $\tilde{f}_j$ ($j = 0, 1, ..., m$), is expressed as:

$$\tilde{f}_j = \sum_{i=1}^{n} (\breve{\boldsymbol{\Phi}}^m_{i,j}|_0 : \mathbf{A}_i^{-1} + \breve{\boldsymbol{\Phi}}^b_{i,j}|_0 : \mathbf{D}_i^{-1} + \breve{\boldsymbol{\Psi}}^m_{i,j}|_0 : \mathbf{A}_i + \breve{\boldsymbol{\Psi}}^b_{i,j}|_0 : \mathbf{D}_i) \tag{4.26}$$

The approximation is expressed in terms of the laminate stiffness matrices of n discretisation points of the structure with different stiffness properties. However, the laminate stiffness matrices cannot be used directly as the primal design variables, since their elements are related to each other and cannot be chosen freely. Although laminate stiffness matrices in the convex conservative separable approximations can be parameterised in terms of the ply angles of the stacking sequence, the developed approximation will no longer be convex, resulting in a lot of local optima. Laminate stiffness matrices can be expressed as linear functions of lamination parameters, hence the convexity of the approximation, when expressed in terms of lamination parameters, is preserved. Other benefits of using lamination parameters as the primal design variables in the first step of the multi-step framework are mentioned in subsection 2.5.2.

If the thickness of a VS laminate is allowed to vary, laminate thickness can be used as a continuous design variable in addition to the lamination parameters in the gradient-based optimisation of the first step of the multi-step optimisation framework. Although the laminate thickness is a discrete variable, assigning a continuous variable to the laminate thickness allows us to study the effect of thickness on the optimum design. For the structural performance measures which are explicit functions of the laminate thickness, and not through the stiffness matrices, e.g. weight or failure index in bending problems as formulated in equation 5.44, the conservative convex separable approximation is modified as:

$$\tilde{f}_j = \sum_{i=1}^{n} (\breve{\boldsymbol{\Phi}}^m_{i,j}|_0 : \mathbf{A}_i^{-1} + \breve{\boldsymbol{\Phi}}^b_{i,j}|_0 : \mathbf{D}_i^{-1} + \breve{\boldsymbol{\Psi}}^m_{i,j}|_0 : \mathbf{A}_i + \breve{\boldsymbol{\Psi}}^b_{i,j}|_0 : \mathbf{D}_i + \breve{\alpha}_{i,j}|_0 \; h_i) \tag{4.27}$$

where $\breve{\alpha}_{i,j}$ is the derivative of the terms in f_j which are explicitly dependent on the laminate thickness.

Due to the separability of the conservative convex separable approximation, equation 4.27, the optimisation problem in equation 4.25 can be stated as n local optimisation problems which can be solved in parallel using the multi-core processors. Each local optimisation problem is formulated as:

$$\min_{\mathbf{V}_i,h_i}(\breve{\boldsymbol{\Phi}}_i^m|_0 : \mathbf{A}_i^{-1} + \breve{\boldsymbol{\Phi}}_i^b|_0 : \mathbf{D}_i^{-1} + \breve{\boldsymbol{\Psi}}_i^m|_0 : \mathbf{A}_i + \breve{\boldsymbol{\Psi}}_i^b|_0 : \mathbf{D}_i + \breve{\alpha}_i h_i) \tag{4.28}$$

where $\breve{\boldsymbol{\Phi}}_i^m$, $\breve{\boldsymbol{\Phi}}_i^b$, $\breve{\boldsymbol{\Psi}}_i^m$, $\breve{\boldsymbol{\Psi}}_i^b$ and $\breve{\alpha}_i$ are the combined sensitivities defined as:

$$\breve{\boldsymbol{\Phi}}_i^m = \sum_{j=1}^{m} \mu_j \breve{\boldsymbol{\Phi}}_{i,j}^m, \qquad \breve{\boldsymbol{\Phi}}_i^b = \sum_{j=1}^{m} \mu_j \breve{\boldsymbol{\Phi}}_{i,j}^b, \qquad \breve{\boldsymbol{\Psi}}_i^m = \sum_{j=1}^{m} \mu_j \breve{\boldsymbol{\Psi}}_{i,j}^m, \qquad \breve{\boldsymbol{\Psi}}_i^b = \sum_{j=1}^{m} \mu_j \breve{\boldsymbol{\Psi}}_{i,j}^b,$$
$$\breve{\alpha}_i = \sum_{j=1}^{m} \mu_j \alpha_{i,j} \tag{4.29}$$

The local optimisation problem in equation 4.28 is parameterised in terms of the lamination parameters and the laminate thickness using equation 2.75. The first and second derivatives of the stiffness matrices in equation 4.28 with respect to the lamination parameters and laminate thickness can be obtained analytically using the chain rule. Therefore, the local optimisation problems can be solved efficiently using a gradient-based optimisation method e.g. sequential quadratic programming (SQP) is used in the implementation by IJsselmuiden [6]. The local optimisation problem, equation 4.28, is constrained with the feasible region of the lamination parameters explained in subsection 2.5.3 and possibly the upper and lower bounds on the laminate thickness.

Global optimisation

The optimal dual variables or Lagrange multipliers are obtained by solving the optimisation problem formulated in equation 4.24. The derivative of the complementary Lagrangian, L_C, with respect to the dual variables, μ_j $(j = 0, 1, ..., m)$, is calculated analytically and the global optimisation problem can be solved efficiently using a gradient-based optimisation method such as sequential quadratic programming (SQP). IJsselmuiden [6] used an internal point method in his implementation to better deal with the large number of constraints. The global optimisation problem is only constrained to have non-negative Lagrange multipliers.

4.4.2 MULTI-MODAL AND MIN-MAX OPTIMIZATION

Some structural responses, e.g. buckling and vibration, have a multi-modal nature. Structural failure is determined by the critical mode which is associated with the lowest buckling load or vibration frequency. Therefore, in structural optimisation, the response due to the critical mode should be optimised. However, the critical mode is a function of the structural design which is changed during the optimisation and if the optimisation problem is formulated to optimise the response due to the initial critical mode, the initial critical mode may no longer be critical when the design is altered during the optimisation. Therefore, considering only the critical mode of the initial design and neglecting multiple modes or considering an insufficient number of modes in the optimisation problem, may lead to the solution convergence problems [129], [130].

Material failure index is another structural response which must be treated similar to the multi-modal structural responses if used as the objective function in the optimisation formulation. The location of the critical point in a structure may change as the design is altered during the optimisation and hence convergence problems may happen if only the critical point of the initial structure is considered in the strength optimisation problem.

The buckling and vibration optimisation problems by considering a cluster of critical modes or the strength optimisation problem by considering the failure indices at all the discretisation points of the structure are min-max problem, i.e. the critical mode or failure index is minimised. The multi-modal or min-max problems are formulated as:

$$\min_{\mathbf{x}} \max(f_k(\mathbf{x})) \tag{4.30}$$

where f_k $(k = 1,2,...,q)$ are the cluster of considered critical responses i.e. inverse of buckling load or frequency or the failure index. This problem can be solved using the bound formulation by Olhoff [115]:

$$\min \beta \qquad \textit{subject to} \qquad \beta \geq f_k(\mathbf{x}) \tag{4.31}$$

in which β is an auxiliary parameter which is set to be the upper bound of the responses from the considered critical modes, f_k $(k = 1,2,...,q)$. The problem in equation 4.31 can be subsequently solved using the dual method presented in section 4.4.1. The Lagrangian is formulated as:

$$L(\boldsymbol{\mu},\mathbf{x}) = \beta + \sum_{k=1}^{q} \mu_k(\tilde{f}_k(\mathbf{x}) - \beta) \tag{4.32}$$

The dual optimisation problem is formulated similar to equation 4.24:

$$\max_{\boldsymbol{\mu}} L_C(\boldsymbol{\mu}) \qquad \textit{subject to} \qquad \mu_j \geq 0 \; (j = 1,2,...,m) \tag{4.33}$$

and by solving equation 4.25 for the complementary Lagrangian, L_C, two conditions are obtained:

$$L_C = \min_{\mathbf{x}} \sum_{k=1}^{q} \mu_k \tilde{f}_k(\mathbf{x}) \qquad \textit{and} \qquad \sum_{k=1}^{q} \mu_k = 1 \tag{4.34}$$

The second condition imposes another constraint on the non-negative Lagrange multipliers corresponding to the multiple modes, μ_k $(k = 1, 2, ..., q)$, such that their summation is equal to unity. This additional constraint is implemented in the global optimisation.

Constrained multi-modal optimisation
In general, optimisation of multi-modal structural responses is subject to the constraints on other structural responses, e.g. the buckling load maximisation with respect to strength constraints. The corresponding convex approximate subproblem is formulated as:

$$\begin{aligned} &\min_{\mathbf{x}} \ \max(\tilde{f}_k(\mathbf{x})) \qquad k = 1, 2, ..., q \\ &\tilde{f}_j(\mathbf{x}) \leq 0 \qquad j = 1, 2, ..., m \\ &x_i^L \leq x_i \leq x_i^U \qquad i = 1, 2, ..., n \end{aligned} \tag{4.35}$$

where $\tilde{f}_k$ is the k th mode in a multi-modal structural response, e.g. inverse of buckling load, and $\tilde{f}_j$ s are m constraints, e.g. the failure indices at m locations in the laminate. The corresponding Lagrangian is formulated as:

$$L(\boldsymbol{\mu}, \mathbf{x}) = \beta + \sum_{k=1}^{q} \mu_k (\tilde{f}_k(\mathbf{x}) - \beta) + \sum_{j=1}^{m} \mu_j \tilde{f}_j(\mathbf{x}) \tag{4.36}$$

Resulting in the following global optimisation problem:

$$\begin{aligned} &\max_{\boldsymbol{\mu}} L_C(\boldsymbol{\mu}) \\ &\textit{subject to} \\ &\mu_j \geq 0 \quad (j = 1, 2, ..., m), \qquad \mu_k \geq 0, \qquad \textit{and} \qquad \sum_{k=1}^{q} \mu_k = 1 \quad (k = 1, 2, ..., q) \end{aligned} \tag{4.37}$$

and the following local optimisation problem:

$$L_C = \min_{\mathbf{x}} (\sum_{k=1}^{q} \mu_k \tilde{f}_k(\mathbf{x}) + \sum_{j=1}^{m} \mu_j \tilde{f}_j(\mathbf{x})) \tag{4.38}$$

In the adaptive damping strategy developed by IJsselmuiden [6], the damping factors are updated in each iteration based on their value at the previous iteration, however, in a multi-modal problem different modes may cross during the optimisation process. Therefore each damping factor is assigned to the right mode using a mode tracking method, e.g. the cross-orthogonality check by Eldred et al. [131].

4.4.3 CONSTRAINT SCREENING

Some of the structural optimisation problems include a large number of constraints, e.g. maximisation of the structural stiffness or buckling load of a structure subjected to the constraint of keeping the failure indices at all the nodes of the corresponding finite element model bellow a certain threshold. The solution of the optimisation problem becomes computationally expensive if all the constraints are considered. This computational cost arises from solving the optimisation problem with a large number of responses and the sensitivity analysis required for each constraint.

In the constraint screening or active set strategy [132], the number of constraints is reduced and only the set of constraints which are active, or likely to become active, are selected to be imposed in the optimisation problem. This set of constraints could be selected from a certain number of the most critical constraints or the constraints which have values larger than a certain threshold. It is assumed that the critical constraints are selected from the constraints of the same response type. The advantage of the constraint screening strategy is that the selected constraints represent the nature of the original problem while limiting the size of the optimisation problem. The disadvantage is that the optimisation problem may take longer to converge or may not converge if the number of selected constraints are not enough, such that the active constraints move inside and outside this set in different iterations, or if the number of selected constraints is less than the number of active constraints. Regionalisation [133] can increase the chance of fast convergence by selecting a few critical constraints in each region of the structure.

The author has implemented the constraint screening strategy, through selection of the critical constraints which are larger than a certain threshold, in the first step implementation by IJsselmuiden [6]. The selected set of constraints and the number of selected constraints may change in different iterations of the successive approximation scheme. In the adaptive damping strategy, developed by IJsselmuiden [6], the damping factors are updated in each iteration based on their value at the previous iteration. However, if new constraints appear in an iteration due to the constraint screening, the corresponding damping factors are initialised based on the initialisation scheme developed by IJsselmuiden [6].

4.5 STEP TWO: REALISTIC STACKING SEQUENCE DESIGN

Different objective functions can be used to retrieve the realistic stacking sequence design from the conceptual stiffness design, for example, Setoodeh et al. [36] minimised the square distance between the realistic and theoretical designs in the lamination parameters space, Pilaka [34] found the optimum realistic stacking sequence by minimisation of the approximate subproblem built at the theoretical design and Van Campen et al. [35] used a combination of the two above mentioned strategies. The fibre angle retrieval process developed by Van Campen et al. [35], first finds the stacking sequence at each point of the structure which best matches the optimum theoretical design obtained from the first step of multi-step optimisation framework. The best stacking sequence is obtained using a genetic algorithm (GA) by finding the least square in the lamination parameters space or by minimising the convex conservative separable approximation of structural responses which is found at the optimum theoretical design. The obtained fibre angle distribution is used as an initialisation in the cellular automata (CA) framework coupled with a gradient-based optimiser to find the optimal spatial distribution of fibre angles including the local steering curvature constraints. In this thesis, the realistic CS and the initial realistic VS laminate designs are retrieved from the corresponding theoretical designs in a least square sense in the lamination parameters space using a GA implemented by Van Campen et al. [35]. The final realistic VS laminate design is obtained using a gradient-based optimisation implemented by Pilaka [34] which minimises the approximate subproblem, built at the theoretical design, subject to the constraints on the steering curvature. The gradient-based optimisation is initialised by the initial realistic VS laminate design obtained from GA.

The definition of steering curvature, which is used as a constraint in the gradient-based optimisation, is presented in subsection 4.5.1. The gradient-based optimisation by Pilaka [34] and its initialisation using GA, developed by Van Campen et al. [35], are described in subsections 4.5.2 and 4.5.3.

4.5.1 STEERING CURVATURE

Local steering curvature

The steering curvature in a discrete fibre angle distribution is defined as the rate of change of fibre angle which is mathematically expressed as the norm of the gradient of fibre angle [34]:

$$\kappa = \|\nabla\theta\| \tag{4.39}$$

The intuitive way to consider the steering curvature constraint in the optimisation problem is to impose it locally to guarantee that the steering curvature at any point of a steered fibre layer will not exceed the critical curvature.

4

Assuming a finite element model with linear shape functions, the steering curvature of each element, κ_e, is expressed in terms of the vector of nodal fibre angles at each element, θ_e, using a stiffness-like matrix, $\mathbf{K}_e$, obtained from the Laplacian matrix of the grid [34]:

$$\kappa_e^2 = \frac{1}{2}\theta_e^T \mathbf{K}_e \theta_e \tag{4.40}$$

The number of local steering curvature constraints is equal to the number of elements in a finite element model which may reach hundreds of thousands. The complexity of the optimisation problem is increased by increasing the number of constraints. The large number of constraints precludes using usual gradient-based optimisation techniques and requires using parallelised local optimisation frameworks such as CA used by Van Campen et al. [35]. The local nature of CA makes it a suitable approach to handle large number of local constraints.

Average steering curvature

One can argue that the steering curvature is related to the smooth fibre paths which are constructed in the third step of the multi-step optimisation framework. The smooth fibre paths are constructed from the spatial distribution of fibre angles using streamline analogy and hence have a global nature. The global nature of smooth fibre paths and the computational cost of including a lot of local steering curvature constraints in the optimisation problem motivate using only an average steering curvature, κ, per ply [34]:

$$\kappa^2 = \frac{1}{2}\theta^T \mathbf{K}\,\theta \tag{4.41}$$

where θ is the vector of all nodal fibre angles in a layer and $\mathbf{K}$ is the stiffness-like matrix assembled from the matrices at element level, $\mathbf{K}_e$.

4.5.2 GRADIENT-BASED OPTIMISATION

In the second step of the multi-step framework developed by Pilaka [34], the Lagrangian of the approximate subproblem built at the optimum conceptual design, L^*, and the average steering curvature of p plies, g_l $(l = 1, 2, ..., p)$, are used as the objective function and constraints and the spatial distribution of fibre angles, $\boldsymbol{\theta}$, are the design variables. The corresponding optimisation problem is formulated as:

$$\begin{aligned} &\min_{\boldsymbol{\theta}} L^*(\boldsymbol{\theta}) \qquad\qquad (4.42)\\ &g_l(\boldsymbol{\theta}) \leq 0 \qquad l = 1, 2, ..., p \end{aligned}$$

In the constrained multi-modal optimisation problem, $L^*(\boldsymbol{\theta})$, is obtained from equation 4.38:

$$L^*(\boldsymbol{\theta}) = \sum_{k=1}^{q} \mu_k^* \tilde{f}_k^*(\boldsymbol{\theta}) + \sum_{j=1}^{m} \mu_j^* \tilde{f}_j^*(\boldsymbol{\theta}) \tag{4.43}$$

where μ_k^* and μ_j^* are the optimum Lagrange multipliers found from the first step of the multi-step framework and for $\tilde{f}_j^*(\boldsymbol{\theta})$ and $\tilde{f}_k^*(\boldsymbol{\theta})$ are built based on the sensitivities of the theoretical design obtained in the first step. For example:

$$\tilde{f}_j^*(\boldsymbol{\theta}) = \sum_{i=1}^{n} (\boldsymbol{\Phi}_{i,j}^m|_* : \mathbf{A}_i^{-1}(\boldsymbol{\theta}) + \boldsymbol{\Phi}_{i,j}^b|_* : \mathbf{D}_i^{-1}(\boldsymbol{\theta}) + \boldsymbol{\Psi}_{i,j}^m|_* : \mathbf{A}_i(\boldsymbol{\theta}) + \boldsymbol{\Psi}_{i,j}^b|_* : \mathbf{D}_i(\boldsymbol{\theta})) \tag{4.44}$$

where $\boldsymbol{\Phi}_{i,j}^m|_*$, $\boldsymbol{\Phi}_{i,j}^b|_*$, $\boldsymbol{\Psi}_{i,j}^m|_*$, and $\boldsymbol{\Psi}_{i,j}^b|_*$ are the sensitivities of the conceptual stiffness design with respect to the laminate stiffness matrices. If the maximum allowable average steering curvature is denoted by κ_{max} , the constraint on the average steering curvature per ply can be formulated as:

$$g_l(\boldsymbol{\theta}) = \frac{1}{2}\theta^T \hat{\mathbf{K}}\, \theta - 1 \leq 0 \qquad l = 1, 2, ..., p \tag{4.45}$$

where $\hat{\mathbf{K}} = \frac{\mathbf{K}}{\kappa_{max}^2}$.

The optimisation problem in equation 4.42 is reformulated as a quadratically constrained quadratic programming (QCQP) optimisation problem by expanding the Lagrangian and the constraints on the average steering curvature per layer as quadratic Taylor series in terms of the nodal fibre angles.

The quadratic Taylor series expansion of the convex conservative separable approximations, $\tilde{f}_j^*(\boldsymbol{\theta})$ and $\tilde{f}_k^*(\boldsymbol{\theta})$, used to build the Lagrangian in equation 4.43, in terms of the nodal fibre angles is in the form of:

$$\tilde{f}^*(\boldsymbol{\theta}) \approx \tilde{f}^*(\boldsymbol{\theta}_0) + \sum_{i=1}^{n} (\, \mathbf{J}_{0i}^T (\boldsymbol{\theta}_i - \boldsymbol{\theta}_{0i}) + \frac{1}{2}(\boldsymbol{\theta}_i - \boldsymbol{\theta}_{0i})^T\ \mathbf{H}_{0i}^T\ (\boldsymbol{\theta}_i - \boldsymbol{\theta}_{0i})\,) \tag{4.46}$$

where $\boldsymbol{\theta}$ and $\boldsymbol{\theta}_0$ are $(p \times n)$ matrices of current and initial spatial distribution of fibre angles in p layers at n nodes, $\boldsymbol{\theta}_i$ and $\boldsymbol{\theta}_{0i}$ are $(p \times 1)$ vectors of current and initial nodal fibre angles in p layers at node i, and $\mathbf{J}_{0i}$ $(p \times 1)$ and $\mathbf{H}_{0i}$ $(p \times p)$ are the gradient vector and Hessian matrix of $\tilde{f}^*$ with respect to $\boldsymbol{\theta}_i$ computed at the initial initial spatial distribution of fibre angles, $\boldsymbol{\theta}_0$:

$$\mathbf{J}_{0i} = \frac{\partial \tilde{f}^*}{\partial \boldsymbol{\theta}_i}|_0, \qquad \mathbf{H}_{0i} = \frac{\partial^2 \tilde{f}^*}{\partial \boldsymbol{\theta}_i^2}|_0 \tag{4.47}$$

4

Detailed derivation of the gradient vector and Hessian matrix can be found in [34]. The iterative Tikhonov regularisation technique is used to ensure that $\mathbf{H}_{0i}$ is positive semi-definite and hence the approximation in equation 4.46 is convex [34]. After assembling the nodal gradient, $\mathbf{J}_{0i}$, and Hessian, $\mathbf{H}_{0i}$, matrices, equation 4.46 is reconstructed as:

$$\tilde{f}^*(\boldsymbol{\theta}) \approx \tilde{f}^*(\boldsymbol{\theta}_0) + \mathbf{J}_0^T(\boldsymbol{\theta}-\boldsymbol{\theta}_0) + \frac{1}{2}(\boldsymbol{\theta}-\boldsymbol{\theta}_0)^T\,\mathbf{H}_0^T\,(\boldsymbol{\theta}-\boldsymbol{\theta}_0) \tag{4.48}$$

where $\mathbf{J}_0$ $(p \times n)$ and $\mathbf{H}_0$ $(p \times p \times n)$ are the gradient and Hessian matrices of $\tilde{f}^*$ with respect to $\boldsymbol{\theta}$ computed at the initial spatial distribution of fibre angles, $\boldsymbol{\theta}_0$. The constraint on the average steering curvature of layer l, equation 4.45, can be also formulated as a quadratic Taylor series in terms of the nodal fibre angles:

$$g_l(\boldsymbol{\theta}_l) \approx g_l(\boldsymbol{\theta}_{0l}) + \mathbf{b}_{0l}^T(\boldsymbol{\theta}_l-\boldsymbol{\theta}_{0l}) + \frac{1}{2}(\boldsymbol{\theta}_l-\boldsymbol{\theta}_{0l})^T\,\hat{\mathbf{K}}_{0l}^T\,(\boldsymbol{\theta}_l-\boldsymbol{\theta}_{0l}) - 1 \leq 0 \tag{4.49}$$

where g_l is the average steering curvature constraint in layer l, $\boldsymbol{\theta}_l$ and $\boldsymbol{\theta}_{0l}$ are $(n \times 1)$ vectors of current and initial spatial distribution of fibre angles at n nodes in layer l, $\mathbf{b}_{0l}$ $(n \times 1)$ and $\hat{\mathbf{K}}_{0l}$ $(n \times n)$ are the gradient vector and Hessian matrix of g_l with respect to $\boldsymbol{\theta}_l$ computed at the initial spatial distribution of fibre angles, $\boldsymbol{\theta}_0$, and:

$$\mathbf{b}_l = \hat{\mathbf{K}}_l\,\boldsymbol{\theta}_l \tag{4.50}$$

Using equations 4.48 and 4.49 for quadratic approximation of the objective and constraint functions, the optimisation problem in equation 4.42 is formulated as a quadratically constrained quadratic programming (QCQP) problem. This QCQP problem is solved using the dual method with a gradient-based optimiser and since the quadratic approximations are convex and continuously differentiable, the solution of the primal and dual problems are identical. Pilaka [34] used the built in functions *fmincon* and *pcg* to solve the dual problem. After finding the optimum fibre angle distribution, the gradients and Hessians are updated and the QCQP problem is formulated at the new fibre angle distribution and solved again. This iterative process is continued until the primary objective function in equation 4.43 is converged.

Imposing the average steering curvature as a constraint in the second step provides a computationally efficient means for restraining the amount of steering. However, it does not guarantee that the local steering curvatures, which are realised as the measure for manufacturability of the steered fibre paths, do not exceed the maximum allowable steering curvature in the fibre placement. On the other hand, the actual local steering curvatures are dependent on the actual steered fibre paths, which are constructed in the third step of the multi-step framework, rather than the norm of gradient of the fibre angle in equation 4.39. Previous studies [34] have shown that using the average steering curvature as a constraint per ply in the second step and the streamline method in the third step is an effective strategy in finding the smooth fibre paths with controlled amount of fibre steering.

The same fibre angle retrieval procedure is applicable when the local steering curvatures are constrained instead of the average steering curvature. However, the number of constraints in step two are increased from one average steering curvature per layer to a lot of local steering curvatures at each discretisation point in each layer and hence solving the optimisation problem becomes computationally more expensive.

Layers with fixed ply angles

Some practical considerations in design of composite laminates may dictate using some straight fibre layers with fixed fibre angles, e.g. placing [±45] sublaminates on the outermost top and bottom surfaces of the laminate. The straight fibre plies in the outermost [±45] sub-laminates cover the possible gaps and overlaps of the steered tows and improve the damage tolerance of the laminate.

In the laminates which possess layers with fixed ply angles, the fibre angle distribution is retrieved from the solution of the QCQP problem formulated by setting the rows, which correspond to the layer(s) with fixed ply angle(s), in the gradients ($\mathbf{J}_0$, $\mathbf{b}_{0l}$) and the rows and columns, which correspond to the layer(s) with fixed ply angle(s), in the Hessians ($\mathbf{H}_0$, $\hat{\mathbf{K}}_{0l}$) to zero.

4.5.3 INITIALISATION OF RETRIEVAL PROCEDURE

The convex conservative separable approximation, equation 4.44, which is used to build the primary objective function, equation 4.43, is a local approximation. This approximation is constructed based on the sensitivity data of the conceptual stiffness design and this sensitivity data is not updated during the second step optimisation. Therefore, the proposed fibre retrieval procedure is a local search and the optimum fibre angle distribution obtained from solving the QCQP problem is dependent on the initial fibre angle distribution.

Solving the QCQP problem with the gradient-based optimisers will usually result in local optima unless the local search starts from a design which is adequately close to the global optimum. The local search, formulated in subsection 4.5.2, can perform effectively when used as an additional search in evolutionary techniques. An initial fibre angle distribution can be found by using the evolutionary techniques, e.g. GA. The objective function which is minimised in the evolutionary techniques can be the square distance between the realistic and conceptual designs in the lamination parameters as in [4] or in the stiffness matrices space. The Lagrangian of the approximate subproblem built using the convex conservative separable approximation of structural responses of the theoretical stiffness design can be also selected as the objective function.

4.6 STEP THREE: STEERED FIBRE PATHS

The realistic fibre angle distribution in the second step needs to be further processed in the third step to obtain the realistic location of course centre-lines to be fed into the fibre placement machine. In the third step of the multi-step optimisation framework, smooth fibre paths are constructed from the spatial distribution of fibre angles based on the streamline, fluid flow, analogy.

In a primary attempt, Setoodeh et al. [36] proposed a method based on the streamline analogy to construct the continuous fibre paths from the discrete distribution of fibre angles in each layer of a rectangular panel. In this method, the spatial distribution of the fibre angles is modeled as a potential flow with unit velocity vectors and the corresponding stream function distribution is obtained. Subsequently, streamlines are plotted by connecting the points which have the same stream function values. The continuous steered fibre paths are used as the centrelines of the courses which are placed using the AFP machine. If the width of the steered courses is constant along the fibre paths, some gaps and overlaps are developed between the adjacent courses. The individual cut and restart capability of the AFP machine can be used to achieve a realistic VS laminate with a constant thickness which is consistent with the corresponding theoretical constant thickness laminate.

The proposed method by Setoodeh et al. [36] is also able to estimate the thickness distribution when the individual tow cut and restart is not implemented. In this method, the smeared continuous thickness distribution is obtained based on the relative distance between the streamlines which are plotted at stream function values increased with a fixed step. The continuous thickness distribution, neglects the discrete nature of the ply thickness, and is correct only when the number of fibre courses tend to infinity and the course width is infinitely small. However, it provides a measure of thickness distribution to evaluate manufacturability of the corresponding steered fibre laminate using the cut and restart capability of the AFP machine.

In a follow-on study, Blom et al. [37] showed that the solution of the potential flow and the resulting thickness distribution is not unique and is dependent on the the inflow boundary conditions and locations where the courses are started. Blom et al. [37] found the optimised inflow boundary conditions and start locations of steered fibre paths which minimise the maximum thickness or maximise the surface smoothness in each ply of a rectangular panel or a cylindrical surface. Blom et al. [37] compared the estimated continuous thickness distribution with the actual discrete thickness distribution resulted from the fibre placement.

Later, Nagy et al. [38] implemented the streamline analogy approach to find the steered fibre paths on the shells with arbitrary surfaces and Pilaka [34] developed an algorithm to maximise the thickness smoothness of the steered fibre paths on the arbitrary surface. In this thesis, implementations of Nagy et al. [38] and Pilaka [34] are used to construct the steered fibre paths.

5

STRENGTH EVALUATION AND APPROXIMATION

5.1 INTRODUCTION

Strength or material failure is evaluated using a function of the actual and limit stresses or strains, which is determined empirically from coupon test data. Based on the data fitting method and material type, different failure criteria are developed. Some of the most frequently used failure criteria for composite laminates include the maximum strain, the maximum stress, Tsai-Hill and Tsai-Wu.

In certain geometric and loading conditions, large normal and shear stresses in the normal direction to the interface of layers are generated. These stresses may trigger laminate delamination, since the strength of the matrix material, which joins adjacent layers, is substantially smaller than the in-plane strength of layers. Laminate delamination, even if restricted to small and localised areas, can affect the integrity of the laminate and degrade the in-plane loading capacity, however, since calculation of delamination stresses is complicated and expensive, here only calculation of in-plane stresses and their corresponding failure modes are considered for the sake of simplicity.

In a general laminate, the laminate strains and the material strength may change in different layers depending on the laminate loading conditions and materials. Even in a laminate with constant through the thickness laminate strains and a unique material, the stresses usually change in different layers due to the differ-

Parts of this chapter have been published in Composites Part B: Engineering **42** (2011) 546-552 [134].

ent ply angles. Therefore, usually one or a few layers reach their limiting strength earlier than the other layers. Failure prediction based on the failure of the first ply is referred to as first ply failure. After first ply failure is happened, the un-failed layers of the laminate may be able to carry at least a portion of the first ply failure load in a stable condition. As the applied load is increased, the failure progresses from one layer to the next layer, this is usually called progressive failure. In this chapter, only first ply failure in considered, progressive failure analysis falls beyond the scope of the research reported here.

The strength measure of each ply in a laminate can be expressed as a function of the ply stress or strain values in the material directions, e.g. fibre direction and normal direction to that, and material strength properties. Ply stresses and strains in the material directions are functions of the ply angles and therefore the failure envelope depends on the ply angle. Lamination parameters, which were used as continuous design variables in the first step of the multi-step optimisation framework described in section 4.4, do not provide a priori knowledge about the orientations of the plies. Therefore, using lamination parameters as design variables in strength optimisation problems is precluded, considering the dependency of the failure envelope on the ply angle. To remedy this problem, Gürdal et al. [135] proposed to incorporate lamination parameters in strength optimisation problems only for a predetermined set of ply orientations. They use Miki's graphical technique in the feasible domain of lamination parameters to maximise the strength of a laminate with a predetermined set of ply orientations subject to in-plane loading. As another example, Kogiso et al. [136] use lamination parameters for reliability based optimisation of a composite laminate consisting of a predetermined set of ply orientations under in-plane loading considering Tsai-Wu first ply failure criterion. The disadvantage of this approach is that the design space is limited by restricting the ply angles to a predefined set.

IJsselmuiden et al. [121] presented a method to facilitate using lamination parameters as design variables for strength optimisation of composite laminates without restricting the ply angles to a predefined set of angles. This approach, which is through mapping the Tsai-Wu failure criterion in the laminate strain space, was first implemented by Nakayasu and Maekawa [137] to evaluate the stochastic behavior of a composite laminate with any lamination angle under a multi-axial stress or strain condition. The failure criterion is expressed as a function of the laminate strains and the ply angles. Therefore, a unique failure surface can be drawn for each ply orientation in the laminate strain space. Two different equations are obtained analytically for surfaces which are tangent to the failure surfaces of all ply orientations. The first envelope is a second order function in terms of laminate strains and the second envelope is a fourth order one, which is comprised of two second order intersecting envelopes. The envelope, which encompasses the common safe region of the failure surfaces of all ply orientations, is safe regardless of ply orientation. Depending on the material properties, the second or the fourth order envelope is the conservative failure envelope.

The developed failure envelopes can be expressed as elliptical equations in terms of principal strains. Therefore, the fourth order failure envelope is expressed as two intersecting ellipses. The advantage of this formulation for the fourth order envelope is that two different constraints, corresponding to each of the two smooth failure ellipses, are used in the optimisation process. Therefore, the possible convergence problems due to the non-smooth fourth order envelope are eliminated.

The failure index, which is defined as the inverse of safety factor, is used for strength evaluation. A failure index is approximated as a first order Taylor series in terms of the strains to reduce the cost of repetitive strength evaluation during optimisation. Furthermore, a convex approximation in terms of the stiffness matrices can be constructed for the failure index expression. Therefore, a convex conservative separable approximation is built which can be used in the multi-step optimisation framework developed in chapter 4.

In this chapter, the conservative failure envelope developed by IJsselmuiden et al. [121] is explained in section 5.2. The elliptical equations of the conservative failure envelope in terms of the principal strains is presented in section 5.3. The safety factor and failure index are defined in section 5.4 as strength measures. Construction of the convex approximation of the failure index, which is suited to be used in the multi-step optimisation framework developed in chapter 4, is described in section 5.5. Finally, the new failure envelope formulation and failure index approximation are verified in section 5.6 by comparing the strength optimisation results for single-point constant stiffness laminates with the results from [6].

5.2 CONSERVATIVE TSAI-WU FAILURE ENVELOPE

Tsai-Wu failure criterion is a widely used failure theory for composite materials which have different strengths in tension and compression. In material coordinates, the Tsai-Wu failure criterion for each ply takes the form of a quadratic function of in-plane stresses [138]:

$$F_{11}\sigma_1^2 + F_{22}\sigma_2^2 + F_{66}\tau_{12}^2 + F_1\sigma_1 + F_2\sigma_2 + 2F_{12}\sigma_1\sigma_2 = 1 \tag{5.1}$$

where F_i and F_{ij} ($i = 1,2$ and $j = 1,2,6$) are defined as:

$$\begin{aligned} &F_{11} = \frac{1}{X_t X_c},\ F_{22} = \frac{1}{Y_t Y_c},\ F_{66} = \frac{-1}{2\sqrt{X_t X_c Y_t Y_c}}, \\ &F_1 = \frac{1}{X_t} - \frac{1}{X_c},\ F_2 = \frac{1}{Y_t} - \frac{1}{Y_c},\ F_{12} = \frac{1}{S^2}, \end{aligned} \tag{5.2}$$

It is also possible to express the Tsai-Wu failure criterion in terms of the in-plane strains in the material coordinates:

$$G_{11}e_1^2 + G_{22}e_2^2 + G_{66}e_{12}^2 + G_1e_1 + G_2e_2 + 2G_{12}e_1e_2 = 1 \tag{5.3}$$

G_i and G_{ij} $(i, j = 1,2,6)$ coefficients are obtained by substituting the material stresses in equation 5.1 with the material strains using the stress-strain relation, equation 2.63. This stress-strain relation for each lamina in the laminate is repeated here for convenience:

$$\begin{bmatrix} \sigma_1 \\ \sigma_2 \\ \tau_{12} \end{bmatrix} = \begin{bmatrix} Q_{11} & Q_{12} & 0 \\ Q_{21} & Q_{22} & 0 \\ 0 & 0 & Q_{66} \end{bmatrix} \begin{bmatrix} e_1 \\ e_2 \\ \gamma_{12} \end{bmatrix} \tag{5.4}$$

where Q_{ij} $(i, j = 1,2,6)$ are the components of the reduced stiffness matrix defined in equation 2.64. Therefore, G_i and G_{ij} $(i, j = 1,2,6)$ coefficients can be expressed as [121]:

$$\begin{aligned}
G_{11} &= Q_{11}^2F_{11} + Q_{12}^2F_{22} + 2F_{12}Q_{11}Q_{12} \\
G_{22} &= Q_{12}^2F_{11} + Q_{22}^2F_{22} + 2F_{12}Q_{12}Q_{22} \\
G_{12} &= Q_{11}Q_{12}F_{11} + Q_{12}Q_{22}F_{22} + F_{12}Q_{12}^2 + F_{12}Q_{11}Q_{22} \\
G_{66} &= 4Q_{66}^2F_{66} \\
G_1 &= Q_{11}F_1 + Q_{12}F_2 \\
G_2 &= Q_{12}F_1 + Q_{22}F_2
\end{aligned} \tag{5.5}$$

5

The material strains can be expressed in terms of the laminate strains and ply angles:

$$\begin{bmatrix} e_1 \\ e_2 \\ \gamma_{12} \end{bmatrix} = \begin{bmatrix} c^2 & s^2 & 2cs \\ s^2 & c^2 & -2cs \\ -cs & cs & c^2 - s^2 \end{bmatrix} \begin{bmatrix} e_x \\ e_y \\ \gamma_{xy} \end{bmatrix} \tag{5.6}$$

where $c = \cos\theta$ and $s = \sin\theta$, and θ is the ply angle measured from the laminate axis, x. By substituting the material strains from equation 5.6 in the Tsai-Wu failure criterion in equation 5.3, the failure surface can be expressed as a function of laminate strains and ply angles:

$$F(e_x, e_y, \gamma_{xy}, c, s) = 0 \tag{5.7}$$

The dependency of the failure surface on the ply angle precludes the use of lamination parameters as design variables in strength optimisation problems. This is because lamination parameters do not provide a priori knowledge about the ply angles. This problem is remedied by using a conservative failure envelope proposed by IJsselmuiden et al. [121]. The conservative failure envelope is based on the Tsai-Wu failure criterion but is independent from the ply angle. It is clear from equation 5.7 that for each ply angle, a unique Tsai-Wu failure surface can be plotted in the laminate strain space. The conservative failure envelope, proposed by IJsselmuiden et al. [121], embodies the safe region common between different failure surfaces for different ply angles. The equation of this failure envelope is obtained by finding the geometric surface which is tangent to the family of failure surfaces for all ply angles:

$$\frac{dF}{d\theta} = 0 \tag{5.8}$$

As it is clear from equation 5.7, F is a function of c and s, and hence using the chain rule the equation of the conservative envelope, equation 5.8, can be re-expressed as:

$$\frac{dF}{d\theta} = c\frac{\partial F}{\partial s} - s\frac{\partial F}{\partial c} = 0 \tag{5.9}$$

Both F and $\frac{dF}{d\theta}$ are functions of c and s, and c and s are dependent through the trigonometric relation:

$$s^2 + c^2 - 1 = 0 \tag{5.10}$$

The equation of the conservative failure envelope is obtained by eliminating c and s from equation 5.9 using Dixon's resultant [139] and equations 5.7, 5.8 and 5.10. This leads to the following two equations, each representing an envelope tangent to all the failure surfaces in the strain space for all ply angles [121]:

$$4u_6^2 I_2^2 + 4u_6 u_1 I_2^2 + 4(1 + u_2 I_1 + u_3 I_1^2)(u_1 - u_6) + (u_4 + u_5 I_1)^2 = 0 \tag{5.11}$$

$$u_1^2 I_2^4 - I_2^2 (u_4 + u_5 I_1)^2 - 2u_1 I_2^2 (1 - u_2 I_1 - u_3 I_1^2) + (1 - u_2 I_1 - u_3 I_1^2)^2 = 0 \tag{5.12}$$

where I_1 is the volumetric strain invariant and I_2 is the maximum shear strain given by:

$$I_1 = e_x + e_y, \qquad I_2 = \sqrt{\left(\frac{e_x - e_y}{2}\right)^2 + \gamma_{xy}^2} \tag{5.13}$$

The terms u_i, ($i = 1...6$) are defined in terms of the G_{ij} coefficients (equation 5.3):

$$\begin{aligned} u_1 &= G_{11} + G_{22} - 2G_{12} \\ u_2 &= (G_1 + G_2)/2 \\ u_3 &= (G_{11} + G_{22} - 2G_{12})/4 \\ u_4 &= G_1 - G_2 \\ u_5 &= G_{11} - G_{22} \\ u_6 &= G_{66} \end{aligned} \tag{5.14}$$

(5.15)

The first equation, equation 5.11, is a quadratic function of strains and represents a single smooth second-order envelope in the laminate strain space. The second equation, equation 5.12, is a quartic function of strains, which represents two intersecting quadratic envelopes in the laminate strain space. In other words, the fourth-order equation, equation 5.12, is factorable into two second-order equations which form a self-intersecting non-smooth envelope. The envelopes from the two equations, equations 5.11 and 5.12, do not intersect each other but may become tangent as shown in figure 5.1.

5

The safe region in the laminate strain space is the area common between all the failure surfaces for all ply angles. Therefore, one of the two equations, equations 5.11 and 5.12, which describe the inner envelope is used as the conservative envelope. The two equations, equations 5.11 and 5.12, are functions of material properties, since u_i are functions of G_{ij} coefficients (equation 5.14), which are functions of the components of the reduced stiffness matrix Q_{ij} and F_i and F_{ij} coefficients (equation 5.5), which are functions of the material properties (equations 2.64 and 5.2). Therefore, the fact that which of the second-order and the fourth-order envelopes is the inner envelope, is determined by the material properties.

In figure 5.1, Tsai-Wu failure surfaces of different ply angles and the second-order and fourth-order envelopes, which are tangent to these failure surfaces, are plotted in the laminate strain space for a few materials. The inner envelope, which is selected as the conservative failure envelope, is determined with a red dotted line. The investigated materials include Carbon-PEEK (AS4), Carbon-Epoxy (IM6) and Boron-Epoxy (B5.6). The properties of these materials are listed in table 5.1 and the stiffness ratio E_1/E_2 ranges from approximately 9 to 17 in these materials. In figure 5.1, γ_{xy} is set to zero and the failure envelopes are plotted in the principal strain space (e_I and e_{II} are the principal strains), however, similar failure envelopes can be generated for a range of γ_{xy} values. Figure 5.1 shows that for each material, one of the two equations 5.11 and 5.12, accurately describes the in-

TABLE 5.1: Material properties [6]

Property	AS4	IM6	B5.6
Longitudinal modulus, E_1 [GPa]	142	177	201
Transverse modulus, E_2 [GPa]	10.3	10.8	21.7
Shear modulus, G_{12} [GPa]	7.2	7.6	5.4
Poisson's ratio, ν_{12} [-]	0.27	0.27	0.17
Longitudinal tensile strength, X_t [MPa]	2280	2860	1380
Longitudinal compressive strength, X_c [MPa]	1440	1875	1600
Transverse tensile strength, Y_t [MPa]	57	49	56.6
Transverse compressive strength, Y_c [MPa]	228	246	125
Shear strength, S [MPa]	71	83	62.6

ner envelope. As it is clear from figure 5.1, the conservative failure envelopes are convex in the strain space, as their boundaries are constructed from the convex Tsai-Wu failure surfaces for different ply angles.

In the following section, a simpler derivation of the conservative failure envelope than that provided by IJsselmuiden et al. [121] is shown. The case of the self intersecting envelope is shown to resolve into two quadratic functions. Thus, it is shown that the conservative approximation of the Tsai-Wu failure criterion is represented by one or two ellipses in principle strain space.

5

5.3 ELLIPTICAL FORMULATION OF THE CONSERVATIVE ENVELOPE

The Tsai-Wu failure criterion in strain space, equation 5.3, can be re-expressed in terms of three strain invariants:

$$\begin{aligned} I_1 &= e_I + e_{II} \\ I_2 &= e_I^2 + e_{II}^2 \\ I_4 &= e_I n_1^2 + e_{II} n_2^2 \end{aligned} \tag{5.16}$$

where e_I and e_{II} are the principal strains, $n_1 = \cos\gamma$ and $n_2 = \sin\gamma$, and γ is the ply angle measured from the principal strain axis. Since Tsai-Wu criterion is a quadratic function of strains (equation 5.3), the expression can be formed as:

$$f = \frac{1}{2}u_1 I_1^2 + u_2 I_1 I_4 + \frac{1}{2}u_3 I_4^2 + u_4 I_2 + u_5 I_1 + u_6 I_4 \tag{5.17}$$

where u_i $(i = 1, 2, \ldots, 6)$ are material invariants. These coefficients can be found by re-writing equation 5.17 in terms of the material strains and comparing it with

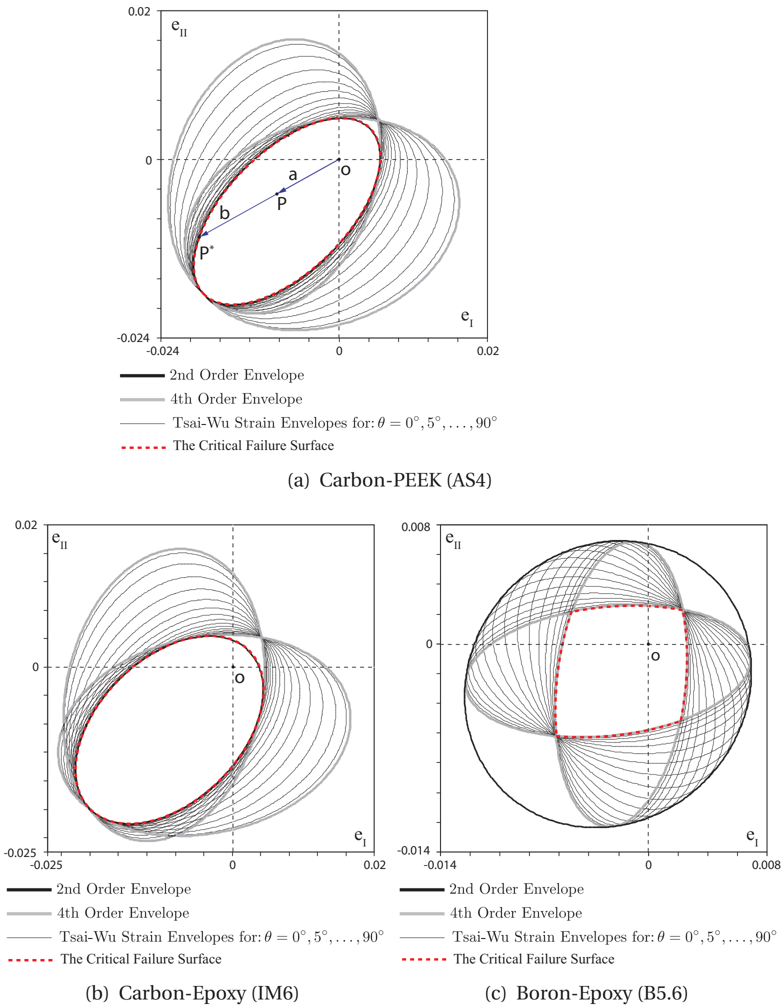

FIGURE 5.1: Conservative failure envelopes plotted in the principal strain space for different materials (regenerated from IJsselmuiden et al. [121])

equation 5.3. For this purpose, the strain invariants in equation 5.16 can be expressed in terms of laminate strains:

$$\begin{aligned} I_1 &= e_x + e_y \\ I_2 &= e_x^2 + e_y^2 + 2\gamma_{xy}^2 \\ I_4 &= e_x c^2 + e_y s^2 + 2\gamma_{xy} cs \end{aligned} \tag{5.18}$$

where $c = \cos\theta$ and $s = \sin\theta$, and θ is the ply angle measured from the laminate axis. Therefore, if material strains are used, $c = 1$ and $s = 0$, and strain invariants are simplified as:

$$\begin{aligned} I_1 &= e_1 + e_2 \\ I_2 &= e_1^2 + e_2^2 + 2e_{12}^2 \\ I_4 &= e_1 \end{aligned} \tag{5.19}$$

The strain invariants in equation 5.19 are substituted in equation 5.17 and the resulting equation is compared with equation 5.3 to find the u_i $(i = 1, 2, \ldots, 6)$ coefficients as:

$$\begin{aligned} u_1 &= G_{22} - G_{66}/2 \\ u_2 &= G_{66}/2 \\ u_3 &= 2G_{12} - 2G_{22} + G_{66} \\ u_4 &= G_{11} - 2G_{12} - G_{66} \\ u_5 &= G_2 \\ u_6 &= G_1 - G_2 \end{aligned} \tag{5.20}$$

As is clear from equations 5.17 and 5.18, Tsai-Wu failure criterion, f, is a function of the ply angle, θ. The conservative failure envelope is formulated by setting the Tsai-Wu failure criterion for the most critical ply angle to 1:

$$\max_{\theta} f = 1 \tag{5.21}$$

Note that only the invariant I_4 is function of θ. Thus maximisation with respect to θ can be replaced by maximisation with respect to I_4. The values of I_4 are not arbitrary, $e_{II} \le I_4 \le e_I$. Thus, the conservative failure envelope is defined by:

$$\max_{I_4} f = 1, \quad e_{II} \le I_4 \le e_I. \tag{5.22}$$

The failure criterion is a quadratic function of I_4. Thus, two distinct cases exist:

- $u_3 < 0$: In this case the failure criterion is concave in I_4 and the maximum in equation 5.17 is easily retrieved by setting the derivative with respect to I_4 to zero. The maximum is obtained at:

$$I_4 = \frac{-(u_2 I_1 + u_6)}{u_3} \tag{5.23}$$

  The failure envelope in this case takes the form:

$$f_{max} = \frac{1}{2}(u_1 - \frac{u_2^2}{u_3})I_1^2 + (u_5 - \frac{u_2 u_6}{u_3})I_1 + u_4 I_2 - \frac{u_6^2}{2u_3} \tag{5.24}$$

- $u_3 \geq 0$: In this case the maximum is obtained at either end of the interval $e_{II} \leq I_4 \leq e_I$. This leads to two possible equations for the failure envelope depending on whether the maximum is attained at one end or the other.

In either case, the final form of the Tsai-Wu strain envelope takes an elliptical form in terms of principal strains:

$$C_{ij} e_i e_j + C_i e_i + C_0 = 0, \quad i = I, II, \tag{5.25}$$

5

The coefficients of Tsai-Wu expressed as an ellipse equation in terms of the principal strains (equation 5.25) for the materials with the critical second order envelope are:

$$\begin{aligned}
C_0 &= -(1/4)u_6^2/u_4 - 1, \\
C_I &= -(1/2)u_3 u_6/u_4 + u_5, \\
C_{II} &= -(1/2)u_3 u_6/u_4 + u_5, \\
C_{I\,I} &= -(1/4)u_3^2/u_4 + u_2 + u_1, \\
C_{I\,II} &= u_1 - (1/4)u_3^2/u_4, \\
C_{II\,II} &= -(1/4)u_3^2/u_4 + u_2 + u_1
\end{aligned} \tag{5.26}$$

For materials with the fourth order envelope as the critical envelope, these coefficients for each of the two branches of the envelope are:

$$\begin{aligned}
C_0(1) &= C_0(2) = -1, \\
C_I(1) &= C_{II}(2) = u_5, \\
C_{II}(1) &= C_I(2) = u_6 + u_5, r \\
C_{I\,I}(1) &= C_{II\,II}(2) = u_2 + u_1, \\
C_{I\,II}(1) &= C_{I\,II}(2) = (1/2)u_3 + u_1, \\
C_{II\,II}(1) &= C_{II}(2) = u_2 + u_1 + u_3 + u_4,
\end{aligned} \tag{5.27}$$

In this section, the conservative Tsai-Wu failure envelopes are expressed using equation 5.25 which is simpler than equations 5.11 and 5.12. The equations of the failure surface, equations 5.11, 5.12 and 5.25, are obtained by setting the value of failure criterion to one. This value is set to one at the right hand side of equations 5.1 and 5.3. Therefore, negative values of the left hand side of equation 5.11, 5.12 and 5.25 mean that the specimen is safe and positive values mean that the specimen has failed.

5.4 STRENGTH CONSTRAINT FORMULATION

Maximum strength design of composite laminates is sometimes performed by minimisation of the failure index defined as the left hand side of equation 5.25 or equations 5.11 and 5.12. However, Groenwold and Haftka [140] showed that for inhomogeneous failure criteria such as Tsai-Wu criterion in contrast to the homogeneous failure criteria such as Tsai-Hill criterion, the optimum laminate obtained from minimisation of the value of the failure criterion is dependent on the actual value of the applied load. To remedy this problem for inhomogeneous failure criteria, Groenwold and Haftka [140] introduced the factor of safety, λ, and proposed to directly maximise λ for strength optimisation. The factor of safety, λ, is defined as the factor multiplying the actual strains such that the scaled strains satisfy the failure envelope. The factor of safety is defined in terms of the lengths of the vectors shown in figure5.1(a) as:

$$\lambda = \frac{b}{a} \tag{5.28}$$

where a is the distance between the origin and an arbitrary point P in the strain space, and b is the length of the vector which starts from the origin, passes through point P and reaches point P^* on the envelope boundary, as shown in figure 5.1(a). The feasible region, where no failure occurs, is defined by the condition:

$$\lambda(\mathbf{e}) \geq 1 \tag{5.29}$$

Groenwold and Haftka [140] show that if the failure criterion is homogeneous, e.g. Tsai-Hill, all the terms are multiplied by the safety factor uniformly. Therefore, maximisation of the safety factor is equivalent to minimisation of the value of the failure index, however, if the failure criterion is inhomogeneous, e.g. Tsai-Wu, the linear terms have a more important role in the failure criterion expression for small safety factors compared to larger safety factors. Therefore, for inhomogeneous failure criteria, the optimum design depends on the value of the safety factor and hence the applied load. Therefore, selection of the failure index as the objective function in the strength optimisation problems with an inhomogeneous failure criterion, may result in a laminate which does not have the maximum safety factor.

The failure index is redefined by IJsselmuiden et al. [121] as:

$$r_s = \frac{1}{\lambda^2} \tag{5.30}$$

The rationale behind the definition in equation 5.30 is that in contrast to λ the failure index r_s is differentiable with respect to the strain and bounded at zero strains. The feasible region is defined by the condition:

$$r_s(\mathbf{e}) \leq 1 \tag{5.31}$$

The failure index r_s as defined by IJsselmuiden et al. [121] is a homogeneous function of second order with respect to strain. To expand the strength constraint using the hybrid approximation (see section 5.5), it is desirable that the strength constraint is defined as a homogeneous function of order one in strains. To achieve this we depart from the definition given in [121] (equation 5.30) and define the failure index as:

$$r_s = \frac{1}{\lambda} \tag{5.32}$$

This definition sacrifices the differentiability at zero strains. This is tolerable given that the strength constraint would not be active at zero strains and may be removed from the optimisation formulation at stress free points. The equation of the failure index is given by substituting e_I and e_{II} in equation 5.25 with e_I/r_s and e_{II}/r_s values on the failure envelope, respectively. After simplification:

$$C_{ij}\, e_i\, e_j \;+\; r_s\, C_i\, e_i \;+\; r_s^2\, C_0 \;=\; 0, \quad i, j \;=\; I,\, II, \tag{5.33}$$

equation 5.33 can be re-expressed as:

$$a_2 + a_1 r_s + a_0 r_s^2 = 0 \tag{5.34}$$

where:

$$a_2 = C_{I\,I}\, e_I^2 + C_{II\,II}\, e_{II}^2 + 2\, C_I\, C_{II}\, e_I\, e_{II}, \qquad a_1 = C_I\, e_I + C_{II}\, e_{II}, \qquad a_0 = C_0 \tag{5.35}$$

Solving for r_s in the second order elliptical envelope or either of the two elliptical branches of the fourth order envelope yields two roots and the largest root is selected as the failure index.

Repetitive evaluation of the failure index is required in strength optimisation. Therefore, it is advantageous to use an approximation of the failure index to reduce the computational costs. For this purpose, the failure index is expanded as a linear function of strains around the approximation point, $\mathbf{e}^{(k)}$, as:

$$r_s(\mathbf{e}) \approx r_s(\mathbf{e})^{(k)} + \mathbf{g}^{(k)^T} \ (\mathbf{e} - \mathbf{e}^{(k)}) \tag{5.36}$$

Using Euler's theorem of homogeneous functions, $\mathbf{g}^T \mathbf{e} = r_s$, the approximation is simplified to:

$$r_s(\mathbf{e}) \approx \mathbf{e}^T \ \mathbf{g}^{(k)} \tag{5.37}$$

where

$$\mathbf{g}^{(k)} = \frac{\partial r_s}{\partial \mathbf{e}}|_{\mathbf{e}=\mathbf{e}^k} \tag{5.38}$$

and $\mathbf{g}$ can be found analytically using the chain rule:

$$\mathbf{g} = \frac{\partial r_s}{\partial e_q} = \sum_{p=I}^{II} \frac{\partial r_s}{\partial e_p} \frac{\partial e_p}{\partial e_q} \tag{5.39}$$

where $e_q = e_x, e_y, \gamma_{xy}$ and

$$\frac{\partial r_s}{\partial e_p} = \frac{\sum_{n=0}^{2} \frac{\partial a_n}{\partial e_p} r_s^{2-n}}{\sum_{n=0}^{2} (2-n)\, a_n r_s^{1-n}} \tag{5.40}$$

As it is clear from equations 2.45-2.47, according to the Sanders theory, the total strain, $\mathbf{e}$, at each point of a shell structure can be expressed in terms of the middle surface strains ($\boldsymbol{\epsilon}(z=0)$), and the changes of curvatures ($\boldsymbol{\kappa}$) as following:

$$\mathbf{e}(z) = \boldsymbol{\epsilon}(z=0) + z\boldsymbol{\kappa} \tag{5.41}$$

where $z \in [-\frac{h}{2}, +\frac{h}{2}]$ is the through the thickness coordinate measured from the middle surface. Therefore, the failure index, r_s, is also a function of the through the thickness coordinate, z. For strength optimisation purpose, it would be beneficial to eliminate the dependency of r_s on z, by considering the point with maximum failure index through the thickness to be safe. Therefore, the strength constraint in equation 5.31 is re-written as [6]:

$$\max_z \ (r_s) \leq 1 \tag{5.42}$$

As mentioned in section 5.2, the failure index, r_s, is a convex function of the total strains, $\mathbf{e}$, and as it is clear from equation 5.41, the strains are linear functions of the through the thickness coordinate, z. It is concluded from the properties of convex functions that r_s is a unimodal function of z with a unique minimum.

Therefore, the maximum failure index will happen at one of the extreme points of the thickness coordinate, $z = -\frac{h}{2}$ or $z = +\frac{h}{2}$ [6]. It is well-known that in practice, depending on the ply angles, the critical failure index does not always happen at one of the outermost plies., however, when using the conservative Tsai-Wu failure envelope, it is assumed that all the possible ply angles could exist at each ply location through the thickness and therefore, one of the outermost plies is critical. Therefore, corresponding to each failure envelope and each point on the middle surface, for out of plane problems two strength constraints calculated at the upper and bottom surfaces ($r_s^{\pm} = r_s(z = \pm\frac{h}{2})$) are considered, while for in-plane problems only one strength constraint is enough. For materials in which the fourth-order envelope is critical, the strength constraints for both of the two intersecting second-order envelopes are considered in the optimisation problem.

The advantage of using the failure envelope defined by IJsselmuiden et al. [121] in strength optimisation problems is that this failure envelope is not a function of the ply angle and hence lamination parameters can be used as design variables. The drawback is that this failure envelope may be excessively conservative in some cases. In the failure envelope developed by IJsselmuiden et al. [121], it is assumed that every possible ply angle is present in each ply of the laminate. The critical boundary of this failure envelope is formed from the Tsai-Wu failure surface of different ply angles. Therefore, if some of these ply angles do not exist, the failure envelope is conservative. IJsselmuiden et al. [121] show that in some cases the failure envelope is excessively conservative, e.g. unidirectional laminates under uniaxial loading and bending dominated laminates.

In the unidirectional laminates, the fibres in all the plies are aligned in a single direction, e.g. 0°. Among different ply angles, intuitively 0° plies have the minimum failure index under uniaxial loading applied in the 0° direction. In contrast, the critical boundary of the conservative failure envelope is formed from the failure surface of the ply angle which has the maximum failure index. This means that the predicted failure index from the conservative failure envelope is significantly overestimated for 0° plies under uniaxial loading. Therefore, if uniaxial loading is applied on a unidirectional laminate, in which all the plies are 0° plies, the failure envelope is excessively conservative.

In bending dominated laminates, the state of strain changes significantly in the thickness direction. As stated earlier, the actual stacking sequence of the plies is not considered in the conservative failure envelope, however, different stacking sequences of a set of fibre angles, which have the same in-plane stiffness properties, have different Tsai-Wu failure indices. This is because the total strain is not constant in the thickness direction and changes for different plies. Therefore, the amount of conservativeness of the failure envelope is different for different stacking sequences of a set of fibre angles and may be excessive for some of them.

5.5 CONVEX APPROXIMATION OF FAILURE INDEX

Construction of the conservative convex separable approximations of the structural responses in the form of equation 4.6 is explained in section 4. These approximations are used in the optimisation framework developed in section 4 to design variable stiffness (VS) composite laminates. The approximations in the form of equation 4.6 consist of two parts; a convex separable part, f_P, and a part for ensuring the strict conservativeness, f_D. To construct the first part, f_P, part of the structural response is expanded linearly in terms of the stiffness matrices and another part is expanded reciprocally. This separation is performed based on the physical nature of the structural performance and/or a numerical algorithm such that the constructed f_P is convex. Construction of the convex separable approximation, f_P, is explained for the structural stiffness and the buckling load in subsection 4.3.3. However, construction of the convex separable approximation for the failure index is postponed to this section, since evaluation of the failure index requires introduction of the conservative failure envelope and definition of the failure index.

Using the equations of the total strains from the Sanders theory, equations 2.45-2.47, and the constitutive relations from the classical lamination theory (CLT), equations 2.71 and 2.72, for a symmetric laminate (the bending-extension coupling stiffness matrix, **B**, is zero), the local total strains are given by:

$$\mathbf{e} = \mathbf{A}^{-1}\,\mathbf{N} + z\mathbf{D}^{-1}\,\mathbf{M} \tag{5.43}$$

Therefore, by substituting equation 5.43 in equation 5.37, the failure index can be locally approximated in the form:

$$r_s = (\mathbf{N}^T\,\mathbf{A}^{-1} + z\mathbf{M}^T\,\mathbf{D}^{-1})\,\mathbf{g} \tag{5.44}$$

where $\mathbf{g} = \mathbf{g}^{(k)}$ and equation 5.44 partly may be approximated as:

$$r_s = \boldsymbol{\Phi}^m : \mathbf{A}^{-1} + \boldsymbol{\Phi}^b : \mathbf{D}^{-1} \tag{5.45}$$

where (:) is matrix contraction (trace of the multiplication), and $\boldsymbol{\Phi}_m$ and $\boldsymbol{\Phi}_b$ are the symmetric matrices, related to the in plane and out of plane parts, defined by:

$$2\,\boldsymbol{\Phi}^m = \mathbf{N}\,\mathbf{g}^T + \mathbf{g}\,\mathbf{N}^T, \qquad 2\,\boldsymbol{\Phi}^b = z(\mathbf{M}\,\mathbf{g}^T + \mathbf{g}\,\mathbf{M}^T) \tag{5.46}$$

The approximation in equation 5.45 is local in the sense that it assumes constant stress resultants. Accounting for changes in the stress resultants will be considered in subsection 5.5.2. In general, $\boldsymbol{\Phi}^m$ and $\boldsymbol{\Phi}^b$ are not positive semi-definite. As explained in section 4.3.3, positive semi-definite $\boldsymbol{\Phi}^m$ and $\boldsymbol{\Phi}^b$ are needed to guarantee the convexity of the local approximation. The convexification procedure is described in the next subsection.

5.5.1 LOCAL CONVEX APPROXIMATION

In this subsection, we force convexity of the local approximation (equation 5.45). The approach is demonstrated for the in plane part of the local approximation and the same procedure applies to the out of plane part. The superscript m is also omitted from $\boldsymbol{\Phi}^m$ and $\boldsymbol{\Psi}^m$ for the sake of avoiding confusion from using more than one superscript. The convexification is done by splitting the matrix $\boldsymbol{\Phi}$ into two parts; a positive semi-definite part $\boldsymbol{\Phi}^+$ and a non-definite part $\boldsymbol{\Phi}^-$. Thus:

$$r_s = \boldsymbol{\Phi}^+ : \mathbf{A}^{-1} + \boldsymbol{\Phi}^- : \mathbf{A}^{-1} \tag{5.47}$$

The non-definite part is expanded in a Taylor series in $\mathbf{A}$ around the approximation point, $\mathbf{A}^{(k)}$, to get:

$$r_s = \boldsymbol{\Phi}^+ : \mathbf{A}^{-1} + \boldsymbol{\Psi}^- : \mathbf{A} + 2\,\boldsymbol{\Phi}^- : \mathbf{A}^{(k)^{-1}} \tag{5.48}$$

to maintain the homogeneity of the approximation, we require:

$$\boldsymbol{\Phi}^- : \mathbf{A}^{(k)^{-1}} = 0 \tag{5.49}$$

Introducing the Cholesky decomposition, $\mathbf{A}^{(k)} = \mathbf{L}\,\mathbf{L}^T$, we may write the above condition as:

$$\operatorname{trace}(\hat{\boldsymbol{\Phi}}^-) = 0 \tag{5.50}$$

where $\hat{\boldsymbol{\Phi}}^- = \mathbf{L}^{-1}\boldsymbol{\Phi}^-\mathbf{L}^{-T}$. In general we would like to minimize the non-definite part. This guarantees that if $\boldsymbol{\Phi}$ is positive definite then the non-definite part is zero. Thus we define the splitting uniquely by the condition:

$$\min ||\hat{\boldsymbol{\Phi}}^-||^2 \quad \text{subject to} \quad \operatorname{trace}(\hat{\boldsymbol{\Phi}}^-) = 0 \ \text{ and } \ \operatorname{eigs}(\hat{\boldsymbol{\Phi}} - \hat{\boldsymbol{\Phi}}^-) \geq 0$$

where $\hat{\boldsymbol{\Phi}} = \mathbf{L}^{-1}\boldsymbol{\Phi}\mathbf{L}^{-T}$.

The solution of this optimisation problem is carried out using spectral decomposition as follows. Let $\hat{\boldsymbol{\Phi}} = \mathbf{T}^T \operatorname{diag}(\mathbf{d})\,\mathbf{T}$ where $\mathbf{T}$ is unitary, $\mathbf{d}$ is a vector containing the eigenvalues and diag($\mathbf{d}$) is the square matrix with the diagonal components equal to the $\mathbf{d}$ components. Let us further represent $\hat{\boldsymbol{\Phi}}^-$ as $\hat{\boldsymbol{\Phi}}^- = \mathbf{T}^T \operatorname{diag}(\mathbf{d}^-)\,\mathbf{T}$, then we get:

$$\min \mathbf{d}^{-T}\mathbf{d}^- \quad \text{subject to} \quad \mathbf{1}^T\mathbf{d}^- = 0 \ \text{ and } \ d_i - d_i^- \geq 0$$

where $\mathbf{1}$ is a vector containing all ones. This is a standard quadratic optimisation problem which allows us to find $\mathbf{d}^-$, hence $\hat{\boldsymbol{\Phi}}^-$ and finally $\boldsymbol{\Phi}^-$. The final form of the local approximation is:

$$r_s = \boldsymbol{\Phi}^+ : \mathbf{A}^{-1} + \boldsymbol{\Psi} : \mathbf{A} \tag{5.51}$$

where $\boldsymbol{\Psi} = -\mathbf{A}^{-1}\boldsymbol{\Phi}^-\mathbf{A}^{-1}$. In the following the + superscript is removed without ambiguity since only the convex form in equation 5.51 is used.

5.5.2 HYBRID APPROXIMATION

We derive a hybrid approximation [124] in the form of equation 4.8 for the failure index at each discretisation point (point in a finite difference model or node in a finite element model) as a function of in-plane and out of plane stiffness matrices at the discretisation points, or regions:

$$r_s \approx r_{s0} + \sum_{j=1}^{n} \boldsymbol{\Phi}_j^m : \mathbf{A}_j^{-1} + \boldsymbol{\Phi}_j^b : \mathbf{D}_j^{-1} + \boldsymbol{\Psi}_j^m : \mathbf{A}_j + \boldsymbol{\Psi}_j^b : \mathbf{D}_j \tag{5.52}$$

The reciprocal terms account for the reciprocal parts of local approximation 5.51. The linear terms account for the linear terms of the local approximations, and the sensitivity of stress resultants **N** and **M** to stiffness changes. The sensitivity analysis was carried out using the adjoint method, the details of which are shown in Appendix A.

5.6 VERIFICATION OF STRENGTH FORMULATION

The strength approximation, equation 5.37, developed by IJsselmuiden [6] is used to find the maximum strength design of a single-point laminate. This approximation is verified by plotting and comparing the optimisation convergence path and failure index contours in the lamination parameters space. In a single-point laminate, a single set of strains and stress resultants exist all over the laminate. The case study is performed for three different materials and different in-plane load configurations. The applied load is a combination of axial and shear loads expressed in general form as:

$$\begin{bmatrix} N_x \\ N_y \\ N_{xy} \end{bmatrix} = \begin{bmatrix} 1-w \\ 0 \\ w \end{bmatrix} N_0 \tag{5.53}$$

where $w \in [0,1]$. $w = 0$ represents pure axial tension or compression, depending on the sign of N_0, and $w = 1$ represents pure shear. Load values of $N_0 = \pm 150\ e^6$ N/m are selected for analysis under axial tension and compression. These load values, if applied on a laminate with all unit dimensions, provide a reasonable range for r_s value. Using the stress resultants in equation 5.53, the strains are obtained analytically from the laminate constitutive relations based on CLT in equation 2.71. The selected laminate is balanced symmetric and the the load case is in-plane, therefore, only two in-plane lamination parameters, V_{1A} and V_{3A}, are used as the design variables

In this chapter, the conservative Tsai-Wu failure envelopes were reformulated in an elliptical form in terms of principal strains. Also, the convex separable approximation of the failure index in terms of laminate stiffness was formulated. This approximation is well suited to be used in the multi-step optimisation framework for optimum design of constant stiffness (CS) and variable stiffness (VS) laminates as shown in [134]. Using the failure envelopes reformulated in this chapter for evaluation of r_s values of the single-point laminates with optimum lamination parameters obtained by IJsselmuiden [6] results in exactly the same r_s values as reported by IJsselmuiden [6]. For further verification, the single-point laminates, made of the same materials and under the same load cases as the ones applied in [6], were deigned in the first step of the multi-step optimisation framework developed in chapter 4 and using the new strength formulation and approximation developed in this chapter. Since the load distribution is unchanged in a single-point laminate, only the local part of the approximation in equation 5.52 was used.

Tables 5.2 and 5.3 show the optimum lamination parameters and r_s values of various materials, which are obtained using the strength formulation presented in this chapter, under combined tension/shear and compression/shear load cases with $w = 0.5$ and a range of combined tension/shear load cases with $w = 0.0, 0.2, \ldots, 1.0$, respectively. The percentage of differences between the obtained values in these tables with those obtained by IJsselmuiden [6] are calculated and depicted in parentheses in front of each value. Although the optimum lamination parameters in these tables have up to 4.3% difference with those obtained by IJsselmuiden [6], this difference is not visible in the r_s values. The r_s values are all identical with those found by IJsselmuiden [6] and only the r_s value for Carbon-PEEK (AS4) and $w = 0.8$ is 0.2% larger than the corresponding value from [6] which is negligible. This 0.2% difference could be partly due to different optimisation formulations and partly due to rounding errors.

TABLE 5.2: Optimum lamination parameters and r_s values and the percentage difference with those reported in [6] for various materials and combined loading with $w = 0.5$

Load case	Materials	V_{1A}	V_{3A}	r_s
Tension/Shear	AS4	0.444 (0.0%)	-0.352 (-0.3%)	0.394 (0.0%)
	IM6	0.558 (0.0%)	-0.293 (0.0%)	0.339 (0.0%)
	B5.6	0.599 (-0.3%)	-0.250 (0.8%)	0.510 (0.0%)
Compression/Shear	AS4	0.152 (-1.9%)	-0.357 (0.0%)	0.353 (0.0%)
	IM6	0.024 (4.3%)	-0.322 (0.0%)	0.279 (0.0%)
	B5.6	-0.066 (-1.2%)	-0.266 (0.0%)	0.412 (0.0%)

TABLE 5.3: Optimum lamination parameters and r_s values and the percentage difference with those reported in [6] for various materials and a range of tension/shear load cases $w = 0.0, 0.2, ..., 1.0$

Materials	w	V_{1A}	V_{3A}	r_s
AS4	0.0	1.0000 (0.0%)	1.0000 (0.0%)	0.1964 (0.0%)
	0.2	0.6926 (0.1%)	0.3055 (0.3%)	0.3072 (0.0%)
	0.4	0.5116 (0.0%)	-0.1632 (0.0%)	0.3718 (0.0%)
	0.6	0.3824 (0.3%)	-0.5306 (-0.2%)	0.4106 (0.0%)
	0.8	0.2322 (-3.7%)	-0.8565 (-3.1%)	0.4268 (0.2%)
	1.0	0.0000 (0.0%)	-1.0000 (0.0%)	0.4550 (0.0%)
IM6	0.0	0.9860 (0.1%)	0.9495 (1%)	0.2052 (0.0%)
	0.2	0.7961 (0.0%)	0.3237 (0.0%)	0.2722 (0.0%)
	0.4	0.6270 (0.2%)	-0.1126 (-0.9%)	0.3215 (0.0%)
	0.6	0.4930 (-0.2%)	-0.4635 (0.2%)	0.3511 (0.0%)
	0.8	0.3090 (0.7%)	-0.8090 (-0.2%)	0.3637 (0.0%)
	1.0	0.0000 (0.0%)	-1.0000 (0.0%)	0.3816 (0.0%)
B5.6	0.0	1.0000 (0.0%)	1.0000 (0.0%)	0.2847 (0.0%)
	0.2	0.7933 (-0.1%)	0.2612 (0.0%)	0.4118 (0.0%)
	0.4	0.6682 (-0.3%)	-0.0932 (1%)	0.4846 (0.0%)
	0.6	0.5337 (-0.2%)	-0.3979 (0.3%)	0.5291 (0.0%)
	0.8	0.3692 (-3.7%)	-0.7117 (-0.7%)	0.5464 (0.0%)
	1.0	0.0000 (0.0%)	-1.0000 (0.0%)	0.5435 (0.0%)

6

OPTIMISATION RESULTS FOR UNSTIFFENED CYLINDERS

6.1 INTRODUCTION

In this chapter, circumferential laminate stiffness tailoring of two cylindrical shells, namely a circular cylinder under bending and an elliptical cylinder under axial compression, is performed for maximum buckling capacity. In the circular cylinder under bending and the elliptical cylinder under axial compression, the axial section force and the shell curvature vary around the circumference, respectively. If the maximum buckling capacity designs are material failure critical, meaning that material failure happens before buckling, strength is used as another design driver in addition to the buckling capacity to make sure that material failure does not happen before buckling.

In the developed framework for circumferential stiffness tailoring of general cross-section cylinders, the semi-analytical solutions for static and buckling analysis of cylindrical shells with arbitrary cross-sections, developed in chapter 3, are used to evaluate the strains and buckling capacity. The strength is measured using the conservative Tsai-Wu failure envelope in the strain space developed by IJsselmuiden et al. [121] which was further reformulated in chapter 5. The conservative convex separable approximations of the buckling factor and failure index are built as described in chapters 4 and 5, respectively. These approximations are used in the multi-step optimisation framework, described in chapter 4, to find the opti-

Parts of this chapter have been published in Composite Structures **94** (2012) 2851-2860 [102].

mum constant stiffness, CS, and circumferentially variable stiffness, VS, laminate designs.

Two types of VS laminates are obtained; constant thickness VS laminates and variable thickness VS laminates. In the constant thickness VS laminates, the laminate stiffness variation is only due to the fibre steering, however, in variable thickness VS laminates, the circumferential laminate stiffness tailoring is due to fibre steering and laminate thickness variation.

Theoretical and realistic CS and constant thickness VS laminate designs are obtained and compared to investigate the effect of fibre steering on the buckling capacity. However, only the theoretical variable thickness VS laminate designs are obtained, due to the current limitation of the second step of the multi-step optimisation framework to constant thickness laminates. The theoretical variable thickness VS laminate designs are compared with the theoretical constant thickness VS laminate designs to investigate the effect of laminate thickness variation on buckling capacity improvement. The stiffness and load redistribution mechanisms due to circumferential laminate stiffness tailoring, which are responsible for structural performance improvement, are discussed for constant and variable thickness laminates. The laminate designs for the circular cylinder under bending and elliptical cylinder under axial compression are discussed in sections 6.2 and 6.3.

6.2 CIRCULAR CYLINDER UNDER BENDING

Circumferential laminate stiffness tailoring of a cylindrical shell with a circular cross-section under bending is investigated by Blom et al. [17] using the functional fibre path definition (section 1.4) to model the stiffness variation. In this section, circumferential stiffness tailoring of the same circular cylinder is performed using the developed framework for circumferential tailoring of general cross-section cylinders. The circular cylinder has a diameter of 609.6 mm (24 in) and a length of 812.8 mm (32 in). The laminate thickness is 4.39 mm (0.1728 in) including 24 layers made of $AS4/8773$ material, the properties of which are given in table 6.1.

The theoretical CS and constant thickness VS laminate designs of the circular cylinder under bending, for maximum buckling moment with consideration of strength constraints, are investigated in subsection 6.2.1. The theoretical variable thickness laminate designs with the same weight as the constant thickness laminates are studied in subsection 6.2.2. The realistic CS and constant thickness VS laminate designs are retrieved from the selected theoretical CS and constant thickness VS laminate designs in subsection 6.2.3.

TABLE 6.1: Material properties of AS4/8773 [17]

Longitudinal modulus, E_1 [GPa / psi]	129.83 / 18.830e6
Transverse modulus, E_2 [GPa / psi]	9.08 / 1.317e6
Shear modulus, G_{12} [GPa / psi]	5.29 / 7.672e5
Poisson's ratio, ν_{12} [-]	0.32
Longitudinal tensile strength, X_t [MPa / psi]	2067.74 / 2.999e5
Longitudinal compressive strength, X_c [MPa / psi]	1158.32 / 1.680e5
Transverse tensile strength, Y_t [MPa / psi]	132.72 / 1.925e4
Transverse compressive strength, Y_c [MPa / psi]	199.81 / 2.898e4
Shear strength, S [MPa / psi]	116.38 / 1.688e4

6.2.1 THEORETICAL CONSTANT THICKNESS LAMINATE

The primary goal of circumferential stiffness tailoring of the circular cylinder under bending, is to maximise the buckling moment. In subsection 4.3.3, the convex separable approximation is built for the inverse of buckling factor instead of the buckling factor. Therefore, the buckling moment maximisation problem is substituted by minimisation of the critical inverse of buckling factor. This multi-modal or min-max optimisation problem is expressed as:

$$\min_{\mathbf{V}} \max(r_{b_k}) \tag{6.1}$$

where r_{b_k} (for $k = 1, 2, ..., q$) is the value of inverse of buckling factor for mode number k and $\mathbf{V}$ is the vector of lamination parameters at all discretisation points. This min-max problem is reformulated using the bound formulation and dual method, as described in subsection 4.4.2, and the corresponding global optimisation, equation 4.24, and local optimisation, equation 4.34, problems are solved in a successive approximation scheme to find the theoretical constant thickness laminate design.

If the maximum buckling moment design is material failure critical, the maximised buckling moment cannot be reached because the material failure happens before buckling. Therefore, consideration of strength as another design driver in the optimisation problem is essential to find a buckling critical design. One way of consideration of strength as a design driver, is to add a constraint on the failure index to the minimisation problem of inverse of buckling factor in equation 6.1. This constrained multi-modal optimisation problem is formulated as:

$$\min_{\mathbf{V}} \max(r_{b_k}) \quad \text{subject to} \quad r_{s_j} \leq d \tag{6.2}$$

where r_{s_j} (for $j = 1, 2, ..., n$) is the failure index of the jth discretisation point and d is the maximum allowable value of the failure index. This is a multi-modal constrained optimisation problem, equation 4.35, with a non-zero right-hand side constraint and the corresponding global and local optimisation problems for finding the theoretical constant thickness laminate design are formulated similar to equations 4.37 and 4.38. By changing the value of d, strength constraints can be relaxed or restrained and different designs can be obtained. The ratio of the buckling moment to the failure moment of a design, which is defined as the safety factor, can be only calculated after optimisation. The appropriate buckling critical design can be selected from the Pareto front showing the buckling moment versus the material failure moment of different designs.

The maximum strength design is chosen as the initial point of the Pareto front and the corresponding optimisation problem, which is a min-max problem, is formulated as:

$$\min_{\mathbf{V}} \max(r_{s_j}) \tag{6.3}$$

The second point on the Pareto front is found by solving the optimisation problem in equation 6.2, initialised from the maximum strength design, and with d slightly greater than the maximum failure index in the maximum strength design. Other points on the Pareto front are found by solving the constrained optimisation problem in equation 6.2, initialised from the previous point on the Pareto front, and by relaxing the constraint on the failure index, d, step by step. Using this strategy, the constrained optimisation problem in equation 6.2 is always started from a feasible design and the points on the Pareto front are found until the improvement in the buckling moment between two consecutive points is less than a certain value. In order to check if any further improvement in the buckling moment is possible, the end point on the Pareto front is the maximum buckling moment design obtained from solving equation 6.1.

Each theoretical constant thickness laminate design on the Pareto front is found by solving the global and local optimisation problems in the first step of the multi-step optimisation problem using the successive approximation strategy described in subsection 4.4. In the first step of the multi-step optimisation framework, only two in-plane lamination parameters, V_{1A} and V_{3A}, and two out of plane lamination parameters, V_{1D} and V_{3D}, are used as design variables to find the theoretical balanced symmetric laminate designs. The multi-modality of the buckling moment maximisation of the considered circular cylinder under bending is 60 buckling modes. The critical conservative Tsai-Wu failure envelope for the material properties listed in table 6.1 is the fourth order envelope (see section 5.2), which can be expressed as two intersecting elliptical envelopes (see section 5.3) resulting in two failure indices at each discretisation point in the cross-section. In addition, in the bending problems, two failure indices are considered for each discretisation point in the cross-section; one for the top and one for the bottom surface (section 5.4).

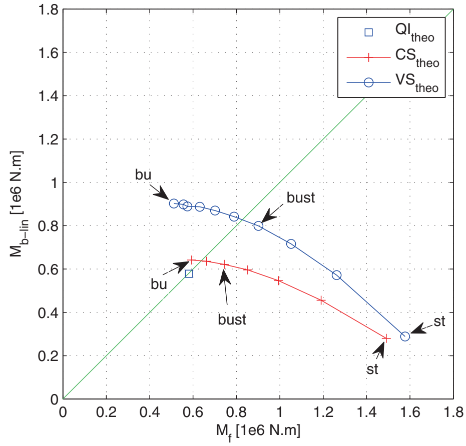

FIGURE 6.1: Pareto fronts of buckling moment versus failure moment for theoretical constant stiffness and variable stiffness constant thickness laminate designs of the circular cylinder under bending, *Note:* M_{b-lin} *= linear buckling moment from the semi-analytical finite difference (SAFD),* M_f *= failure moment from SAFD and conservative Tsai-Wu failure envelope,* QI_{theo} *= theoretical quasi-isotropic laminate,* CS_{theo} *= theoretical constant stiffness laminates,* VS_{theo} *= theoretical variable stiffness laminates, bu = maximum buckling capacity design,* $bust$ *= selected design for maximum buckling capacity with strength constraints, and* st *= maximum strength design*

6

Therefore, four failure indices exist at each discretisation point in the cross-section of the considered circular cylinder. The large number of strength constraints in equation 6.2 is handled in a constraint screening strategy which considers only a small set of constraints, within the 5% most critical constraints, and updates this set in each design iteration of the successive approximation strategy.

The Pareto fronts showing the buckling moment versus the failure moment of theoretical CS and VS designs for the circular cylinder under bending are plotted in figure 6.1. To construct the Pareto front in figure 6.1, the failure moment of the maximum strength design is chosen as the design moment and the value of d is increased in steps of 0.25, starting from $d = 1.25$. At $d = 1$, the failure index is constrained to be equal or less than the failure index of the maximum strength design and hence the design for $d = 1$ is the maximum strength design.

As it is clear from figure 6.1, theoretical CS and VS laminate designs for maximum buckling moment, $CS - bu_{theo}$ and $VS - bu_{theo}$, for the considered circular cylinder under bending are placed above the diagonal line and hence are material failure critical. Among the buckling critical designs on each Pareto front, which

TABLE 6.2: Linear and non-linear buckling moments and failure moments of theoretical quasi-isotropic, QI_{theo}, selected theoretical constant stiffness, $CS-bust_{theo}$, and selected theoretical variable stiffness constant thickness, $VS-bust_{theo}$, laminate designs for maximum buckling moment with strength constraints in the circular cylinder under bending, *Note:* M_{b-lin} = *linear buckling moment from the semi-analytical finite difference (SAFD) and Abaqus*^{TM}, $M_{b-nonlin}$ = *nonlinear buckling moment from Abaqus*^{TM}, M_f = *failure moment from SAFD and conservative Tsai-Wu failure envelope and* Imp = *improvements of* $VS-bust_{theo}$ *over* $CS-bust_{theo}$ *calculated as* $(M(VS)-M(CS))/M(CS)$

Design	QI_{theo}	$CS-bust_{theo}$	$VS-bust_{theo}$	Imp(%)
M_{b-lin} (SAFD) [kN.m]	601	622	799	28.5
M_{b-lin} (Abaqus^{TM}) [kN.m]	592	630	808	28.2
$M_{b-nonlin}$ (Abaqus^{TM}) [kN.m]	565	584	749	28.3
M_f (SAFD) [kN.m]	581	744	902	21.1

are placed below the diagonal line, the maximum buckling moment design with an acceptable safety factor is selected for retrieving the realistic design. The selected theoretical designs, $CS-bust_{theo}$ and $VS-bust_{theo}$, have safety factors of 1.19 and 1.12 based on the semi-analytical finite difference (SAFD) results which correspond to $d = 2$ and $d = 1.75$, respectively.

6

The buckling and failure moments of the theoretical quasi-isotropic, QI_{theo}, selected theoretical CS, $CS-bust_{theo}$, and selected theoretical VS, $VS-bust_{theo}$, laminate designs and the improvements of $VS-bust_{theo}$ over $CS-bust_{theo}$ design, Imp, are shown in table 6.2. The linear buckling moments from the SAFD are compared with the linear and nonlinear buckling moments computed from the commercial finite element code Abaqus^{TM} using clamped boundary conditions similar to Blom et al. [17]. The linear buckling moments from SAFD are in good agreement with those obtained from Abaqus^{TM} with less than 2% difference. The amount of improvement in the linear buckling moment of the $VS-bust_{theo}$ over the $CS-bust_{theo}$ laminate design is 28.2% based on the Abaqus^{TM} results.

To obtain the nonlinear buckling moment, first a nonlinear static analysis is performed on the cylindrical shell under a bending moment which is less than but close to the linear buckling moment. Then a linear buckling analysis is performed on the deformed shape of the cylindrical shell which is obtained from the nonlinear static analysis. Nonlinear buckling moment is the sum of the static bending moment and the linear buckling moment. The nonlinear buckling moments are maximum 8% lower than the linear buckling moments from Abaqus^{TM}. This can be interpreted as no significant loss of stiffness happens in the prebuckling regime. Based on the Abaqus^{TM} results, the amount of improvement in the nonlinear buckling moment of the $VS-bust_{theo}$ over the $CS-bust_{theo}$ laminate design is 28.3% which is very similar to the improvement in the linear buckling moment.

The lamination parameters for three theoretical CS laminate designs, the maximum strength design, $CS - st_{theo}$, the selected maximum buckling moment design with strength constraints, $CS - bust_{theo}$, and the maximum buckling moment design, $CS - bu_{theo}$, are:

$$CS - st_{theo} : [V_{1A}, V_{3A}, V_{1D}, V_{3D}] = [0.94, 1.00, 0.84, 1.00]$$
$$CS - bust_{theo} : [V_{1A}, V_{3A}, V_{1D}, V_{3D}] = [0.14, 0.23, 0.34, -0.48]$$
$$CS - bu_{theo} : [V_{1A}, V_{3A}, V_{1D}, V_{3D}] = [-0.04, 0.10, 0.24, -0.51]$$

The lamination parameter distributions for three theoretical VS laminate designs; the maximum strength design, $VS - st_{theo}$, the selected maximum buckling moment design with strength constraints, $VS - bust_{theo}$, and the maximum buckling moment design, $VS - bu_{theo}$, are shown in figure 6.2.

Improvement mechanisms

The mechanisms of buckling moment improvement due to circumferential stiffness tailoring, are investigated by inspecting the axial strain and sectional force distributions around the circumference and the critical buckling mode shapes of theoretical laminate designs, QI_{theo}, $CS - bust_{theo}$ and $VS - bust_{theo}$ of the circular cylinder under bending. The axial strain and sectional force distributions at the cross-section, which is placed in the middle of two end cross-sections, are obtained from Abaqus^{TM} and plotted in figure 6.3 versus the normalised distance in the circumferential direction from the point with the maximum axial tension.

As it is clear from figure 6.3(a), the axial strain distribution of all the three theoretical laminate designs has a sinusoidal pattern since the two end cross-sections of the cylinder remain planar. In the QI_{theo} and $CS - bust_{theo}$ laminate designs, zero axial strains happen at 0.25 and 0.75 of the normalised circumferential distance while this is not the case for the $VS - bust_{theo}$ laminate design. In other words, the neutral axis in the cross-section of the QI_{theo} and $CS - bust_{theo}$ laminate designs is coincident with the diameter of the circular cross-section about which the bending moment is applied, while the neutral axis in the cross-section of the $VS - bust_{theo}$ laminate design is shifted toward the tension side.

As depicted in figure 6.3(b), due to uniform stiffness distribution of the QI_{theo} and $CS - bust_{theo}$ designs, the axial section force distribution is sinusoidal and zero axial section forces happen at 0.25 and 0.75 of the normalised circumferential distance. The axial section force distribution is the same for the QI_{theo} and $CS - bust_{theo}$ designs, while as shown in figure 6.3(a), the magnitudes of the maximum axial compressive and tensile strains for $CS - bust_{theo}$ design are less than those for the QI_{theo} design. Therefore, the $CS - bust_{theo}$ design is stiffer than QI_{theo} in the axial direction. The buckling moment improvement of the $CS - bust_{theo}$ laminate

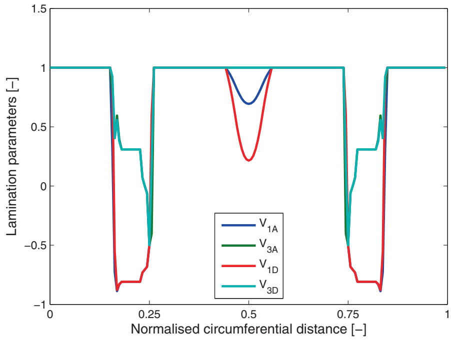

(a) $VS - st_{theo}$

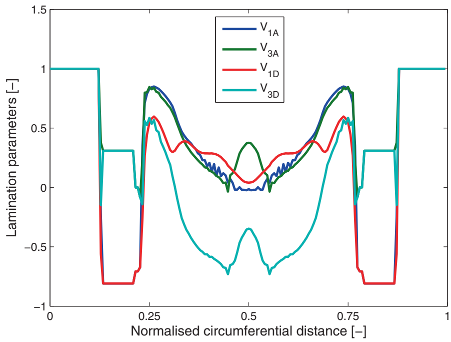

(b) $VS - bust_{theo}$

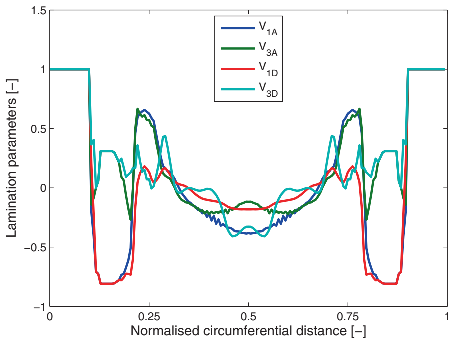

(c) $VS - bu_{theo}$

FIGURE 6.2: Distribution of lamination parameters in theoretical variable stiffness constant thickness laminate for the maximum strength design, $VS - st_{theo}$, the selected design for maximum buckling moment with strength constraints, $VS - bust_{theo}$, and the maximum buckling moment design, $VS - bu_{theo}$, of the circular cylinder under bending, *Note: circumferential distance starts from the point with the maximum axial tension*

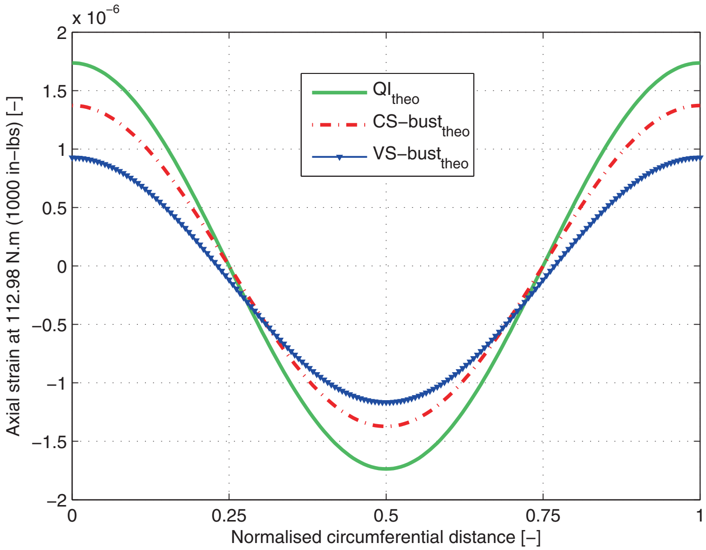

(a) Axial strain

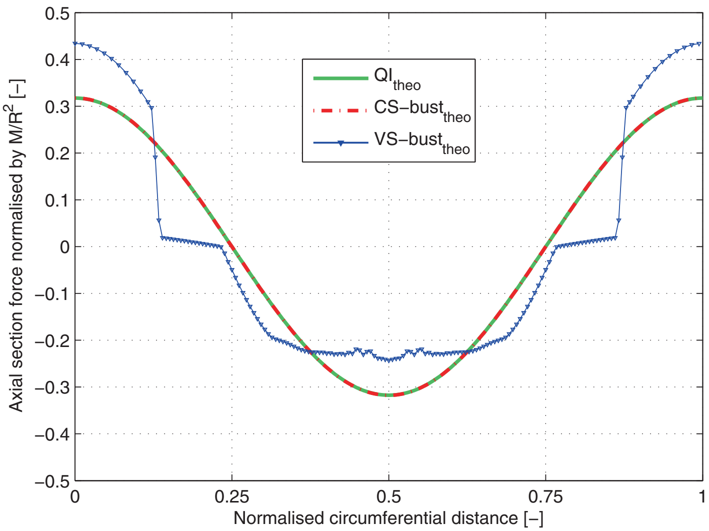

(b) Axial section force

FIGURE 6.3: Axial strain and axial section force of theoretical quasi-isotropic, QI_{theo}, selected theoretical constant stiffness, $CS-bust_{theo}$, and selected theoretical variable stiffness constant thickness, $VS-bust_{theo}$, laminate designs for maximum buckling moment with strength constraints in the circular cylinder under bending based on Abaqus^{TM} results, *Note: circumferential distance starts from the point with the maximum axial tension*

6

design with respect to the QI_{theo} laminate design is merely due to the change of laminate stiffness.

The axial section force of the $VS-bust_{theo}$ laminate design is calculated at the same bending moment as the $CS-bust_{theo}$ laminate designs. The axial section force distribution of the $VS-bust_{theo}$ laminate design is not sinusoidal and is almost uniform on the compression side. The magnitude of maximum axial compressive section force for the $VS-bust_{theo}$ laminate design is less than the $CS-bust_{theo}$ laminate designs, while the maximum axial tensile section force for the $VS-bust_{theo}$ laminate design is larger than the $CS-bust_{theo}$ laminate designs. Therefore, the buckling moment of the $VS-bust_{theo}$ laminate design is improved with respect to the $CS-bust_{theo}$ laminate design due to the lower magnitude of the maximum axial compressive section force in the $VS-bust_{theo}$ laminate design. This load redistribution mechanism, which increases the buckling moment, is due to the circumferential stiffness tailoring that reduces the local stiffness in the compression side of the cross-section and stiffens the tension side in the axial direction. Therefore, the axial section load is released in the compression side and transferred to the tension side.

Although the buckling modes are very close, numerically critical linear buckling mode shapes for the QI_{theo}, $CS-bust_{theo}$ and $VS-bust_{theo}$ laminate designs of the circular cylinder are shown in figure 6.4. In the $CS-bust_{theo}$ and especially $VS-bust_{theo}$ laminate designs, the buckling modes expand to a larger area in the compression side of the cross-section, which means that the material is used more efficiently.

6

6.2.2 THEORETICAL VARIABLE THICKNESS LAMINATE

The buckling moment maximisation problem for finding the theoretical variable thickness VS laminate design is formulated as:

$$\begin{aligned} &\min_{\mathbf{V},\mathbf{H}} \max(r_{b_k}) \\ &\text{subject to} \\ &\frac{1}{n}\sum_{j=1}^{n} H_j \leq H_{CT} \quad \text{and} \quad H_{min} \leq H_j \leq H_{max} \end{aligned} \tag{6.4}$$

This problem is formulated similar to the buckling moment maximisation problem for finding the theoretical constant thickness laminate design, equation 6.1, with an additional design variable and two additional constraints. The additional design variable, **H**, is the vector of laminate thickness at the discretisation points. The additional constraints restrain the average laminate thickness, and hence the weight, of the variable thickness laminate to be equal or less than the laminate

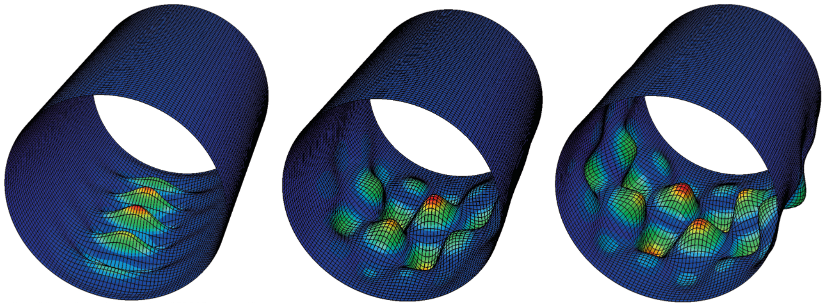

(a) QI_{theo} (b) $CS - bust_{theo}$ (c) $VS - bust_{theo}$

FIGURE 6.4: Critical buckling modes of theoretical quasi-isotropic, QI_{theo}, selected theoretical constant stiffness, $CS - bust_{theo}$, and selected theoretical variable stiffness constant thickness, $VS - bust_{theo}$, laminate designs for maximum buckling moment with strength constraints in the circular cylinder under bending from Abaqus^{TM}

thickness of the constant thickness laminate, H_{CT}, and set the lower and upper bounds of the varying laminate thickness to H_{min} and H_{max}, respectively. The optimisation problems for maximum buckling moment with strength constraints and maximum strength of variable thickness laminate designs are formulated similar to equations 6.2 and 6.3 for constant thickness laminate designs and by adding the constraints on the laminate thickness in equation 6.4.

The theoretical variable thickness laminate designs are obtained by solving the formulated global and local optimisation problems, as described in subsection 4.4.2, in the first step of the multi-step optimisation framework. Similar to the constant thickness VS laminate, the variable thickness VS laminate are balanced symmetric since only four lamination parameters are considered as the design variable in the first step of the multi-step optimisation framework. Multi-modality of the buckling moment maximisation problem is 60 and the constraint screening strategy is used for solving the buckling moment maximisation problem with strength constraints. The circular cylinder with the baseline constant thickness VS laminate has 24 layers and the circular cylinder with the variable thickness VS laminate is obtained for two cases; in the first case the laminate thickness is bounded between 16 and 32 layers and in the second case is bounded between 20 and 28 layers.

Pareto fronts showing the buckling moment versus failure moment of the theoretical variable thickness VS laminates are obtained using the same strategy described in subsection 6.2.1 for constant thickness laminates. These Pareto fronts

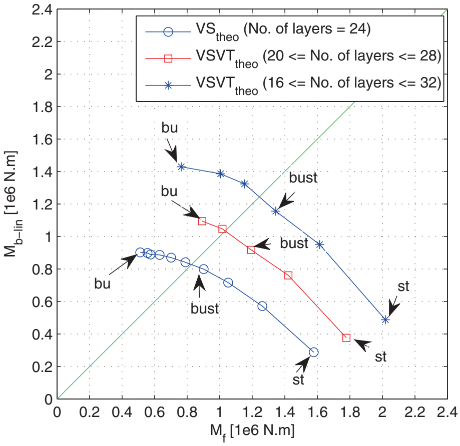

FIGURE 6.5: Pareto fronts of buckling moment versus failure moment for theoretical variable stiffness constant thickness and variable stiffness variable thickness laminate designs of the circular cylinder under bending, *Note:* M_{b-lin} *= linear buckling moment from the semi-analytical finite difference (SAFD) and* M_f *= failure moment from SAFD and conservative Tsai-Wu failure envelope,* VS_{theo} *= theoretical variable stiffness constant thickness laminates,* $VSVT_{theo}$ *= theoretical variable stiffness variable thickness laminates, bu = maximum buckling capacity design,* $bust$ *= selected design for maximum buckling capacity with strength constraints,* st *= maximum strength design*

6

are shown in figure 6.5 and compared with the Pareto fronts of the theoretical constant thickness VS laminates.

As it is clear from figure 6.5, the theoretical variable thickness VS laminate designs for maximum buckling moment, $VSVT-bu_{theo}$, are above the diagonal line and material failure critical. Among the buckling critical theoretical variable thickness VS laminate designs, which are placed below the diagonal line, the designs with the maximum buckling moments are selected. The selected theoretical variable thickness VS designs, $VSVT-bust_{theo}$, with 16 to 32 layers and 20 to 28 layers have safety factors of 1.08 and 1.20, respectively, and both correspond to $d = 1.5$ when the bending moment of the maximum strength design is selected as the design moment.

In tables 6.3 and 6.4, the linear buckling and failure moments of the $VSVT-bust_{theo}$ designs are listed and compared with those of the $VS-bust_{theo}$ designs and the amount of improvements are shown. The linear buckling moments from the SAFD solution and Abaqus^{TM} are in good agreement with less than 2% difference. The amounts of improvement in the linear buckling moments of the $VSVT-$

TABLE 6.3: Linear and non-linear buckling moments and failure moment of the selected variable stiffness constant thickness, $VS-bust_{theo}$, and the selected variable thickness $(20 \le \text{No. of layers} \le 28)$ variable stiffness, $VSVT-bust_{theo}$, laminate designs for maximum buckling moment with strength constraints in the circular cylinder under bending, *Note:* M_{b-lin} *= linear buckling moment from the semi-analytical finite difference (SAFD) and Abaqus*^{TM}, $M_{b-nonlin}$ *= nonlinear buckling moment from Abaqus*^{TM}, M_f *= failure moment from SAFD and conservative Tsai-Wu failure envelope and* Imp *= improvements of* $VSVT-bust_{theo}$ *over* $VS-bust_{theo}$ *calculated as* $(M(VSVT)-M(VS))/M(VS)$

Design	$VS-bust_{theo}$	$VSVT-bust_{theo}$	Imp(%)
M_{b-lin} (SAFD) [kN.m]	799	918	14.8
M_{b-lin} (Abaqus^{TM}) [kN.m]	808	934	15.5
$M_{b-nonlin}$ (Abaqus^{TM}) [kN.m]	749	881	17.7
M_f (SAFD) [kN.m]	902	1193	30

TABLE 6.4: Linear and non-linear buckling moments and failure moment of the selected variable stiffness constant thickness, $VS-bust_{theo}$, and the selected variable thickness $(16 \le \text{No. of layers} \le 32)$ variable stiffness, $VSVT-bust_{theo}$, laminate designs for maximum buckling moment with strength constraints in the circular cylinder under bending, *Note:* M_{b-lin} *= linear buckling moment from the semi-analytical finite difference (SAFD) and Abaqus*^{TM}, $M_{b-nonlin}$ *= nonlinear buckling moment from Abaqus*^{TM}, M_f *= failure moment from SAFD and conservative Tsai-Wu failure envelope and* Imp *= improvements of* $VSVT-bust_{theo}$ *over* $VS-bust_{theo}$ *calculated as* $(M(VSVT)-M(VS))/M(VS)$

Design	$VS-bust_{theo}$	$VSVT-bust_{theo}$	Imp(%)
M_{b-lin} (SAFD) [kN.m]	799	1156	44.7
M_{b-lin} (Abaqus^{TM}) [kN.m]	808	1176	45.4
$M_{b-nonlin}$ (Abaqus^{TM}) [kN.m]	749	1097	46.5
M_f (SAFD) [kN.m]	902	1344	49.1

$bust_{theo}$ laminates with 20 to 28 layers and 16 to 32 layers over the $VS-bust_{theo}$ laminate are 15.5% and 45.4%, respectively, based on the Abaqus^{TM} results. The nonlinear buckling moments are dropped up to 9% with respect to the linear buckling moments, which shows that the stiffness is not decreased significantly before the buckling. The amounts of improvement in the nonlinear buckling moments of the $VSVT-bust_{theo}$ laminates with 20 to 28 layers and 16 to 32 layers over the $VS-bust_{theo}$ laminate are 17.7% and 46.5%, respectively, based on the Abaqus^{TM} results.

The distributions of lamination parameters and laminate thickness in the theoretical variable thickness VS laminate designs for the maximum strength design, $VSVT-st_{theo}$, selected design, $VSVT-bust_{theo}$, and the maximum buckling, $VSVT-bu_{theo}$, designs of the circular cylinders, with laminate thickness bounded

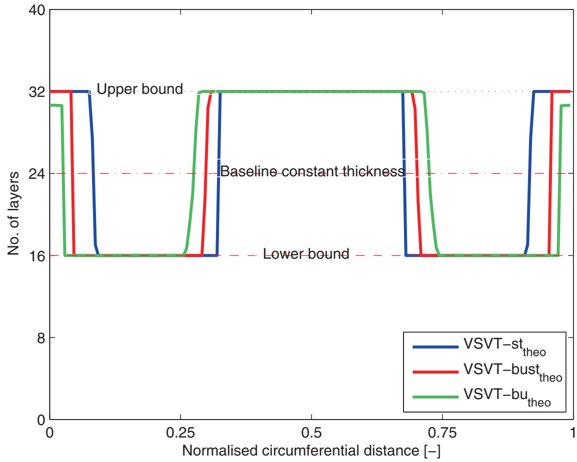

FIGURE 6.6: Distribution of laminate thickness in theoretical variable thickness (16 ≤ No. of layers ≤ 32) variable stiffness laminate designs for maximum strength, $VSVT-st_{theo}$, for maximum buckling moment with strength constraints, $VSVT-bust_{theo}$, and for maximum buckling moment, $VSVT-bu_{theo}$, of the circular cylinder under bending

between 16 and 32 layers, are shown in figures 6.7 and 6.6. The laminate thickness distribution in figure 6.6 is such that the maximum laminate thickness is assigned to the cross-sectional areas with the maximum compression and tension and other areas in the cross-section have the minimum laminate thickness. The area with the maximum laminate thickness in the compression side is larger than this area in the tension side. The distributions of lamination parameters of the variable thickness VS laminates in figures 6.7 show similarities to the distributions of lamination parameters of the constant thickness VS laminates in figure 6.2.

Improvement mechanisms

The distribution of axial strain and sectional force around the circumference of the $VSVT-bust_{theo}$ laminates are plotted in figures 6.8 and compared with those of the $VS-bust_{theo}$ laminates to investigate the effect of laminate thickness variation. The distributions are based on the Abaqus^{TM} results and plotted versus the normalised circumferential distance from the point with the maximum axial tension in the cross-section of the circular cylinder.

The axial strain distributions of the theoretical VS designs are sinusoidal as depicted in figure 6.8(a). The neutral axis of the $VSVT-bust_{theo}$ laminate with 20

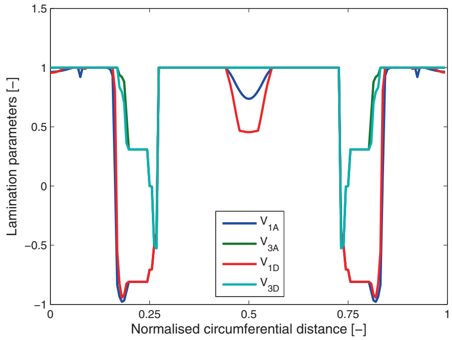

(a) $VSVT-st_{theo}$

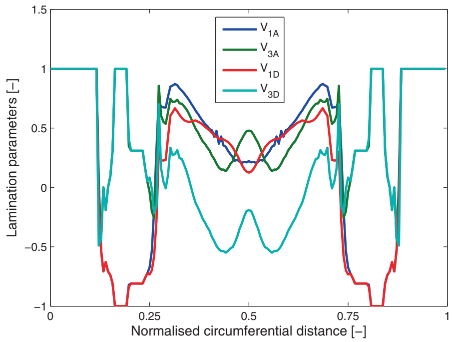

(b) $VSVT-bust_{theo}$

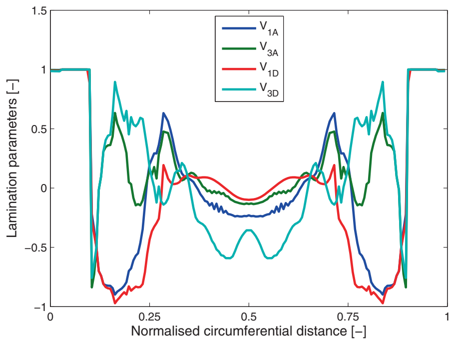

(c) $VSVT-bu_{theo}$

FIGURE 6.7: Distribution of lamination parameters in theoretical variable thickness (16 $\leq$ No. of layers $\leq$ 32) variable stiffness laminate designs for the maximum strength, $VSVT-st_{theo}$, for maximum buckling moment with strength constraints, $VSVT-bust_{theo}$, and for maximum buckling moment, $VSVT-bu_{theo}$, of the circular cylinder under bending

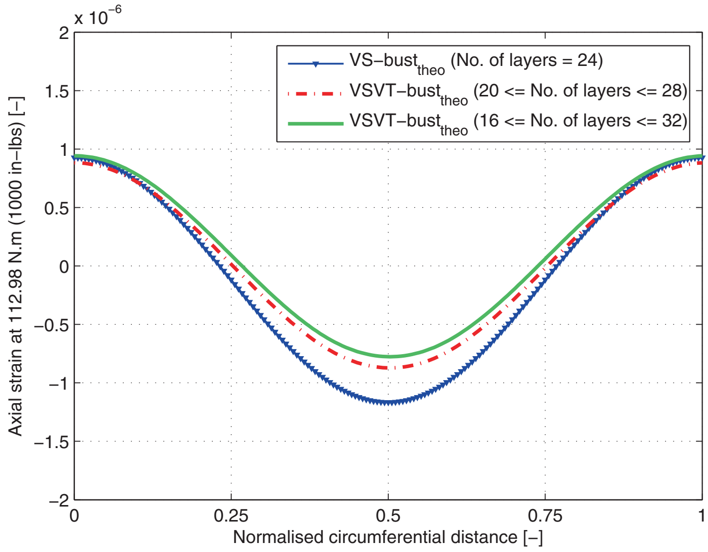

(a) Axial strain

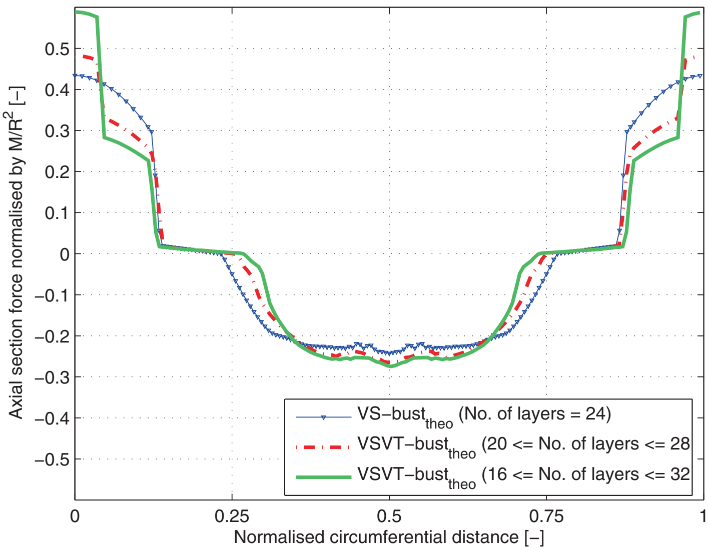

(b) Axial section force

FIGURE 6.8: Axial strain and axial section force of theoretical variable stiffness constant thickness, $VS-bust_{theo}$, and theoretical variable stiffness variable thickness, $VSVT-bust_{theo}$, laminate designs for maximum buckling moment with strength constraints in the circular cylinder under bending based on Abaqus^{TM} results, *Note: circumferential distance starts from the point with the maximum axial tension*

to 28 layers is coincident with the diameter of the cross-section about which the bending moment is applied, however, the neutral axis in the cross-section of the $VS-bust_{theo}$ and $VSVT-bust_{theo}$ laminate design with 16 to 32 layers is shifted towards the tension and compression sides, respectively.

Figure 6.8(b) shows that the distributions of the axial section force in the $VSVT-bust_{theo}$ laminate designs have almost the same pattern as the $VS-bust_{theo}$ laminate design. However, the magnitudes of the maximum axial section forces in the tension and compression sides of the $VSVT-bust_{theo}$ laminates are larger and slightly larger than the $VS-bust_{theo}$ laminate, respectively. These differences happen in the cross-sectional areas with the maximum laminate thickness and are larger for the $VSVT-bust_{theo}$ laminate with 16 to 32 layers than the $VSVT-bust_{theo}$ laminate with 20 to 28.

The in-plane and out of plane stiffness matrices are proportional to the first and third power of the laminate thickness. Although the in-plane stiffness matrix is increased by increasing the laminate thickness in the compression side, the axial section load is not considerably changed since the magnitude of the maximum axial strain in the compression side is reduced in the $VSVT-bust_{theo}$ laminates. However, the out of plane stiffness in the buckling critical areas is increased with the third power of the laminate thickness and hence the buckling moment is increased. Since the maximum axial strain in the tension side is almost the same in the $VS-bust_{theo}$ and $VSVT-bust_{theo}$ laminates, the axial section load in the tension side is increased in the areas with the maximum thickness laminate in $VSVT-bust_{theo}$. The numerically critical buckling modes of the $VSVT-bust_{theo}$ laminates are shown in figure 6.9.

6.2.3 REALISTIC CONSTANT THICKNESS LAMINATE

The realistic CS and constant thickness VS laminate designs include the stacking sequence of the straight and steered fibre laminates, respectively, which are retrieved from the selected theoretical CS and constant thickness VS laminate designs in the second step of the multi-step optimisation framework. For the circular cylinder, the stacking sequence of the straight and steered fibre laminates are retrieved for a 24 layer balanced symmetric laminate; $[\pm\theta_1, \pm\theta_2, \pm\theta_3, \pm\theta_4, \pm\theta_5, \pm\theta_6]_s$.

The realistic CS laminate design, $CS-bust_{real}$, is retrieved from the selected theoretical CS laminate design, $CS-bust_{theo}$, using a genetic algorithm (GA) by minimising the squares distance between the theoretical and realistic lamination parameters in the lamination parameters space. The stacking sequence of the re-

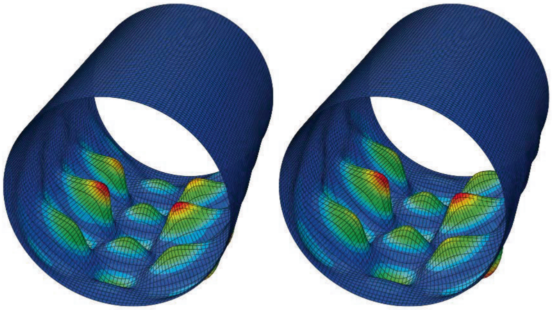

(a) $VSVT - bust_{theo}$ ($20 \leq$ No. of layers ≤ 28)
(b) $VSVT - bust_{theo}$ ($16 \leq$ No. of layers ≤ 32)

FIGURE 6.9: Critical buckling modes of theoretical variable stiffness variable thickness, $VSVT - bust_{theo}$, laminate designs for maximum buckling moment with strength constraints in the circular cylinder under bending from Abaqus^{TM}

trieved realistic CS laminate design, $CS - bust_{real}$, is:

$$CS - bust_{real}(\text{circular cylinder}) : [\pm\theta_1, \pm\theta_2, \pm\theta_3, \pm\theta_4, \pm\theta_5, \pm\theta_6]_s = [\pm 42.3, \pm 40.2, \pm 18.6, 0_2, \pm 81.2, \pm 83.7]_s \tag{6.5}$$

The realistic VS laminate design, $VS - bust_{real}$, is retrieved from the selected theoretical VS laminate design, $VS - bust_{theo}$, in the second step of the multi-step optimisation framework. The optimum fibre angle distribution of the realistic VS laminate design, $VS - bust_{real}$, is obtained from the optimisation problem in equation 4.42 which minimises of the convex conservative separable approximation of the complementary Lagrangian, built at the theoretical design, $VS - bust_{theo}$, subject to a constraint on the average steering curvature. The optimisation problem in equation 4.42 is solved using a gradient-based optimiser which is initialised with a fibre angle distribution obtained from GA.

Tightening the constraint on the average steering curvature, limits the rate of change of fibre angles and hence the amount of buckling moment improvement due to fibre steering. By increasing the allowable average steering curvature, the improvement in the buckling moment of the retrieved realistic laminates is increased. However, even for a large average steering curvature, the buckling moment of the realistic laminate designs is less than the theoretical designs. This is mainly due to the limited number of layers which are supposed to provide the theoretical optimum stiffness distribution. Here, the realistic VS laminate design, $VS-bust_{real}$, of the circular cylinder under bending is retrieved at an enough large average steering curvature of κ = 161.42 m^{-1} (4.1 in^{-1}), such that increasing the average steering curvature beyond that does not improve the buckling moment of the retrieved realistic design.

The distribution of lamination parameters for the theoretical, GA obtained and realistic laminate designs are depicted in figure 6.10. It is clear from figure 6.10 that the distribution of lamination parameters obtained from GA, has a zigzag pattern, while the distribution of lamination parameters in the realistic laminate is smooth due to the application of an average steering curvature constraint. It is also visible that the distribution of lamination parameters in the realistic laminate is somewhat similar to the theoretical laminate. Although the out of plane lamination parameters, V_{2D} and V_{4D}, are zero in the theoretical balanced symmetric laminate, V_{2D} and V_{4D} have small non-zero values in the realistic balanced symmetric laminate due to the limited number of layers. The difference in the distribution of other four lamination parameters, V_{1A}, V_{3A}, V_{1D}, and V_{3D}, in the theoretical and realistic laminates is also interpreted as a result of limited number of layers.

The buckling and failure moment for the $CS-bust_{real}$ and $VS-bust_{real}$ laminate designs and the improvements of $VS-bust_{real}$ over the $CS-bust_{real}$ laminate designs are shown in table 6.5. The difference between the buckling moments calculated from SAFD and Abaqus^{TM} is less than 2%. The safety factors of the $CS-bust_{real}$ and $VS-bust_{real}$ laminate designs, based on the SAFD results, are 1.03 and 1.12, respectively. The percentage of variation of the buckling and failure moments of the realistic designs with respect to the theoretical designs, in table 6.2, are shown inside the parentheses. The linear and nonlinear buckling moments of the realistic laminate designs are up to 5% less than the theoretical laminate designs based on Abaqus^{TM} results. This reduction is interpreted as a result of limited number of layers in the $CS-bust_{real}$ and $VS-bust_{real}$ laminate designs, considering the fact that the $VS-bust_{real}$ laminate is retrieved at a large average steering curvature of κ = 161.42 m^{-1} (4.1 in^{-1}), beyond which the buckling moment is not improved. Improvements in the linear and non-linear buckling moments of the $VS-bust_{real}$ over the $CS-bust_{real}$ laminate design are 29.6% and 23.9% based on Abaqus^{TM} results. The nonlinear buckling moments are dropped up to 9% with respect to the linear buckling moments.

The linear buckling and failure moments of the best VS laminate design in [17] are reported as 699.12 kN.m (6188 in-kips) and 700.25 kN.m (6198 in-kips), respectively, providing a safety factor of 1.001. The linear buckling and failure moments of the $VS-bust_{real}$ laminate design in table 6.5 are 766.80 kN.m (6787 in-kips) and 862.49 kN.m (7634 in-kips) from the SAFD analysis and lead to a safety factor of 1.124, which is about 12% higher. The linear buckling moment of the $VS-bust_{real}$

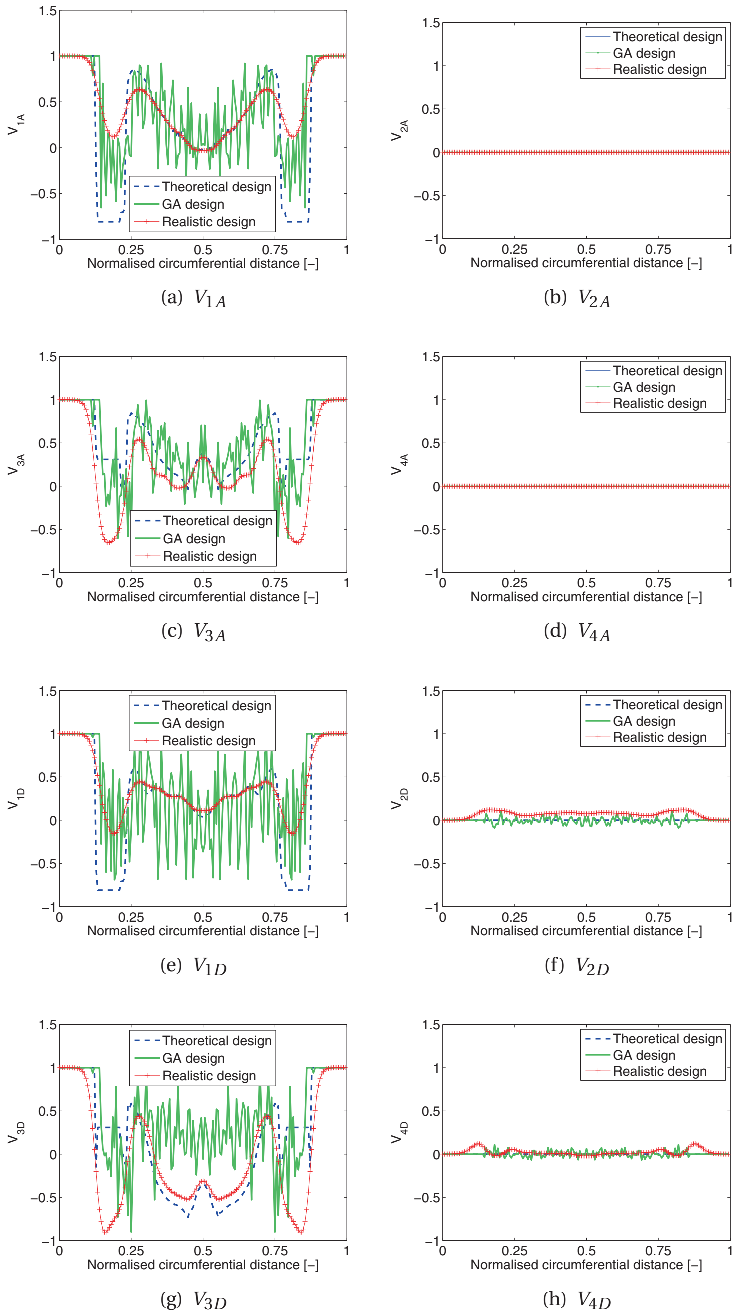

FIGURE 6.10: Distribution of lamination parameters in the theoretical variable stiffness constant thickness laminate, $VS-bust_{theo}$, laminate design obtained from GA and realistic variable stiffness constant thickness laminate, $VS-bust_{real}$, of the circular cylinder under bending

TABLE 6.5: Linear and non-linear buckling moments and failure moment of realistic constant stiffness, $CS-bust_{real}$, and realistic variable stiffness constant thickness, $VS-bust_{real}$, laminate designs for maximum buckling moment with strength constraints in the circular cylinder under bending, *Note: M_{b-lin} = linear buckling moment from SAFD and Abaqus*^{TM}), $M_{b-nonlin}$ *= nonlinear buckling moment from Abaqus*^{TM}, M_f *= failure moment from SAFD and conservative Tsai-Wu failure envelope,* Imp *= improvements of* $VS-bust_{real}$ *over* $CS-bust_{real}$ *calculated from* $(M(VS)-M(CS))/M(CS)$ *and the values inside parenthesis show the percentage of drop with respect to the corresponding values of the theoretical designs in table 6.2*

Design	$CS-bust_{real}$	$VS-bust_{real}$	Imp(%)
M_{b-lin} (SAFD) [kN.m]	607 (-2 %)	767 (-4 %)	26.2
M_{b-lin} (Abaqus^{TM}) [kN.m]	602 (-5 %)	780 (-4 %)	29.6
$M_{b-nonlin}$ (Abaqus^{TM}) [kN.m]	577 (-1 %)	716 (-5 %)	23.9
M_f (SAFD) [kN.m]	623 (-19 %)	862 (-5 %)	38.4

laminate design from Abaqus^{TM} analysis is 780.24 kN.m (6906 in-kips) in table 6.5 which is 11.6% higher than the corresponding value of the design presented in [17]. The maximum allowable deflection value of $1.58e-6$ m ($6.22e-5$ in) under 0.11298 kN.m (1 in-kips) bending moment, is considered to be a constraint in [17]. This displacement value for the $VS-bust_{real}$ design in table 6.5 is $1.37e-9$ m ($5.38e-8$ in), which satisfies the constraint. The superior performance of the $VS-bust_{real}$ design in table 6.5 with respect to the VS laminate design in [17] is due to the limited design space dictated from using the functional fibre path definition, using a laminate with fixed ply angle layers, $[\pm 45, \pm\theta_1, 0, 90, \pm\theta_3, 0, 90, \pm\theta_5]_s$, application of 10% robustness constraint and different steering curvature in [17].

6

The steered fibre paths are obtained from the fibre angle distributions using the streamline analogy in the third step of the multi-step optimisation framework. The retrieved fibre paths for realistic designs are shown in figure 6.11 on the expanded surface of the circular cylinder.

The distributions of the axial strain and sectional force in the realistic laminate designs are plotted in figures 6.12 and 6.13 based on Abaqus^{TM} results. These distributions are very similar and close to the distributions of the axial strain and sectional force in the theoretical laminate designs and hence the buckling moment improvement mechanisms in the realistic laminates are the same as those described for the theoretical laminates in subsection 6.2.1.

The numerically critical buckling mode shapes of the $CS-bust_{real}$ and $VS-bust_{real}$ laminate designs are depicted in figure 6.14. These buckling modes are expanded to a large area in the compression side and show some twisting deformation due to the bending-twisting coupling. The bending-twisting coupling is due to the existence of small non-zero values of V_{2D} and V_{4D} lamination parame-

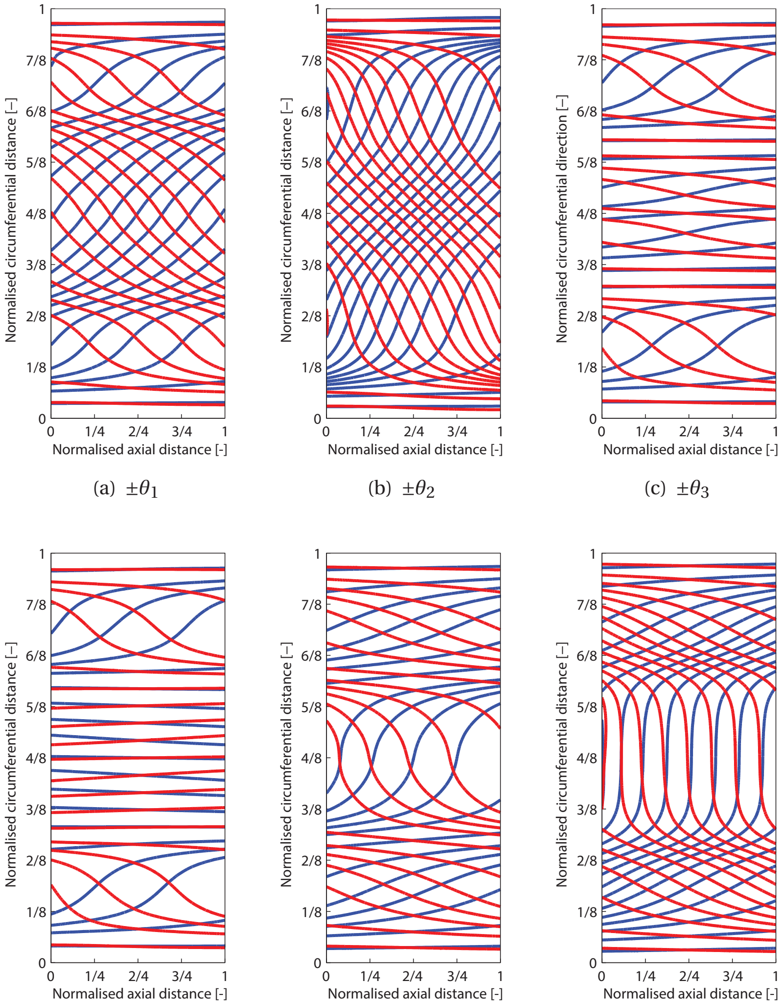

(a) $\pm\theta_1$ (b) $\pm\theta_2$ (c) $\pm\theta_3$

(d) $\pm\theta_4$ (e) $\pm\theta_5$ (f) $\pm\theta_6$

FIGURE 6.11: Optimum steered fibre paths of the realistic variable stiffness constant thickness design, $VS-bust_{real}$, with a 24 ply balanced symmetric laminate, $[\pm\theta_1,\pm\theta_2,\pm\theta_3,\pm\theta_4,\pm\theta_5,\pm\theta_6]_s$, plotted on the expanded surface of the cylinder, retrieved from the theoretical variable stiffness constant thickness design for maximum buckling moment with strength constraints, $VS-bust_{theo}$, in the circular cylinder under bending, *Note: circumferential distance starts from the point with the maximum axial tension*

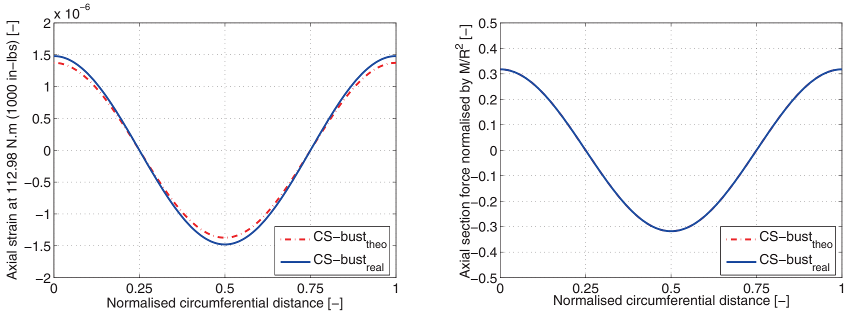

(a) Axial strain (b) Axial section force

FIGURE 6.12: Axial strain and axial section force of realistic constant stiffness, $CS-bust_{real}$, and theoretical constant stiffness, $CS-bust_{theo}$, laminate designs for maximum buckling moment with strength constraints in the circular cylinder under bending based on Abaqus^{TM} results, *Note: circumferential distance starts from the point with the maximum axial tension*

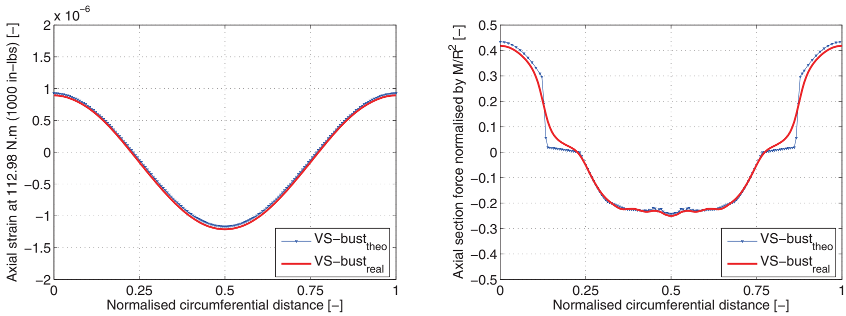

(a) Axial strain (b) Axial section force

FIGURE 6.13: Axial strain and axial section force of realistic variable stiffness constant thickness, $VS-bust_{real}$, and theoretical variable stiffness constant thickness, $VS-bust_{theo}$, laminate designs for maximum buckling moment with strength constraints in the circular cylinder under bending based on Abaqus^{TM} results, *Note: circumferential distance starts from the point with the maximum axial tension*

6

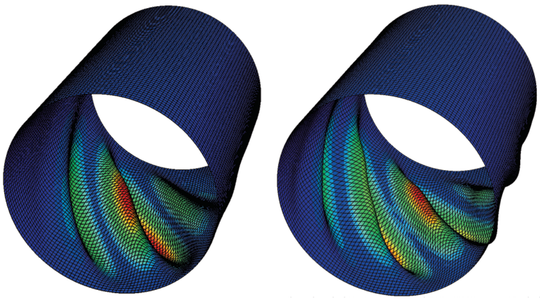

(a) $CS-bust_{real}$ (b) $VS-bust_{real}$

FIGURE 6.14: Critical buckling modes of realistic constant stiffness, $CS-bust_{real}$, and realistic variable stiffness constant thickness, $VS-bust_{real}$, laminate designs for maximum buckling moment with strength constraints in the circular cylinder under bending from Abaqus^{TM}

ters and hence D_{16} and D_{26} terms in the out of plane stiffness matrix of the realistic designs. The D_{16} and D_{26} terms, which are small compared to the other terms of the out of plane stiffness matrix for a balanced symmetric laminate, can be eliminated by using infinite number of very thin layers.

6

6.3 ELLIPTICAL CYLINDER UNDER AXIAL COMPRESSION

Circumferential stiffness tailoring of elliptical cross-section cylinders under axial compression has been studied by Sun and Hyer [88]. The philosophy behind their approach is to tailor the laminate stiffness such that all the points around the circumference of the elliptical cylinder buckle at the same strain value. Therefore, by eliminating the points which are more prone to buckling in a QI or CS laminate through stiffness tailoring, the material is used more efficiency and the buckling load is increased.

In this section, circumferential laminate stiffness tailoring of the same elliptical cylinder as the one studied by Sun and Hyer [88] is investigated using the developed framework for circumferential tailoring of general cross-section cylinders. The semi-minor and semi-major axes of the elliptical cross-section are 125 mm and 87.5 mm, respectively and the length of the cylinder is 320 mm. The laminate thickness is 1.12 mm including 8 layers made of a medium modulus graphite-epoxy fiber-reinforced composite material with the material properties listed in table 6.6.

TABLE 6.6: Material properties of a medium modulus graphite-epoxy [39]

Longitudinal modulus, E_1 [GPa / psi]	130 / 18.855e6
Transverse modulus, E_2 [GPa / psi]	9.70 / 1.407e6
Shear modulus, G_{12} [GPa / psi]	5 / 7.252e5
Poisson's ratio, ν_{12} [-]	0.30
Longitudinal tensile strength, X_t [MPa / psi]	1500 / 2.176e5
Longitudinal compressive strength, X_c [MPa / psi]	1250 / 1.813e5
Transverse tensile strength, Y_t [MPa / psi]	50 / 0.725e4
Transverse compressive strength, Y_c [MPa / psi]	200 / 2.901e4
Shear strength, S [MPa / psi]	100 / 1.450e4

6.3.1 THEORETICAL CONSTANT THICKNESS LAMINATE

The theoretical constant thickness laminate designs for maximum buckling load are found by solving the min-max optimisation problem in equation 6.1 in the first step of the multi-step optimisation framework. The design variables in the first step are four lamination parameters, V_{1A}, V_{3A}, V_{1D} and V_{3D}, to find the theoretical balanced symmetric laminates. The multi-modality of the buckling load maximisation problem for the elliptical cylinder is 100. The theoretical CS and constant thickness VS laminate designs for maximum buckling load of the elliptical cylinder under axial compression are buckling critical and hence consideration of strength constraints in the optimisation problem is not required.

The buckling and failure loads of the theoretical QI, QI_{theo}, maximum buckling load CS, $CS-bu_{theo}$, and maximum buckling load VS ,$VS-bu_{theo}$, laminate designs and the improvements of $VS-bu_{theo}$ over $CS-bu_{theo}$ design are shown in table 6.7. The safety factors of the $CS-bu_{theo}$ and $VS-bu_{theo}$ laminate designs are 2.05 and 1.61 based on the SAFD results. The linear and nonlinear buckling loads are found from Abaqus^{TM} using simply supported boundary conditions and the difference between the linear buckling loads from Abaqus^{TM} and SAFD is less than 4%. Based on the Abaqus^{TM} results, the nonlinear buckling load is dropped up to 7% with respect to the linear buckling loads and the improvements in the linear and nonlinear buckling loads of the $VS-bu_{theo}$ over the $CS-bu_{theo}$ laminate design are 36.5% and 37.5%, respectively.

The lamination parameters of the theoretical CS laminate design for maximum buckling load, $CS-bu_{theo}$, are:

$$CS-bu_{theo}:[V_{1A},V_{3A},V_{1D},V_{3D}] = [-0.14, 0.07, 0.15, -0.35] \tag{6.6}$$

The distribution of lamination parameters of the theoretical VS designs for maximum buckling load, $VS-bu_{theo}$, is shown in figure 6.15.

6

TABLE 6.7: Linear and non-linear buckling loads and failure load of theoretical quasi-isotropic, QI_{theo}, selected theoretical constant stiffness, $CS-bu_{theo}$, and selected theoretical variable stiffness constant thickness, $VS-bu_{theo}$, laminate designs for maximum buckling load in elliptical cylinder under axial compression, *Note:* F_{b-lin} *= linear buckling load from the semi-analytical finite difference (SAFD) and Abaqus*^{TM}*,* $F_{b-nonlin}$ *= nonlinear buckling load from Abaqus*^{TM}*,* F_f *= failure load from SAFD and conservative Tsai-Wu failure envelope (chapter 5) and* Imp *= improvements of* $VS-bust_{theo}$ *over* $CS-bust_{theo}$ *calculated from* $(F_{VS}-F_{CS})/F_{CS}$

Design	QI_{theo}	$CS-bu_{theo}$	$VS-bu_{theo}$	$Imp(\%)$
F_{b-lin} (SAFD) [kN]	156	168	229	36.7
F_{b-lin} (Abaqus^{TM}) [kN]	150	169	231	36.7
$F_{b-nonlin}$ (Abaqus^{TM}) [kN]	147	158	217	37.5
F_f (SAFD) [kN]	363	345	369	7

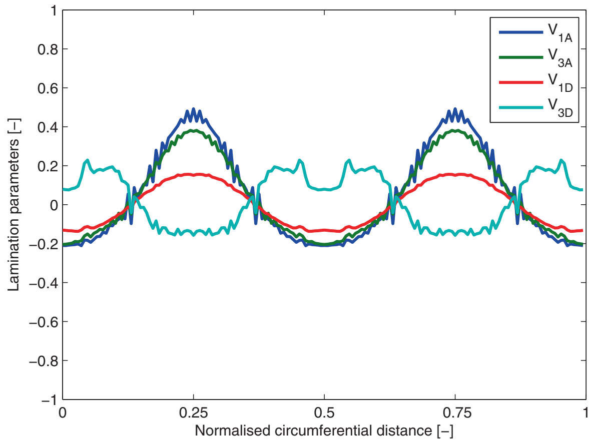

FIGURE 6.15: Distribution of lamination parameters in theoretical variable stiffness laminate design for maximum buckling load, $VS-bu_{theo}$, of the elliptical cylinder under axial compression, *Note: circumferential distance starts from the point at the end of the semi-minor axis*

6

Improvement mechanisms
The distributions of the axial strain and sectional force of the QI_{theo}, $CS-bu_{theo}$ and $VS-bu_{theo}$ laminate designs of the elliptical cylinder are shown in figure 6.16. These distributions are obtained from the Abaqus^{TM} results and plotted versus the normalised circumferential distance from the point at the end of the semi-minor axis of the cross-section of the elliptical cylinder.

It is clear figure 6.16(a) that the axial strain distribution of the QI_{theo}, $CS-bu_{theo}$ and $VS-bu_{theo}$ laminate designs are uniform, because the two ends of the cylinder remain planar and parallel. As it is shown in figure 6.16(b), the axial sectional force of the QI_{theo} and $CS-bu_{theo}$ laminate designs are uniform due to the uniform laminate stiffness distribution. However, the axial sectional force of the $VS-bu_{theo}$ laminate design is redistributed such that the axial compressive sectional force in the areas of the elliptical cross-section with larger radius of curvature is less than that in the areas with smaller radius of curvature. This is due to circumferential stiffness tailoring which reduces the stiffness in the areas with larger radius of curvature and stiffens the areas with smaller radius of curvature.

Numerically critical linear buckling mode shapes of the QI_{theo}, $CS-bu_{theo}$ and $VS-bu_{theo}$ laminate designs designs are shown in figure 6.17. In the QI_{theo} and $CS-bu_{theo}$ laminate designs, cross-sectional areas with larger radius of curvature are more prone to buckle. However, in the $VS-bu_{theo}$ laminate design, due to the axial sectional force redistribution in figure 6.16(b), the buckling modes are expanded all around the elliptical cross-section. Therefore, the material around the circumference is used more efficiently to maximise the buckling load.

6

6.3.2 THEORETICAL VARIABLE THICKNESS LAMINATE

The theoretical variable thickness laminate design for maximum buckling load is obtained by solving the min-max optimisation problem in equation 6.4 in the first step of the multi-step optimisation framework. Similar to the constant thickness VS laminates, only four lamination parameters, V_{1A}, V_{3A}, V_{1D} and V_{3D}, are used as the design variables in the first step to find the theoretical variable thickness balanced symmetric laminates. The multi-modality of the buckling load maximisation problem for the considered elliptical cylinder is 100. The elliptical cylinder with a constant thickness laminate has 8 layers and the elliptical cylinder with a variable thickness laminate is bounded between 4 and 12 layers. The theoretical variable thickness VS laminate design for maximum buckling load, $VSVT-bu_{theo}$ is buckling critical and hence consideration of strength constraints is not necessary.

The buckling and failure loads of the $VSVT-bu_{theo}$ laminate design of the elliptical cylinder are listed in table 6.8, and compared with those of the constant thickness VS, $VS-bu_{theo}$, laminate design and the amount of improvements of

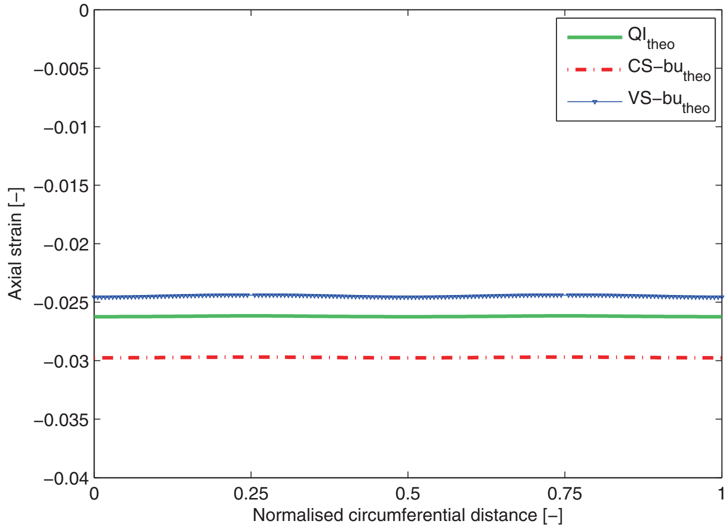

(a) Axial strain at $1e6$ N

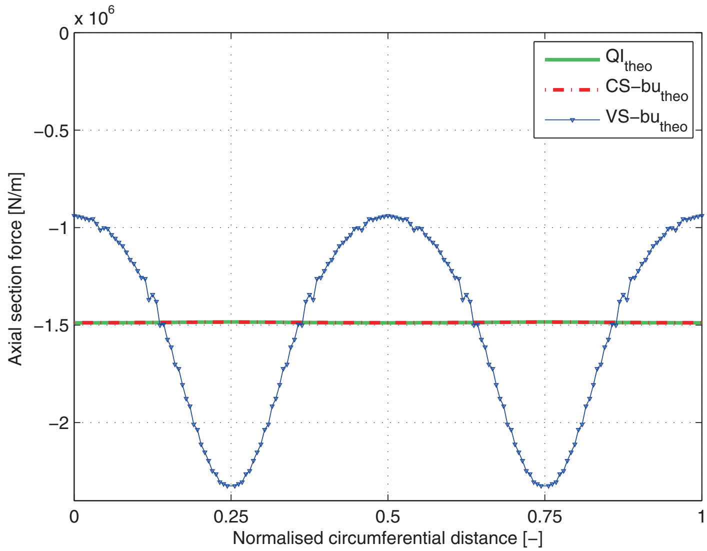

(b) Axial section force at $1e6$ N

FIGURE 6.16: Axial strain and axial section force of theoretical quasi-isotropic, QI_{theo}, selected theoretical constant stiffness, $CS-bu_{theo}$, and selected theoretical variable stiffness constant thickness, $VS-bu_{theo}$, laminate designs for maximum buckling load in the elliptical cylinder under axial compression based on Abaqus^{TM} results, *Note: circumferential distance starts from the point at the end of the semi-minor axis*

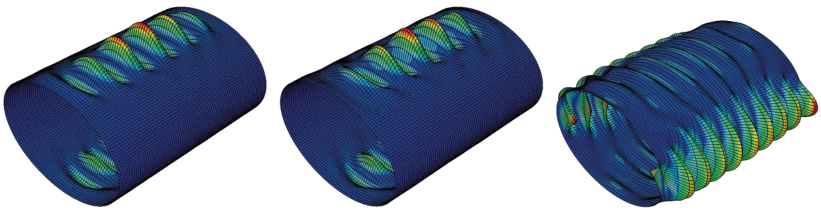

(a) QI_{theo} (b) $CS-bu_{theo}$ (c) $VS-bu_{theo}$

FIGURE 6.17: Critical buckling modes of theoretical quasi-isotropic, QI_{theo}, selected theoretical constant stiffness, $CS-bu_{theo}$, and selected theoretical variable stiffness constant thickness, $VS-bu_{theo}$, laminate designs for maximum buckling load in the elliptical cylinder under axial compression from Abaqus^{TM}

TABLE 6.8: Linear and non-linear buckling load and failure load of variable stiffness constant thickness, $VS-bu_{theo}$, and variable thickness (4 < No. of layers < 8) variable stiffness, $VSVT-bu_{theo}$, laminate designs for maximum buckling load in elliptical cylinder under axial compression, *Note:* F_{b-lin} *= linear buckling load from the semi-analytical finite difference (SAFD) and Abaqus*^{TM}, $F_{b-nonlin}$ *= nonlinear buckling load from Abaqus*^{TM}, F_f *= failure load from SAFD and conservative Tsai-Wu failure envelope and* Imp *= improvements of* $VSVT-bu_{theo}$ *over* $VS-bu_{theo}$ *calculated as* $(F_{VSVT}-F_{VS})/F_{VS}$

Design	$VS-bu_{theo}$	$VSVT-bu_{theo}$	Imp(%)
F_{b-lin} (SAFD) [kN]	229	285	24.4
F_{b-lin} (Abaqus^{TM}) [kN]	231	286	24
$F_{b-nonlin}$ (Abaqus^{TM}) [kN]	217	270	24.4
F_f (SAFD) [kN]	369	393	6.5

the $VSVT-bu_{theo}$ over the $VS-bu_{theo}$ laminate design are shown. The difference between the linear buckling loads from SAFD and Abaqus^{TM} is less than 1%. Based on the SAFD results, the safety factor of the $VSVT-bu_{theo}$ laminate design is 1.37. The nonlinear buckling load is reduced about 6% with respect to the linear buckling load, based on the Abaqus^{TM} results. The improvements in the linear and nonlinear buckling loads of the $VSVT-bu_{theo}$ over the $VS-bu_{theo}$ laminate design are 24% and 24.4%, respectively, based on the Abaqus^{TM} results.

The distribution of lamination parameters and laminate thickness for the $VSVT-bu_{theo}$ laminate design of the elliptical cylinder are shown in figures 6.18 and 6.19.

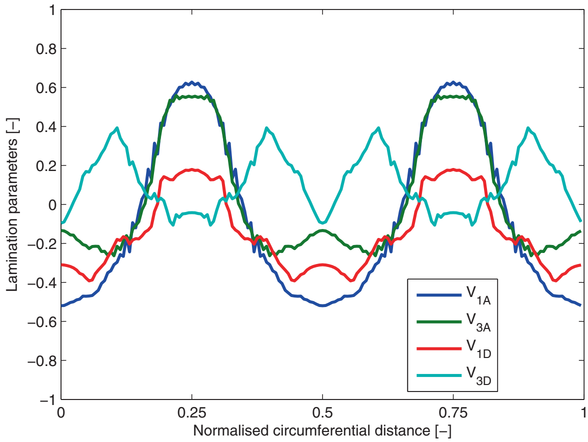

FIGURE 6.18: Distribution of lamination parameters in theoretical variable thickness (4 $\leq$ No. of layers $\leq$ 12) variable stiffness laminate design for maximum buckling load, $VSVT - bu_{theo}$, in the elliptical cylinder under axial compression

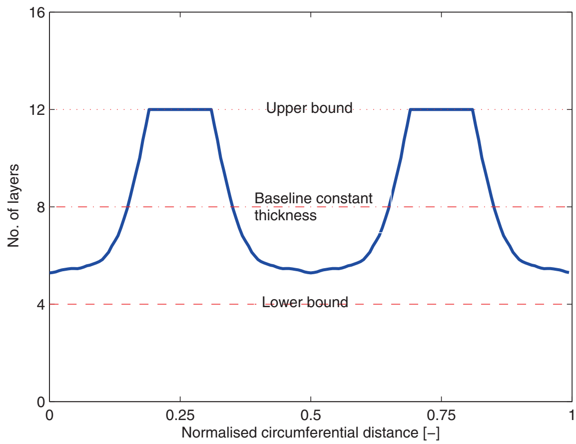

FIGURE 6.19: Distribution of laminate thickness in theoretical variable thickness (4 $\leq$ No. of layers $\leq$ 12) variable stiffness laminate design for maximum buckling load, $VSVT - bu_{theo}$, in the elliptical cylinder under axial compression

Improvement mechanisms

The distributions of axial strain and sectional force of the $VSVT - bu_{theo}$ laminate design of the elliptical cylinder are shown in figure 6.20 and compared with these distributions for the $VS - bu_{theo}$ laminate design. These distributions are from the Abaqus^{TM} results and plotted versus the normalised circumferential distance from the point at the end of the semi-minor axis.

As it is clear from figure 6.20(a), the distribution of axial strain of the $VSVT - bu_{theo}$ laminate design is uniform similar to the $VS - bu_{theo}$ laminate design. This is because the two end cross-sections of the elliptical cylinder under axial compression remain planar and parallel. However, the axial compressive strain of the $VSVT - bu_{theo}$ laminate is less than the $VS - bu_{theo}$ laminate, which means that the $VSVT - bu_{theo}$ laminate is stiffer than the $VS - bu_{theo}$ laminate in the axial direction.

The thickness distribution of the $VSVT - bu_{theo}$ laminate design in figure **??**, further increases the in-plane stiffness and hence the axial section compression load in the cross-sectional areas with smaller radius of curvature and further reduces it in the cross-sectional areas with larger radius of curvature, compared to the $VS - bu_{theo}$ laminate design. Although the cross-sectional areas with smaller radius of curvature are more buckling resistant due to their geometric properties, increasing the out of plane stiffness with the third power of the laminate thickness in these areas, further increases the buckling resistance of these areas.

The numerically critical buckling modes of the elliptical cylinder with the $VSVT - bu_{theo}$ laminate is shown in figure 6.21. The expansion of the buckling mode in the $VSVT - bu_{theo}$ laminate design is limited to the cross-sectional areas with larger radius of curvature. Comparing this with the all around the circumference expansion of the buckling mode in the $VS - bu_{theo}$ laminate design, in figure 6.17, shows the effect of increased out of plane stiffness in the the cross-sectional areas with smaller radius of curvature in the $VSVT - bu_{theo}$.

6.3.3 REALISTIC CONSTANT THICKNESS LAMINATE

The realistic CS and constant thickness VS laminate designs for maximum buckling load of the elliptical cylinder are retrieved from the corresponding theoretical designs in the second step of the multi-step framework. The straight and steered fibre laminates are retrieved for an 8 layer balanced symmetric layup configuration; $[\pm\theta_1, \pm\theta_2]_s$.

The stacking sequence of the realistic CS laminate design, $CS - bu_{real}$, which is retrieved from the theoretical CS laminate design for maximum buckling load,

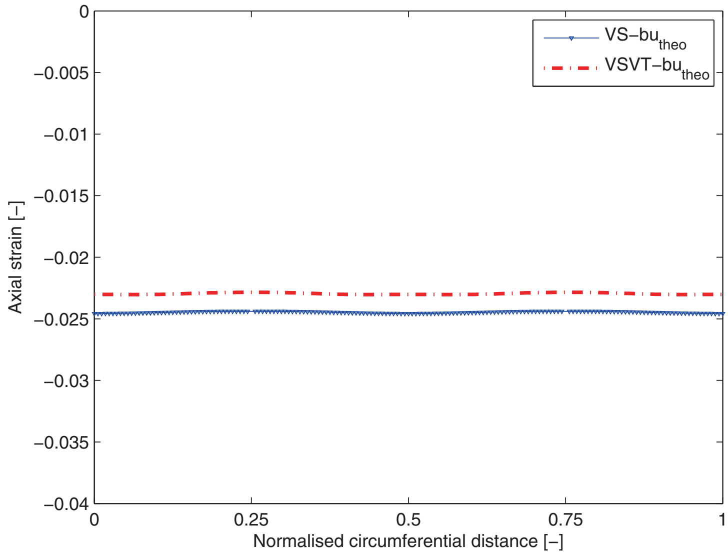

(a) Axial strain at $1e6$ N

6

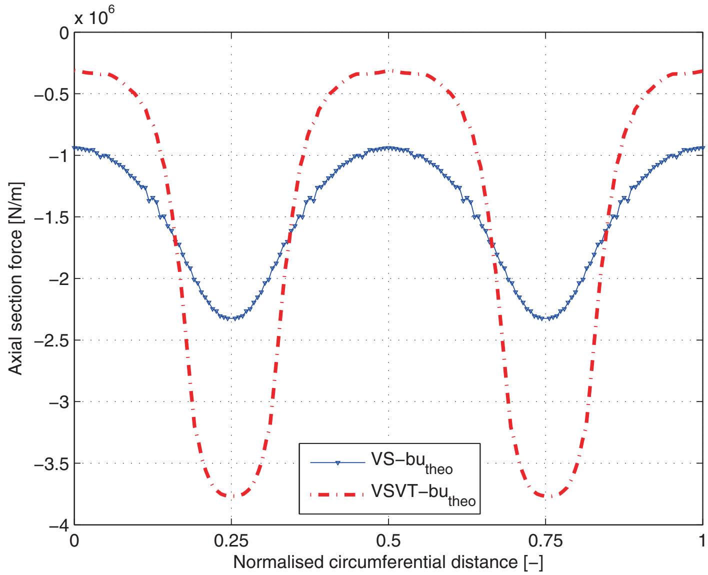

(b) Axial force at $1e6$ N

FIGURE 6.20: Axial strain and axial section force of theoretical variable stiffness constant thickness, $VS-bu_{theo}$, and theoretical variable stiffness variable thickness, $VSVT-bu_{theo}$, laminate designs for maximum buckling load in the elliptical cylinder under axial compression based on Abaqus^{TM} results, *Note: circumferential distance starts from the point at the end of the semi-minor axis*

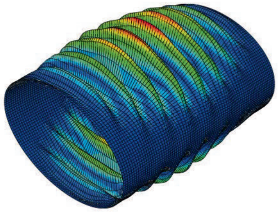

FIGURE 6.21: Critical buckling mode of variable stiffness variable thickness laminate design for maximum buckling load, $VSVT - bu_{theo}$, in elliptical cylinder under axial compression from Abaqus^{TM}

$CS - bu_{theo}$, by using a GA is:

$$CS - bu_{real}\text{(elliptical cylinder)} : [\pm\theta_1, \pm\theta_2] = [\pm 31/\pm 78.5]_s \tag{6.7}$$

The fibre angle distribution in each layer of the realistic constant thickness VS laminate design, $VS - bu_{real}$, is obtained by using a GA for initialisation and subsequently a gradient-based optimiser. As explained in section 4.5, the gradient-based optimiser minimises the approximation of the complementary Lagrangian built at the theoretical design, $VS - bu_{theo}$, subject to a constraint on the average steering curvature. The $VS - bu_{real}$ laminate design for the elliptical cylinder is retrieved at an average steering curvature of $\kappa = 3$ m^{-1} which beyond that the buckling load of the retrieved realistic laminates is not improved.

The distribution of lamination parameters for the theoretical, GA obtained and realistic laminate designs are depicted in figure 6.22. It is clear that the zigzag distribution of lamination parameters in the design obtained from GA is turned into a smoother distribution of lamination parameters in the realistic design due to imposing an average steering curvature constraint. The difference in the distribution of lamination parameters in the theoretical and realistic laminate designs, and as such existence of small non-zero values for V_{2D} and V_{4D}, is due to the limited number of layers in the considered stacking sequence, $[\pm\theta_1, \pm\theta_2]$.

The buckling and failure load of the $CS - bu_{real}$ and $VS - bu_{real}$ laminate designs and the improvements of $VS - bu_{real}$ over the $CS - bu_{real}$ laminate designs are shown in table 6.5. Based on the SAFD results, the safety factors of the $CS - bu_{real}$ and $VS - bu_{real}$ laminate designs are 1.79 and 1.47, respectively. The difference between the linear buckling loads from SAFD and Abaqus^{TM} is up to 12%. As shown inside the parentheses, the linear and nonlinear buckling loads of the realistic VS laminate designs are up to 17% less than those of the theoretical VS laminate designs based on the Abaqus^{TM} results. This difference between

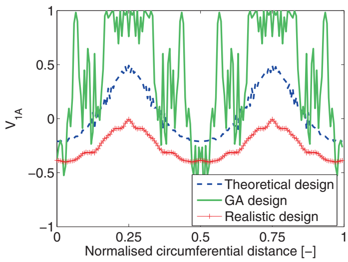

(a) V_{1A}

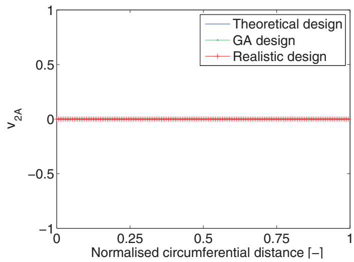

(b) V_{2A}

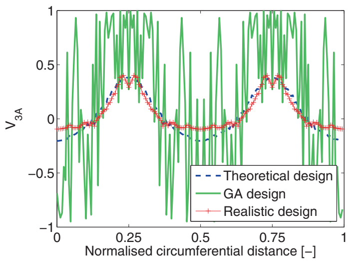

(c) V_{3A}

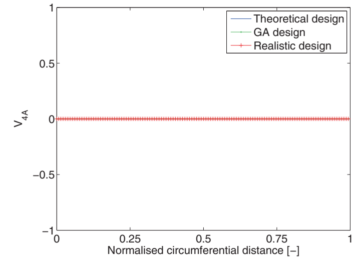

(d) V_{4A}

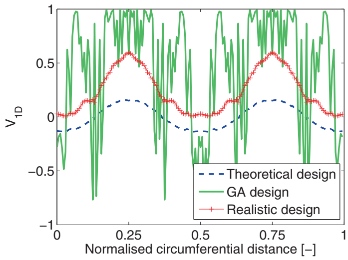

(e) V_{1D}

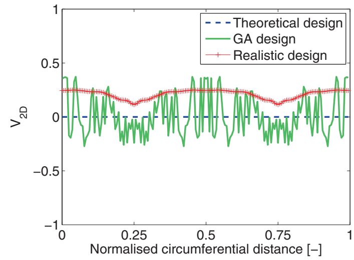

(f) V_{2D}

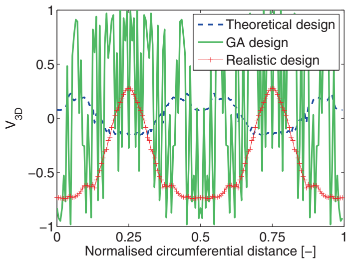

(g) V_{3D}

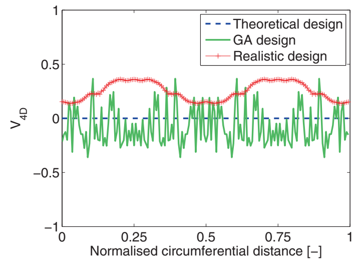

(h) V_{4D}

FIGURE 6.22: Distribution of lamination parameters in the theoretical variable stiffness constant thickness laminate, $VS-bu_{theo}$, laminate design obtained from GA and realistic variable stiffness constant thickness laminate, $VS-bu_{real}$, of the elliptical cylinder under axial compression

TABLE 6.9: Linear and non-linear buckling loads and failure load of realistic constant stiffness, $CS-bu_{real}$, and realistic variable stiffness constant thickness, $VS-bu_{real}$, laminate designs for maximum buckling load in the elliptical cylinder under axial compression, *Note:* F_{b-lin} *= linear buckling load from the semi-analytical finite difference (SAFD) and Abaqus*^{TM}, $F_{b-nonlin}$ *= nonlinear buckling load from Abaqus*^{TM}, F_f *= failure load from SAFD and conservative Tsai-Wu failure envelope,* Imp *= improvements of* $VS-bu_{real}$ *over* $CS-bu_{real}$ *calculated from* $(M(VS)-M(CS))/M(CS)$ *and the values inside parenthesis show the percentage of drop with respect to the corresponding theoretical designs in table 6.7*

Design	$CS-bu_{real}$	$VS-bu_{real}$	Imp(%)
F_{b-lin} (SAFD) [kN]	164 (-2%)	177 (-29%)	7.9
F_{b-lin} (Abaqus^{TM}) [kN]	167 (-1%)	197 (-17%)	17.9
$F_{b-nonlin}$ (Abaqus^{TM}) [kN]	157 (-1%)	190 (-14%)	21.3
F_f (SAFD) [kN]	293 (-18%)	261 (-42%)	-11.1

the realistic and theoretical CS laminate designs is about 1%. Therefore, the 17% difference between the buckling loads of the realistic and theoretical VS laminate designs can be interpreted as the result of poor initialisation of the gradient-based optimiser, in addition to the limited number of layers, considering that an enough large average steering curvature, $\kappa = 3$ m^{-1}, is considered in the fibre angle retrieval process. Based on the Abaqus^{TM} results, the nonlinear buckling loads is decreased up to 7% with respect to the linear buckling loads and the linear and non-linear buckling load improvements are 17.9% and 21.3%, respectively. The linear buckling load of the $VS-bu_{real}$ laminate design from Abaqus^{TM} analysis is 197.4 kN which is 18.2% higher than the value of 166.9 kN reported in [39]

The steered fibre paths are obtained from the fibre angle distributions of the $VS-bu_{real}$ laminate design using the streamline analogy in the third step of the multi-step optimisation framework. The retrieved fibre paths for the $VS-bu_{real}$ laminate design are shown on the expanded surface of the elliptical cylinder in figure 6.11.

The numerically critical buckling mode shapes of the $CS-bu_{real}$ and $VS-bu_{real}$ laminate designs are depicted in figure 6.24. These buckling mode of the $VS-bu_{real}$ laminate design is expanded all around the elliptical cross-section, which shows that the material is used more efficiently.

The distributions of the axial strain and sectional force in the realistic laminate designs are plotted in figure 6.25 based on Abaqus^{TM} results. These distributions are very similar and close to the distributions of the axial strain and sectional force in the theoretical laminate designs and hence the buckling load improvement mechanisms in the realistic laminates are the same as those described for the theoretical laminates in subsection 6.3.3.

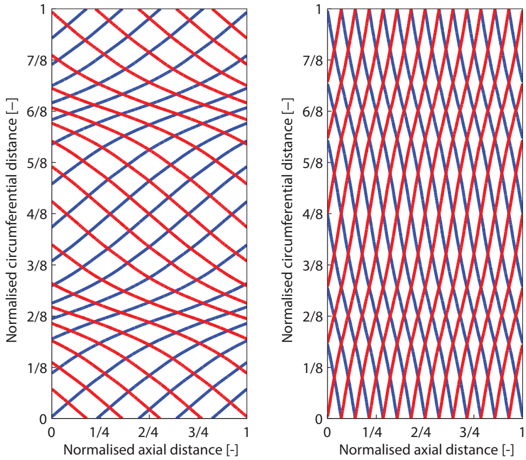

(a) $\pm\theta_1$ (b) $\pm\theta_2$

FIGURE 6.23: Optimum steered fibre paths of the realistic variable stiffness constant thickness design, $VS-bu_{real}$, with an 8 ply balanced symmetric laminate, $[\pm\theta_1,\pm\theta_2]_s$, plotted on the expanded surface of the cylinder, retrieved from the theoretical variable stiffness constant thickness laminate design for maximum buckling load, $VS-bu_{theo}$, in the elliptical cylinder under axial compression, *Note: circumferential distance starts from the point at the end of the semi-minor axis*

6

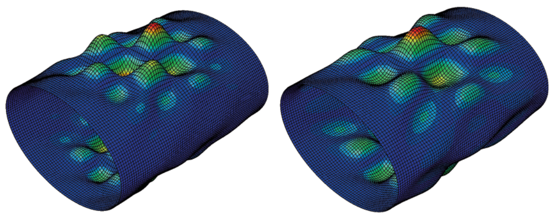

(a) $CS-bu_{real}$ (b) $VS-bu_{real}$

FIGURE 6.24: Critical buckling modes of realistic constant stiffness, $CS-bu_{real}$, and realistic variable stiffness constant thickness, $VS-bu_{real}$, laminate designs for maximum buckling load in the elliptical cylinder under axial compression from Abaqus^{TM}

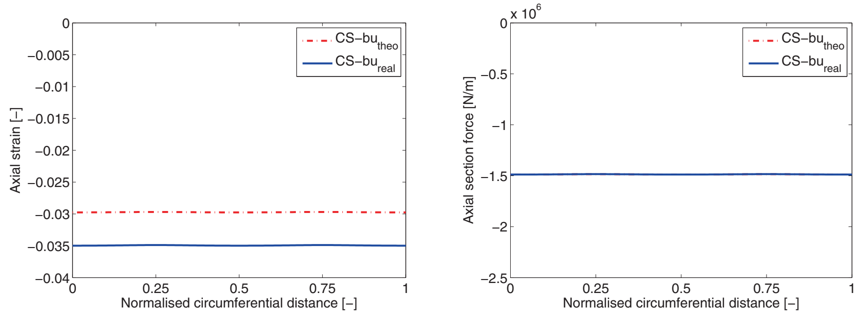

(a) Axial strain at $1e6$ N (b) Axial force at $1e6$ N

FIGURE 6.25: Axial strain and axial section force of realistic constant stiffness, $CS - bu_{real}$, and theoretical constant stiffness, $CS - bu_{theo}$, laminate designs for maximum buckling load in the elliptical cylinder under axial compression based on the Abaqus^{TM} results, *Note: circumferential distance starts from the point at the end of the semi-minor axis*

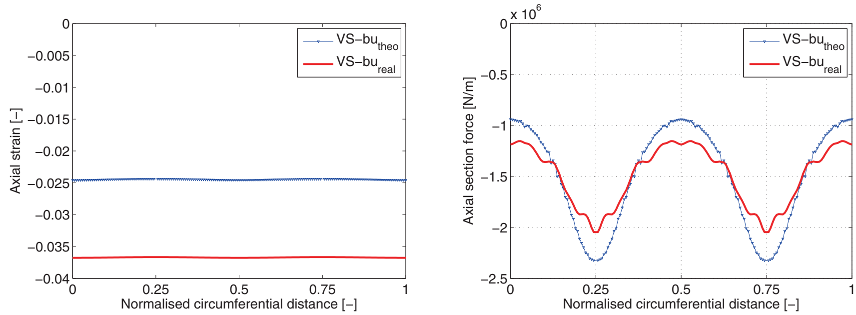

(a) Axial strain at $1e6$ N (b) Axial force at $1e6$ N

FIGURE 6.26: Axial strain and axial section force of realistic variable stiffness constant thickness, $VS - bu_{real}$, and theoretical variable stiffness constant thickness, $VS - bu_{theo}$, laminate designs for maximum buckling load in the elliptical cylinder under axial compression based on the Abaqus^{TM} results, *Note: circumferential distance starts from the point at the end of the semi-minor axis*

7

OPTIMISATION RESULTS FOR STIFFENED CIRCULAR CYLINDER

7.1 INTRODUCTION

This chapter is devoted to circumferential laminate stiffness tailoring of circular cylindrical shells stiffened with longitudinal stiffeners under bending moment for maximum buckling capacity. In addition to the buckling capacity, material failure is considered as another design driver in the cases where the maximum buckling capacity design is material failure critical. To this end, the semi-analytical solutions for static and buckling analysis of longitudinally stiffened cylindrical shells, developed in chapter 3, is used to evaluate the strains and buckling capacity. Similar to the unstiffened cylinders, the strength is evaluated using the conservative Tsai-Wu failure envelope in the strain space, which was introduced in chapter 5. The approximations of the buckling capacity and strength, which are introduced and developed in chapters 4 and 5 respectively, are used in the multi-step optimisation framework developed in chapter 4 to find the optimum CS and circumferentially VS laminate designs.

For case studies, two circular cylindrical shells under bending moment with different thickness to radius ratios are selected. The laminate thickness and material of both cylindrical shells are selected to be identical to those of the unstiffened circular cylindrical shell described in chapter 6. The laminate thickness is 4.39 mm (0.1728 in) including 24 layers made of $AS4/8773$ material, the properties of which are given in table 6.1. As shown in figure 7.1, the small cylinder has a diameter of 609.6 mm (24 in) and a length of 812.8 mm (32 in), which are identical to the the

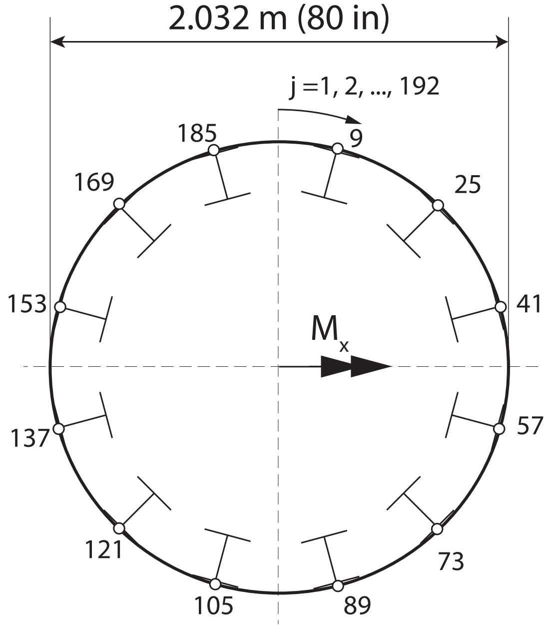

(a) Large circular cylinder with 457.2 mm (18 in) length and 4.39 mm (0.1728 in) thickness and 12 stiffeners with cross-section No. 5

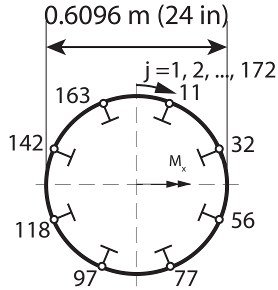

(b) Small circular cylinder with 812.8 mm (32 in) length and 4.39 mm (0.1728 in) thickness and 8 stiffeners with cross-section No. 4

FIGURE 7.1: Cross-sections of stiffened circular cylinders under bending moment, *Note: j = number of discretisation point in the cross-section*

unstiffened circular cylinder in chapter 6. The large cylinder has a diameter of 2032 mm (80 in) and a length of 457.2 mm (18 in), to resemble a fuselage section placed between two frames.

The small and large cylinders are stiffened with 8 stiffeners and 12 longerons with I cross-sections No. 4 and 5, the geometric properties of which are shown in figure 7.2 and listed in table 7.1. In both cylinders, the stiffeners are composed of a quasi-isotropic (QI) laminate made of the same material, *AS*4/8773, as the cylindrical shells. It is assumed that the stiffeners are perfectly bonded to the internal surface of the cylindrical shell as depicted in figure 7.1 and the shell-stiffener debonding failure is not considered in the design process. In this chapter, circum-

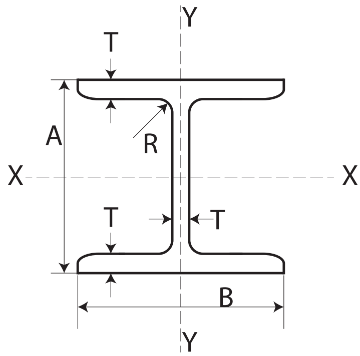

FIGURE 7.2: I cross-section of the stiffeners

TABLE 7.1: Geometric properties of different I cross-sections selected for stiffeners [113]

Property	No. 4	No. 5
A [mm / in]	63.5 / 2.5	101.6 / 4
B [mm / in]	50.8 / 2.0	101.6 / 4
T [mm / in]	2.39 / 0.094	7.95 / 0.313
R [mm / in]	3.96 / 0.156	6.35 / 0.250
Area [1e3 mm^2 / in^2]	0.504 / 0.781	0.392 / 0.607
I_{xx} [1e6 mm^4 / in^4]	0.2735 / 0.6571	3.919 / 9.415
I_{yy} [1e6 mm^4 / in^4]	0.0493 / 0.1184	1.264 $\tilde{3}$.037

ferential laminate stiffness tailoring of the selected longitudinally stiffened circular cylinders for maximum buckling moment are investigated in section 7.2. Since the maximum buckling moment designs of the cylinder with larger thickness to radius ratio are material failure critical, the laminate designs of this cylinder for maximum buckling moment with strength constraints are studied in section 7.3.

7.2 MAXIMUM BUCKLING MOMENT DESIGN

In this section, first the theoretical CS and constant thickness VS laminate designs for maximum buckling moment are obtained in subsection 7.2.1. To investigate the effect of laminate thickness variation in addition to fibre steering, theoretical variable thickness VS laminate designs are obtained and compared with the theoretical constant thickness VS laminate designs in subsection 7.2.2. The realistic CS and constant thickness VS laminate designs are retrieved from the corresponding theoretical designs in subsection 7.2.3.

7.2.1 THEORETICAL CONSTANT THICKNESS LAMINATE

The theoretical CS and constant thickness VS laminate designs of the two circular cylindrical shells are obtained for the maximum buckling capacity by solving the optimisation problem in equation 6.1 in the first step of the multi-step optimisation framework. Two in-plane lamination parameters, V_{1A} and V_{3A}, and two out of plane lamination parameters, V_{1D} and V_{3D}, are used as design variables to find the theoretical balanced symmetric laminate designs and 60 buckling modes are considered in the multi-modal buckling optimisation problem.

The optimum lamination parameters of the theoretical CS laminates designs for maximum buckling moment, $CS-bu_{theo}$, are:

$$CS-bu_{theo}\ \text{(Small cylinder)} : [V_{1A}, V_{3A}, V_{1D}, V_{3D}] = [-0.67, 0.29, -0.31, -0.34]$$
$$CS-bu_{theo}\ \text{(Large cylinder)} : [V_{1A}, V_{3A}, V_{1D}, V_{3D}] = [-0.90, 0.50, -0.54, -0.08]$$

The distribution of lamination parameters for the maximum buckling moment theoretical VS laminate designs, $VS-bu_{theo}$, of the circular cylinders are shown in figure 7.3.

The buckling and material failure moment of the theoretical QI, QI_{theo}, maximum buckling moment CS, $CS-bu_{theo}$, and maximum buckling moment VS, $VS-bu_{theo}$, laminate designs and the improvements of $VS-bu_{theo}$ over $CS-bu_{theo}$ designs for the two selected stiffened circular cylindrical shells are listed in table 7.2. The linear buckling moment values from the SAFD method are in good agreement with Abaqus^{TM} results, showing a maximum difference of less than 13%. Based on Abaqus^{TM} results, the amount of improvement in the buckling moment of $VS-bu_{theo}$ over $CS-bu_{theo}$ laminate designs are 68.2% and 43.2% for the small and large cylinders, respectively.

7

Based on the SAFD results, the safety factors of the laminate designs of the small cylinder are less than one, 0.34 and 0.43 for the $CS-bu_{theo}$ and $VS-bu_{theo}$ designs respectively, while the safety factors of the laminate designs of the large cylinder are greater than one, 1.06 and 1.01 for the $CS-bu_{theo}$ and $VS-bu_{theo}$ designs respectively. Therefore, in the small cylinder, the laminate designs for maximum buckling moment are material failure critical and consideration of strength constraints in the optimisation problem is essential. Maximum buckling moment design of the small cylinder with consideration of strength constraints is investigated in section 7.3, however, for better understanding of the mechanisms involved in buckling capacity improvement due to circumferential stiffness tailoring, the theoretical the realistic laminate designs for maximum buckling capacity of both cylinders are studied in this section and in section 7.2.3, respectively.

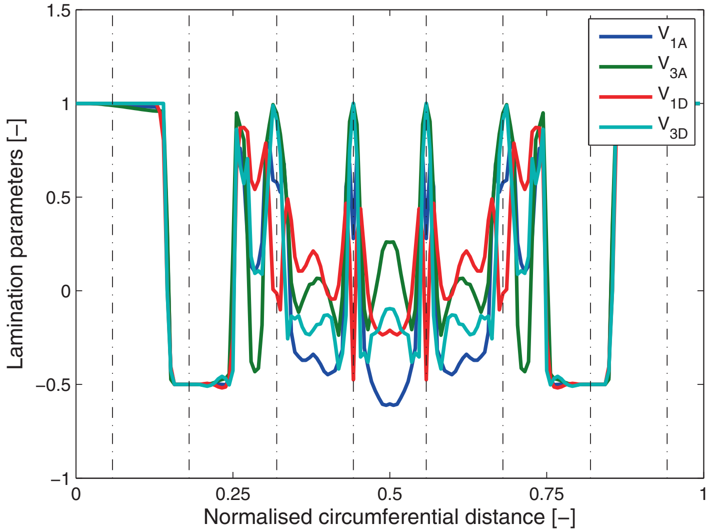

(a) $VS-bu_{theo}$ design design of the small cylinder

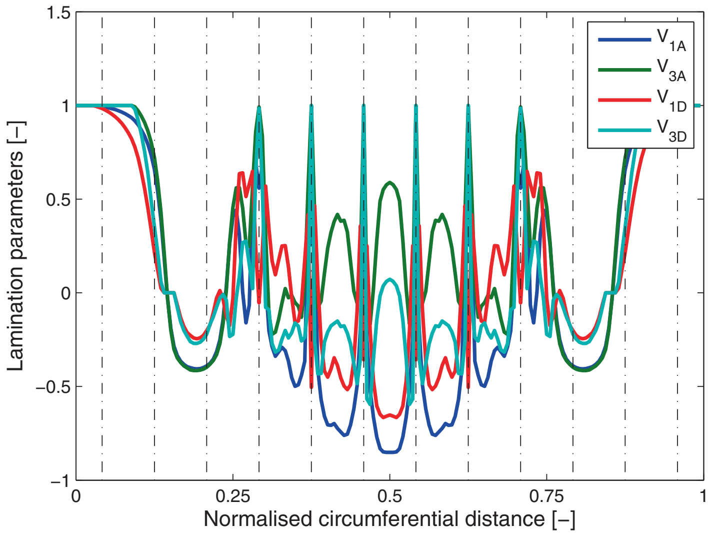

(b) $VS-bu_{theo}$ design design of the large cylinder

FIGURE 7.3: Distribution of lamination parameters in theoretical variable stiffness constant thickness laminate designs for maximum buckling moment, $VS-bu_{theo}$, of the stiffened circular cylinders under bending, *Note: normalised circumferential distance starts from the point with maximum axial tension*

7

TABLE 7.2: Linear buckling moments and failure moments of theoretical quasi-isotropic, QI_{theo}, theoretical constant stiffness, $CS-bu_{theo}$, and theoretical variable stiffness constant thickness, $VS-bu_{theo}$, laminate designs for maximum buckling moment in stiffened circular cylinders under bending, *Note:* M_{b-lin} *= linear buckling moment from the semi-analytical finite difference (SAFD) and Abaqus*^{TM}, M_f *= failure moment from SAFD and conservative Tsai-Wu failure envelope and* Imp *= improvements of* $VS-bu_{theo}$ *over* $CS-bu_{theo}$ *calculated as* $(M(VS)-M(CS))/M(CS)$

Cylinder	Bending moment	QI_{theo}	$CS-bu_{theo}$	$VS-bu_{theo}$	$Imp(\%)$
Small	M_{b-lin} (SAFD) [kN.m]	828	1304	2126	63.1
Small	M_{b-lin} (Abaqus^{TM}) [kN.m]	816	1252	2107	68.2
Small	M_f (SAFD) [kN.m]	810	454	919	102.3
Large	M_{b-lin} (SAFD) [kN.m]	3841	8107	11974	47.7
Large	M_{b-lin} (Abaqus^{TM}) [kN.m]	4327	8820	12629	43.2
Large	M_f (SAFD) [kN.m]	12769	8625	12150	40.9

Improvement mechanisms

The distributions of the axial section force and axial strain of the theoretical laminate designs, QI_{theo}, $CS-bu_{theo}$ and $VS-bu_{theo}$, for the selected stiffened circular cylindrical shells are obtained from Abaqus^{TM} and plotted versus the normalised circumferential distance in figures 7.4 and 7.5.

The two end cross-sections of the circular cylinder remain planar during bending deformation and hence the axial strain distributions of all laminate designs are sinusoidal as depicted in figures 7.4(a) and 7.5(a). Similar to the unstiffened circular cylinder in subsection 6.2.1, the neutral axis of the QI_{theo} and $CS-bu_{theo}$ laminate designs are coincident with the diameter of the circular cross-section, about which the bending moment is applied, while the neutral axis of the $VS-bu_{theo}$ laminate design is moved toward the tension side.

7

The axial sectional force distributions of QI_{theo} and $CS-bu_{theo}$ laminate designs, shown in figures 7.4(b) and 7.5(b), are also sinusoidal due to the uniform stiffness distribution. Unlike the unstiffened circular cylinder, in the stiffened circular cylinders the axial section force distributions of QI_{theo}, $CS-bu_{theo}$ laminate designs, which are calculated at the same bending moment, are not the same. The reason is different load distributions between the cylindrical shell and the stiffeners due to the different laminate stiffness properties in QI_{theo} and $CS-bu_{theo}$ designs. The magnitudes of the maximum axial compressive and tensile section forces for $CS-bu_{theo}$ design are less than those for the QI_{theo} design, while the magnitudes of the maximum axial compressive and tensile strains for $CS-bu_{theo}$ design are larger than those for the QI_{theo} design. Therefore, the QI_{theo} laminate design is stiffer than the $CS-bu_{theo}$ laminate design in the axial direction.

As shown in figures 7.4(b) and 7.5(b), the axial section force distributions of the $VS-bu_{theo}$ laminate designs are not sinusoidal due to the circumferential stiffness

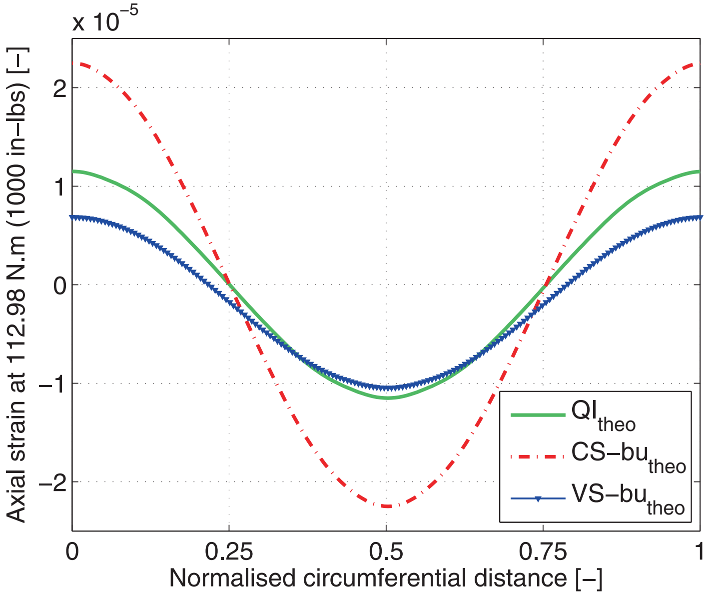

(a) Axial strain

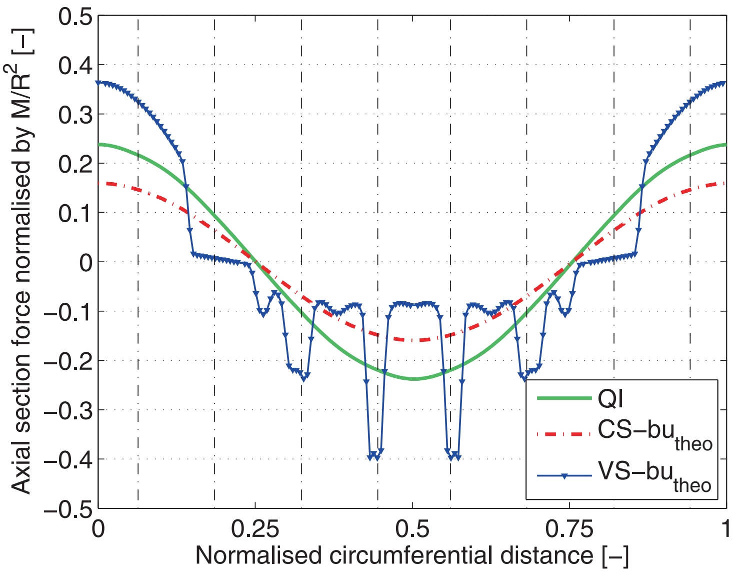

(b) Axial section load

FIGURE 7.4: Axial strain and axial section force of theoretical quasi-isotropic, QI_{theo}, theoretical constant stiffness, $CS-bu_{theo}$, and theoretical variable stiffness constant thickness, $VS-bu_{theo}$, laminate designs for maximum buckling moment in the stiffened small circular cylinders under bending based on Abaqus^{TM} results, *Note: normalised circumferential distance starts from the point with the maximum axial tension and dash-dot lines indicate the location of stiffeners in the cross-section*

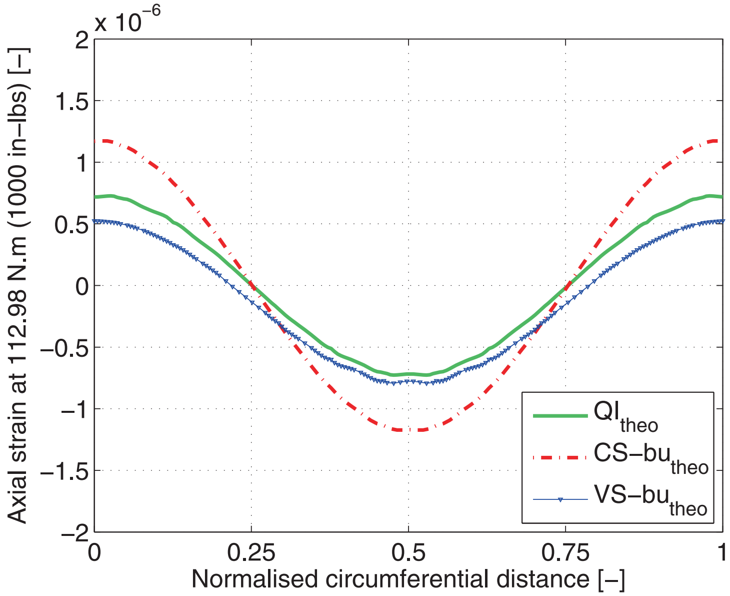

(a) Axial strain

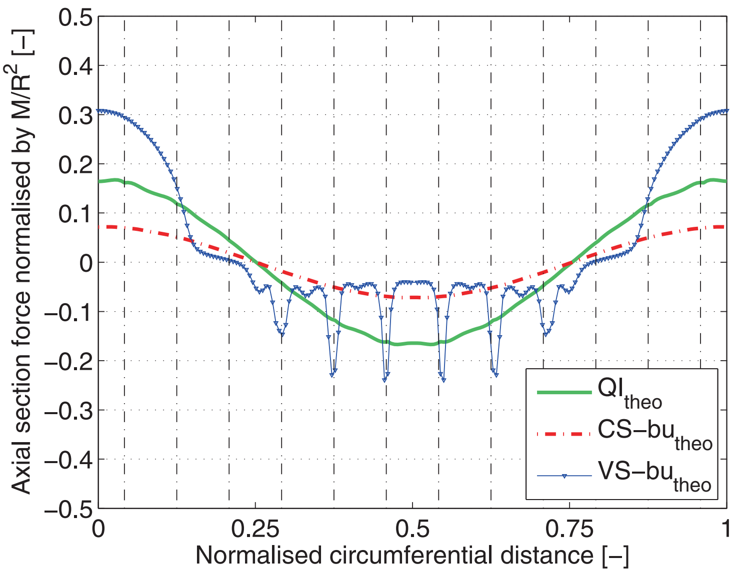

(b) Axial section load

FIGURE 7.5: Axial strain and axial section force of theoretical quasi-isotropic, QI_{theo}, theoretical constant stiffness, $CS-bu_{theo}$, and theoretical variable stiffness constant thickness, $VS-bu_{theo}$, laminate designs for maximum buckling moment in the stiffened large circular cylinders under bending based on Abaqus^{TM} results, *Note: normalised circumferential distance starts from the point with the maximum axial tension and dash-dot lines indicate the location of stiffeners in the cross-section*

tailoring. The maximum axial tensile section force of the $VS - bu_{theo}$ laminate design is larger than that of the $CS - bu_{theo}$ laminate design. In the unstiffened cross-sectional areas, placed between stiffeners, the distribution of axial compressive section force of the $VS - bu_{theo}$ laminate design is almost uniform and its magnitude is reduced compared to the $CS - bu_{theo}$ laminate designs. In the stiffened cross-sectional locations, the magnitude of axial compressive section force of the $VS - bu_{theo}$ laminate design is increased compared to the unstiffened cross-sectional areas. The maximum magnitude of the axial compressive section force in the stiffened cross-sectional locations of the $VS - bu_{theo}$ laminate is larger than that of the $CS - bu_{theo}$ laminate design.

Therefore, the buckling capacity of the $VS - bu_{theo}$ laminate is increased compared to the $CS - bu_{theo}$ laminate due to the reduced magnitude of axial section force in the unstiffened cross-sectional locations placed in the compression side. There are two mechanisms involved in this reduction; a global load redistribution mechanism which reduces the maximum axial compressive section force and increases the maximum axial tensile section force similar to the buckling capacity improvement mechanism of the unstiffened circular cylinder under bending moment, described in subsection 6.2.1, and a local load redistribution mechanism which redirects the axial compressive section force from the middle of the unstiffened cross-sectional areas from to the stiffened locations which is similar to the buckling load improvement mechanism of the uni-axial compressive panel with imply supported enforced straight edges as shown by IJsselmuiden et al. [33].

The critical buckling modes for the QI_{theo}, $CS - bu_{theo}$ and $VS - bu_{theo}$ laminate designs of the stiffened circular cylindrical shells are shown in figures 7.6 and 7.7. It is clear that the local buckling modes of the $VS - bu_{theo}$ laminate design are expanded to a larger area in the compression side of the cross-section to use the material more efficiently.

7.2.2 THEORETICAL VARIABLE THICKNESS LAMINATE

For the selected longitudinally stiffened cylindrical shells, the theoretical variable thickness VS laminate designs, with the same weight as the constant thickness VS laminates, are obtained for maximum buckling capacity by solving the optimisation problem in equation 6.4 in the first step of the multi-step optimisation framework. The baseline constant thickness laminate is comprised of 24 layers and the number of layers of the variable thickness laminate is bounded between 16 and 32 layers. Similar to the constant thickness laminates, two in-plane lamination parameters, V_{1A} and V_{3A}, and two out of plane lamination parameters, V_{1D} and V_{3D}, are used as design variables to find the theoretical balanced symmetric laminate designs and 60 buckling modes are considered in the multi-modal buckling optimisation problem.

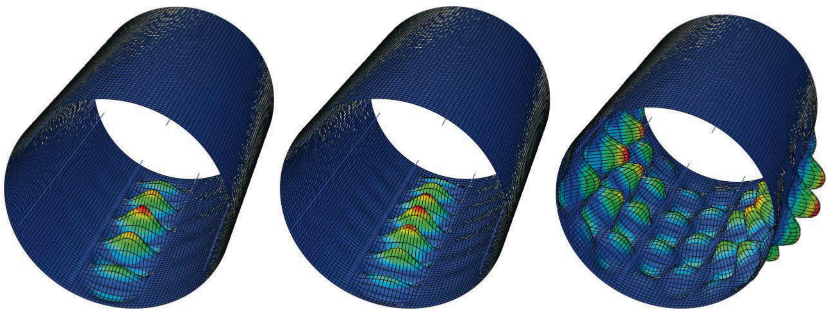

(a) QI_{theo} (b) $CS-bu_{theo}$ (c) $VS-bu_{theo}$

FIGURE 7.6: Critical buckling modes of theoretical quasi-isotropic, QI_{theo}, theoretical constant stiffness, $CS-bu_{theo}$, and theoretical variable stiffness constant thickness, $VS-bu_{theo}$, laminate designs for maximum buckling moment of the stiffened small circular cylinder under bending

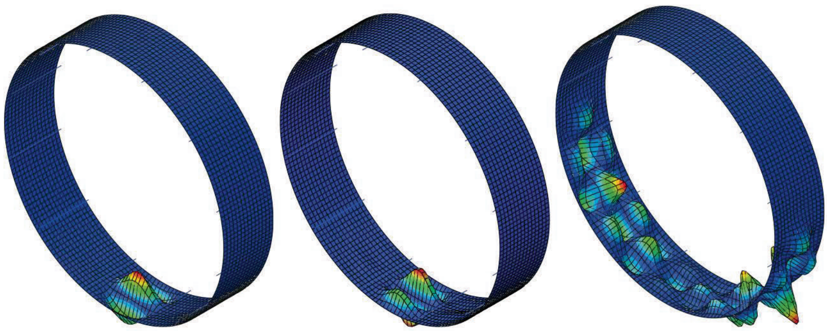

(a) QI_{theo} (b) $CS-bu_{theo}$ (c) $VS-bu_{theo}$

FIGURE 7.7: Critical buckling modes of theoretical quasi-isotropic, QI_{theo}, theoretical constant stiffness, $CS-bu_{theo}$, and theoretical variable stiffness constant thickness, $VS-bu_{theo}$, laminate designs for maximum buckling moment of the stiffened large circular cylinder under bending

TABLE 7.3: Linear buckling moments of theoretical variable stiffness constant thickness, $VS - bu_{theo}$, and theoretical variable stiffness variable thickness, $VSVT - bu_{theo}$, laminate designs for maximum buckling moment of stiffened circular cylinder under bending, *Note:* M_{b-lin} *= linear buckling moment from the semi-analytical finite difference (SAFD) and Abaqus*^{TM}*, and* Imp *= improvements of* $VSVT - bu_{theo}$ *over* $VS - bu_{theo}$ *calculated as* $(M(VSVT) - M(VS))/M(VS)$

Cylinder	Bending moment	$VS - bu_{theo}$	$VSVT - bu_{theo}$	Imp(%)
Small	M_{b-lin} (SAFD) [kN.m]	2126	3318	56.0
Small	M_{b-lin} (Abaqus^{TM}) [kN.m]	2107	3159	50.0
Large	M_{b-lin} (SAFD) [kN.m]	11974	18237	52.3
Large	M_{b-lin} (Abaqus^{TM}) [kN.m]	12150	19157	57.7

The optimum distributions of lamination parameters and laminate thickness for the two selected longitudinally stiffened cylinders are depicted in Figs 7.8 an 7.9, respectively.

In table 7.3, the linear buckling moments of the variable thickness VS laminate designs for maximum buckling moment, $VSVT - bu_{theo}$, are listed and compared with the linear buckling moments of the baseline constant thickness VS laminate designs for maximum buckling moment, $VS - bu_{theo}$. The linear buckling moments of the $VSVT - bu_{theo}$ designs from SAFD and Abaqus^{TM} are in good agreement with less than 6% difference. By varying the laminate thickness in addition to the fibre steering, based on the ^{TM} results, the buckling capacity improvements of 50% and 57.7% are theoretically achievable in the small and large cylinders, respectively.

Improvement mechanisms

The distributions of the axial strain and section load of the $VSVT - bu_{theo}$ laminate design of the stiffened circular cylinders are depicted in figures 7.10 and 7.11. The distributions of axial strain for both cylinders, shown in figures 7.10(a) and 7.11(a), are sinusoidal. The distributions of the axial section load in the compressive unstiffened cross-sectional areas between the stiffeners are the same for the $VS - bu_{theo}$ and $VSVT - bu_{theo}$ laminate designs and therefore the buckling moment improvements are due to the increased bending stiffness.

The critical buckling modes of the $VSVT - bu_{theo}$ laminate designs are depicted in figures 7.12 and 7.13. The effect of the increased laminate thickness in the compression side of the cross-section of the stiffened small cylinder is visible in the critical buckling mode shape of the stiffened small cylinder in figure 7.12.

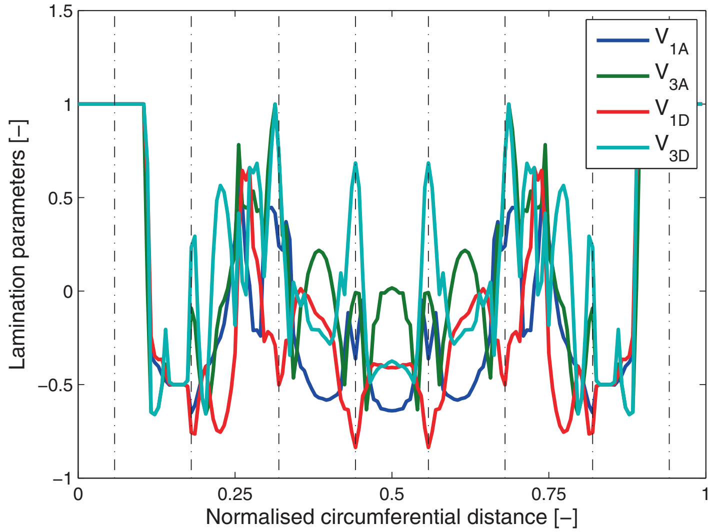

(a) $VSVT - bu_{theo}$ design of the small cylinder

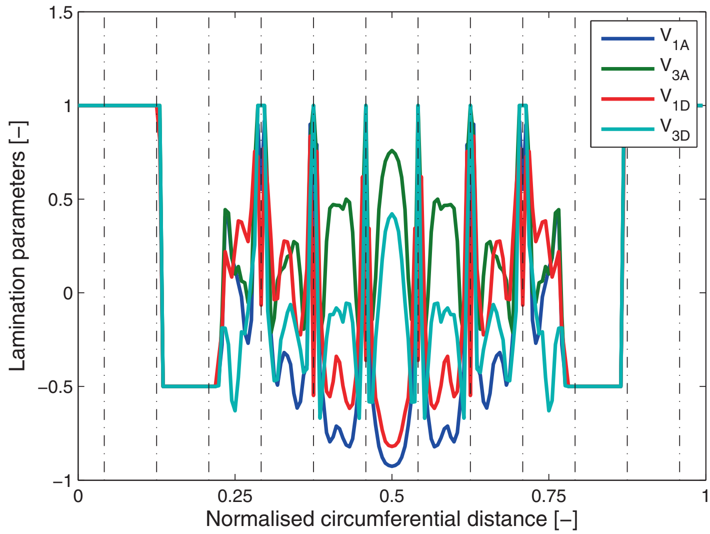

(b) $VSVT - bu_{theo}$ design of the large cylinder

FIGURE 7.8: Distribution of lamination parameters in theoretical variable stiffness variable thickness laminate designs for maximum buckling moment, $VSVT - bu_{theo}$, in stiffened circular cylinders under bending, *Note: normalised circumferential distance starts from the point with maximum axial tension*

7

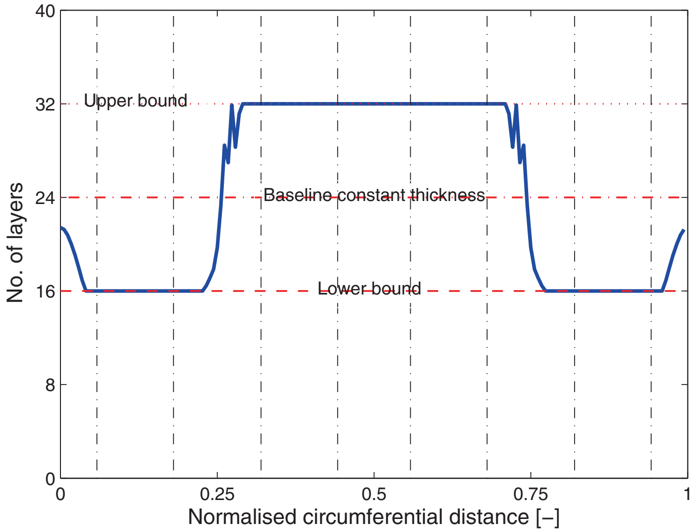

(a) $VSVT - bu_{theo}$ design of the small cylinder

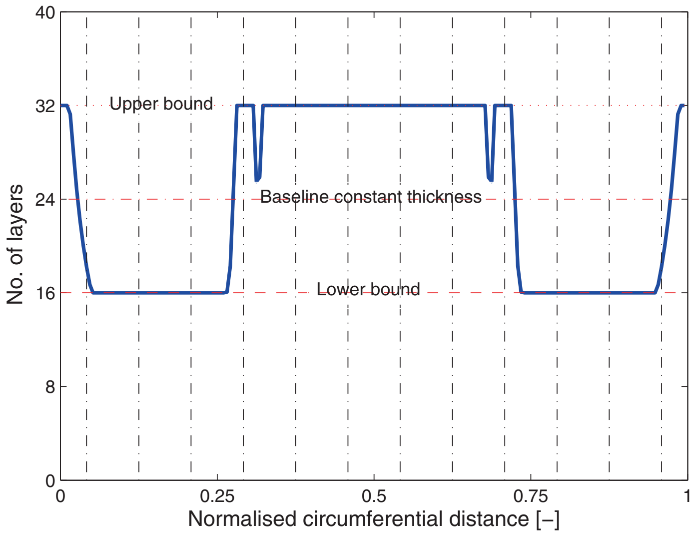

(b) $VSVT - bu_{theo}$ design of the large cylinder

FIGURE 7.9: Laminate thickness variation in theoretical variable stiffness variable thickness laminate designs for maximum buckling moment, $VSVT - bu_{theo}$, in stiffened circular cylinders under bending, *Note: normalised circumferential distance starts from the point with maximum axial tension*

7

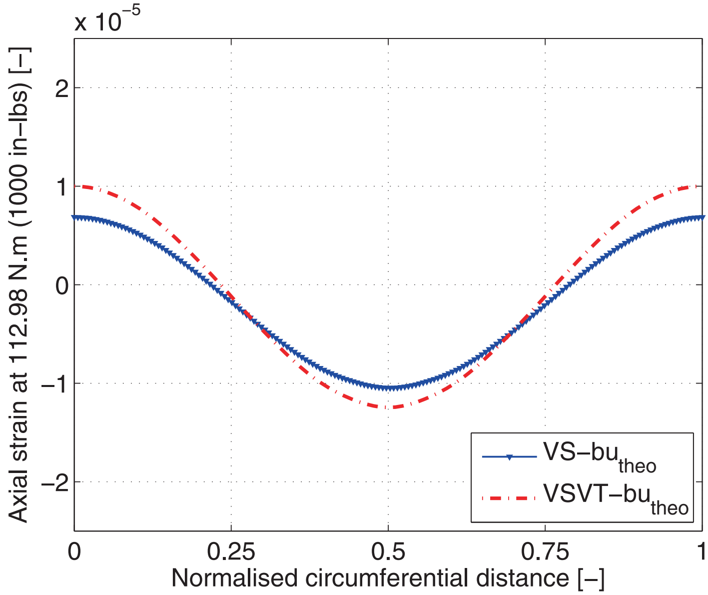

(a) Axial strain

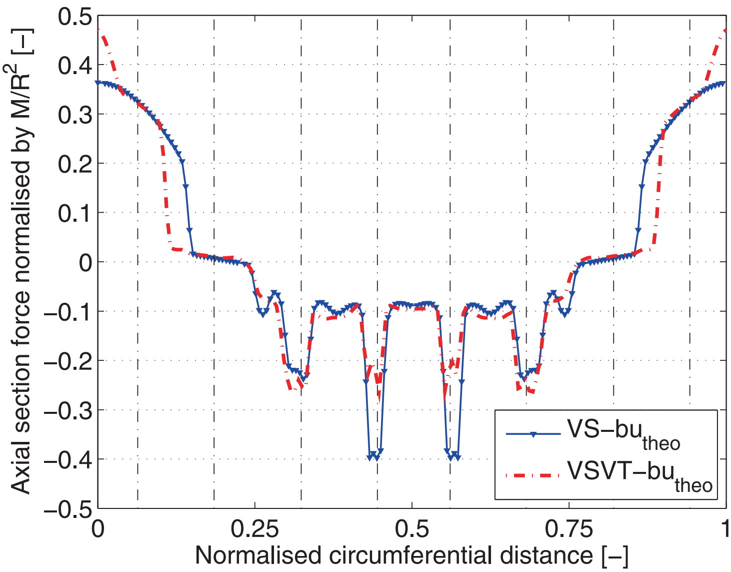

(b) Axial section force

FIGURE 7.10: Axial strain and axial section force of theoretical variable stiffness constant thickness, $VS-bu_{theo}$, and variable stiffness variable thickness, $VSVT-bu_{theo}$, laminate designs for maximum buckling moment of the stiffened small circular cylinder under bending based on Abaqus^{TM} results, *Note: normalised circumferential distance starts from the point with the maximum axial tension*

7

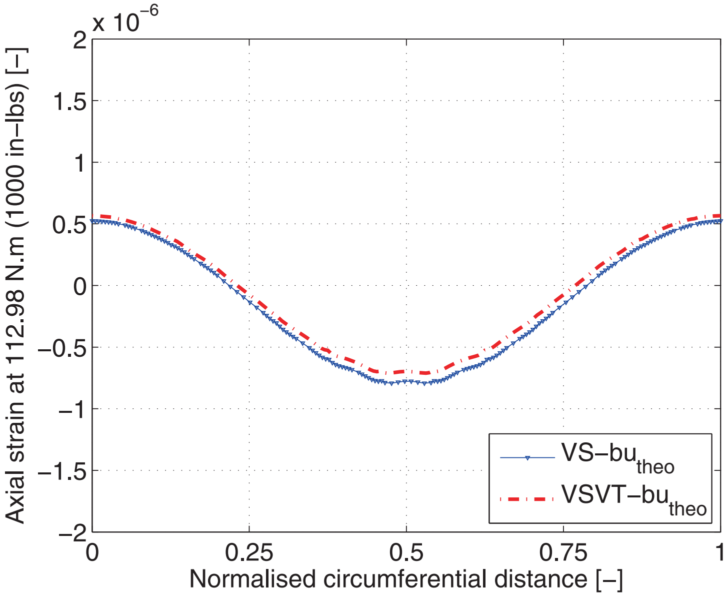

(a) Axial strain

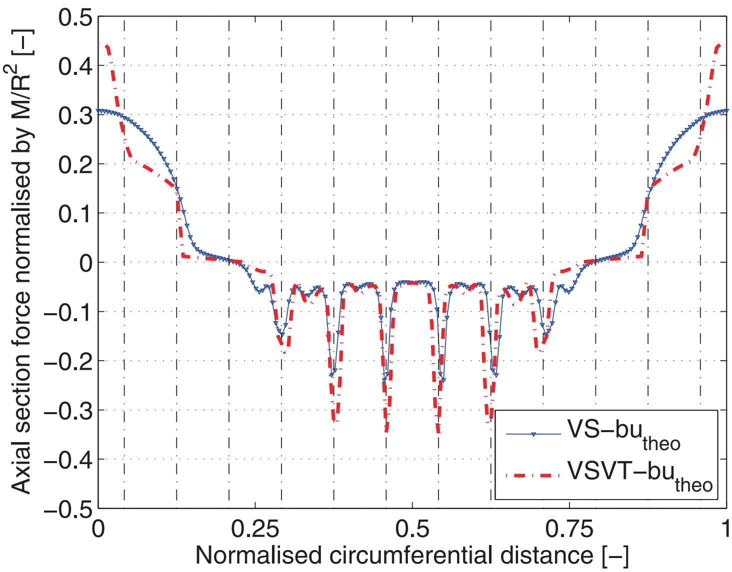

(b) Axial section force

FIGURE 7.11: Axial strain and axial section force of theoretical variable stiffness constant thickness, $VS-bu_{theo}$, and variable stiffness variable thickness, $VSVT-bu_{theo}$, laminate designs for maximum buckling moment of the stiffened large circular cylinder under bending based on Abaqus^{TM} results, *Note: normalised circumferential distance starts from the point with the maximum axial tension*

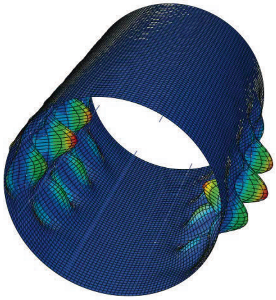

FIGURE 7.12: Critical buckling mode of theoretical variable stiffness variable thickness laminate design for maximum buckling moment, $VSVT-bu_{theo}$, of the stiffened small circular cylinder under bending moment based on Abaqus^{TM} results

FIGURE 7.13: Critical buckling mode of theoretical variable stiffness variable thickness laminate design for maximum buckling moment, $VSVT-bu_{theo}$, of the stiffened large circular cylinder under bending moment based on Abaqus^{TM} results

7.2.3 REALISTIC CONSTANT THICKNESS LAMINATE

In the second step of the multi-step optimisation framework, the realistic CS and constant thickness VS laminate designs are retrieved from the corresponding theoretical designs for maximum buckling capacity, found in the first step. The straight and steered fibre laminates are retrieved in the form of 24 layer balanced symmetric laminates, $[\pm\theta_1,\pm\theta_2,\pm\theta_3,\pm\theta_4,\pm\theta_5,\pm\theta_6]_s$.

The realistic CS laminates for maximum buckling moment, $CS-bu_{real}$, which are retrieved from the corresponding theoretical CS laminates, $CS-bu_{theo}$, using GA, are:

$$\begin{aligned} CS-bu_{real}\ \text{(Small)} :& [\pm\theta_1,\pm\theta_2,\pm\theta_3,\pm\theta_4,\pm\theta_5,\pm\theta_6]_s = \\ & [\pm 21.0,\pm 63.8,\pm 68.5,\pm 68.9,\pm 70.2,\pm 71.0]_s \\ CS-bu_{real}\ \text{(Large)} :& [\pm\theta_1,\pm\theta_2,\pm\theta_3,\pm\theta_4,\pm\theta_5,\pm\theta_6]_s = \\ & [\pm 31.0,\pm 64.8,\pm 68.9,\pm 71.1,\pm 72.7,\pm 72.9]_s \end{aligned}$$

The circumferential distributions of fibre angles in each ply of the realistic constant thickness VS laminate designs for maximum buckling moment, $VS-bu_{real}$, are retrieved from the corresponding theoretical constant thickness VS designs, $VS-bu_{theo}$, while constraining the average steering curvature. Pareto fronts showing the linear buckling and material failure moments of the $VS-bu_{real}$ designs versus the amount of average steering curvature, κ, are depicted in figure 7.14.

As described in subsection 6.2.3, performance of the theoretical designs is considered to be an upper-bound for the performance of realistic designs primarily due to the limited number of layers, the ply angles or the fibre angle distributions of which are used as design variables to find the realistic CS or VS laminates, respectively. It is clear from figure 7.14, the buckling and failure moments of the retrieved realistic VS laminates are less than the buckling and failure moments of the theoretical VS laminate designs.

By tightening the constraint on the average steering curvature of realistic VS laminates, the buckling and failure moments are degraded as shown in figure 7.14. The realistic VS laminate designs are expected to be superior than the theoretical CS laminate designs, even for small steering curvatures. However, as it is depicted in figure 7.14, the buckling moment of the realistic VS laminates becomes equal and less than the buckling moment of the theoretical CS design at average steering curvatures of 2.95 m^{-1} (0.075 in^{-1}) and 1.97 m^{-1} (0.05 in^{-1}) for the small and large cylinders, respectively.

As described in subsection 4.5.3, the gradient-based optimiser in the second-step of the multi-step optimisation framework, finds the fibre angle distribution which minimises the Lagrangian built from the convex conservative separable approximations of inverse of buckling moment at the theoretical VS design. There-

7

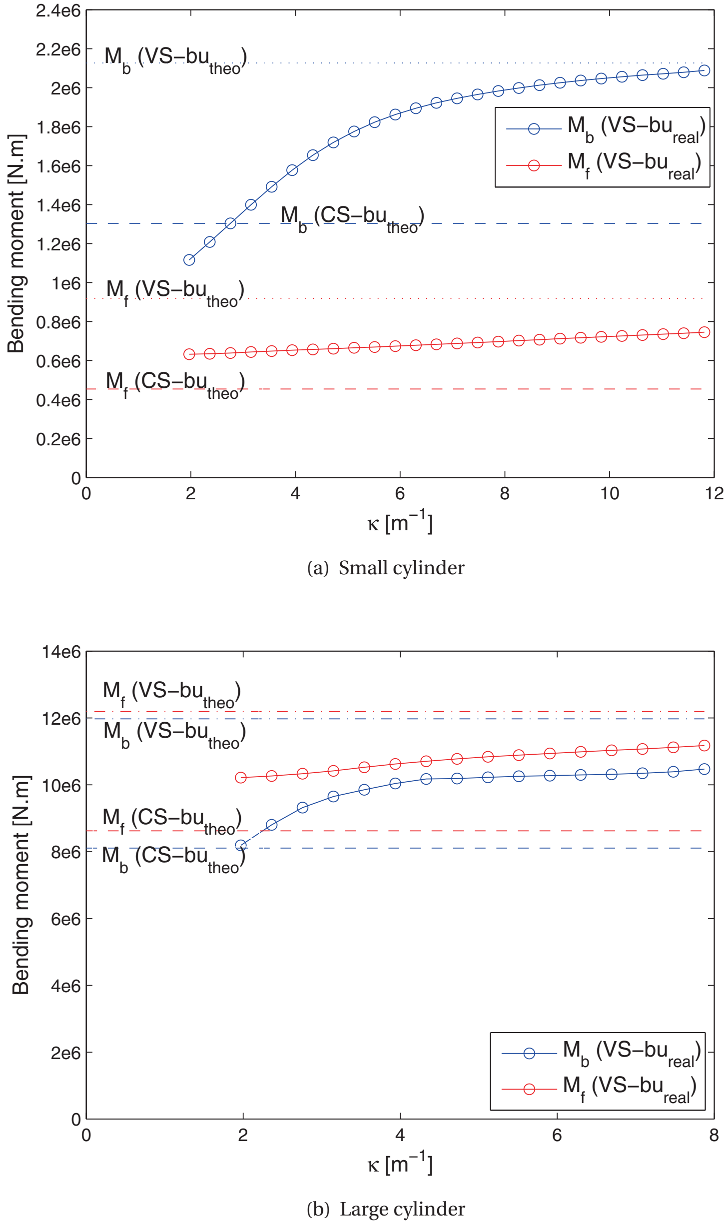

(a) Small cylinder

(b) Large cylinder

FIGURE 7.14: Pareto fronts showing the linear buckling moment, M_b, and failure moment, M_f, versus the average steering curvature of the retrieved realistic variable stiffness constant thickness laminate designs for maximum buckling moment, $VS-bu_{real}$, of the stiffened circular cylinders under bending moment based on semi-analytical finite difference (SAFD) results

fore, the gradient-based optimisation in the second step is a local search and hence the retrieved realistic VS laminate is dependent on the initial fibre angle distribution used. The pareto fronts in figure 7.14, are obtained by starting from an initial fibre angle distribution found by best matching the distribution of lamination parameters in theoretical designs using genetic algorithm (GA). Other points of the Pareto front are found from the gradient-based optimisation initialised from the fibre angle distribution of the previous point on the Pareto front and a large enough average steering curvature and tightening the constraint on the average steering curvature step by step. The local nature of the gradient-based fibre angle retrieval process and the initialisation pattern used, are the reasons for the buckling moment of the retrieved realistic VS designs with small average steering curvature values to become less than the buckling moment of the theoretical CS design.

Selection of the realistic VS design for manufacturing should be performed by calculating the local steering curvature in each of the retrieved realistic VS designs and comparing it with the maximum allowable local steering curvature which is a function of course width and material type. Since manufacturing of the realistic VS laminates is beyond the scope of this work, here, selection of the retrieved realistic VS designs is performed visually from the steered fibre paths which are enough smooth. The steered fibre paths are generated based on the streamline analogy in the third step of the multi-step optimisation framework. The steered fibre paths for average steering curvatures of $\kappa = 6.30\ \mathrm{m}^{-1}$ ($\kappa = 0.16\ \mathrm{in}^{-1}$) and $\kappa = 3.15\ \mathrm{m}^{-1}$ ($\kappa = 0.08\ \mathrm{in}^{-1}$) for the small and large cylinders are shown in figures 7.15 and 7.16, respectively. The dashed lines represent the longitudinal stiffeners.

It is well-known that the effect of layers which are placed further from the middle-surface of the shell, $\pm\theta_1$ layers in this case, on the out of plane stiffness matrix is more than the effect of layers which are placed closer to the middle-surface, $\pm\theta_6$ layers in this case, however, all the layers have the same effect on the in-plane stiffness matrix. Therefore, it is expected that for maximum buckling moment, the steered outer layers are mostly driven by the out of plane stiffness requirements while the steered inner layers mostly provide the optimum section force distribution.

It is clear from figures 7.15 and 7.16 that the steered fibre paths placed on the compression side of the circular cross-section, from 2/8 to 6/8 of the normalised circumferential distance, of both cylinders have a similar pattern. In the inner layers, the fibres are more aligned in the axial direction at the stiffener locations to have larger in-plane stiffness A_{11} and more in the circumferential direction in between the stiffeners to have smaller in-plane stiffness A_{11} and hence transfer the axial section force from the unstiffened areas to the stiffened locations, which have a larger out-of plane stiffness and are less buckling critical. In the outer layers, the fibres tend to align in the circumferential direction at the stiffener locations to in-

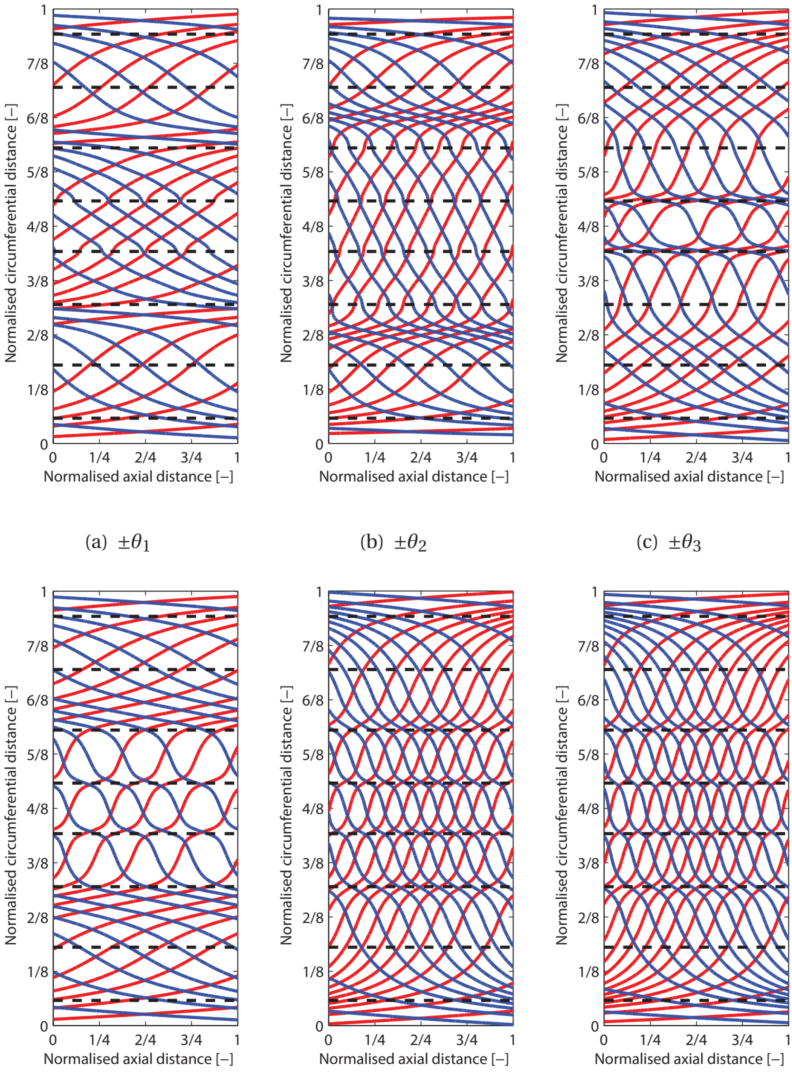

(a) $\pm\theta_1$ (b) $\pm\theta_2$ (c) $\pm\theta_3$

(d) $\pm\theta_4$ (e) $\pm\theta_5$ (f) $\pm\theta_6$

FIGURE 7.15: Optimum steered fibre paths of the realistic variable stiffness constant thickness design, $VS-bu_{real}$, with a 24 ply balanced symmetric laminate, $[\pm\theta_1,\pm\theta_2,\pm\theta_3,\pm\theta_4,\pm\theta_5,\pm\theta_6]_s$, plotted on the expanded surface of the cylinder, retrieved at average steering curvature $\kappa = 6.30\ \text{m}^{-1}$ ($\kappa = 0.16\ \text{in}^{-1}$) from the theoretical variable stiffness constant thickness design for maximum buckling moment, $VS-bu_{theo}$, in the stiffened small circular cylinder, *Note: normalised circumferential distance starts from the point with maximum axial tension and the dashed lines are the longitudinal stiffeners*

7

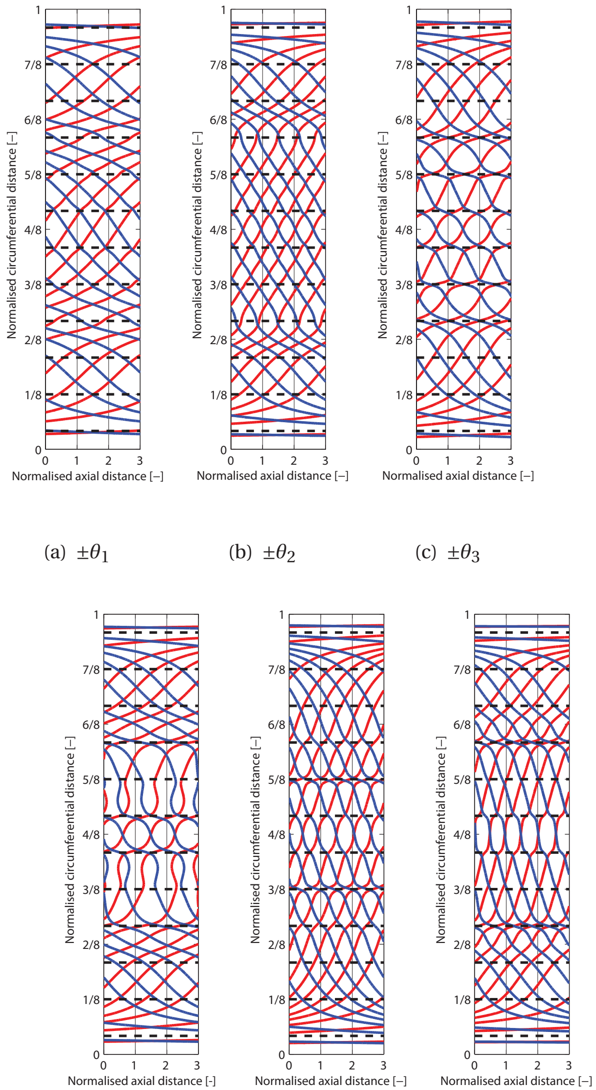

(a) $\pm\theta_1$ (b) $\pm\theta_2$ (c) $\pm\theta_3$

(d) $\pm\theta_4$ (e) $\pm\theta_5$ (f) $\pm\theta_6$

FIGURE 7.16: Optimum steered fibre paths of the realistic variable stiffness constant thickness design, $VS-bu_{real}$, with a 24 ply balanced symmetric laminate, $[\pm\theta_1,\pm\theta_2,\pm\theta_3,\pm\theta_4,\pm\theta_5,\pm\theta_6]_s$, plotted on the expanded surface of a cylinder three times longer than the original stiffened large circular cylinder, retrieved at average steering curvature $\kappa = 3.15\ \mathrm{m}^{-1}$ ($\kappa = 0.08\ \mathrm{in}^{-1}$) from the theoretical variable stiffness constant thickness design for maximum buckling moment, $VS-bu_{theo}$, in the stiffened large circular cylinder, *Note: normalised circumferential distance starts from the point with maximum axial tension and the dashed lines are the longitudinal stiffeners*

TABLE 7.4: Linear buckling moments and failure moment of realistic constant stiffness, $CS-bu_{real}$, and realistic variable stiffness constant thickness, $VS-bu_{real}$, laminate designs for maximum buckling moment in the stiffened circular cylinders under bending, *Note:* M_{b-lin} *= linear buckling moment from the semi-analytical finite difference (SAFD) and Abaqus*^{TM}), M_f *= failure moment from SAFD and conservative Tsai-Wu failure envelope,* Imp *= improvements of* $VS-bu_{real}$ *over* $CS-bu_{real}$ *calculated from* $(M(VS)-M(CS))/M(CS)$ *and the values inside parenthesis show the percentage of drop with respect to the corresponding values of the theoretical designs in table 7.2*

Cylinder	Bending moment	$CS-bu_{real}$	$VS-bu_{real}$	Imp(%)
Small	M_{b-lin} (SAFD) [kN.m]	1218 (-7 %)	1895 (-11 %)	55.5
Small	M_{b-lin} (Abaqus^{TM}) [kN.m]	1177 (-6 %)	1843 (-13 %)	56.4
Small	M_f (SAFD) [kN.m]	532 (17 %)	679 (-26 %)	27.6
Large	M_{b-lin} (SAFD) [kN.m]	7252 (-11 %)	9698 (-24 %)	33.1
Large	M_{b-lin} (Abaqus^{TM}) [kN.m]	7788 (-13 %)	9946 (-26 %)	27.7
Large	M_f (SAFD) [kN.m]	9211 (7 %)	10419 (-17 %)	13.1

crease the bending stiffness D_{22} at the stiffener locations and tend to align in the axial direction in between the stiffeners to increase the out of plane stiffness component D_{11} for the unstiffened areas in between the stiffeners. The steered fibre paths in the tension side of the circular cross-section smoothly tend to align in the axial direction in the cross-sectional location with maximum axial section force, at normalised circumferential distance 0 or 1.

The linear buckling moment and failure moment of the retrieved realistic VS designs of both cylinders are listed in table 7.4. The linear buckling moments obtained from Abaqus^{TM} are in good agreement with the SAFD results with less than 8% difference. The percentage of variation of the buckling and failure moments of the realistic designs with respect to the theoretical designs, in table 7.2, are shown inside the parentheses. The linear buckling moments of the realistic designs are dropped compared to the corresponding theoretical designs. Based on Abaqus^{TM} results, these drops are -6% and -13% for the CS laminate designs of the small and large cylinders and -13% and -26% for the VS laminate designs of the small and large cylinders, respectively. The amount of buckling moment improvements based on Abaqus^{TM} results for the realistic VS designs with respect to the realistic CS designs are 56.4% and 27.7% for the small and large cylinders, respectively. The safety factors of the realistic laminate designs of the small cylinder are less than one, 0.44 and 0.36 for the $CS-bu_{real}$ and $VS-bu_{real}$ laminates respectively and the safety factors of the realistic laminate designs of the large cylinder are greater than one, 1.27 and 1.08 for the $CS-bu_{real}$ and $VS-bu_{real}$ laminates, respectively.

The distributions of axial strain and section force for the realistic laminates of the small and large cylinders are plotted in figures 7.17 and 7.18, respectively, and compared with those of the corresponding theoretical laminates. As it is clear from figures 7.17(d) and 7.18(d), the distribution of the axial section force and hence the buckling moment improvement of the realistic and theoretical constant thickness VS laminate designs are the same.

The critical buckling modes of the $CS - bu_{real}$ and $VS - bu_{real}$ laminate designs of the stiffened circular cylindrical shells are shown in figures 7.19 and 7.20. The expanded buckling mode shapes of the theoretical VS laminate designs in figures 7.6(c) and 7.7(c) are confined to one unstiffened area between two stiffeners as shown in figures 7.19(b) and 7.20(b).

7.3 MAXIMUM BUCKLING MOMENT DESIGN WITH CONSTRAINT ON STRENGTH

It was shown in section 7.2 that the maximum buckling moment designs of the longitudinally stiffened small circular cylinder are material failure critical. Therefore, in this section the optimisation problem is formulated to find the maximum buckling moment designs with consideration of strength constraints. Theoretical and realistic constant thickness laminate designs are investigated in subsections 7.3.1 and 7.3.2, respectively.

7.3.1 THEORETICAL CONSTANT THICKNESS LAMINATE

The design drivers for finding the theoretical designs in the first step of the multi-step optimisation framework are the buckling moment and material strength of the stiffened small circular cylindrical shell. Pareto fronts, which show the buckling moment versus the material failure moment, are constructed for theoretical laminate designs of the stiffened small circular cylinder under bending moment similar to the Pareto fronts built for unstiffened circular cylinders in subsection 6.2.1. Only four lamination parameters V_{1A}, V_{3A}, V_{1D} and V_{3D} are selected as the design variables in the first step of the multi-step framework and the multi-modality of the buckling optimisation problem is 60.

Pareto fronts of buckling moment values versus the failure moment values of theoretical designs, based on the SAFD analysis results, are shown in figure 7.21. The failure moment values of the designs located below the diagonal line are larger than their buckling moment values. Among these buckling critical designs, the maximum buckling moment CS and VS designs are selected, which have safety factors of 1.12 and 1.23.

The optimum set of lamination parameters in the selected theoretical CS design for maximum buckling moment with strength constraints, $CS - bust_{theo}$, is:

$$CS - bust_{theo} : [V_{1A}, V_{3A}, V_{1D}, V_{3D}] = [0.08, 0.45, 0.52, -0.13]$$

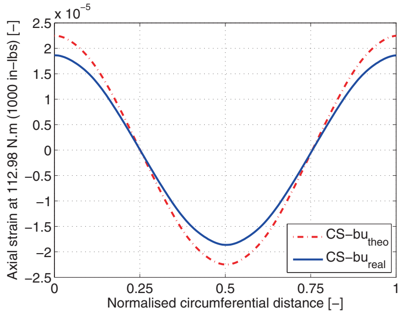

(a) Axial strain in the CS laminate

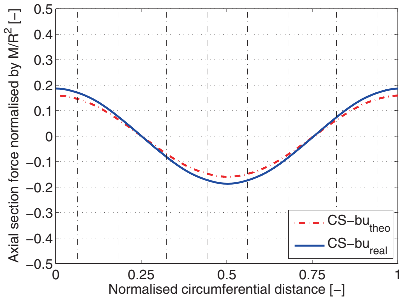

(b) Axial section load in the CS laminate

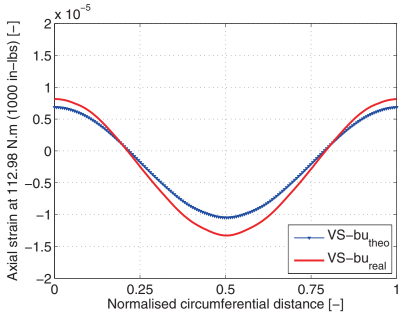

(c) Axial strain in the VS laminate

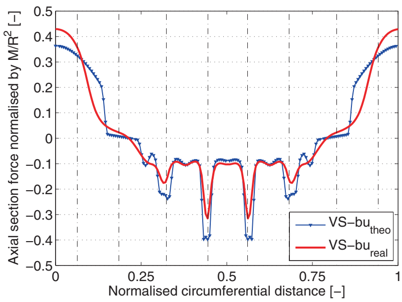

(d) Axial section load in the VS laminate

FIGURE 7.17: Axial strain and axial section force of realistic constant stiffness, $CS-bu_{real}$, theoretical constant stiffness, $CS-bu_{theo}$, realistic variable stiffness constant thickness, $VS-bu_{real}$, and theoretical variable stiffness constant thickness, $VS-bu_{theo}$, laminate designs for maximum buckling moment in the stiffened small circular cylinders under bending based on Abaqus^{TM} results, *Note: normalised circumferential distance starts from the point with the maximum axial tension and dash-dot lines indicate the location of stiffeners in the cross-section*

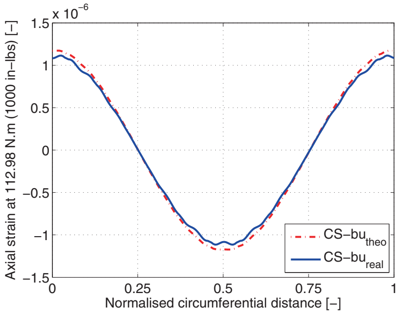

(a) Axial strain in the CS laminates

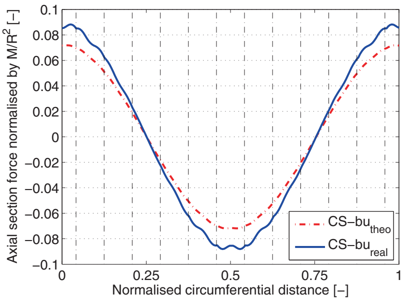

(b) Axial section load in the CS laminates

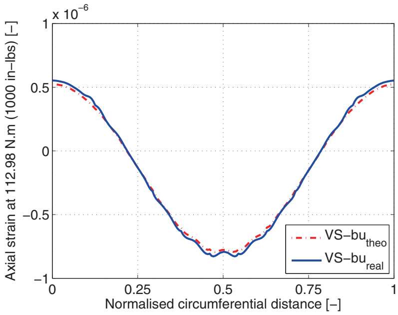

(c) Axial strain in the VS laminates

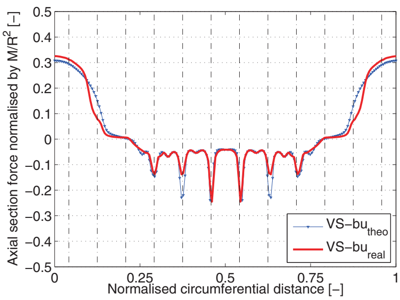

(d) Axial section load in the VS laminates

FIGURE 7.18: Axial strain and axial section force of realistic constant stiffness, $CS - bu_{real}$, theoretical constant stiffness, $CS - bu_{theo}$, realistic variable stiffness constant thickness, $VS - bu_{real}$, and theoretical variable stiffness constant thickness, $VS - bu_{theo}$, laminate designs for maximum buckling moment in the stiffened large circular cylinders under bending based on Abaqus^{TM} results, *Note: normalised circumferential distance starts from the point with the maximum axial tension and dash-dot lines indicate the location of stiffeners in the cross-section*

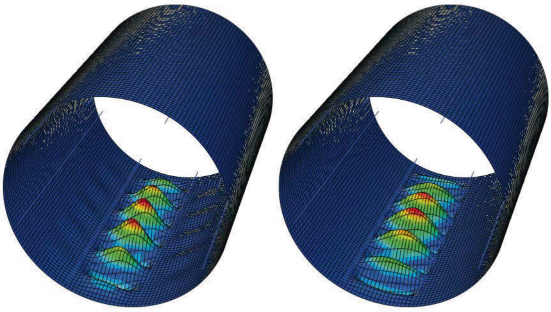

(a) $CS - bu_{real}$ (b) $VS - bu_{real}$

FIGURE 7.19: Critical buckling modes of realistic constant stiffness, $CS - bu_{real}$, and realistic variable stiffness constant thickness, $VS - bu_{real}$, laminate designs for maximum buckling moment of the stiffened small circular cylinder under bending from Abaqus^{TM}

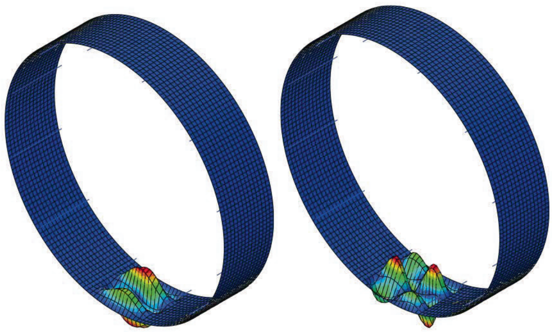

(a) $CS - bu_{real}$ (b) $VS - bu_{real}$

FIGURE 7.20: Critical buckling modes of realistic constant stiffness, $CS - bu_{real}$, and realistic variable stiffness constant thickness, $VS - bu_{real}$, laminate designs for maximum buckling moment of the stiffened large circular cylinder under bending from Abaqus^{TM}

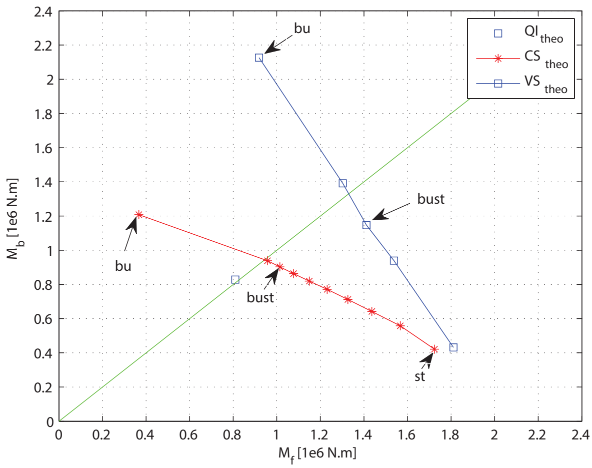

FIGURE 7.21: Pareto fronts of buckling moment versus failure moment for theoretical constant stiffness and variable stiffness constant thickness laminate designs of the stiffened small circular cylinder under bending, *Note:* M_{b-lin} *= linear buckling moment from the semi-analytical finite difference (SAFD),* M_f *= failure moment from SAFD and conservative Tsai-Wu failure envelope,* QI_{theo} *= theoretical quasi-isotropic laminate,* CS_{theo} *= theoretical constant stiffness laminates,* VS_{theo} *= theoretical variable stiffness laminates,* bu *= maximum buckling capacity design,* $bust$ *= selected design for maximum buckling capacity with strength constraints, and* st *= maximum strength design*

The optimum distribution of lamination parameters of the theoretical VS designs, $VS - bust_{theo}$, is shown in figure 7.22.

The linear buckling and failure moments of the designs for maximum buckling moment with strength constraints including the theoretical CS, $CS - bust_{theo}$, and the theoretical VS, $VS - bust_{theo}$, laminates are listed in table 7.5 using SAFD and Abaqus^{TM} analyses. The SAFD buckling moments are in good agreement with the results from the commercial finite element software Abaqus^{TM} and show less than 5% difference. The amount of improvement in the buckling moment of the VS design with respect to the CS design is 23.3% based on Abaqus^{TM} linear buckling moment results.

The distributions of axial strain and axial section force around the circumference of the stiffened cylinder with theoretical laminate designs are obtained from Abaqus^{TM} and plotted versus the normalised circumferential distance in figure 7.23. Locations of stiffeners in the circumference are specified by dash-dot lines.

7

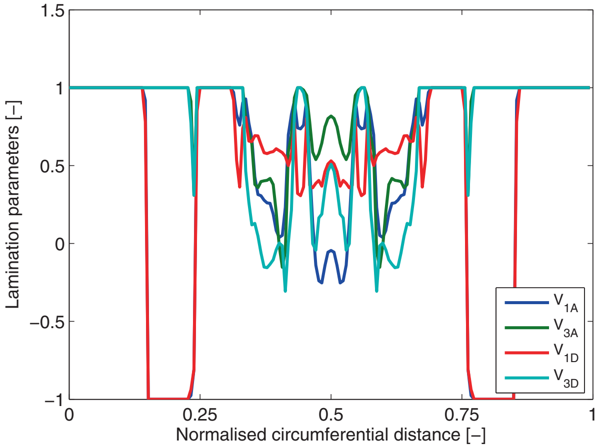

FIGURE 7.22: Distribution of lamination parameters in theoretical variable stiffness constant thickness laminate design for maximum buckling moment with strength constraints, $VS-bu_{theo}$, of the stiffened small circular cylinder under bending, *Note: normalised circumferential distance starts from the point with maximum axial tension*

TABLE 7.5: Linear buckling moments and failure moments of selected theoretical constant stiffness, $CS-bust_{theo}$, and selected theoretical variable stiffness constant thickness, $VS-bust_{theo}$, laminate designs for maximum buckling moment with strength constraints in the circular cylinder under bending, *Note:* M_{b-lin} *= linear buckling moment from the semi-analytical finite difference (SAFD) and Abaqus*^{TM}, M_f *= failure moment from SAFD and conservative Tsai-Wu failure envelope and* Imp *= improvements of* $VS-bust_{theo}$ *over* $CS-bust_{theo}$ *calculated as* $(M(VS)-M(CS))/M(CS)$

Design	$CS-bust_{theo}$	$VS-bust_{theo}$	Imp(%)
M_{b-lin} (SAFD) [kN.m]	903	1147	27.0
M_{b-lin} (Abaqus^{TM}) [kN.m]	876	1097	25.3
M_f (SAFD) [kN.m]	1013	1412	39.4

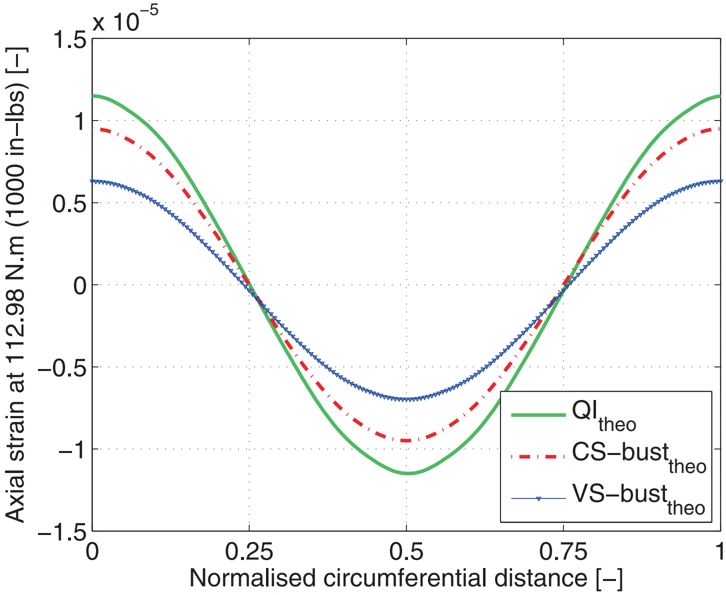

(a) Axial strain

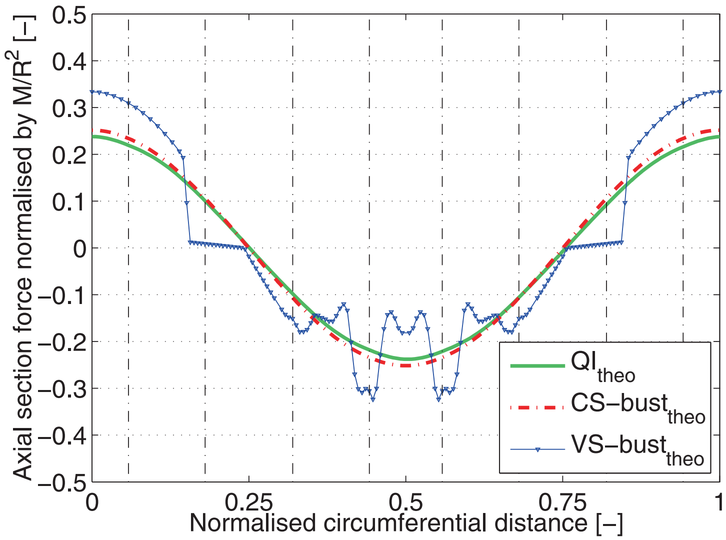

(b) Axial section load

FIGURE 7.23: Axial strain and axial section force of theoretical quasi-isotropic, QI_{theo}, selected theoretical constant stiffness, $CS-bust_{theo}$, and selected theoretical variable stiffness constant thickness, $VS-bust_{theo}$, laminate designs for maximum buckling moment with strength constraints in the stiffened small circular cylinders under bending based on Abaqus^{TM} results, *Note: normalised circumferential distance starts from the point with the maximum axial tension and dash-dot lines indicate the location of stiffeners in the cross-section*

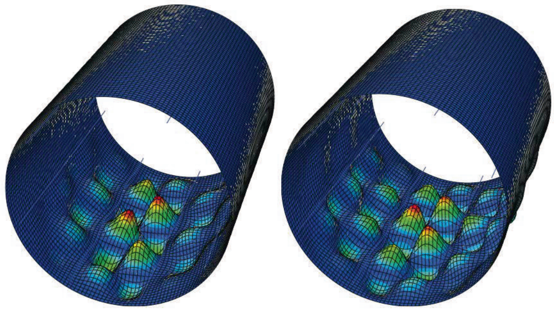

(a) $CS-bust_{theo}$ (b) $VS-bust_{theo}$

FIGURE 7.24: Critical buckling modes of selected theoretical constant stiffness, $CS-bust_{theo}$, and selected theoretical variable stiffness constant thickness, $VS-bust_{theo}$, laminate designs for maximum buckling moment with strength constraints in the stiffened small circular cylinder under bending from Abaqus^{TM}

Critical buckling modes of the $CS-bust_{theo}$ and $VS-bust_{theo}$ designs of the stiffened small circular cylinder are shown and compared in Fig 7.24.

7.3.2 REALISTIC CONSTANT THICKNESS LAMINATE

The optimum ply angles of the realistic CS laminate design, $CS-bust_{real}$, and the optimum distribution of fibre angles in each ply for the realistic VS laminate design, $VS-bust_{theo}$, are retrieved from the selected theoretical laminate designs, $CS-bust_{theo}$ and $VS-bust_{theo}$, respectively.

The realistic straight and steered fibre laminates are retrieved in the form of a balanced symmetric layup with 24 layers, $[\pm\theta_1\ ,\ \pm\theta_2\ ,\ \pm\theta_3\ ,\ \pm\theta_4\ ,\ \pm\theta_5\ ,\ \pm\theta_6]_s$. The following realistic straight fibre laminate is found by best matching with the theoretical optimum lamination parameters using GA :

$$
\begin{aligned}
CS-bust_{real}: &[\pm\theta_1,\pm\theta_2,\pm\theta_3,\pm\theta_4,\pm\theta_5,\pm\theta_6]_s = \\
&[\pm 30.1,\pm 30.1,\pm 14.4, 0.0_2, 90.0_2, 90.0_2]_s
\end{aligned}
$$

The Pareto front showing the buckling and failure moments of the retrieved realistic VS laminates versus the average steering curvature is depicted in figure 7.25. To have a fair comparison with the retrieved realistic VS designs for maximum buckling moment in section 7.2.3, the realistic VS designs for maximum buckling moment with strength constraints at an average steering curvature of $\kappa = 6.30\ \text{m}^{-1}$ ($\kappa = 0.16\ \text{in}^{-1}$) is selected. This design is indicated as $VS-bust_{real}$ design and the

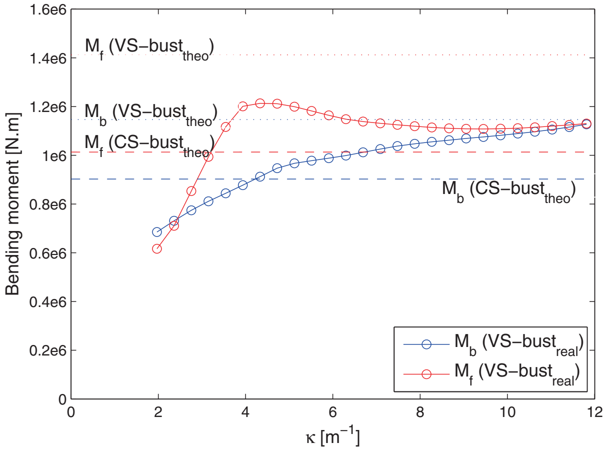

FIGURE 7.25: Pareto fronts showing the linear buckling moment, M_b, and failure moment, M_f, versus the average steering curvature of the retrieved realistic variable stiffness constant thickness laminate designs for maximum buckling moment with strength constraints, $VS-bust_{real}$, of the stiffened small circular cylinders under bending moment based on semi-analytical finite difference (SAFD) results

steered fibre paths for the realistic laminate are shown in figure 7.26. The dashed lines are representatives of longitudinal stiffeners.

The buckling and failure moments of the realistic CS, $CS-bust_{real}$, and realistic VS, $VS-bust_{real}$, laminate designs for maximum buckling moment with strength constraints are listed in table 7.6. The SAFD buckling moments are compared with the linear buckling moments from the commercial finite element software Abaqus^{TM} and show good agreement with less than 2% difference. The drops in the linear buckling moment of the realistic CS and VS designs with respect to the corresponding theoretical designs, shown inside the parentheses, are −17% and −11%, respectively based on the Abaqus^{TM} results. The amount of improvement in the buckling moment of the VS designs with respect to the CS designs is 16.7% based on Abaqus^{TM} linear buckling moment results.

Critical buckling modes of the $CS-bust_{real}$ and $VS-bust_{real}$ laminate designs of the stiffened small circular cylinder are shown and compared in Fig 7.27. It is clear that the buckling mode shape in the compression side of the cross-section of the $VS-bust_{real}$ laminate is expanded to a larger area compared to the $CS-bust_{real}$ laminate.

The distributions of axial strain and section force for the realistic laminates of

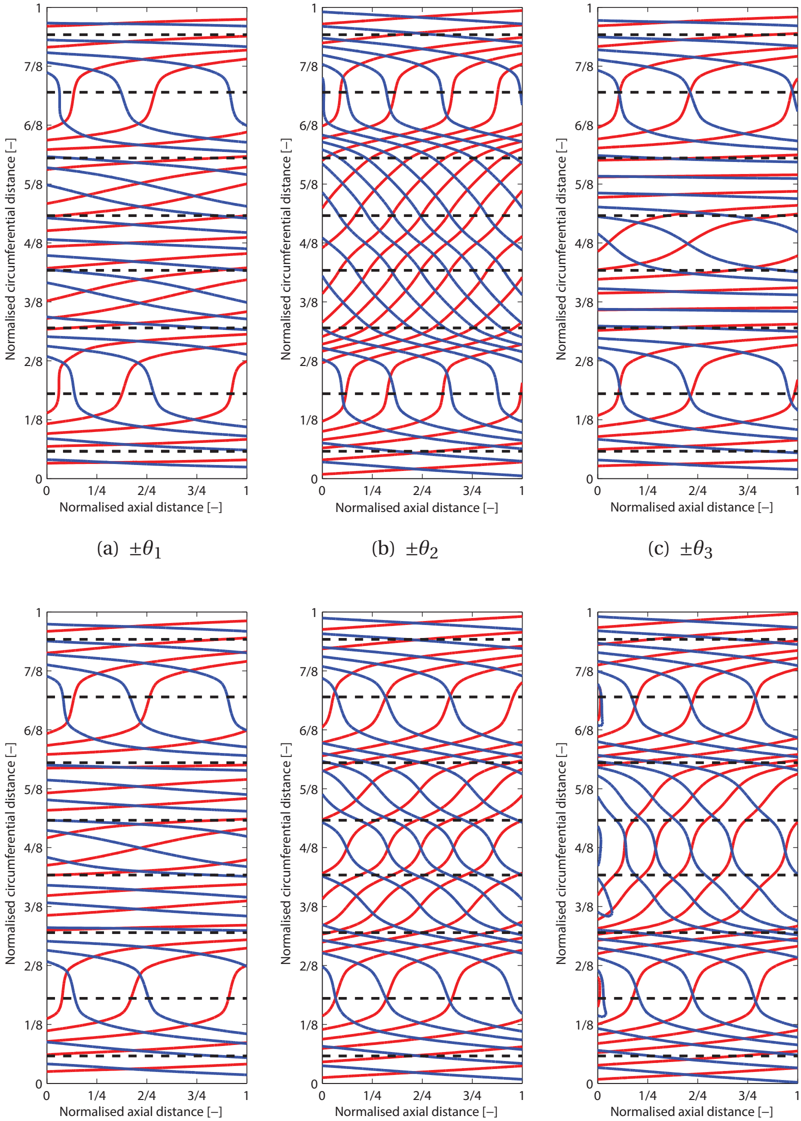

(a) $\pm\theta_1$ (b) $\pm\theta_2$ (c) $\pm\theta_3$

(d) $\pm\theta_4$ (e) $\pm\theta_5$ (f) $\pm\theta_6$

FIGURE 7.26: Optimum steered fibre paths of the realistic variable stiffness constant thickness design, $VS-bu_{real}$, with a 24 ply balanced symmetric laminate, $[\pm\theta_1,\pm\theta_2,\pm\theta_3,\pm\theta_4,\pm\theta_5,\pm\theta_6]_s$, plotted on the expanded surface of the cylinder, retrieved at average steering curvature $\kappa = 6.30$ m^{-1} ($\kappa = 0.16$ in^{-1}) from the theoretical variable stiffness constant thickness design for maximum buckling moment with strength constraints, $VS-bust_{theo}$, in the stiffened small circular cylinder, *Note: normalised circumferential distance starts from the point with maximum axial tension and the dashed lines are the longitudinal stiffeners*

TABLE 7.6: Linear and non-linear buckling moments and failure moments of realistic CS and constant thickness VS laminate design for maximum buckling moment with strength constraints in the stiffened small circular cylinder under bending, Note: M_{b-lin} = linear buckling moment, M_f = failure moment and $Imp = (M(VS) - M(CS))/M(CS)$

Design	$CS - bust_{real}$	$VS - bust_{real}$	$Imp(\%)$
M_{b-lin} (SAFD) [kN.m]	761 (-19%)	999 (-14 %)	31.1
M_{b-lin} (Abaqus^{TM}) [kN.m]	748 (-17 %)	986 (-11 %)	31.9
M_f (SAFD) [kN.m]	608 (-66 %)	1148 (-23 %)	88.8

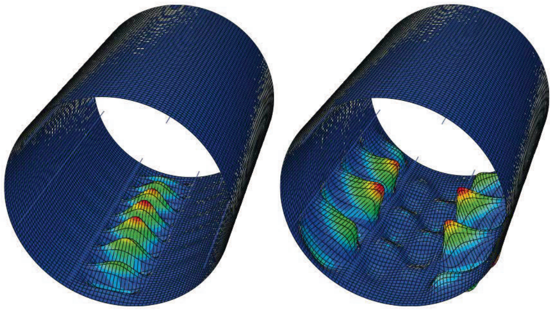

(a) $CS - bust_{real}$ (b) $VS - bust_{real}$

FIGURE 7.27: Critical buckling modes of realistic constant stiffness, $CS - bust_{real}$, and realistic variable stiffness constant thickness, $VS - bust_{real}$, laminate designs for maximum buckling moment with strength constraints in the circular cylinder under bending from Abaqus^{TM}

the stiffened small cylinder are plotted in figure 7.28 and compared with those of the corresponding theoretical laminates. As shown in figure 7.28(d), the distribution of the axial section force in the realistic VS laminate is similar to the theoretical VS laminate with less fluctuations due to the restrained average steering curvature.

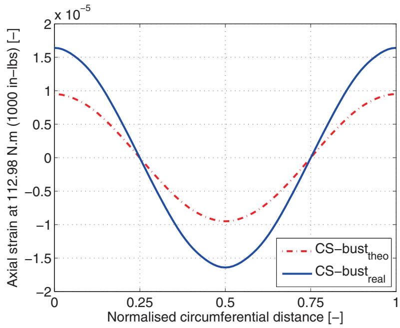

(a) Axial strain in the CS laminate

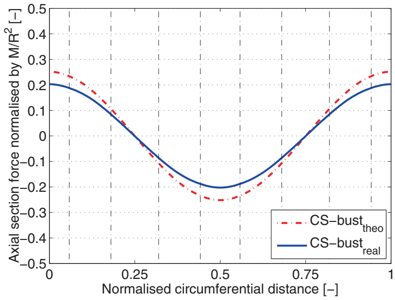

(b) Axial section load in the CS laminate

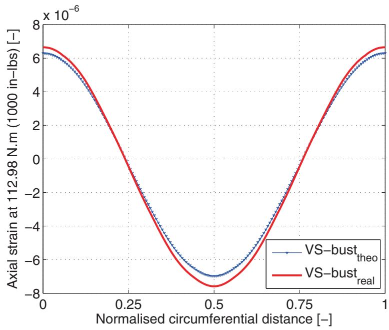

(c) Axial strain in the VS laminate

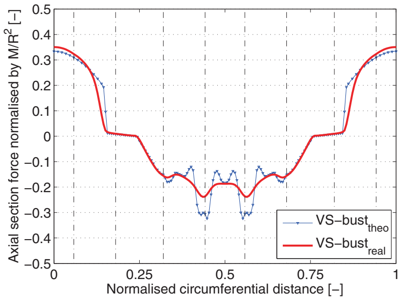

(d) Axial section load in the VS laminate

FIGURE 7.28: Axial strain and axial section force of realistic constant stiffness, $CS-bust_{real}$, theoretical constant stiffness, $CS-bust_{theo}$, realistic variable stiffness constant thickness, $VS-bust_{real}$, and theoretical variable stiffness constant thickness, $VS-bust_{theo}$, laminate designs for maximum buckling moment with strength constraints in the stiffened small circular cylinders under bending based on Abaqus^{TM} results, *Note: normalised circumferential distance starts from the point with the maximum axial tension and dash-dot lines indicate the location of stiffeners in the cross-section*

8

CONCLUSIONS AND RECOMMENDATIONS

8.1 CONCLUSIONS

A computationally efficient framework was developed for circumferential laminate stiffness tailoring of general cross-section cylinders to maximise the buckling capacity. In addition to buckling capacity, material strength constraints were considered as design drivers to ensure that the material failure did not happen before buckling. The strains, required to compute the material strength measure, and the buckling capacity were evaluated from static and buckling analyses performed using a computationally efficient semi-analytical solution.

The semi-analytical solution method was developed for static and buckling analysis of unstiffened and longitudinally stiffened cylindrical shells with general cross-sections. In the developed semi-analytical solution, only the cross-section of the cylinder was discretised. The circumferential discretisation was consistent with the circumferential stiffness tailoring and was computationally more efficient than the full finite element discretisation due to less degrees of freedom. The semi-analytical solution showed good agreement with the finite element analysis for unstiffened and longitudinally stiffened circular and elliptical cylinders (chapter 3).

A multi-step optimisation framework, developed by the ASCM group at TUDelft, was used to obtain the optimum variable stiffness (VS) laminate, tailored in the circumferential direction of the cylinder, and the baseline optimum constant stiffness (CS) laminate designs. In the first step of the multi-step framework, the output is a theoretical or conceptual optimum distribution of laminate stiffness properties, which does not provide information about the realistic layup, and the design drivers are the structural performance measures. In the seconds step, the output is the realistic optimum fibre angle or distribution of fibre angles in each layer of the CS or VS laminates, respectively. The design drivers of the second step are the theoretical designs, found in the first step, and the steering curvature constraint, which is a manufacturing constraint in automated fibre placement. In the third step, the outputs are the steered fibre paths of the VS laminate and the design driver is the optimum fibre angle distribution found in the second step (chapter 4).

The multi-step framework is based on convex separable approximations of the design drivers, which for the work reported here, were the buckling capacity and material strength. Construction of the convex separable approximation of the buckling capacity, based on the insight into the physics of the buckling problem, was explained (chapter 4).

The main contributions made by the author to the multi-step optimisation framework were to develop convex separable approximations for the material strength and to implement a constraint screening strategy in the first step to handle optimisation problems with a huge number of constraints e.g. buckling optimisation with strength constraints (chapters 4 and 5).

A failure envelope, which is developed based on the requirements of the multi-step optimisation framework, was introduced for evaluation of material strength. This failure envelope is based on the Tsai-Wu failure criterion, independent of the ply angles and conservative. The independency of the conservative failure envelope on the ply angle allows material strength to be used as a design driver in the first step of the multi-step optimisation framework, where lamination parameters were used as design variables. In this thesis, the conservative Tsai-Wu failure envelope was re-expressed as one or two elliptical equations in the strain space, depending on the material properties, to facilitate its usage in the first step of the multi-step framework (chapter 5).

8

A convex separable approximation of the failure index, which is a measure of material strength, was constructed in this thesis. Physical insight into the failure index was not sufficient to construct the convex separable approximation of failure index and hence a numerical algorithm was developed to be used in combination with physical insight. The developed numerical algorithm can be used to construct the convex approximation of any structural response without the need for a physical insight into the structural response (chapter 5).

The developed framework for circumferential laminate stiffness tailoring of general cross-section cylinders was applied on two unstiffened cylindrical shells, namely a circular cylinder under bending and an elliptical cylinder under axial compression, and two longitudinally stiffened circular cylinder under bending with different thickness to radius ratios. In each case, the theoretical and realistic CS and constant thickness VS laminate designs for maximum buckling capacity, and if necessary with consideration of strength constraints, were obtained and the buckling capacity improvements due to fibre steering and the corresponding mechanisms were investigated.

- The theoretical CS and constant thickness VS laminate designs for maximum buckling moment of the considered unstiffened circular cylinder were material failure critical. Therefore, buckling critical theoretical laminate designs were obtained by consideration of strength constraints in the optimisation problem. The selected theoretical CS and constant thickness VS laminate designs have safety factors of 1.19 and 1.12, respectively (chapter 6).
- The theoretical CS and constant thickness VS laminate designs for maximum buckling load of the considered unstiffened elliptical cylinder were buckling critical with safety factors of 2.05 and 1.61, respectively. Therefore, inclusion of strength constraints in the optimisation problem was not essential unless designs with larger safety factors were required (chapter 6).
- The theoretical CS and constant thickness VS laminate designs for maximum buckling moment of the large longitudinally stiffened circular cylinder under bending were buckling critical with safety factors of 1.06 and 1.01, respectively. However, the theoretical CS and constant thickness VS laminate designs for maximum buckling moment of the small longitudinally stiffened circular cylinder were material failure critical. Therefore, strength constraints were considered in the optimisation problem and the theoretical CS and constant thickness VS laminate designs with safety factors of 1.12 and 1.23 were selected (chapter 7).

Significant improvements were obtained in the linear buckling capacity of the selected theoretical constant thickness VS over the selected theoretical CS laminate designs. These improvements for the unstiffened circular, unstiffened elliptical, large and small stiffened circular cylinders were 28.2%, 36.7%, 43.2% and 25.3%, respectively (chapters 6 and 7).

The buckling load of the realistic laminate designs were less than the theoretical laminate designs. This was mainly due to the finite thickness of layers which limits the number of layers in the realistic CS and VS laminates with a certain thickness and constraining the average steering curvature in realistic constant thickness VS laminates (chapters 6 and 7).

A source of difference in the performance of theoretical and realistic balanced symmetric laminate designs was presence of small non-zero values for the two out of plane lamination parameters, V_{2D} and V_{4D}, in the realistic designs due to the limited number of layers, while only two in-plane lamination parameters, V_{1A} and V_{3A}, and two out of plane lamination parameters, V_{1D} and V_{3D}, were used as design variables to obtain the theoretical designs. The twist-bending coupling effect, due to V_{2D} and V_{4D}, was clearly visible in the critical buckling modes of the realistic CS and constant thickness VS laminate designs of the unstiffened circular cylinder (chapters 6 and 7).

The realistic CS and constant thickness VS laminate designs, retrieved from the selected theoretical laminate designs, were buckling critical similar to the corresponding theoretical laminate designs. However, the magnitudes of safety factor may change (chapters 6 and 7).

The improvements in the linear buckling capacity of realistic constant thickness VS laminates over realistic CS laminates were 29.6%, 17.9%, 27.7% and 31.9% for the unstiffened circular, unstiffened elliptical, large and small stiffened circular cylinders, respectively. The buckling capacity improvement of the steered fibre laminates with respect to the straight fibre ones, was due to the stiffness and section load redistribution (chapters 6 and 7).

- In the unstiffened circular cylinder under bending, the neutral axis of the constant thickness VS laminate was shifted toward the tension side. The axial section force distribution of the constant thickness VS laminate was almost uniform in the compression side of the cross-section, while this distribution for the CS laminate was sinusoidal. The magnitudes of the maximum axial section forces on the tension and compression sides of the constant thickness VS laminate were larger and smaller than the CS laminate, respectively. This was due to the stiffness tailoring that reduced the local stiffness in the compression side and stiffened the tension side. Therefore, the load was released in the compression side and transferred to the tension side. This mechanism increased the buckling load and expanded the buckling modes to a larger area in the compression side (chapter 6).

- In the unstiffened elliptical cylinder under axial compression, buckling modes of quasi-isotropic (QI) and CS laminates showed that the regions of the cross-section with larger radius of curvature were more prone to buckle. In the constant thickness VS laminates, due to the circumferential stiffness tailoring, the axial compressive section load was redistributed such that less compressive section load was carried by the regions with larger radius of curvature and more compressive section load was transferred to the areas with smaller radius of curvature, which were more buckling resistant. The buckling modes were expanded all around the circumference of the elliptical cylinder due to the stiffness tailoring, to use the material more efficiently (chapter 6).

- In the stiffened circular cylinder under bending, improvement in the buckling moment of the constant thickness VS laminate design compared to the CS laminate design was due to two mechanisms; A global load redistribution, similar to the constant thickness VS laminate design of the unstiffened circular cylinder under bending, which released the load in the compression side of the cross-section and transferred it to the tension side of the cross-section and a local load redistribution in each area between two stiffeners in the compression side of the cross-section, which reduced the compressive load in the middle of that local area and transferred it to the stiffened locations. The local load redistribution was similar to the buckling load improvement mechanism in the VS laminate design of a panel under in-plane uni-axial compression. These mechanisms were reflected in the pattern of steered fibre paths (chapter 7).

To investigate the effect of laminate thickness variation in addition to fibre steering in buckling capacity improvement, the theoretical variable thickness VS laminates of the considered case studies, the unstiffened and stiffened circular cylinders under bending and the unstiffened elliptical cylinder under axial compression, were obtained and compared with the corresponding theoretical constant thickness VS laminates (chapters 6 and 7).

Significant improvements were obtained in the buckling capacity of the theoretical variable thickness VS laminate over the theoretical constant thickness VS laminate with the same weight. Improvements of up to 45.4%, 24%, 57.7% and 50% were obtained for the selected unstiffened circular, unstiffened elliptical, large and small stiffened circular cylinders. These improvements showed the potential of laminate thickness variation in addition to fibre steering in buckling capacity improvement. The buckling capacity improvements were due to stiffness and sectional force redistribution (chapters 6 and 7).

- In the variable thickness VS laminates of the considered unstiffened and stiffened circular cylinders under bending, the laminate thickness was increased in the cross-section areas with the maximum axial compressive and tensile section loads. The axial section load of the variable thickness VS laminate in the thicker area of the tension side of the cross-section, was larger than that of the constant thickness VS laminate. In the unstiffened regions of the compression side of the cross-section, the axial section load of the variable thickness VS laminate was almost uniform and equal to that of the constant thickness VS laminate. Therefore, the main mechanism of buckling moment improvement was due to the increased out of plane stiffness, which is proportional with the third power of the laminate thickness, in the increased thickness area in the compression side (chapters 6 and 7).

- In the variable thickness VS laminate of the considered unstiffened elliptical cylinder under axial compression, the laminate thickness was increased in the cross-sectional areas with the smaller radius of curvature, which were geometrically more buckling resistant. The axial section load distributions in the constant and variable thickness VS laminate designs had the same pattern; the magnitude of axial compressive section load in the areas with smaller radius of curvature was larger than its magnitude in the areas with larger radius. The increased axial compressive section load and out of plane stiffness in the cross-sectional areas with smaller radius, which were more in the variable thickness VS laminate than the constant thickness VS laminate, were the main reasons of buckling load improvement. The effect of out of plane stiffness was evaluated to be more than the axial compressive section load, due to its third power proportionality with the thickness and the buckling mode shapes (chapter 6).

Nonlinear buckling loads of the obtained designs were close to the linear buckling loads. This showed that no significant loss of stiffness happened in the prebuckling regime. The amount of improvements in the linear and nonlinear buckling loads of the VS laminate designs compared to the CS laminate designs were almost the same or close (chapters 6 and 7).

8.2 RECOMMENDATIONS

- The semi-analytical solution method can be implemented in a finite element context, instead of finite difference, to handle cross-sections with more complex geometries.
- The effect of stiffness tailoring on post-buckling behaviour of the designed laminates should be investigated.
- The configuration of stiffeners, i.e their location, laminate and geometry, can be selected as design variables in addition to the steered fibre paths to investigate the interaction between stiffeners and stiffness tailoring due to fibre steering.
- Robustness constraints, e.g. 10% rule, are already formulated in the lamination parameters space and can be included in the first step of the multi-step framework for finding the theoretical designs. These constraints should also be imposed in the retrieved realistic designs.
- Laminate thickness was treated as a continuous design variable in theoretical designs, while it is a discrete design variable in the realistic designs.

Therefore, considering the large improvements of variable thickness laminates over constant thickness ones, the second step of the multi-step framework should be improved to retrieve realistic variable thickness laminates by determining the exact location and order of ply drops.

- The final outputs of the third step of the multi-step framework are the streamlines representing the steered fibre paths in each layer of the realistic VS laminates. The exact location of the centreline of each course and the exact cut-restart locations should be determined for manufacturing of the steered fibre constant thickness laminates.

- Using the cut-restart ability of the AFP machine, gaps and overlaps can be eliminated to the small triangular areas at the cut-restart locations and the laminate thickness becomes almost uniform. The small triangular gaps and overlaps should be taken into account in the structural analysis to investigate their effect on the structural performance.

A

Sensitivity analysis

A.1 Strength

In this section, the sensitivity of the failure index of discretisation point e with respect to the in-plane stiffness matrix of discretisation point j, $\boldsymbol{\Psi}_j^m$ and inverse of the in-plane stiffness matrix of discretisation point j, $\boldsymbol{\Phi}_j^m$, is derived. As shown in equation 5.37, the failure index can be approximated linearly in terms of strain. From equation 5.44 for the in-plane case:

$$r_s = \mathbf{N}^T \, \mathbf{A}^{-1} \, \mathbf{g} \tag{A.1}$$

The sensitivity of the failure index with respect to inverse of in-plane stiffness matrix is composed of two parts:

$$\frac{dr}{d\mathbf{A}_j^{-1}} = \frac{\partial r}{\partial \mathbf{A}_{j=e}^{-1}} + \frac{\partial r}{\partial \mathbf{N}} \frac{d\mathbf{N}}{d\mathbf{A}_j^{-1}} \tag{A.2}$$

The first term in Equation A.2 is the local part which is due to change of stiffness while load distribution is constant:

$$\frac{\partial r}{\partial \mathbf{A}_{j=e}^{-1}} = \frac{1}{2}(\mathbf{g}\mathbf{N}^T + \mathbf{N}\mathbf{g}^T) \tag{A.3}$$

and the second term is due to the change of load distribution when the stiffness properties of one element changes. Derivative of failure index with respect to the element load vector can be easily calculated as:

$$\mathbf{s} = \frac{dr}{d\mathbf{N}} = \mathbf{A}^{-1}\mathbf{g} \tag{A.4}$$

and by defining,

$$f_{loc} = \mathbf{s}^T\mathbf{N} = \mathbf{s}^T\mathbf{ABU} \tag{A.5}$$

where $\mathbf{B}$ is the strain-displacement relation matrix and $\mathbf{U}$ is the displacement vector, we obtain:

$$\frac{\partial r}{\partial \mathbf{N}}\frac{d\mathbf{N}}{d\mathbf{A}_j^{-1}} = \frac{df_{loc}}{d\mathbf{A}_j^{-1}} \tag{A.6}$$

In order to calculate $\frac{df_{loc}}{d\mathbf{A}_j^{-1}}$, it is more convenient to differentiate with respect to the stiffness:

$$\frac{df_{loc}}{d\mathbf{A}_j} = \frac{\partial f_{loc}}{\partial \mathbf{A}_{j=e}} + \frac{\partial f_{loc}}{\partial \mathbf{U}}\frac{d\mathbf{U}}{d\mathbf{A}_j} \tag{A.7}$$

The first part of A.7 is again local and evaluated easily:

$$\frac{\partial f_{loc}}{\partial \mathbf{A}_{j=e}} = \mathbf{s}^T\mathbf{BU} \tag{A.8}$$

and in order to find the second part adjoint sensitivity analysis method is applied:

$$\frac{df_{loc}}{d\mathbf{A}_j} = \frac{df_{loc}}{d\mathbf{A}_{j=e}} - \mathbf{V}^T\frac{d\mathbf{K}}{d\mathbf{A}_j}\mathbf{U} \tag{A.9}$$

where $\mathbf{V}$ is the adjoint displacement and $\mathbf{K}$ is the static stiffness matrix. The adjoint force is defined as:

$$\mathbf{f}_{ad} = \frac{df_{loc}}{d\mathbf{U}} = \mathbf{B}^T\mathbf{As} \tag{A.10}$$

therefore $\mathbf{V}$ is found from:

$$\mathbf{KV} = \mathbf{f}_{ad} \tag{A.11}$$

The sensitivity of failure index at the considered element with respect to the inverse of in-plane stiffness at element j is denoted by $\boldsymbol{\Phi}_j^m$:

$$\boldsymbol{\Phi}_j^m = \frac{\partial r}{\partial \mathbf{A}_j^{-1}} \tag{A.12}$$

whereas $\boldsymbol{\Psi}_j^m$ is the sensitivity with respect to in-plane stiffness:

$$\boldsymbol{\Psi}_j^m = \frac{\partial r}{\partial \mathbf{A}_j} \tag{A.13}$$

These sensitivities are related through:

$$\boldsymbol{\Phi}_j^m = -\mathbf{A}_j\boldsymbol{\Psi}_j^m\mathbf{A}_j \tag{A.14}$$

References

References

[1] J. N. Reddy, *Mechanics of Laminated Composite Plates and Shells: Theory and Analysis.* CRC press, 2004.

[2] H. Ghiasi, D. Pasini, and L. Lessard, "Optimum stacking sequence design of composite materials part i: Constant stiffness design," *Composite Structures*, vol. 90, no. 1, pp. 1–11, 2009.

[3] H. Ghiasi, K. Fayazbakhsh, D. Pasini, and L. Lessard, "Optimum stacking sequence design of composite materials part ii: Variable stiffness design," *Composite Structures*, vol. 93, no. 1, pp. 1–13, 2010.

[4] J. M. J. F. Van Campen, "Optimum lay-up design of variable stiffness composite structures," Ph.D. dissertation, Delft University of Technology, 2011.

[5] A. W. Blom, "Structural performance of fiber-placed, variable-stiffness composite conical and cylindrical shells," Ph.D. dissertation, Delft University of Technology, 2010.

[6] S. T. IJsselmuiden, "Optimal design of variable stiffness composite structures using lamination parameters," Ph.D. dissertation, Delft University of Technology, 2011.

[7] D. O. Evans, "Fiber placement." in *ASM International, Materials Park, OH*, 2001, pp. 477–479.

[8] B. F. Tatting and Z. Gürdal, "Automated finite element analysis of elastically-tailored plates," *NASA CR*, vol. 212679, 2003.

[9] A. Deturk, R. Diaz, G. Digiovanni, and B. Hyman, "Exploratory tests on fiber-reinforced plates with circular holes under tension." *AIAA Journal*, vol. 7, no. 9, pp. 1820–1821, 1969.

[10] S.-S. Yau and T.-W. Chou, "Strength of woven-fabric composites with drilled and molded holes," *Composite Materials Testing and Design, ASTM STP-972, American Society for Testing and Materials, Philadelphia, PA*, pp. 423–437, 1988.

[11] S. L. Gunderson and J. A. Lute, "The use of preformed holes for increased strength and damage tolerance of advanced composites," *Journal of reinforced plastics and composites*, vol. 12, no. 5, pp. 559–569, 1993.

[12] S. Jones and M. Platts, "Using internal fibre geometry to improve the performance of pin-loaded holes in composite materials," *Applied Composite Materials*, vol. 3, no. 2, pp. 117–134, 1996.

[13] M. Tosh and D. Kelly, "On the design, manufacture and testing of trajectorial fibre steering for carbon fibre composite laminates," *Composites Part A: Applied Science and Manufacturing*, vol. 31, no. 10, pp. 1047–1060, 2000.

[14] Z. Gürdal and R. Olmedo, "In-plane response of laminates with spatially varying fiber orientations: variable stiffness concept," *AIAA journal*, vol. 31, no. 4, pp. 751–758, 1993.

[15] B. F. Tatting and Z. Gürdal, *Design and manufacture of elastically tailored tow placed plates*. National Aeronautics and Space Administration, Langley Research Center, 2002.

[16] A. W. Blom, S. Setoodeh, J. M. Hol, and Z. Gürdal, "Design of variable-stiffness conical shells for maximum fundamental eigenfrequency," *Computers & Structures*, vol. 86, no. 9, pp. 870–878, 2008.

[17] A. Blom, P. Stickler, and Z. Gürdal, "Optimization of a composite cylinder under bending by tailoring stiffness properties in circumferential direction," *Composites Part B: Engineering*, vol. 41, no. 2, pp. 157–165, 2010.

[18] A. W. Blom, B. F. Tatting, J. M. Hol, and Z. Gürdal, "Fiber path definitions for elastically tailored conical shells," *Composites part B: engineering*, vol. 40, no. 1, pp. 77–84, 2009.

[19] L. Parnas, S. Oral, and U. Ceyhan, "Optimum design of composite structures with curved fiber courses," *Composites science and technology*, vol. 63, no. 7, pp. 1071–1082, 2003.

[20] S. Honda, Y. Oonishi, Y. Narita, and K. Sasaki, "Vibration analysis of composite rectangular plates reinforced along curved lines," *Journal of System Design and Dynamics*, vol. 2, no. 1, pp. 76–86, 2008.

[21] S. Honda, Y. Narita, and K. Sasaki, "Maximizing the fundamental frequency of laminated composite plates with optimally shaped curvilinear fibers," *Journal of System Design and Dynamics*, vol. 3, no. 6, pp. 867–876, 2009.

[22] S. Nagendra, S. Kodiyalam, J. E. Davis, and V. Parthasarathy, "Optimization of tow fiber paths for composite design," in *Proceedings of the 36th AIAA/ASME/ASCE/AHS/ASC Structures, Structural Dynamics and Materials (SDM) Conference, New Orleans, LA*, 1995.

[23] S. Honda and Y. Narita, "Vibration design of laminated fibrous composite plates with local anisotropy induced by short fibers and curvilinear fibers," *Composite Structures*, vol. 93, no. 2, pp. 902–910, 2011.

[24] A. Alhajahmad, M. M. Abdalla, and Z. Gürdal, "Design tailoring for pressure pillowing using tow-placed steered fibers," *Journal of Aircraft*, vol. 45, no. 2, pp. 630–640, 2008.

[25] C. Waldhart, Z. Gürdal, and C. Ribbens, "Analysis of tow placed, parallel fiber, variable stiffness laminates," in *Proceedings of the 37th AIAA/ASME/ASCE/AHS/ASC Structures, Structural Dynamics and Materials (SDM) Conference, Salt Lake City, UT*, 1996.

[26] Y. Katz, R. Haftka, and E. Altus, "Optimization of fiber directions for increasing the failure load of a plate with a hole," in *ASC technical conference*, vol. 4, 1989, pp. 62–71.

[27] M. Hyer and H. Lee, "The use of curvilinear fiber format to improve buckling resistance of composite plates with central circular holes," *Composite structures*, vol. 18, no. 3, pp. 239–261, 1991.

[28] M. Hyer and R. Charette, "Use of curvilinear fiber format in composite structure design," *AIAA journal*, vol. 29, no. 6, pp. 1011–1015, 1991.

[29] R. T. Haftka and J. H. Starnes, "Stiffness tailoring for improved compressive strength of composite plates with holes," *AIAA journal*, vol. 26, no. 1, pp. 72–77, 1988.

[30] J. Huang and R. Haftka, "Optimization of fiber orientations near a hole for increased load-carrying capacity of composite laminates," *Structural and Multidisciplinary Optimization*, vol. 30, no. 5, pp. 335–341, 2005.

[31] S. Setoodeh, M. Abdalla, and Z. Gürdal, "Design of variable stiffness laminates using lamination parameters," *Composites Part B: Engineering*, vol. 37, no. 4, pp. 301–309, 2006.

[32] M. Abdalla, S. Setoodeh, and Z. Gürdal, "Design of variable stiffness composite panels for maximum fundamental frequency using lamination parameters," *Composite structures*, vol. 81, no. 2, pp. 283–291, 2007.

[33] S. T. IJsselmuiden, M. M. Abdalla, and Z. Gürdal, "Optimization of variable-stiffness panels for maximum buckling load using lamination parameters," *AIAA journal*, vol. 48, no. 1, pp. 134–143, 2010.

[34] V. K. Pilaka, "Design of realistic variable stiffness laminates: A gradient-based optimizer for retrieving fiber orientation angles with average curvature constraints from lamination parameter distributions," Master's thesis, Delft University of Technology, 2010.

[35] J. Van Campen, C. Kassapoglou, and Z. Gürdal, "Design of fiber-steered variable-stiffness laminates based on a given lamination parameters distribution," in *Proceedings of the 52nd AIAA/ASME/ASCE/AHS/ASC Structures, Structural Dynamics and Materials (SDM) Conference. Denver, Colorado*, 2011.

[36] S. Setoodeh, A. W. Blom, M. M. Abdalla, and Z. Gürdal, "Generating curvilinear fiber paths from lamination parameters distribution," in *Proceedings of the 47th AIAA/ASME/ASCE/AHS/ASC Structures, Structural Dynamics and Materials (SDM) Conference. Newport, RI*, 2006.

[37] A. W. Blom, M. M. Abdalla, and Z. Gürdal, "Optimization of course locations in fiber-placed panels for general fiber angle distributions," *Composites Science and Technology*, vol. 70, no. 4, pp. 564–570, 2010.

[38] A. Nagy, M. Abdalla, and Z. Gürdal, "The geometry of fibre placement on general surfaces: Fibrepaths from fibre-angle distributions," Delft University of Technology, Internal report, 2010.

[39] M. Sun and M. Hyer, "Use of material tailoring to improve buckling capacity of elliptical composite cylinders," *AIAA journal*, vol. 46, no. 3, pp. 770–782, 2008.

[40] J. Tasi, "Effect of heterogeneity on the stability of composite cylindrical shells under axial compression." *AIAA journal*, vol. 4, no. 6, pp. 1058–1062, 1966.

[41] L. ZitzEvancih, "Designing graphite cylinders to resist buckling," in *Proceedings of AIAA/SAE/ASME/ASEE 21st Joint Propulsion Conference. Monterey, California*. American Institute of Aeronautics and Astronautics, 1985, pp. 8–10, doi:10.2514/6.1985-1101.

[42] B. Tripathy and K. Rao, "Stiffened composite axisymmetric shells-optimum lay-up for buckling by ranking," *Computers & structures*, vol. 46, no. 2, pp. 299–309, 1993.

[43] A. Rao and P. Shyju, “A meta-heuristic algorithm for multi-objective optimal design of hybrid laminate composite structures,” *Computer-Aided Civil and Infrastructure Engineering*, vol. 25, no. 3, pp. 149–170, 2010.

[44] S. Kobayashi, K. Koyama, H. Seko, and K. Hirose, “Compressive buckling of graphite-epoxy composite circular cylindrical shells,” in *Proceedings of International Conference on Composite Materials ICCM-IV*, 1982, pp. 555–564.

[45] H.-T. Hu and S. S. Wang, “Optimization for buckling resistance of fiber-composite laminate shells with and without cutouts,” *Composite structures*, vol. 22, no. 1, pp. 3–13, 1992.

[46] C.-C. Liang and H.-W. Chen, “Optimum design of fiber-reinforced composite cylindrical skirts for solid rocket cases subjected to buckling and overstressing constraints,” *Composites Part B: Engineering*, vol. 34, no. 3, pp. 273–284, 2003.

[47] C.-U. Kim, J.-H. Kang, C.-S. Hong, and C.-G. Kim, “Optimal design of filament wound structures under internal pressure based on the semi-geodesic path algorithm,” *Composite structures*, vol. 67, no. 4, pp. 443–452, 2005.

[48] Y. Hirano, “Buckling of angle-ply laminated circular cylindrical shells,” *Journal of Applied Mechanics*, vol. 46, pp. 233–234, 1979.

[49] Y. Nshanian and M. Pappas, “Optimal laminated composite shells for buckling and vibration,” *AIAA journal*, vol. 21, no. 3, pp. 430–437, 1983.

[50] K. Min and F. De Charentenay, “Optimum weight design of sandwich cylinders with orthotropic facings and core under combined loads,” *Computers & structures*, vol. 24, no. 2, pp. 313–322, 1986.

[51] G. Sun and J. Hansen, “Optimal design of laminated-composite circular-cylindrical shells subjected to combined loads,” *Journal of applied mechanics*, vol. 55, no. 1, pp. 136–142, 1988.

[52] G. Sun, “A practical approach to optimal design of laminated cylindrical shells for buckling,” *Composites science and technology*, vol. 36, no. 3, pp. 243–253, 1989.

[53] S. Adali, E. Summers, and V. Verijenko, “Optimisation of laminated cylindrical pressure vessels under strength criterion,” *Composite structures*, vol. 25, no. 1, pp. 305–312, 1993.

[54] R. Zimmermann, "Quick optimum buckling design of axially compressed, fiber composite cylindrical shells," *AIAA journal*, vol. 33, no. 10, pp. 1993–1995, 1995.

[55] Y. Xie, H. Yan, and Z. Liu, "Buckling optimization of hybrid-fiber multilayer-sandwich cylindrical shells under external lateral pressure," *Composites science and technology*, vol. 56, no. 12, pp. 1349–1353, 1996.

[56] M. Walker, T. Reiss, and S. Adali, "Multiobjective design of laminated cylindrical shells for maximum torsional and axial buckling loads," *Computers & structures*, vol. 62, no. 2, pp. 237–242, 1997.

[57] M. Walker, T. Reiss, and S. Adali, "Minimum weight design of composite hybrid shells via symbolic computation," *Journal of the Franklin Institute*, vol. 334, no. 1, pp. 47–56, 1997.

[58] A. Smerdov, "A computational study in optimum formulations of optimization problems on laminated cylindrical shells for buckling i. shells under axial compression," *Composites science and technology*, vol. 60, no. 11, pp. 2057–2066, 2000.

[59] A. Smerdov, "A computational study in optimum formulations of optimization problems on laminated cylindrical shells for buckling ii. shells under external pressure," *Composites science and technology*, vol. 60, no. 11, pp. 2067–2076, 2000.

[60] S. Adali, V. E. Verijenko, and A. Richter, "Minimum sensitivity design of laminated shells under axial load and external pressure," *Composite structures*, vol. 54, no. 2, pp. 139–142, 2001.

[61] J. Foldager, J. Hansen, and N. Olhoff, "Optimization of the buckling load for composite structures taking thermal effects into account," *Structural and Multidisciplinary Optimization*, vol. 21, no. 1, pp. 14–31, 2001.

[62] T. Messager, M. Pyrz, B. Gineste, and P. Chauchot, "Optimal laminations of thin underwater composite cylindrical vessels," *Composite Structures*, vol. 58, no. 4, pp. 529–537, 2002.

[63] M. Walker and R. Smith, "A methodology to design fibre reinforced laminated composite structures for maximum strength," *Composites Part B: Engineering*, vol. 34, no. 2, pp. 209–214, 2003.

[64] P. Y. Tabakov and E. Summers, "Lay-up optimization of multilayered anisotropic cylinders based on a 3-d elasticity solution," *Computers & structures*, vol. 84, no. 5, pp. 374–384, 2006.

[65] R. Azarafza, S. Khalili, A. Jafari, and A. Davar, "Analysis and optimization of laminated composite circular cylindrical shell subjected to compressive axial and transverse transient dynamic loads," *Thin-Walled Structures*, vol. 47, no. 8, pp. 970–983, 2009.

[66] E. Lindgaard, E. Lund, and K. Rasmussen, "Nonlinear buckling optimization of composite structures considering worst shape imperfections," *International Journal of Solids and Structures*, vol. 47, no. 22, pp. 3186–3202, 2010.

[67] K. Y. Maalawi, "Use of material grading for enhanced buckling design of thin-walled composite rings/long cylinders under external pressure," *Composite Structures*, vol. 93, no. 2, pp. 351–359, 2011.

[68] C. Yuan, O. Bergsma, S. Koussios, L. Zu, and A. Beukers, "Optimization of sandwich composites fuselages under flight loads," *Applied composite materials*, vol. 19, no. 1, pp. 47–64, 2012.

[69] M. J. Powell, "An efficient method for finding the minimum of a function of several variables without calculating derivatives," *The computer journal*, vol. 7, no. 2, pp. 155–162, 1964.

[70] J. Onoda, "Optimal laminate configurations of cylindrical shells for axial buckling," *AIAA journal*, vol. 23, no. 7, pp. 1093–1098, 1985.

[71] H. Fukunag and G. N. Vanderplaats, "Stiffness optimization of orthotropic laminated composites using lamination parameters," *AIAA journal*, vol. 29, no. 4, pp. 641–646, 1991.

[72] J. L. Grenestedt, "Optimization of bent composite cylinders," *Composite structures*, vol. 30, no. 1, pp. 103–108, 1995.

[73] J. Grenestedt and P. Gudmundson, "Layup optimization of composite material structures," in *IUTAM Symposium on Optimal Design with Advanced Materials*, 1993, pp. 311–336.

[74] C. G. Diaconu, M. Sato, and H. Sekine, "Buckling characteristics and layup optimization of long laminated composite cylindrical shells subjected to combined loads using lamination parameters," *Composite structures*, vol. 58, no. 4, pp. 423–433, 2002.

[75] R. Matsuzaki and A. Todoroki, "Stacking-sequence optimization using fractal branch-and-bound method for unsymmetrical laminates," *Composite Structures*, vol. 78, no. 4, pp. 537–550, 2007.

[76] J. C. Riddick, "Prebuckling, buckling, and postbuckling response of segmented circular composite cylinders," Ph.D. dissertation, Virginia Polytechnic Institute and State University, 2001.

[77] J. C. Riddick and M. W. Hyer, "Response of segmented-stiffness composite cylinders to axial end shortening," *Composite structures*, vol. 40, no. 2, pp. 103–114, 1997.

[78] M. Hyer and J. Riddick, "Internal pressure loading of segmented-stiffness composite cylinders," *Composite structures*, vol. 45, no. 4, pp. 311–320, 1999.

[79] J. C. Riddick and M. W. Hyer, "Buckling and postbuckling analysis of segmented-stiffness circular composite cylinders," *Proceedings of 42st SDM Conference AIAA*, 2001.

[80] J. C. Riddick and M. W. Hyer, "Postbuckling behavior of segmented circular composite cylinders," *AIAA journal*, vol. 42, no. 1, pp. 185–195, 2004.

[81] J. C. Riddick and M. W. Hyer, "Influence of imperfections on buckling and postbuckling of segmented composite cylinders," in *Proceedings of the 43rd AIAA/ASME/ASCE/AHS/ASC Structures, Structural Dynamics, and Materials Conference. Denver, Colorado.* American Institute of Aeronautics and Astronautics, 2002.

[82] M. S. Darlow and J. Creonte, "Optimal design of composite helicopter power transmission shafts with axially varying fiber layup," *Journal of the American Helicopter Society*, vol. 40, no. 2, pp. 50–56, 1995.

[83] M. Paschero and M. W. Hyer, "Improvement of axial load capacity of elliptical cylindrical shells," *AIAA Journal*, vol. 47, no. 1, pp. 142–156, 2009.

[84] B. F. Tatting, "Analysis and design of variable stiffness composite cylinders," Ph.D. dissertation, Virginia Polytechnic Institute and State University, 1998.

[85] K. C. Wu, "Design and analysis of tow-steered composite shells using fiber placement," in *Proceedings of the American society for composites, 23rd technical conference. Memphis, TN, USA*, 2008.

[86] K. C. Wu, B. F. Tatting, B. H. Smith, R. S. Stevens, G. P. Occhipinti, J. B. Swift, D. C. Achary, and R. P. Thornburgh, "Design and manufacturing of tow-steered composite shells using fiber placement," in *Proceedings of the 50th AIAA/ASME/ASCE/AHS/ASC Structures, Structural Dynamics and Materials Conference. Palm Springs, California.* American Institute of Aeronautics and Astronautics, 2009.

[87] K. Chauncey Wu, B. Stanford, G. Hrinda, Z. Wang, R. Martin, and H. Kim, "Structural assessment of advanced composite tow-steered shells," in *Proceedings of the 54th AIAA/ASME/ASCE/AHS/ASC Structures, Structural Dynamics and Materials Conference. Boston, Massachusetts.* American Institute of Aeronautics and Astronautics, 2013.

[88] M. Sun and M. W. Hyer, "Use of material tailoring to improve buckling capacity of elliptical composite cylinders," *AIAA journal*, vol. 46, no. 3, pp. 770–782, 2008.

[89] H.-C. Lo and M. W. Hyer, "Fundamental frequencies of elliptical composite cylinders with circumferentially varying fiber orientation," *AIAA journal*, vol. 50, no. 4, pp. 928–937, 2012.

[90] A. W. Leissa, *Vibration of shells.* Scientific and Technical Information Office, National Aeronautics and Space Administration, 1973.

[91] C. Weatherburn, *Differential geometry.* Cambridge University, 1927, vol. 1.

[92] I. Sokolnikoff and R. Specht, *Mathematical theory of elasticity.* McGraw-Hill New York, 1956, vol. 83.

[93] A. Saada, *Elasticity: Theory and Applications.* Pergamon Press Inc., New York, 1974.

[94] G. Caprino and C. Visconti, "A note on specially orthotropic laminates," *Journal of Composite Materials*, vol. 16, pp. 395–399, 1982.

[95] S. Tsai and N. Pagano, "Invariant properties of composite materials." DTIC Document, Tech. Rep., 1968.

[96] H. Hahn and S. Tsai, *Introduction to composite materials.* CRC, 1980.

[97] V. Hammer, M. Bendsøe, R. Lipton, and P. Pedersen, "Parametrization in laminate design for optimal compliance," *International journal of solids and structures*, vol. 34, no. 4, pp. 415–434, 1997.

[98] C. G. Diaconu, M. Sato, and H. Sekine, “Feasible region in general design space of lamination parameters for laminated composites,” *AIAA journal*, vol. 40, no. 3, pp. 559–565, 2002.

[99] M. Bloomfield, C. Diaconu, and P. Weaver, “On feasible regions of lamination parameters for lay-up optimization of laminated composites,” *Proceedings of the Royal Society A: Mathematical, Physical and Engineering Science*, vol. 465, no. 2104, pp. 1123–1143, 2009.

[100] J. Foldager, J. Hansen, and N. Olhoff, “A general approach forcing convexity of ply angle optimization in composite laminates,” *Structural and Multidisciplinary Optimization*, vol. 16, no. 2, pp. 201–211, 1998.

[101] S. Setoodeh, M. Abdalla, and Z. Gürdal, “Approximate feasible regions for lamination parameters aiaa-2006-6973,” in *11th AIAA/ISSMO Multidisciplinary Analysis and Optimisation Conference, Portsmouth, Virginia, 6–8 September*, 2006.

[102] A. Khani, M. Abdalla, and Z. Gürdal, “Circumferential stiffness tailoring of general cross section cylinders for maximum buckling load with strength constraints,” *Composite Structures*, vol. 94, no. 9, pp. 2851 – 2860, 2012.

[103] A. Khani, M. Abdalla, and Z. Gürdal, “Circumferential stiffness tailoring of long composite non-circular cylinders,” in *Proceedings of the 8th World Congress on Structural and Multidisciplinary Optimization*. ISSMO, June 1-5 2009, lisbon, Portugal.

[104] W. Voigt, “Theoretische studienüber die elasticitätsverhÃď’ltnisse der krystalle,” *Göttinger Abhandlungen*, vol. 34, p. 53, 1887.

[105] M. Paschero and M. Hyer, “Improvement of axial load capacity of elliptical cylindrical shells,” *AIAA journal*, vol. 47, no. 1, pp. 142–156, 2009.

[106] M. Paschero and M. Hyer, “Improvement of axial buckling capacity of elliptical lattice cylinders,” *AIAA journal*, vol. 49, no. 2, pp. 396–410, 2011.

[107] S. B. Dong, J. B. Kosmatka, and H. C. Lin, “On saint-venant’s problem for an inhomogeneous, anisotropic cylinder—part i: Methodology for saint-venant solutions,” *Journal of Applied Mechanics*, vol. 68, no. 3, pp. 376–381, 2001.

[108] L. Kantorovich and V. Krylov, *Approximate Methods of Higher Analysis*. Noordhoff, Groningen, 1958, vol. 162.

[109] E. Sternberg and J. Knowles, “Minimum energy characterizations of saint-venant’s solution to the relaxed saint-venant problem,” *Archive for Rational Mechanics and Analysis*, vol. 21, no. 2, pp. 89–107, 1966.

[110] D. Iesan, “On saint-venant’s problem,” *Archive for Rational Mechanics and Analysis*, vol. 91, no. 4, pp. 363–373, 1986.

[111] C. Dym, *Stability theory and its applications to structural mechanics*. Dover Publications, 2002.

[112] “Abaqus manual, version 6.11,” Dassault systems, 2011.

[113] E. F. Bruhn, R. Bollard *et al.*, *Analysis and design of flight vehicle structures*. SR Jacobs Indianapolis, 1973.

[114] S. T. IJsselmuiden, M. M. Abdalla, O. Seresta, and Z. Gürdal, “Multi-step blended stacking sequence design of panel assemblies with buckling constraints,” *Composites Part B: Engineering*, vol. 40, no. 4, pp. 329–336, 2009.

[115] N. Olhoff, “Multicriterion structural optimization via bound formulation and mathematical programming,” *Structural optimization*, vol. 1, no. 1, pp. 11–17, 1989.

[116] C. Fleury and L. A. Schmit, *Dual methods and approximation concepts in structural synthesis*. National Aeronautics and Space Administration, Scientific and Technical Information Branch, 1980, vol. 3226.

[117] D. B. Adams, L. T. Watson, Z. Gürdal, and C. M. Anderson-Cook, “Genetic algorithm optimization and blending of composite laminates by locally reducing laminate thickness,” *Advances in Engineering Software*, vol. 35, no. 1, pp. 35–43, 2004.

[118] M. Autio, “Determining the real lay-up of a laminate corresponding to optimal lamination parameters by genetic search,” *Structural and multidisciplinary optimization*, vol. 20, no. 4, pp. 301–310, 2000.

[119] S. Setoodeh, M. M. Abdalla, and Z. Gürdal, “Design of variable–stiffness laminates using lamination parameters,” *Composites Part B: Engineering*, vol. 37, no. 4, pp. 301–309, 2006.

[120] M. M. Abdalla, S. Setoodeh, and Z. Gürdal, “Design of variable stiffness composite panels for maximum fundamental frequency using lamination parameters,” *Composite structures*, vol. 81, no. 2, pp. 283–291, 2007.

[121] S. T. IJsselmuiden, M. M. Abdalla, and Z. Gürdal, "Implementation of strength-based failure criteria in the lamination parameter design space," *AIAA journal*, vol. 46, no. 7, pp. 1826–1834, 2008.

[122] J. Barthelemy and R. Haftka, "Approximation concepts for optimum structural design - a review," *Structural and Multidisciplinary Optimization*, vol. 5, no. 3, pp. 129–144, 1993.

[123] S. Setoodeh, M. M. Abdalla, S. T. IJsselmuiden, and Z. Gürdal, "Design of variable-stiffness composite panels for maximum buckling load," *Composite Structures*, vol. 87, no. 1, pp. 109–117, 2009.

[124] R. Haftka and Z. Gürdal, *Elements of structural optimization.* Springer, 1992, vol. 11.

[125] O. Storaasli and J. Sobieszczanski, "On the accuracy of the taylor approximation for structure resizing," *AIAA Journal*, vol. 12, no. 2, pp. 231–233, 1974.

[126] A. K. Noor and H. E. Lowder, "Structural reanalysis via a mixed method," *Computers & Structures*, vol. 5, no. 1, pp. 9–12, 1975.

[127] J. H. Starnes Jr and R. T. Haftka, "Preliminary design of composite wings for buckling, strength, and displacement constraints," *Journal of Aircraft*, vol. 16, no. 8, pp. 564–570, 1979.

[128] K. Svanberg, "A class of globally convergent optimization methods based on conservative convex separable approximations," *SIAM Journal on Optimization*, vol. 12, no. 2, pp. 555–573, 2002.

[129] A. P. Seyranian, E. Lund, and N. Olhoff, "Multiple eigenvalues in structural optimization problems," *Structural Optimization*, vol. 8, no. 4, pp. 207–227, 1994.

[130] M. Bruyneel, B. Colson, and A. Remouchamps, "Discussion on some convergence problems in buckling optimisation," *Structural and Multidisciplinary Optimization*, vol. 35, no. 2, pp. 181–186, 2008.

[131] M. Eldred, V. Venkayya, and W. Anderson, "Mode tracking issues in structural optimization," *AIAA journal*, vol. 33, no. 10, pp. 1926–1933, 1995.

[132] E. J. Haug and J. S. Arora, *Applied optimal design: mechanical and structural systems.* Wiley New York, 1979, vol. 153.

[133] L. A. Schmit and H. Miura, "Approximation concepts for efficient structural synthesis," *NASA CR*, vol. 2552, 1976.

[134] A. Khani, S. IJsselmuiden, M. Abdalla, and Z. Gürdal, "Design of variable stiffness panels for maximum strength using lamination parameters," *Composites Part B: Engineering*, vol. 42, no. 3, pp. 546–552, 2011.

[135] Z. Gürdal, R. Haftka, and P. Hajela, *Design and optimization of laminated composite materials.* Wiley New York, 1999.

[136] N. Kogiso, S. Nakagawa, and Y. Murotsu, "Lamination parameters applied to reliability-based in-plane strength design of composites," *AIAA journal*, vol. 41, no. 11, pp. 2200–2207, 2003.

[137] H. Nakayasu and Z. Maekawa, "A comparative study of failure criteria in probabilistic fields and stochastic failure envelopes of composite materials," *Reliability Engineering & System Safety*, vol. 56, no. 3, pp. 209–220, 1997.

[138] I. Daniel, O. Ishai, I. Daniel, and I. Daniel, *Engineering mechanics of composite materials.* Oxford university press New York, 1994, vol. 3.

[139] A. Dixon, "The eliminant of three quantics in two independent variables," *Proceedings of the London Mathematical Society*, vol. 2, no. 1, pp. 49–69, 1909.

[140] A. Groenwold and R. Haftka, "Optimization with non-homogeneous failure criteria like tsai-wu for composite laminates," *Structural and Multidisciplinary Optimization*, vol. 32, no. 3, pp. 183–190, 2006.

Summary

Automated fibre placement (AFP) machines are able to place simultaneously several bundles of fibres, called tows, on a surface. Using AFP machines, it is also possible to manufacture composite laminates with fibres placed in curvilinear paths. The fibre orientations and stiffness properties of these laminates are spatially varied and hence they are called variable stiffness (VS) laminates in contrast to the traditional laminates with straight fibres which are called constant stiffness (CS) laminates.

Past research has shown that the structural performance of laminated composite structures can be improved by spatial tailoring of laminate stiffness. One of the widely used structural components in aerospace industry are cylindrical shells. In this thesis, a computationally efficient framework was developed for circumferential laminate stiffness tailoring of unstiffened and longitudinally stiffened cylindrical shells with arbitrary cross-sections to maximise the buckling capacity with consideration of strength constraints. In addition, the AFP manufacturing constraint on the maximum curvature of curvilinear fibre paths was considered. This constraint was applied to avoid wrinkling of the fibres placed inside the turn of a curved tow. The aforementioned framework utilised computationally efficient analysis and optimisation tools.

A semi-analytical solution was developed for static and buckling analysis of cylindrical shells under axial force, bending, and torsion, or a combination thereof. The semi-analytical solution was developed based on the analytical displacement field from the Saint-Venant's solution and using finite difference for the discretised cross-section. Due to the limitation of discretisation to the circumferential direction, the semi-analytical finite difference (SAFD) solution is compatible with circumferential tailoring, has fewer degrees of freedom than the full finite element analysis and is computationally more efficient.

A multi-step optimisation framework was developed in the ASCM group of TUDelft to find the optimum straight and steered fibre laminates. The design drivers related to the structural performance and manufacturing are considered in different steps of the multi-step framework and the most suitable optimisation algorithm is used in each step. In the first step of the multi-step framework, the output is the theoretical or conceptual optimum distribution of laminate stiffness properties, which does not provide information about the realistic layup, and the

design drivers are the structural performance measures. In the seconds step, the output is the realistic optimum fibre angle or distribution of fibre angles in each layer of the CS or VS laminates, respectively. The design drivers of the second step are the theoretical designs, found in the first step, and the steering curvature constraint. In the third step, the outputs are the steered fibre paths of the VS laminate and the design driver is the optimum fibre angle distribution found in the second step. The multi-step framework is based on convex separable approximations of the structural performance measures, i.e. buckling factor and material failure index.

The material failure envelope is dependent on the ply angles, however, instead of the ply angles, lamination parameters are used as design variables in the first step of the multi-step framework. This problem is resolved using a conservative Tsai-Wu failure envelope developed by IJsselmuiden et al. [139], which is independent of the ply angles. The main contribution made by the author to the multi-step optimisation framework was to develop convex separable approximations of the material failure index.

The developed framework for circumferential laminate stiffness tailoring of arbitrary cross-section cylinders was applied on two unstiffened cylindrical shells, namely a circular cylinder under bending and an elliptical cylinder under axial compression, and two longitudinally stiffened circular cylinder under bending with different thickness to radius ratios. Significant improvements, from %25.3 to %43.2, were obtained in the linear buckling capacity of the selected theoretical VS laminates over the selected theoretical CS laminate designs. The buckling load of the realistic laminate designs were less than the theoretical laminate designs mainly due to the limited number of layers of the realistic CS and VS laminates and constraining the steering curvature in realistic VS laminates. The improvements in the linear buckling capacity of the realistic VS laminates over the realistic CS laminates were between %17.9 and %31.9. The buckling capacity improvement of the steered fibre laminates with respect to the straight fibre ones, was due to the stiffness and section load redistribution.

In the the unstiffened circular cylinder under bending, the axial section force distribution of the VS laminate was almost uniform in the compression side of the cross-section, while this distribution for the CS laminate was sinusoidal. The magnitude of the maximum axial section forces on the compression side of the VS laminate was smaller than the CS laminate and hence the buckling capacity was improved.

In the unstiffened elliptical cylinder under axial compression with the VS laminate, the axial compressive section load was redistributed such that less compressive section load was carried by the regions with larger radius of curvature, which were more prone to buckling in the quasi-isotropic (QI) and CS laminates, and more compressive section load was transferred to the areas with smaller radius of curvature, which were more buckling resistant in the QI and CS laminates. Therefore, the material around the elliptical cross-section of the cylinder with the VS laminate was used more efficiently, the buckling modes were expanded all around the circumference and the buckling load was increased.

In the stiffened circular cylinder under bending, improvement in the buckling moment of the VS laminate design compared to the CS laminate design was due to two mechanisms; A global load redistribution, similar to the unstiffened circular cylinder under bending, and a local load redistribution in each area between two stiffeners in the compression side of the cross-section, which further reduced the magnitude of the compressive load in the middle of that local area by transferring it to the stiffened locations.

To investigate the effect of laminate thickness variation in addition to fibre steering in buckling capacity improvement, the theoretical variable thickness VS laminates of the considered case studies were obtained and compared with the corresponding theoretical constant thickness VS laminates. Significant improvements, from 24% to 57.7%, were obtained in the buckling capacity of the theoretical variable thickness VS laminate over the theoretical constant thickness VS laminate with the same weight. The effect of the laminate thickness variation in buckling capacity improvements was mainly due to the increased out of plane stiffness in the buckling critical regions, however, in the elliptical cylinder, the laminate thickness variation was effective in buckling capacity improvement also through load redistribution.

Nonlinear buckling capacities of the obtained designs were close to the linear buckling capacities. This showed that no significant loss of stiffness happened in the prebuckling regime.

SAMENVATTING

Machines voor automatische vezelplaatsing (AFP) zijn in staat om meerdere vezelbundels, ook wel tows genaamd, gelijktijdig op een oppervlak te plaatsen. Met behulp van AFP machines is het ook mogelijk om composiet laminaten te maken met vezels die in gekromde banen zijn geplaatst. De vezeloriëntaties en stijfheidseigenschappen zijn in zulke laminaten ruimtelijk variabel en worden daarom ook wel variabele stijfheid (VS) laminaten genoemd in tegenstelling tot conventionele laminaten met rechte vezels welke constante stijfheid (CS) laminaten worden genoemd.

Onderzoek uit het verleden laat zien dat de mechanische prestaties van een gelamineerde composieten constructie verbeterd kunnen worden door ruimtelijke herverdeling van de stijfheid van het laminaat. Een in de lucht- en ruimtevaartindustrie wijdverbreid onderdeel is de cilindrische schaal. Voor dit proefschrift werd een numeriek efficiënte methode ontwikkeld voor stijfheidsherverdeling in omtreksrichting voor zowel onverstijfde als in lengterichting verstijfde cilindrische schalen van willekeurige doorsnede ten einde de kniklast van de schaal te vergroten rekening houdend met de grenzen aan de sterkte van het materiaal. Daarnaast werd ook rekening gehouden met de bij AFP behorende beperking van de maximaal mogelijke kromming in vezelpaden. Deze beperking werd opgelegd om het rimpelen van vezels in de binnenbocht van een gekromde tow te vermeiden. In de voornoemde methode werd gebruikt gemaakt van numeriek efficiënte analyse en optimalisatie tools.

Een semi-analytische oplossing werd afgeleid voor statische en knik analyse van cilindrische schalen onder een axiale belasting, een buigmoment, een torsiemoment of een combinatie daarvan. De semi-analytische oplossing werd afgeleid aan de hand van het analytische vervormingsveld van Saint-Venants oplossing en gebruikmakend van finiete differentiatie voor de gediscretiseerde doorsnede. Door alleen in omtreksrichting te discretiseren heeft de semi-analytische finiete differentiatie (SAFD) methode minder vrijheidsgraden dan volledige eindige elementen analyse en is daardoor numeriek efficiënter.

Een meerstaps optimalisiatiemethode voor optimale laminaten met rechte en gestuurde vezels is binnen de ASCM groep van de TU Delft ontwikkeld. De aan mechanische prestaties en productie gerelateerde ontwerp drijvers worden elk in verschilleden optimalisatiestappen meegenomen en het meeste geschikte algoritme wordt toegepast in iedere stap. De uitkomst van de eerste stap van de meerstapsmethode is de theoretische of conceptuele verdeling van laminaateigenschappen, welke geen informatie bieden over de realistische lagenopbouw, en waarvan de verdeling gedreven wordt door de mechanische prestaties. De uitkomst van de tweede stap is een realistische optimale vezelhoekverdeling in elke laag van het CS of VS laminaat, respectievelijk. De drijvers van de tweede stap zijn het theoretische ontwerp gevonden in de eerste stap en de toelaatbare kromming van de vezels. De uitkomst van de derde stap zijn gestuurde vezelpaden van het VS laminaat. De drijvers van de derde stap zijn de vezelhoekverdeling uit de tweede stap. De meerstapsmethode is gebaseerd op convexe separabele benaderingen van de mate van mechanische prestatie, bedoeld zijn de knikfactor en de materiaalbezwijkindex.

De materiaalbezwijkenvelop hangt af van de oriÃńntatie van elke laag in het laminaat. In de eerste optimalisatiestap van de meerstapsmethode worden echter lamineeringsparameters gebruikt als ontwerpvariabelen. Dit probleem wordt omzeild door het gebruik van een conservatieve Tsai-Wu bezwijkenvelop ontwikkeld door IJsselmuiden et al. [139], die onafhankelijk is van laagoriëntaties. De belangrijkste bijdrage van de auteur aan de meerstapsmethode was de afleiding van de convexe separabele benadring van de bezwijkindex.

De hier ontwikkelde methode voor de laminaatstijfheidsherverdeling in omtreksrichting van cilinders met een willekeurige doorsnede is toegepast op twee onverstijfde cilindrische schalen, namelijk een ronde cilinder belast in buiging en een axiaal belaste elliptische cilinder, en op twee in de lengterichting verstijfde en in buiging belaste ronde cilinders met verschillende ratioâĂŹs in radius en wanddikte. Significante verbeteringen, van 25.3% tot 43.2%, werden behaald voor de lineaire kniklast voor de geselecteerde theoretische VS laminaatontwerpen ten opzichte van de geselecteerde CS laminaatontwerpen. De kniklast voor de realistische laminaatontwerpen was minder dan voor de theoretische laminaatontwerpen, voornamelijk door het beperkte aantal lagen in de realistische CS en VS laminaten en door de beperking in de toelaatbare kromming in realistische VS laminaten. De verbeteringen in de lineaire kniklast van de realistische VS laminaten ten opzichte van de realistische CS laminaten lagen tussen 17.9% en 31.9%. De verbetering in kniklast van de laminaten met gestuurde vezels ten opzichte van de laminaten met rechte vezels kon verklaard worden door de herverdeling in stijfheid en sectiebelasting.

De axiale sectiebelastingsverdeling was voor het VS laminaatontwerp van de onverstijfde ronde cilinder in buiging nagenoeg uniform aan de op druk belaste zijde van de doorsnede, terwijl deze verdeling voor het CS laminaat een sinusoÃŕde was. De grootte van de maximale axiale sectiebelasting aan de op druk belaste zijde van het VS laminaat was kleiner dan voor het CS laminaat en dus was de kniklast verbeterd.

In de onverstijfde elliptische cilinder belast in axiale compressie werd met het VS laminaat de axiale drukbelasting dusdanig herverdeeld dat de secties met een grotere krommingstraal, die voor quasi-isotrope (QI) en CS laminaten gevoeliger waren voor knik, minder belast werden, terwijl de secties met een sterkere krommingsstraal zwaarder belast werden, die voor quasi-isotrope (QI) en CS laminaten juist beter bestand waren tegen knik. Het materiaal in de elliptische doorsnede werd hierdoor in de cilinder met het VS laminaat efficiënter benut, knikmodi werden over de gehele omtrek van de cilinder verdeeld en de kniklast werd verhoogd.

De verbetering in kniklast voor de verstijfde in buiging belaste cilinder voor het VS laminaat ten opzichte van het VS laminaat kon aan twee mechanismen worden toegeschreven; een globale lastherverdeling, vergelijkbaar met de herverdeling die optrad voor de onverstijfde cilinder in buiging, en een lokale lastherverdeling in de ruimte tussen twee verstijvers aan de op druk belaste zijde van de doorsnede, waardoor de drukbelasting in het midden van de sectie nog verder verlaagd werd door overdracht van de belasting aan de verstijvers.

Om het effect van de variatie in laminaatdikte naast dat van vezelsturen op de verbetering in kniklast te bestuderen, werden de theoretische VS laminaatontwerpen met variabele dikte voor de hiervoor genoemde ontwerpstudies berekend en vergeleken met het beste theoretishe VS ontwerp met constante dikte. Significante verbeteringen, tussen de 24% tot 57.7%, werden behaald voor de kniklast van de theortische variabele dikte VS laminaten met het zelfde gewicht. Het effect van diktevariatie op verbetering van de kniklast kwam met name door een toename in materiaaldikte in voor de kniklast kritische regio's. Desalniettemin droeg de variatie in laminaatdikte voor de elliptisch cilinder ook bij aan lastherverdeling.

De niet-lineaire kniklasten lagen voor de berekende ontwerpen dicht bij de lineaire kniklasten. Dit liet zien dat er geen significant verlies in stijfheid optrad in het pre-knik regiem.